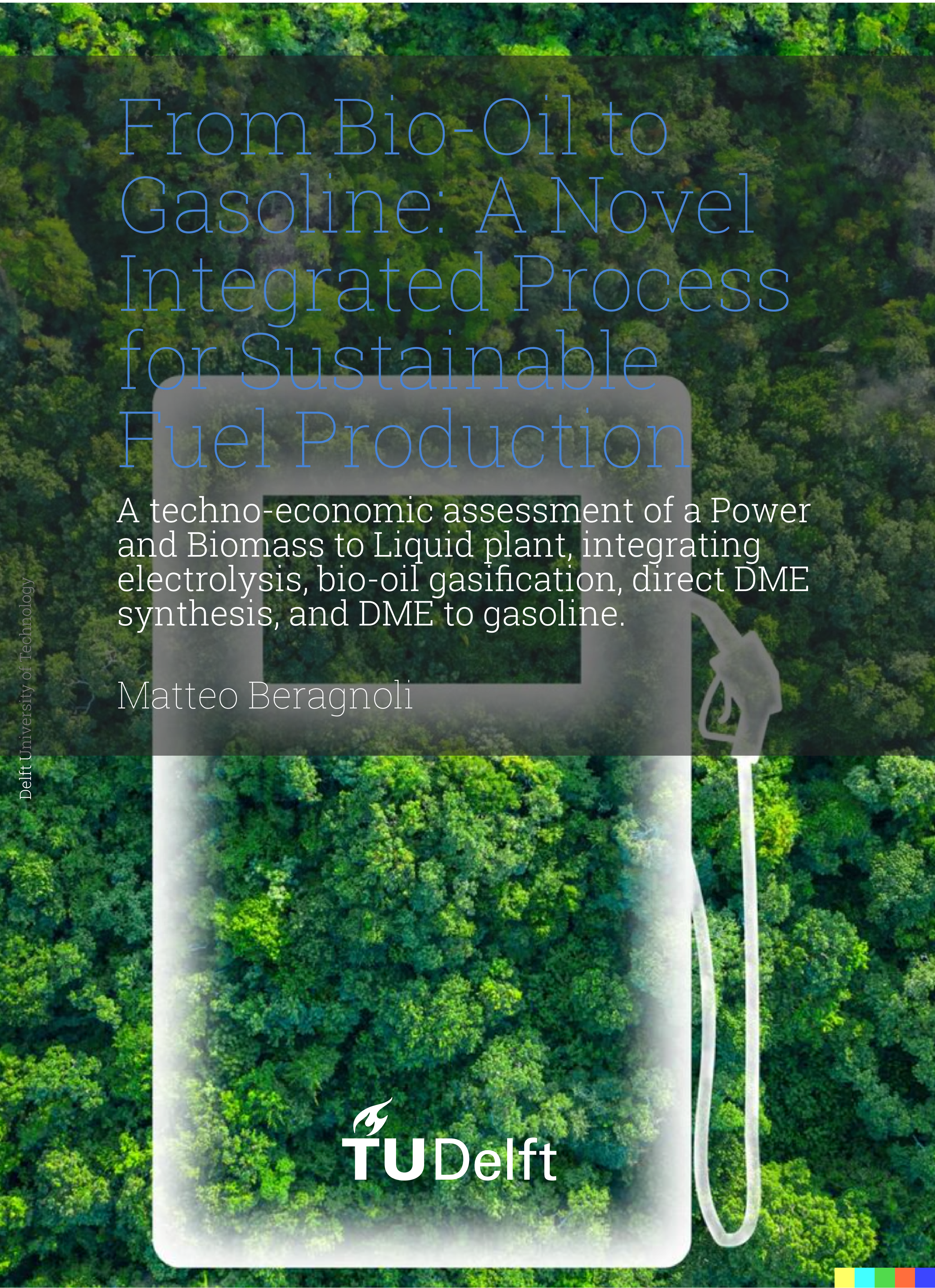

From Bio-Oil to Gasoline: A Novel Integrated Process for Sustainable Fuel Production

A techno-economic assessment of a Power and Biomass to Liquid plant, integrating electrolysis, bio-oil gasification, direct DME synthesis, and DME to gasoline.

Matteo Beragnoli

Delft University of Technology

From Bio-Oil to Gasoline: A Novel Integrated Process for Sustainable Fuel Production

A techno-economic assessment of a Power and Biomass to Liquid plant, integrating electrolysis, bio-oil gasification, direct DME synthesis, and DME to gasoline.

by

Matteo Beragnoli

Student Name	Student Number
Beragnoli Matteo	5282373

TU Delft Supervisor:	Wiebren de Jong
Committee member:	Luis Cutz
Committee member:	Mahinder Ramdin

Faculty of Mechanical, Maritime, and Materials Engineering - 3me

Cover: ©Getty - extended with DALL-E by OpenAI

TU Delft

To my family

Abstract

The intensification of human and industrial activities since the Industrial Revolution has led to a significant increase in global greenhouse gas emissions, posing a threat to life on our planet. As the transportation sector contributes to 23% of global CO_2 emissions, it is imperative to reduce its carbon footprint. Developing a worldwide sustainable biofuel production chain is crucial for this purpose. The Biomass4transport project, a collaboration between TU Delft and the Biomass Technology Group, aims to achieve this by focusing on the production of second-generation biofuels in the Dutch context.
In this context, a techno-economic analysis of a Power and Biomass to Liquid (PBtL) plant that incorporates water electrolysis, pyrolysis oil gasification, and synthesis gas upgrading for gasoline production is presented.

The PBtL plant processes 5000 kg/h of pine wood-derived pyrolysis oil, which undergoes gasification in an oxygen-blown entrained flow gasifier. Subsequent purification steps include cyclones, filters, for the removal of particulate matter and solid ZnO sorbents for the removal of H_2S. A solid oxide electrolysis cell produces hydrogen and oxygen streams; the former adjusts the H2:CO_x ratio before syngas upgrading, while the latter serves as an oxidizing agent in the gasifier. The synthesis gas is converted to dimethyl ether (DME) in a one-step direct conversion membrane reactor, enabling in-situ water removal and enhanced conversion performance. In a subsequent reactor, DME is upgraded to a hydrocarbon mixture, which is further processed to obtain gasoline and LPG.

The process has been modelled by integrating Aspen Plus, Matlab - where an isothermal plug flow membrane reactor model has been coded - and Excel. Material recycling and heat integration strategies have been employed to enhance the plant's performance in terms of product yield and energy efficiency.

Finally, an economic analysis entailing the calculation of the Net Present Value (NPV) of the plant has been conducted, to assess the conditions under which the plant becomes profitable.

The process has an energy efficiency of 51.8% but could potentially rise to 61.8% with an optimized strategy for hydrogen extraction from the sweep gas of the DME membrane reactor. Due to the absence of CO_2 extraction along the process, the carbon efficiency of the process is 95.7%. Both values are higher than the ones of PBtL processes based on hydrogen-enhanced methanol-to-gasoline processes found in literature.

Additionally, the economic analysis showed that the plant is not profitable in the current market conditions. However, with a decline in the price of electricity and/or a reduction in the taxation rate for gasoline, the plant could become profitable, as shown by the sensitivity analysis on the NPV.

Contents

List of Figures

List of Tables

Nomenclature

Abbreviations

Abbreviation	Definition
AEL	Alkaline Electrolysis
AEMEL	Anion Exchange Membrane Electrolysis
BEC	Bare Erected Cost
BoD	Basis of Design
BtL	Biomass to Liquid
BTX	Benzene, toluene, xylene aromatics
CC	Carbon Conversion
CF	Cash Flow
CGE	Cold Gas Efficiency
COP	United Nations Climate Change Conference
DEA	Diethanolamine
DME	Dimethyl Ether
DtG	DME to Gasoline
EPCC	Engineering Procurement and Construction Cost
EoS	Equation of State
ER	Equivalence Ratio
ETOC	Escalated Total Overnight Cost
FT	Fischer-Tropsch
GAC	Granular Activated Carbon
GHSV	Gas Hourly Space Velocity
HER	Hydrogen Evolution Reaction
IE	Interest Expense
IEA	International Energy Agency
IDC	Interest During Construction
ILUC	Indirect Land Use Change
IRENA	International Renewable Energy Agency
KIT	Karlsruhe Institute of Technology
LCA	Life Cycle Assessment
LCOF	Levelized Cost Of Fuel
LFO	Light Fuel Oil
MEA	Monoethanolamine
MDEA	Methyldiethanolamine
MOFs	Metal-Organic Frameworks
MtG	Methanol-to-Gasoline
NC	Non Conventional
NETL	National Energy Technology Laboratory
NPV	Net Present Value
NZE	Net Zero Emissions
OER	Oxygen Evolution Reaction
PAC	Powdered Activated Carbon
PBtL	Power and Biomass-to-Liquid
PEMEL	Proton Exchange Membrane Electrolysis
PR BM	Peng-Robinson model Boston-Mathias modifications
RON	Research Octane Number
RR	Recycle rate

Abbreviation	Definition
SEDMES	Sorption-Enhanced DME Synthesis
SOA	State Of the Art
SR	Stoichiometric Ratio
StD	Syngas to DME
TASC	Total As Spent Cost
TIGAS	Topsøe Integrated Gasoline Synthesis
TOC	Total Overnight Cost
TPC	Total Plant Cost
WGS	Water Gas Shift
YDD	Yearly Debt Disbursement

1

Introduction

1.1. The Urgency of Climate Change: A Global Emergency

Since the beginning of the Industrial Revolution, the rapid rise in population and the intensification of human activity have made it possible for humans to alter the climate of the Earth on a global scale. The continuous release of carbon dioxide and other greenhouse gases into the atmosphere has been an ongoing phenomenon, largely attributable to the combustion of coal, natural gas, and petroleum [1]. As a result, the amount of CO_2 present in the atmosphere has skyrocketed in the last century, and it has reached unprecedented levels in at least the last 800000 years [2], as it is shown by Figure 1.1.

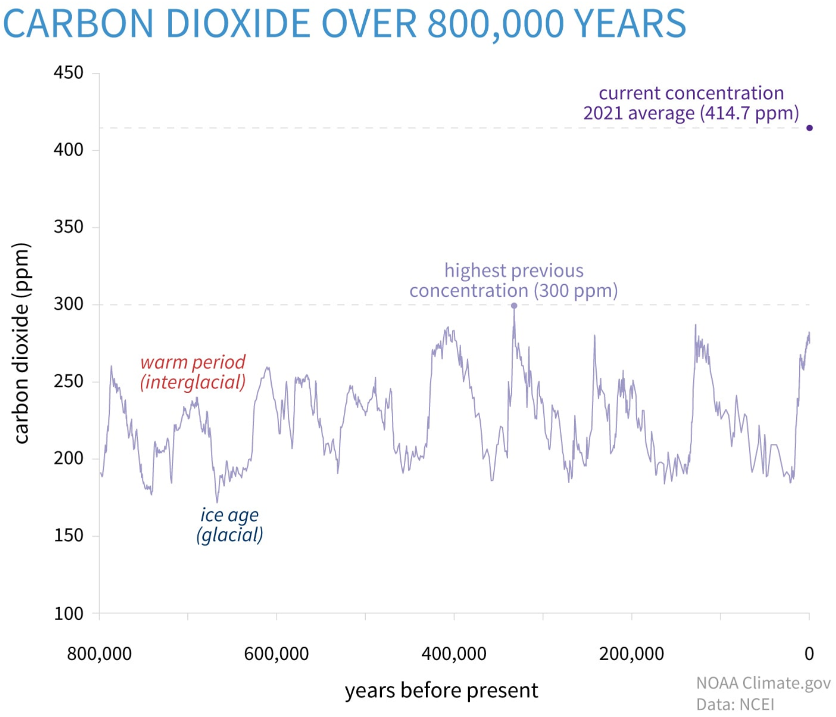

Figure 1.1: Atmospheric carbon dioxide concentration (in ppm) in the last 800 000 years [2]

The scientific community has established through multiple lines of evidence that this increase in atmospheric carbon dioxide is causing a warming of the global climate system [3],[4], [5]. This warming trend is evidenced by the fact that the past nine years have been the warmest recorded since modern record-keeping began in 1880 [6]. The rising temperatures have far-reaching consequences, including rising sea levels, increased frequency of droughts and floods in certain regions, and the struggle of numerous plant and animal species to survive [7].

These impacts underscore the urgency of addressing the issue of climate change and reducing the emission of greenhouse gases (GHG).

In order to fight this global emergency that transcends national borders, 195 governments came together at the United Nations Climate Change Conference (COP21) on December 12, 2015, and signed the Paris Agreement with the objective of enhancing the global response to climate change. The Paris Agreement aims to limit the increase in the global average temperature to well below 2°C above pre-industrial levels and to pursue efforts to restrict the temperature increase to 1.5°C above pre-industrial levels [8]. Six years later, at the 2021 United Nations Climate Change Conference (COP26), nations once again gathered to discuss climate change and signed the Glasgow Climate Pact [9]. Governments acknowledged that, while the goal of limiting the rise in global temperature to 1.5°C is still attainable, it requires a renewed commitment to action. Sir Alok Kumar Sharma, COP26 President, stated that the Paris Agreement's goal of limiting temperature increase is still "alive", however, "its pulse is weak and it will only survive if we keep our promises and translate commitments into rapid action" [10]. In reality, the global temperature was projected to rise by 2.7 to 3.7°C, requiring governments to take additional measures in the next decade to align with the limits set by the Paris Agreement. In line with its commitment to global climate action under the Paris Agreement, the European Union aims to be climate-neutral by 2050, in a scenario defined as Net Zero Emissions by 2050 (NZE).

As of today, even though projected emissions reductions have accelerated, the world remains far from achieving the 1.5° pathway, as can be observed in Figure 1.2. This means that the global energy system must accelerate its transformation significantly, shifting away from fossil fuels toward efficiency, electrification, and new fuels [11].

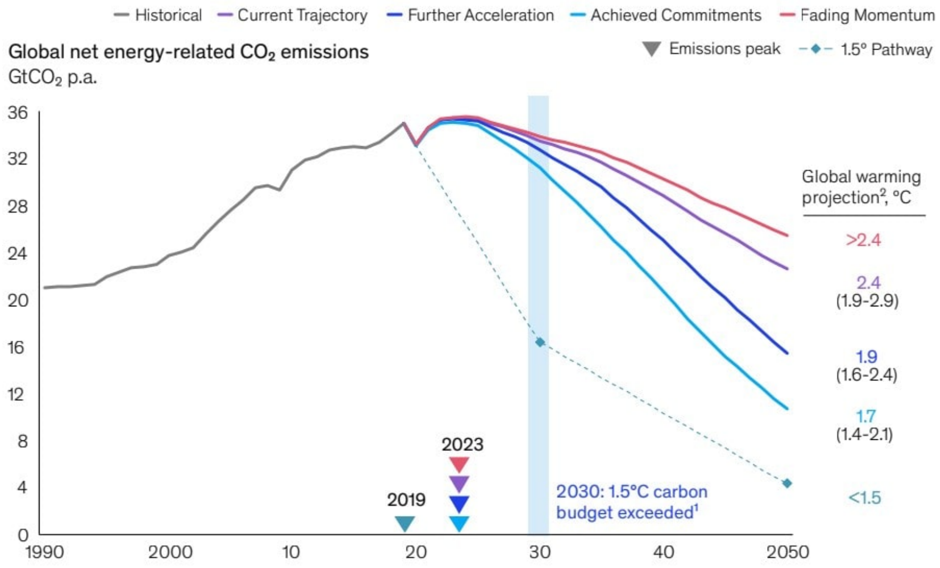

Figure 1.2: Global net energy-related CO_2 emissions, from 1990 to 2050 [11]

1.2. Reducing CO2 Emissions in the Transportation Sector

According to the International Energy Agency (IEA), one of the sectors that are still not on track in order to reach the limitations set by the Paris Agreement and the NZE scenario, despite recent advancements in the field, is the transport sector [12].

Transportation is the backbone of the economy and plays a vital role in the movement of goods and people. It is therefore not surprising that this sector significantly contributes to CO_2 emissions. The IEA reports that transport CO_2 emissions account for 23% of global energy-related CO_2 emissions, making it the second largest contributor after power generation from coal [13]. Furthermore, the trend in transport emissions has been increasing at an average rate of nearly 1.7% annually from 1990 to 2021, outpacing the growth rate of emissions from other end-use sectors [12].

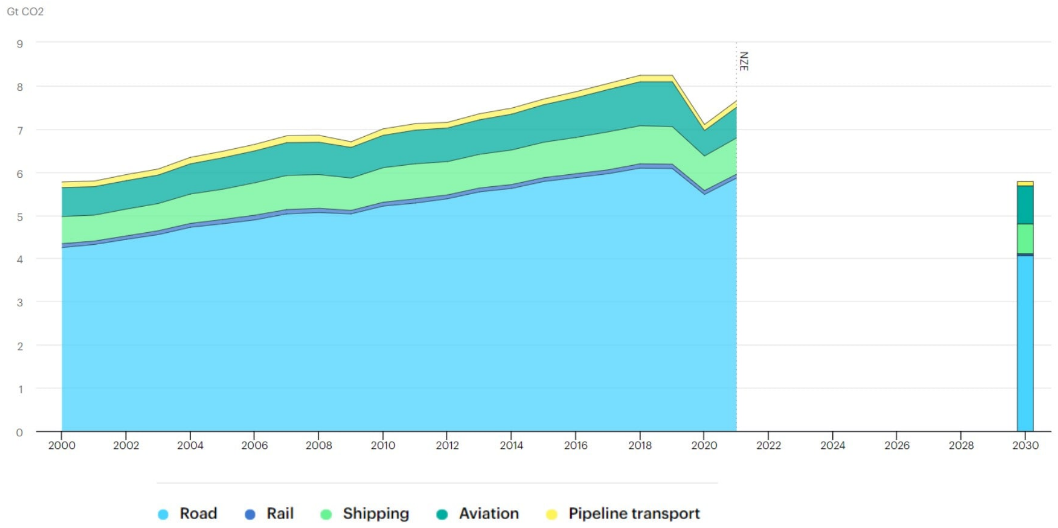

Figure 1.3: Global CO_2 emissions from transport by sub-sector in the Net Zero Scenario from 2000 to 2030 [12]

As observable in Figure 1.3, in order to align with the NZE scenario, a substantial decrease in CO_2 emissions from the transport sector is necessary. This reduction, estimated at approximately 3% per year by 2030, requires efforts in the near future, especially in the area of road transport, to facilitate a significant renewal of the vehicle fleet.

Currently, the transport sector still heavily relies on fossil fuels. Electrification is widely recognized as the path to achieving a major reduction of CO_2 emissions in this sector. However, it is debatable whether a single solution is adequate to address such a complex issue, without generating other problems. Therefore, alternatives such as hydrogen-powered vehicles and biofuels should also be considered.
Exclusive reliance on battery electric vehicles for fleet renewal could result in a shortage of battery minerals such as lithium, cobalt, and nickel. Mining these minerals is complicated and does not come without drawbacks. In addition to this, the growing demand for battery minerals has prompted an interest in deep-sea mining, which could severely impact sensitive, deep-sea ecosystems [14].
At the same time, the use of biofuels as the sole strategy for transport GHG emissions reduction might lead to the Indirect Land Use Change (ILUC) effect, where natural habitats and agricultural land are converted to biomass production, resulting in decreased biodiversity [15]. Additionally, even hydrogen fuel cell vehicles have their own drawbacks, such as the requirement for lithium-ion batteries as energy buffers to withstand the constantly varying power load required by a driver (leading again to the need for battery minerals). Finally, with a well-developed and widely spread hydrogen economy, hydrogen leaks might become substantial in absolute terms and contribute to warming effects, such as the production of tropospheric ozone or stratospheric cooling due to an increase in water vapour generated by hydrogen oxidation [16].

Thus, it is foreseeable that the attainment of ambitious goals in reducing CO_2 emissions without causing other potential adverse effects on the environment will only be possible with a multifaceted approach, where biofuels will play a crucial role [11].

.

1.3. Advanced biofuels and Power-and-Biomass-to-Liquid processes

Second-generation biofuels, also referred to as advanced biofuels are fuels that are produced from non-edible feedstocks. While first-generation biofuels are derived from high sugar-starch feedstocks and edible oil feedstocks, advanced biofuels are made from lignocellulosic biomass, woody crops, agricultural residues, or waste [17]. They have been introduced due to concerns over land availability and competition for feedstocks from the food industry. As reported by different sources, [11], [18], interest in these fuels is rising and their demand over the next decades is projected to increase significantly, potentially accounting for up to 37% of energy demand in transport by 2050 [11]. Starting from lignocellulosic biomass, several conversion technologies can be employed to transform the feedstock into a valuable chemical, as suggested by Figure 1.4.

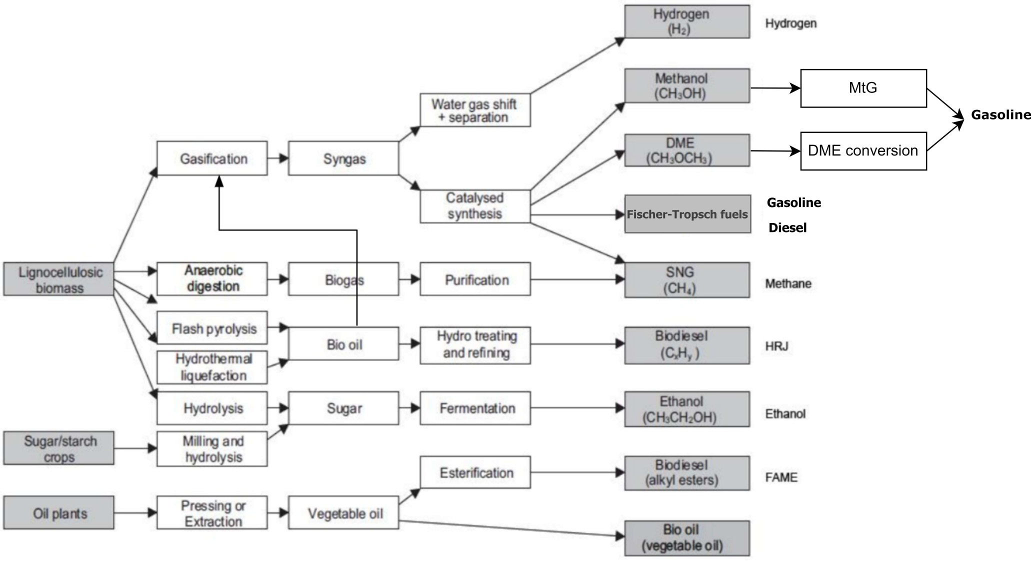

Figure 1.4: Conversion routes from biomass feedstock to chemicals. Adapted from [19].

Biochemical and thermochemical routes that yield a liquid starting from a biobased feedstock are termed Biomass-to-Liquid (BtL). A great variety of liquid chemicals can be produced via BtL processes, such as methane, ethylene, ethane, propane, butane, methanol, ethanol, dimethyl ether (DME), ammonia, bio-diesel, gasoline, etc. [20].
In some processes, after pre-treatments of the feedstock, BtL routes include the production of synthesis gas, rich in carbon monoxide (CO) and hydrogen (H_2), in a process called gasification. The syngas can then be processed further and converted into a liquid product. To do so, it is necessary to modify the proportion of CO and H_2 to an appropriate level, depending on the upgrading process chosen and the final product desired. In conventional BtL processes. the optimal ratio is typically achieved through the implementation of a water-gas shift reaction (WGS):

$$CO + H_2O \leftrightarrow CO_2 + H_2 \tag{1.1}$$

As can be seen from Equation 1.1, increasing the ratio of H_2:CO results in a corresponding increase in the concentration of carbon dioxide, which must subsequently be removed downstream of the gasification process [21], resulting in a loss of carbon and translating into low carbon efficiency (see Equation 2.5 of the process).
This suggests that the integration of electrolyzers with biofuel production presents new promising possibilities, as a hydrogen stream can be generated from water and renewable electricity and utilized to set the H_2:CO ratio, without diminishing the carbon content of the final product. This transforms the traditional biofuel production process, into an enhanced ”Power and Biomass-to-Liquid” (PBtL) process, as it utilizes renewable power and biomass feedstock as inputs (see Figure 1.5).

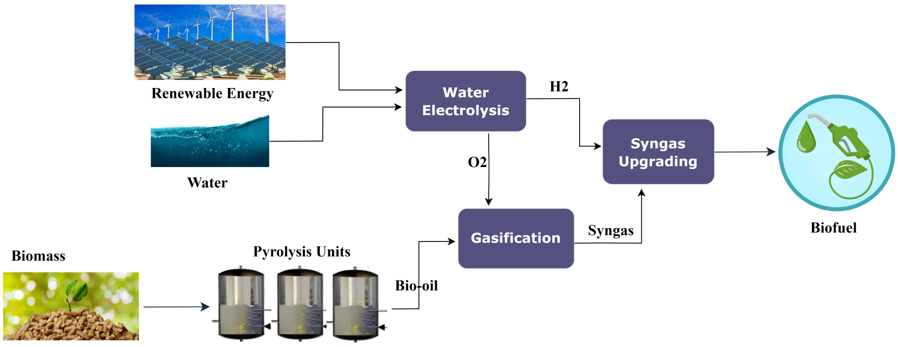

Figure 1.5: Simplified overview of a Power and Biomass to Liquid process.

The integration of electrolysis into these plants leads to three main benefits:

- It enhances the carbon efficiency 2.5 of the process, thereby increasing the carbon content of the final product.
- In power grids with significant penetration of renewable energies, where the generation of renewable power may exceed demand, surplus energy can be stored in a biofuel, easier to transport and store with respect to hydrogen.
- Electrolysis generates an oxygen stream, which can be used as oxidizing agent during bio-oil gasification in an oxygen-blown gasifier.

1.4. Research context and process selection

1.4.1. Biomass4Transport

In the Netherlands, the climate goals established by the Paris Agreement have been incorporated into the Climate Agreement [22]. In this document, it is stated that "the government is convinced that the use of biomass at present and heading toward 2030 and 2050 is crucial for the sustainability of our economy and the realization of the climate target". Regarding transport, the ambition of the government is to have all new cars emission-free by at the latest 2030. In the interim, heavy road transport will use synthetic biofuels as a transition measure. Furthermore, between 2030-2050, electric and biofuels will make up hybrid standards.

In this context, the "Biomass4Transport" project was created, with the aim of developing a chain of production of sustainable, second-generation biofuels for transport purposes [23]. This national project entails a collaboration between TU Delft and Biomass Technology Group (BTG), a Dutch company specialized in the conversion of biomass into fuels, energy, and biobased raw materials [24].
One of the steps for the Biomass4Transport project involves process system analysis, to investigate the techno-economic feasibility of different plant configurations. This thesis focuses on the process modelling and simulation of a PBtL plant to produce sustainable gasoline.

1.4.2. Process choice

Integrating water electrolysis with bio-oil gasification offers the possibility of following different routes downstream of the gasifier to obtain a valuable chemical as a final product, such as methanol, methane, Fischer-Tropsch fuels, etc. Many studies have analyzed such processes from both a technical and economic point of view, showing the potential of electrolysis integration in conventional BtL. For instance, Hanafi [25] has developed a bio-derived synthetic natural gas production plant model for the Biomass4Transport project.

The final product of the process that is investigated in this thesis project is sustainable gasoline. This specific biofuel has been suggested from the beginning by BTG. As explained above, sustainable gasoline will be key to helping the transition to zero-emission mobility and will replace conventional fossil-derived gasoline in hybrid vehicles. In addition to this, it is worth noting that sustainable gasoline can be used in a blend with conventional gasoline and it is easy to integrate into the current infrastructures.

One way to produce synthetic gasoline from a synthesis gas obtained via biomass or bio-oil gasification is through the Fischer-Tropsch (FT) synthesis, a series of chemical reactions discovered in 1926 by Franz Fischer and Hans Tropsch. The main advantage of this route resides in the fact that this is a well-established technology. Several studies have been performed to investigate the possible integration of FT synthesis in PBtL plants. Although plant configurations are different in these analyses, some common conclusions can be identified. Carbon Conversion efficiency (Eq. 2.5) can be improved with electrolysis integration and with respect to BtL plants, and in PBtL it reaches values above 90% [21], [26], [27], [28], [29]. However, the main disadvantage of FT for gasoline production is a low selectivity of C_{5-11} hydrocarbons (always lower than $\sim$ 50%) [30], [31], [32] crucial in the production of gasoline.

Another common route for the production of synthetic gasoline is the two-step process of syngas conversion to methanol and the subsequent Methanol-to-Gasoline (MtG) conversion. This process has been introduced by

Mobil in 1970 and resulted in a selectivity of gasoline production of 80% [33]. In the MtG route, methanol is dehydrated to form DME, which is then converted into light olefins and finally into higher olefins, paraffins, and aromatics. (see Figure 1.6).

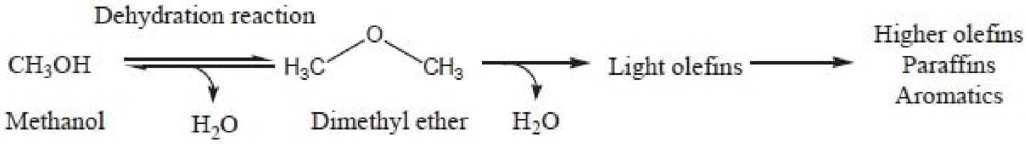

Figure 1.6: Overall reactions involved in the MtG process [33].

While in the past the synthesis gas was produced via fossil fuels, the growing interest in biomass conversion technologies suggests the possibility of obtaining a carbon-neutral process for the production of gasoline. Hannula [34] and Hennig et Hasse [35] investigated in a techno-economic analysis such PBtL plant for the production of gasoline and obtained a CC efficiency of 79% and 70%, respectively, using oxygen gasification of biomass. Both studies claim that the process becomes economically favourable only at hydrogen costs below 2.7 €/kg.

The overall costs associated with synthetic fuel processes can be diminished through increased plant integration. This can be accomplished by leveraging the one-step direct synthesis of DME from syngas (StD) and its subsequent conversion to gasoline (DtG), as opposed to the conventional two-step indirect DME synthesis [36] employed in the traditional Methanol-to-Gasoline (MtG) process.
In addition to increased plant integration, the direct synthesis of DME exhibits thermodynamic superiority over the two-step DME synthesis. This can be attributed to the concurrent production of methanol from CO and H_2, and its dehydration to DME within the same reactor, which results in a shift towards the product side of the methanol formation reaction, as it will be elucidated in Section 2.4.2. Generally, numerous advantages of StG and DtG compared to Syngas-to-Methanol-to-Gasoline have been reported, such as increased yield, enhanced CO and H_2 conversion, and improved catalyst life [37].

This concept has been used by Haldor Topsøe in the 80s in a process known as Topsøe Integrated Gasoline Synthesis (TIGAS), with the purpose of reducing overall plant costs [38]. The TIGAS process was however not based on biomass-derived syngas but on natural gas. More recently, researchers at the Karlsruhe Institute of Technology (KIT) have implemented this technology in their novel BtL process called bioliq® [39] and at the Qingdao Institute of Bioenergy and Bioprocess Technology a pilot plant for biomass to liquid fuels by integrating gasification, StD, and DtG has been built and successfully operated [40]. Furthermore, Ni et al. managed to achieve with such a process an 80.6% selectivity of C_{5-11} hydrocarbons in a highly integrated lab-scale plant [32].

Considering these advantages and the fact that techno-economic assessments of a plant that integrates bio-oil gasification, water electrolysis, direct syngas conversion to DME, and DME to gasoline conversion, have not been performed yet, while other processes have already been investigated, this research targets the process plant analysis of the process illustrated in a simplified schematic in Figure 1.7.

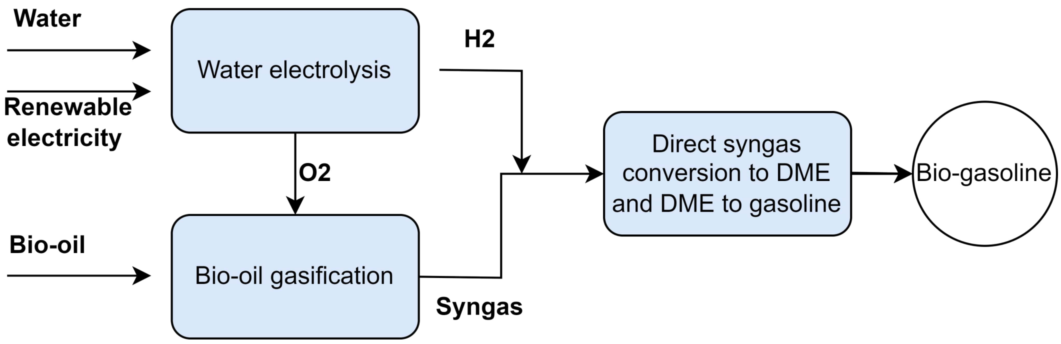

Figure 1.7: Simplified schematic of the process analyzed.

1.5. Project Description and Research Questions

This thesis aims to investigate the techno-economic feasibility of an integrated process to produce sustainable gasoline from pyrolysis bio-oil, using gasification, water electrolysis, direct conversion of syngas to DME (StD), and DME to gasoline conversion (DtG).

The main research question that this project seeks to explore is the following:

- ***What is a feasible design for a plant that integrates gasification of pyrolysis bio-oil, water electrolysis, direct syngas conversion to DME, and DME to gasoline conversion, with an estimated feedstock input of 5000 kg/h, in the context of the Netherlands?***

In order to address the main research question concerning the design of an integrated plant, the inquiry is divided into three interrelated sub-questions that cover various aspects of the project.

1. *Which process sub-units, along with their corresponding characteristics and operating conditions, must be chosen to attain a feasible integrated plant?*
2. *How can heat integration and material recycling strategies enhance the overall performance of the integrated plant?*
3. *What are the essential conditions for ensuring the economic viability of the proposed integrated plant?*

The first sub-question aims to identify the most suitable process sub-units, their characteristics, and operating conditions that contribute to a feasible design. This step is crucial for understanding the fundamental components and their integration within the plant, which will drive the overall efficiency and effectiveness of the system. The second sub-question seeks to explore heat integration and material recycling strategies to further enhance the plant's performance, ensuring that the design is both energy-efficient and environmentally sustainable. Lastly, the third sub-question is concerned with determining the necessary conditions for the integrated plant to be economically viable, which is fundamental for assessing its practicality and potential impact on the energy sector in the Netherlands. Together, these sub-questions will provide a comprehensive analysis of the design, performance, and feasibility of the proposed integrated plant, ultimately answering the main research question.

1.6. Thesis Outline and Methodology

Thesis Outline

The thesis commences with a comprehensive literature review (Chapter 2), which aims to provide a detailed overview of each subprocess of the plant. In order to partly answer the first research sub-question, the literature review presents a discussion of the theoretical fundamentals and the current state-of-the-art in terms of operating conditions, reactors, and kinetic models for the sub-processes. The primary objective of this chapter is to establish a foundation of knowledge that will inform the development of the Basis of Design (BoD), which is presented in Chapter 3.

In Chapter 4, the various models of the sub-units are explained and their validation is presented. Then, in the following chapter, the results of the simulations, the heat integration and material recycling strategies, are explained. Furthermore, an analysis of the plant's performance is given. In Chapter 6 the economic analysis is outlined and in the last chapter conclusions and recommendations are elucidated.

Methodology

Utilizing Aspen Plus® and Matlab software, process simulations are executed to determine the plant's optimal operating conditions and evaluate its performance with respect to gasoline yield, efficiency, and carbon conversion efficiency. This, together with the literature research, addresses the first sub-research question of the study.

Subsequently, the model is employed to investigate the impact of heat integration and recycle streams, thereby addressing the second sub-research question.

Lastly, to respond to the third sub-research question, an economic analysis is conducted using a discounted cash flow analysis, to calculate the Net Present Value of the plant.

This comprehensive methodology enables a thorough investigation of the research questions.

2
Literature Study

The purpose of this chapter is to present the results of a literature review that aimed to investigate various methods for producing sustainable gasoline from bio-oil, as well as explore the underlying technologies that can be employed as sub-units within the process. The study focused on examining the fundamentals, operating conditions, and current state of the art of these technologies, with the overall objective of building a foundation of knowledge that can help during the definition of the Basis of Design for the process and the subsequent modelling efforts.

The literature study begins with a section on the pyrolysis of biomass and follows with a section about bio-oil gasification. It is important to note that pyrolysis units are not included in the process model. However, understanding pyrolysis and its resulting product is important to assess the advantages and disadvantages of its integration into the biogasoline production chain.
The literature review continues with a section on water electrolysis and follows with one on syngas upgrading to gasoline via DME conversion. This research gives insight into the requirements for the synthesis gas cleaning that must be operated prior to its conversion, which is the following topic covered. At last, an overview of PBtL process analyses available in the literature is given.

2.1. Pyrolysis of Biomass

2.1.1. Fundamentals

Pyrolysis is the thermal decomposition of organic material in an oxygen-free atmosphere [41]. This thermochemical process can be used to convert biomass feedstock into organic vapour, solid residues, and permanent gases (CO, CO_2, H_2, CH_4). Upon cooling, the vapours condense into a liquid, commonly referred to as pyrolysis oil or bio-oil, that can be improved or processed for the production of energy, electricity, fuels, and chemicals [42]. Solid products (char), are carbonaceous, they contain a large amount of ash-containing compounds, and retain most of the inorganic elements present in the feedstock.
Pyrolysis is typically performed at temperatures ranging from 200 to 550°C, and under atmospheric pressure or lower [41]. When pyrolysis is conducted at temperatures between 400 and 550°C and small biomass particles (less than two millimetres) are used, very high heating rates are achieved resulting in maximal liquid production. This process is called fast pyrolysis.

As stated above, pyrolysis oil, also known as bio-oil, is the liquid byproduct of the pyrolysis process which is collected through condensers downstream of the reactor. With optimization, the yield of the pyrolysis process can reach approximately 70-80% [41],[43]. Bio-oil is composed of a mixture of water and various oxygenated organic compounds and is not usually a final product. It is either used as a feedstock (i.e. for gasification) or further refined to be used as a feedstock for fuel and chemical production.
Literature research showed that in a considerable amount of process plant design studies where BtL or PBtL plant models have been developed, pyrolysis units were excluded as it will be discussed in Section 2.6 It is indeed not imperative to incorporate a pyrolysis reactor before gasification, in the design of a biomass-to-liquid system, since alternative options such as direct feeding of biomass feedstock into gasifiers exist. If the pyrolysis process is performed in a separate reactor, it is necessary to take into account the additional capital costs associated with

its inclusion in the overall cost calculation of the system [44]. Nevertheless, integrating fast pyrolysis before the gasification process has a considerable number of advantages:

- **Decentralized pyrolysis units:** The installation of entire plants in strategic zones in proximity to the sources of biomass can be challenging or even impossible. However, decentralized pyrolysis units are significantly smaller and thus offer the potential for localized installation, strategically situated and distantly from the remainder of the system.
- **Higher volumetric density :** Bio-oil has an increased volumetric energy density when compared to solid biomass (see Figure 2.1). As a result, storing and transporting it becomes more convenient economically, even over long distances [45]. The low volumetric energy density of raw biomass makes the implementation of large-scale biomass conversion technologies challenging, due to the issue of accumulating enormous volumes of biomass feedstock at the plant location. When bio-oil is used as feedstock for the plant, its higher energy density facilitates the storage of higher energy content in smaller volumes at the plant site. [46]. In addition to this, pyrolysis oil and finely ground pyrolysis coke can be mixed to form a slurry, which can reach a tenfold energy content on a volume basis with respect to the raw biomass [45].
- **Separation of inorganic elements:** Over 95% of the inorganic elements present in the raw biomass are retained in the solid phase (which is separated from the vapours) and therefore do not end up in the bio-oil (provided that char is not blended with the oil to form a slurry). Inorganics are undesirable in further processing since they can be responsible for catalyst poisoning [41].
- **Higher feedstock flexibility:** Pyrolysis oil can be derived from virtually any lignocellulosic biomass, with varying yields, but similar properties [47].
- **Pressurization**: Pyrolysis oil is easier and cheaper to pressurize with respect to solid biomass. [41]

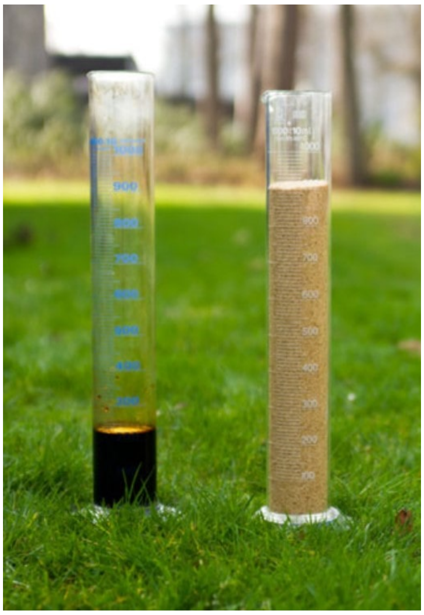

Figure 2.1: Pyrolysis oil (left) and pinewood from which it originates (right). Both cylinders contain the same amount of energy, showing that during pyrolysis the volumetric energy content increased considerably [42].

The ultimate analysis and the proximate analysis of the bio-oil used in the experiments of Leijenhorst are reported in Table 2.1.

Table 2.1: Bio-oil composition: ultimate and proximate analysis

Ultimate Analysis			**Proximate Analysis**	
Elements (dry)	(wt%)			(wt%)
C	57.4		Moisture	21.1
H	6.6		Ash	0.009
N	<0.1		Volatile matter	99.98
O	35.9		Fixed carbon (FC)	0.001
S	0.0046			

2.2. Gasification of Biomass

2.2.1. Fundamentals

Gasification is a thermochemical fuel conversion technology carried out at high temperatures using a gaseous agent to convert a liquid or solid fuel into a product gas [42]. The outcome of the thermochemical process is either a fuel gas, which can be utilized as a fuel source to generate heat and/or power or a synthesis gas, also known as syngas, which serves as a raw material for the manufacture of chemicals and fuels [41]. Bio-oil gasification processes can be divided into two categories on the basis of gasifying agents used in these processes. The first is referred to as the non-catalytic partial oxidation process, in which oxygen is utilized as a gasifying agent to produce syngas. The second category is known as the steam reforming or steam gasification processes, utilizing only steam as the gasifying agent to generate a hydrogen-rich gas [46]. In this study, the focus will be on the first group, since oxygen can be obtained from the integrated electrolysis unit and used as the oxidizing agent.

Bio-oils produced by fast pyrolysis must be atomized prior to feeding into a fluidized bed gasifier or an entrained flow gasifier. In this process, a relatively low dynamic viscosity, in the range of 5-30 mPa s is crucial. Since water is an integral part of the bio-oil (15-30 wt%), the single-phase chemical solution generally has a lower viscosity compared to heavier fuel oils and it is easier to atomize. However, if reducing the viscosity is necessary, pyrolysis oil can be preheated as shown in Figure 2.2 [46], where the viscosity-temperature relation is compared to the ones of typical light fuel oil used for heating purposes and heavy fuel oil used in heavy-duty applications.

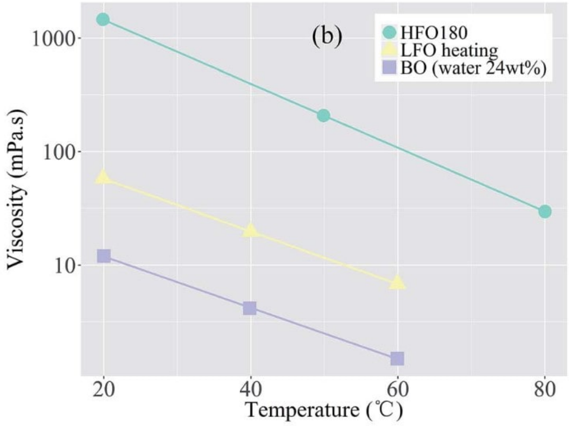

Figure 2.2: Temperature effect on dynamic viscosity of bio-oil and light fuel oil for heating (LFO heating) and heavy fuel oil 180 cSt (HFO 180) [46].

The gasification process of bio-oil droplets is composed of four stages, including drying, pyrolysis, oxidation, and reduction. Due to the high heating rate and the small size of bio-oil droplets, these stages tend to occur simultaneously, making it difficult to distinguish sharp boundaries between them. During the drying phase, the water content in the bio-oil mixture evaporates and separates from the bio-oil, causing it to become more viscous. It is therefore evident that a higher water content in the bio-oil results in a higher energy requirement for evaporation, decreasing the efficiency of the process. During this phase, heat is transferred from the gas phase to the small liquid droplets.

The following conversion step is pyrolysis. Two undesirable products generated during the pyrolysis phase are soot and tar. Soot is a mass of impure carbon particles, while tar is a complex mixture of condensable hydrocarbons, tar is undesirable because of various problems associated with condensation, leading to problems in the process equipment [48]. Luckily soot normally constitutes 1-2 wt% on the basis of bio-oil feed flow. Tar concentration in the product gas is highly dependent on the reaction conditions and might lead to problems in the process if its content is too high [44], [49].

Reactions and process parameters

Several reactions are involved in the oxidation and reduction steps. The most important reactions are the char-oxygen reactions, which have the highest reaction rates [46]. In these reactions, C and O_2 react to form CO and CO_2 in exothermic reactions.

$$C + O_2 \rightarrow CO_2 \tag{2.1}$$

$$2C + O_2 \rightarrow 2CO \tag{2.2}$$

Additionally, H_2 is formed via the gasification of char in the water-gas reaction (endothermic) and via the WGS reaction (see Equation 1.1).

$$C + H_2O \leftrightarrow CO + H_2 \tag{2.3}$$

Finally, another important reaction according to De Jong et al.[42] is the Boudouard reaction:

$$C + CO_2 \leftrightarrow 2CO \tag{2.4}$$

Other reactions take place during gasification. For further reference, the review by Zheng et al. [46] and the book by De Jong et al. give a good overview [42].

It is important to introduce some output parameters to characterize the gasification process and the syngas quality. First, Carbon Conversion (CC) efficiency (sometimes named carbon efficiency) is defined as the ratio between the amount of carbon present in the outlet gas and the amount of carbon contained in the feed:

$$CC = \left(1 - \frac{\dot{m}_{c,residue}}{\dot{m}_{c,feed}}\right) \tag{2.5}$$

This parameter indicates the efficiency of the carbon conversion process, i.e., how much of the feedstock carbon is converted into the desired product. It is worth mentioning that this parameter is not only used to assess gasification performance but is also relevant to evaluate a full process.

Secondly, the efficiency of the gasification process can also be assessed via the cold gas efficiency (CGE), given by the ratio of the total energy content of the product gas to the energy content of the feedstock:

$$CGE = \left(\frac{\sum \dot{m}_i \cdot LHV_i}{\dot{m}_{fuel} \cdot LHV_{fuel}}\right) \tag{2.6}$$

The cold gas efficiency (CGE), quantifies the effectiveness of the gasification process by evaluating the ratio of the cumulative energy content of the product gas, determined through the product of individual mass flow rates ($\dot{m}_i$) and their respective lower heating values (LHV_i), to the energy content of the feedstock, calculated by multiplying the feedstock mass flow rate ($\dot{m}_{fuel}$) and its lower heating value (LHV_{fuel}). These two parameters are not sufficient to assess the performance of a gasification process, as the composition of the product gas is also crucial. Specifically, high concentrations of H_2 and CO are generally required and the proportion of the two gasses is also of significant relevance. Depending on the syngas upgrading process that follows gasification (i.e. Fischer-Tropsch synthesis, methanol synthesis, DME direct conversion), different H_2:CO values should be targeted. Generally, as reported by various sources the H_2:CO ratio after gasification of bio-oil can vary between 0.6 and 1 [41], [46], [50], depending on the process conditions.

Another important aspect to assess the gas product quality is the tar amount, which as shown experimentally by Zheng et al. [51], the tar content decreases when the ER increases. A higher oxygen concentration favours the oxidation of intermediate products such as tar.

The oxygen equivalence ratio

Let us now introduce an important process parameter, the Oxygen Equivalence Ratio (ER), defined as:

$$ER = \frac{(\dot{m}_{O2}/\dot{m}_{fuel})}{(\dot{m}_{O2}/\dot{m}_{fuel})_{,stoic}} \tag{2.7}$$

where:
$(\dot{m}_{O2}/\dot{m}_{fuel})$ is the actual ratio between the mass flow of oxygen and the mass flow of fuel;
$(\dot{m}_{O2}/\dot{m}_{fuel})_{,stoic}$ is the stoichiometric ratio (SR), that is the ratio of the mass flow of oxygen and the mass flow of fuel in stoichiometric conditions.
This parameter is sometimes replaced with its inverse, referred to as the stoichiometric oxygen ratio λ.
The ER gives information on the quantity of oxygen fed to the reaction with respect to the stoichiometric combustion of the fuel. When ER = 0, the conversion happens in absence of oxygen, meaning that ER = 0 indicates pyrolysis. When ER > 1, combustion in excess of oxygen takes place.
For fuels having a certain molecule equation, the SR can be easily figured out from the equations of its oxidation reaction. For a fuel such as bio-oil, without a certain molecular structure, the SR is not straightforward. In their paper, Zhu and Venderbosch illustrate three methods to estimate the SR, based on the chemical composition of the bio-oil [52]. The three methods give values of the SR within 5% accuracy, based on the relative error. The second method proposed assumes that the fuel only consists of elements C, H, and O and uses the composition to calculate a unified molecule formula CH_xO_y. Then, the SR can be calculated from the oxidation reaction:

$$CH_xO_y + mO_2 \rightarrow CO_2 + nH_2O \tag{2.8}$$

with:
$n = \frac{x}{2}$, and
$m = \frac{2+n-y}{2}$.

The value of the ER ratio crucially influences the characteristics of the product gas. Higher ER values signify higher concentrations of the targeted main gasification constituents, H_2, and CO in the synthesis gas [42]. This is explained by a higher concentration of oxygen with an increase in the ER. Thus, oxidation of CO and H_2 to CO_2 and H_2O are favoured [46]. However, rising the ER also means that the endothermic reactions will increasingly prevail and, as a result, the temperatures might decrease to values that are too low to sustain the gasification process. This can be overcome by external heat or by increasing lambda to enhance the partial oxidation reactions which generate heat in situ [42].
Zheng et al. suggest ER values between 0.2 and 0.3 [46], however, in the experiments of Marklund et al. slightly higher values were used (0.4 to 0.5) [50]. Zheng et al. studied the effect of gasification conditions on the H_2:CO ratio experimentally, with different oxidizing agents [51]. As can be observed from Figure 2.3, shifting the ER from 0.1 to 0.5 corresponds to a downward trend of the H_2:CO ratio when using air or oxygen-enriched air, while it does not affect the pure oxygen case. This can be explained by the increasing concentration of N_2 in the first two cases, which absorbs heat and thus reduces the temperature in the gasifier and thus decrease the rate of H_2 production reactions which are endothermic.

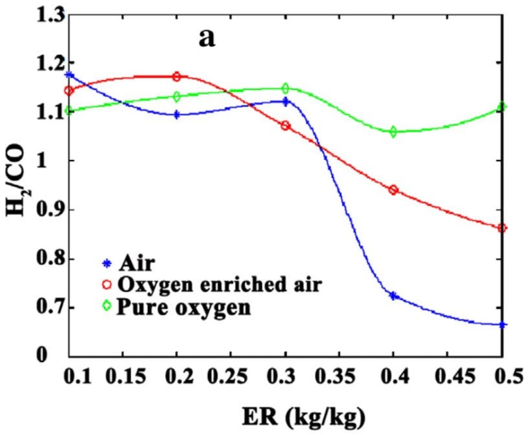

Figure 2.3: ER effect on the gas composition in bio-oil gasification for different oxidizing agents [51].

The steam to carbon ratio

When steam is used as a component of the oxidizer flow supplied to the gasifier, and when a significant amount of water is present in the fuel, another important parameter for the final gas composition can be introduced: the steam-to-carbon ratio (SC).

$$SC = \frac{\dot{m}_{steam} + \dot{m}_{moist}}{\dot{m}_c} \tag{2.9}$$

Where:
$\dot{m}_{steam}$ is the mass flow of steam supplied to the gasifier,
$\dot{m}_{moist}$ is the mass flow of water present in the fuel,
$\dot{m}_c$ is the mass flow of carbon present in the fuel.
Therefore, SC represents the ratio of the total mass flow of water to the mass flow of carbon present in the fuel. This can be expressed both on a mass and a molar basis [42], [46].

In general, increasing the SC leads to a higher CO_2 concentration and a lower CO concentration. This is due to the higher concentration of water, which favours the water gas shift reaction (Eq. 1.1), producing carbon dioxide and hydrogen. The concentration of hydrogen also increases with a higher SC. However, as found experimentally by Guo et al., there is an optimum of the SC for the hydrogen yield, and with very high SC, both CC and H_2 concentration decrease [53]. This is because, as explained before, water acts as a heat sink, since it has to be evaporated prior to gasification.

Operating conditions

Temperature plays an important role in the gasification process. Generally, higher temperatures favour endothermic reactions, while lower temperatures favour exothermic reactions. Due to this, increasing the gasification temperature results in higher H_2 production, because the water-gas reaction (Eq. 2.3) is endothermic. At the same, time oxidation reactions are theoretically favoured by a lower temperature. However, high temperatures can help to provide the activation energy needed to start the reaction and increase the rate of the reaction. As a result, oxidation reactions in bio-oil gasification are enhanced by high temperatures. This contributes to higher CGE and CC. CO concentration dependency on temperature is difficult to predict, as exothermic and endothermic reactions are intertwined [46]. Finally, tar cracking is enhanced by a higher temperature thus, the tar content in the synthesis gas decreases with an increase in gasification temperatures.

Reactors: Entrained Flow Gasifiers

Several different types of gasifiers have been developed since the invention of gasification. For the non-catalytic partial oxidation of bio-oil, pressurized entrained flow gasifiers are the most suitable among other gasifiers [46]. In these gasifiers, the fuel (in this case the bio-oil) is fed into the reactor from the top, possibly together with steam or inerts in order to control the temperature. The oxidizing agent (generally air or oxygen) fed to the gasifier, surrounds and entrains the fuel droplets or particles as they flow through the reactor.
Entrained flow gasifiers are also easy to scale up and guarantee high conversion efficiencies. Moreover, they produce good-quality syngas, with low concentrations of tar and methane, due to the high temperatures applied (1200°C-1500°C) [41].
It is important to mention that, if the feedstock is rich in inorganic components, a slag layer is formed inside the reactor. This must be continuously removed, complicating the gasifier design and introducing additional costs. However, during the pyrolysis process most of the inorganics are removed, enabling the use of non-slagging gasifiers. Typical operating pressures in entrained flow gasifiers range from atmospheric to very high pressures such as 80 bar. For instance, the entrained flow gasifier used in the already mentioned bioliq® process has been designed to operate at 40 or 80 bar [45]. However, the entrained flow gasifier located at the Energy Technology Center in Sweden and used in the experiments of Leijenhorst [41], has been operated at 6 bar.

2.3. Water Electrolysis

2.3.1. Introduction

Water electrolysis is an electrochemical process used to split water (H_2O) into its constituents H_2 and O_2, using electricity. It represents the main path for the production of green hydrogen since it can be coupled with renewable energy sources, such as solar panels and wind turbines. Hydrogen offers a wide range of opportunities for the energy market. It is first of all an energy carrier, which can be stored in the long term and transported. Thus, it can be employed to store renewable energy in case of excess demand. Furthermore, H_2 is also a fuel, which can be used in fuel cell applications (i.e. vehicles, ships, planes, and power generation) and in gas turbines. In the context of synthetic fuels, hydrogen can also play a crucial role, as it can be used as a feedstock together with CO and CO_2 [54].

2.3.2. Fundamentals

Water electrolysis is described by its fundamental chemical reaction:

$$2H_2O \rightarrow 2H_{2(g)} + O_{2(g)} \tag{2.10}$$

Since this is a non-spontaneous reaction, a DC electrical current must be used to drive the reaction. When a potential difference is applied at the electrodes, oxygen is produced at the anode, and hydrogen is produced at the cathode.
The total energy consumed in the reaction is quantified by the reaction enthalpy ΔH, defined as:

$$\Delta \mathrm{H} = \Delta \mathrm{G} + \mathrm{T}\Delta \mathrm{S} \tag{2.11}$$

Where ΔG is the change in Gibbs free energy and ΔS is the entropy change.

The change in Gibbs free energy corresponds to the minimum amount of energy required to make the reaction happen. It is useful to relate ΔG and ΔH to voltages since energy is supplied as electrical energy.
The open circuit potential U_{rev} [V], or reversible cell voltage, indicates the equilibrium potential of the reaction and represents the theoretical minimum voltage of electrolysis operation.

$$U_{rev} = -\frac{\Delta G}{nF} = -1.23\,V \tag{2.12}$$

Where F = 96485 C/mol is Faraday's constant, and n=2 is the number of electrons transferred per reaction.
Another important voltage that characterizes electrolysis is the thermoneutral potential U_{tn}, the voltage which is necessary not only to drive the cell reaction but to also provide the heat necessary to keep a constant reaction temperature.

$$U_{tn} = -\frac{\Delta H}{nF} = -1.48\,V \tag{2.13}$$

It is important to note that the values 1.23 V and 1.48 V, which are usually taken as indicative of the reversible and thermoneutral potential, are valid at standard conditions. Since both ΔH and ΔG are temperature dependent, U_{rev} and U_{tn}, also vary with temperature, as can be observed in Figure 2.4.

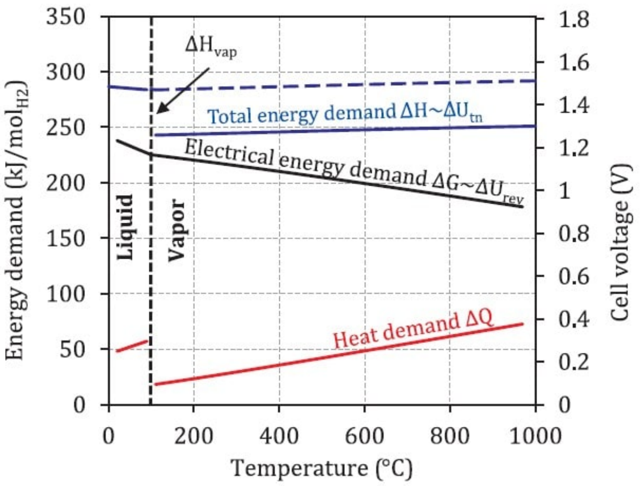

Figure 2.4: ΔH, ΔG, and thermal energy ΔQ of an ideal electrolysis process as a function of the temperature [54].

The applied cell voltage can be expressed as the sum of the reversible potential, the overvoltages caused by ohmic resistance U_{ohm}, limitations in electrode kinetics (activation overvoltages) U_{act}, and mass transport (concentration overvoltages) U_{con} [54]:

$$U = U_{rev} + U_{ohm} + U_{act} + U_{con}. \tag{2.14}$$

Furthermore, an important parameter is the current density j [A/m^2], defined as:

$$j = \frac{I}{A} \tag{2.15}$$

Current density and cell voltage are related and their relation can be visualized by the I-U curve, shown in Figure 2.5.

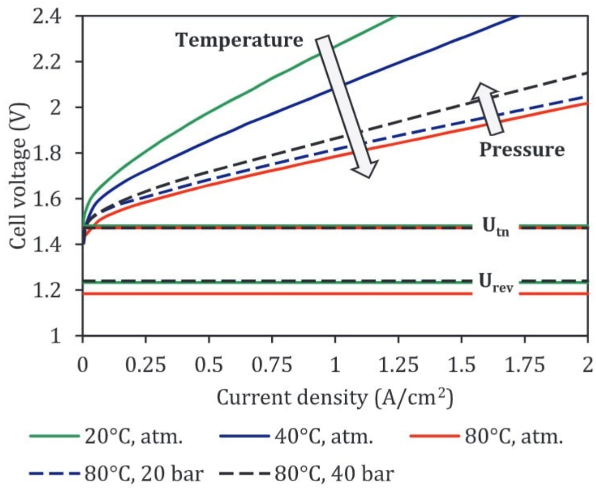

Figure 2.5: Influence of temperature and pressure on the characteristic I-U curve of a PEM electrolysis cell [54].

The efficiency of electrolysis can be expressed in different ways. The two most common ways to express it are the following:

$$\eta_{rev} = \frac{\Delta G}{\Delta G + Losses} = \frac{U_{rev}}{U} \tag{2.16}$$

$$\eta_{tn} = \frac{\Delta H}{\Delta H + Losses} = \frac{U_{tn}}{U} \tag{2.17}$$

Where U [V] is the applied cell potential.
Efficiency can also be expressed in terms of heating value:

$$\eta_{LHV} = \frac{\dot{m}_{H2} LHV}{P_{el}} \tag{2.18}$$

Where $\dot{m}$ is the mass of hydrogen produced per unit time [kg/h], LHV is the lower heating value in mass basis [MJ/kg], and P_{el} is the electrical power required to operate the stack (stack efficiency) or the whole system (system efficiency). Sometimes the lower heating value is replaced by the higher heating value HHV.

The Gibbs free energy ΔG, and therefore, the equilibrium potential U_{rev} are pressure dependent. This dependency can be explained with some assumptions by a simplification of the Nernst equation. Without considering losses, and at equilibrium we can express the equilibrium potential at a certain temperature T and pressure p U_{rev}(T,p) as:

$$U_{rev}(T,p) = U_0 - \frac{RT}{2F} lnK_c \tag{2.19}$$

Where U_0 is the equilibrium potential at standard conditions and K_c is the equilibrium constant.
Rewriting the equilibrium constant, we get to:

$$U_{rev} = \frac{\Delta G}{2F} - \frac{RT}{2F} ln \frac{(a_{H_2})(a_{O_2})^{0.5}}{(a_{H_2O})} \tag{2.20}$$

Where a_{H_2}, a_{O_2}, and a_{H_2O} are the activity coefficients hydrogen, oxygen, and water, and R=8.314 J mol^{-1} is the universal gas constant.

In the case of high-temperature electrolysis, water vapour can be treated as an ideal gas (since its compressibility factor approaches 1). Assuming ideal gas behaviour for water vapour, hydrogen, and oxygen, the simplified Nernst equation can be rewritten as:

$$U_{rev} = \frac{\Delta G^0}{2F} - \frac{RT}{2F} ln \frac{(p_{H_2})(p_{O_2})^{0.5}}{(p_{H_2O})} \tag{2.21}$$

Where p_{H_2}, p_{O_2}, and p_{H_2O} are the partial pressures of hydrogen, oxygen, and water.

2.3.3. Different water electrolysis technologies

Four main water electrolysis technologies can be identified, based on the electrolyte, operating conditions, and ionic agents: alkaline electrolysis cells (AEL), proton exchange membrane electrolysis cells (PEMEL), anion exchange membrane electrolysis (AEMEL), and solid oxide electrolysis cells (SOEL).

Alkaline electrolysis

Alkaline water electrolysis is the most mature and well-established technology for industrial production [55]. In alkaline electrolyzers, the electrodes are immersed in a liquid electrolyte separated by a diaphragm. The electrolyte is stored in two tanks, where it is also separated from the product gases H_2 and O_2. The electrode material is generally nickel, which can be coated or raw. It is operated at temperatures ranging from 30 to 90°C and pressures ranging from atmospheric to $\sim$ 50 bar. The charge carriers are OH$^-$ ions, which travel through the separator from the cathode to the anode. Thus, the fundamental chemical reaction (Eq. 2.10) can be subdivided into two different reactions:

$$2H_2O + 2e^- \rightarrow H_2 + 2OH^- \quad \text{Cathode partial reaction} \tag{2.22}$$

$$2OH^- \rightarrow H_2O + \frac{1}{2}O_2 + 2e^- \quad \text{Anode partial reaction} \tag{2.23}$$

Proton exchange membrane electrolysis

In PEM electrolyser cells, the anode and cathode are separated by a solid polymer electrolyte, also known as the proton exchange membrane. The acidic regime provided by the proton exchange membrane requires the use of noble metal catalysts, like iridium for the anode and platinum for the cathode [54]. Its operating temperatures range from 20 to 80°C. Commercial PEMEL systems today operate at pressures of 30-40 bar but prototypes delivering hydrogen at several hundred bar have been demonstrated [56]. In PEM electrolysis water is supplied at the anode and the following partial reactions take place:

$$2H^+ + 2e^- \rightarrow H_2 \quad \text{Cathode partial reaction} \tag{2.24}$$

$$H_2O \rightarrow \frac{1}{2}O_2 + 2H^+ + 2e^- \quad \text{Anode partial reaction} \tag{2.25}$$

Anion exchange membrane electrolysis

AEMEL electrolysis has been developed in order to resolve the need for very expensive metal catalysts in PEMEL. While PEMEL happens in an acidic environment, AEMEL happens in a basic environment. The anode and the cathode are separated by a solid electrolyte, the anion exchange membrane. The ionic conduction is provided by the transport of OH$^-$ ions which diffuse from the cathode to the anode. Commonly used anode and cathode electrode materials are transition metal-based electrocatalysts, especially Nickel and NiFeCo alloy materials respectively [55], which are cheaper than iridium and platinum used in PEMEL. Currently, the operating pressure range of AEMEL goes from atmospheric to around 35 bar [57] and its operating temperature range is similar to the one of AEL and PEMEL. In AEMEL water is supplied at the cathode and the following partial reactions take place:

$$2H_2O + 2e^- \rightarrow H_2 + 2OH^- \quad \text{Cathode partial reaction} \tag{2.26}$$

$$2OH^- \rightarrow \frac{1}{2}O_2 + H_2O \quad \text{Anode partial reaction} \tag{2.27}$$

Solide oxide electrolysis.

A solid oxide electrolyzer cell consists of a solid oxide electrolyte that separates the anode and the cathode. The solid exchange membrane is crossed by O^{2-} ions from the cathode to the anode. Differently from PEMEL and AEL, in SOEL water is supplied in form of vapor since the operating temperature range is higher compared to the other two technologies (500-900°C). As Figure 2.4 shows, the minimum electrical energy demand is reduced at high temperatures. Furthermore, high-temperature electrolysis guarantees improved kinetics and the possible heat utilization of internal losses [54]. Thanks to the improved kinetics, platinum group metals are not required as catalysts [55]. Generally, Ni–YSZ electrodes are employed at the hydrogen side, while LSM ($La_{0.8}Sr_{0.2}MnO_{3-\delta}$) is normally used at the oxygen side. SOEL is performed at pressures ranging from ambient up to 10 bar. The partial reactions in SOEL are:

$$H_2O + 2e^- \rightarrow H_2 + O^{2-} \quad \text{Cathode partial reaction} \tag{2.28}$$

$$O^{2-} \rightarrow \frac{1}{2}O_2 + 2e^- \quad \text{Anode partial reaction} \tag{2.29}$$

Comparison between AEL, PEMEL, AEMEL, and SOEL

The four different electrolysis technologies present significant differences.

The operating temperature range of AEL, PEMEL, and AEMEL is similar, while SOEL operates at much higher temperatures. This implies that water must be preheated and evaporated, and suggests that heat integration with subsequent exothermal processes (such as DME synthesis) represents an interesting application. [54].

One of the major disadvantages of AEL, AEMEL, and PEMEL is gas crossover [58]. Oxygen and hydrogen gasses can travel from one electrode to the other, due to different mechanisms, creating a potential safety hazard. This is particularly true for AEL, where the crossover is caused mainly by electrolyte mixing: gasses dissolve in the electrolyte, which is recirculated from the liquid-gas separator back to the stack. SOEL suffers less with respect to the other two technologies.

As explained above, high pressure is advantageous for electrolysis. High-pressure AEL and PEMEL units already exist, while at the moment, AEMEL and SOEL generally operate at pressures close to ambient pressure. However, it can be inferred that with future developments SOEL will operate at pressures higher than 20 bar and high-pressure AEMEL will be available [57]. For instance, Dossow et al. and Hillestad et al. assume in their system model that future commercial SOEL units can operate at an elevated pressure of 40 bar [21], [26]. Apart from being beneficial for efficiency, the operating pressure choice is important for the integration with the rest of the system. If the oxygen produced is fed to the gasifier, its pressure must be higher than the pressure of the gasifier [21].

The four technologies can also be compared in terms of efficiency. Due to high temperatures, which favor thermodynamics and kinetics SOEL cells are more efficient than AEL, PEMEL, which can now reach efficiencies between 63-71% and 60-68% respectively, according to the market survey of Buttler et al. [54]. Working at lower temperatures AEMEL is also intrinsically less efficient with respect to SOEL, with efficiencies of 57-59% with the current state of the art, as reported by Kumar et Lim [55]. Experimentally verified SOEL cells have reached higher values of stack efficiencies (Eq. 2.18): at KIT a stack efficiency of about 89% was reached [59], while the SOEL cell developed by Sunfire reached 78% [60].

Another aspect to consider in the choice of electrolysis technology to integrate into the process is flexibility, intended as a combination of load range, and load gradients. The minimum load of AEL is usually dependent on gas crossover issues happening at low current densities. As the current density is reduced, the concentration of H_2 and O_2 at the opposite electrode increases, thus creating an explosion risk. Even though the problem is less severe for PEMEL, at high pressure or with thinner membranes, gas crossover might become critical at low current densities, therefore reducing the load range [54]. SOEL is reversible and can theoretically operate from -100% to 100%. However, if the cell is operated below U_{tn} heat must be supplied to prevent stack cooling. Sanz-Bermejo et al. have developed a model to understand what partial load range is feasible for a solid oxide fuel cell. The analysis showed that their system was able to operate from 10-100% power load, thus suggesting good compatibility with renewable power sources [61].

Transient operation is easier for PEMEL, and AEL systems, which can react quickly to dynamic power profiles and change their load in a few seconds [58]. AEMEL and PEMEL have the best dynamic behavior among the four technologies. Furthermore, having lower operating temperatures, they can be heated up to the nominal temperature relatively fast. On the other end, a SOEL module has to be held at a high operating temperature (700-900°C) in idle mode. Otherwise, a long start-up time is necessary to avoid the degradation of the cells. It can be concluded that the transient operation of a SOEL system is more complicated rather than AEL, AEMEL, and PEMEL, due to thermal management, however, with good heat integration and efficient thermal insulation SOEL coupling with renewable energy sources is possible [62].

Durability (stack lifetime) is also unfavorable for SOEL when compared to AEL and PEMEL. It is estimated that AEL stacks can operate up to 60 000 h, PEMEL stacks have a lifetime between 50 and 80 000 h, while due to higher degradation, SOEL stacks only reach about 20 000 h. AEMEL also shows a lower lifetime compared to AEL and PEMEL, due to limited membrane stability. Kumar and Lim, report a lifetime of 30 000 h with the current state of the art [55]. However, for both SOEL and AEMEL, the reduced durability can be related to the different maturity of the technologies and will improve in the next decades.

AEL is undoubtedly the most well-established and mature technology for green hydrogen production, considering that the first industrial large-scale alkaline electrolyzer went into operation in 1939 [55]. PEMEL has been introduced in the 1960s and it is now a commercial technology. SOEL is still in the development phase, although some companies, such as the already mentioned Sunfire, have commercial applications for solid oxide electrolysis cells. AEMEL technology is in the developmental stage up to the kW scale.

2.4. Syngas Upgrading to Gasoline

2.4.1. Introduction

After bio-oil gasification, a CO_x and H_2 rich synthesis gas can be processed for further upgrading to hydrocarbon. Water electrolysis yields a hydrogen stream, which can be used to adjust the H_2:CO_x ratio of the syngas in order to obtain the appropriate gas composition dictated by the reactions of the next conversion process.

However, the synthesis gas resulting from the gasification process is usually not applicable directly in downstream conversion processes as it can contain impurities that must be removed prior to other process steps [42]. This means that gas cleaning has to be implemented after bio-oil gasification. Impurities present in the gas can poison the catalyst or damage the process equipment. Depending on which catalysts and temperatures are used in the gas-upgrading processes, gas cleanup technologies can be chosen. For this reason, gas-cleaning technologies will be discussed in a later section.

The final product of the process is gasoline, a mixture of organic compounds used as fuel in spark-ignited internal combustion engines. Within the hydrocarbons present in this liquid fuel, C_{5-11} hydrocarbons are the primary components.

As discussed in Section 1.4.2, different routes can be followed for the production of synthetic gasoline from syngas. Due to the low selectivity of C_{5-11} in Fischer-Tropsch synthesis, and due to the several process plant design analysis on PBtL available in the literature [21], [26], [27], [28], [29], FT was discarded.

Methanol-to-Gasoline is another possible route that can be chosen. However, the integration of this process with biomass gasification and water electrolysis has also been already analyzed [34], [35].

2.4.2. Syngas direct conversion to DME

DME can be produced in two distinct ways: the indirect route and the direct route. The former is based on methanol synthesis performed in one reactor and its subsequent dehydration to DME in a different reactor. In the latter, DME is produced in a single stage, using bi-functional catalysts [36]. Direct DME conversion, is proven to be superior to the indirect route: apart from the advantages coming from a higher plant integration, if the methanol synthesis and the methanol dehydration are conducted in the same reactor, the consumption of methanol due to the latter reaction shifts the thermodynamic equilibrium of the former towards the product side, increasing the overall DME yield.

Reactions

The direct synthesis of DME from syngas containing H_2, CO, and CO_2 follows mainly two overall reactions:

$$3CO + 3H_2 \leftrightarrow CH_3OCH_3 + CO_2 \tag{2.30}$$

$$2CO + 4H_2 \leftrightarrow CH_3OCH_3 + H_2O \tag{2.31}$$

The difference between the two reactions is that Equation 2.30 includes the WGS reaction (Eq. 1.1), while Equation 2.31 does not. The basic reactions involved in the process are the methanol synthesis from CO (Eq. 2.32), the methanol synthesis from CO_2 (Eq. 2.33), the methanol dehydration reaction (Eq. 2.34), and for the overall Equation 2.30, the WGS (Eq. 1.1).

$$CO + 2H_2 \leftrightarrow CH_3OH \tag{2.32}$$

$$CO_2 + 3H_2 \leftrightarrow CH_3OH + H_2O \tag{2.33}$$

$$2CH_3OH \leftrightarrow CH_3OCH_3 + H_2O \tag{2.34}$$

In each overall reaction (Eq.2.30 and Eq. 2.31), the equilibrium conversion reaches its maximum peak when the H_2:CO ratio in the syngas corresponds to the stochiometric value, 1 for Equation 2.30 and 2 for Equation 2.31. Taking into account the WGS reaction, the conversion results in a mixture of DME and CO_2, which is the main by-product [37].

Catalysts

The catalysts used in the direct route have a hydrogenation function suitable for the methanol synthesis reaction and a solid-acid function for the methanol dehydration reaction to DME. Generally, they are hybrid catalysts, derived from the optimization of Cu-type catalysts used in the MtG process. The catalysts used for the methanol synthesis are generally Cu-based catalysts, while common dehydration solid-acid catalysts are zeolites (i.e. ZSM-5) or gamma-alumina (i.e. γ-Al_2O_3). For instance, Cu-Zn-Al/γ-Al_2O_3 hybrid catalysts were used in the demonstration of a commercial plant by Korea Gas Technology Corp and a pilot-scale plant by Air Products and Chemicals, Inc. Following this plant, Wang et al. used the same catalyst in their experiments [40]. Ni et al. also used a similar catalyst based on a mixture of Cu-Zn-Al methanol synthesis catalyst and acidic γ-Al_2O_3 in the upper bed of their reactor and achieved high syngas conversion and gasoline selectivity in the overall syngas to gasoline (StG) process [32].

Operating conditions

The operating temperatures of the direct DME conversion are around 250°C and 260°C, as reported by different sources [32], [39], [40]. This is because with Cu-based catalyst, CO conversion happens at 250-300°C but at temperatures above 260°C the catalyst can be irreversibly deactivated [39]. DME productivity decreases at temperatures higher than 270°C because reactions of direct synthesis of DME are exothermic [63] and chemical equilibrium is thus unfavoured at high temperatures.

Since methanol synthesis is governed by a mole-reducing reaction (see Eq. 2.32), increasing the pressure, shifts the equilibrium towards the products, resulting in a higher CO conversion. However, as Wang et al. suggest, increasing pressure also results in higher energy consumption and more practical difficulties. In addition to this, coke-generating reactions are enhanced by increasing pressure, and coke formation results in faster deactivation of the catalyst [36], [63]. The literature review showed that the operating pressure can be chosen between 2 MPa and around 6 MPa. For instance, Wang et al. pressurized the reactor to 2-3.5 MPa [40], Ni et al. at 4 MPa [32], Stiefel et al. at 5.1 MPa [39].

The characteristics of the feed significantly influence the process results. It is therefore important to analyze the effect of the H_2:CO ratio and the CO_2:CO ratio.

To assess the thermodynamic performance, the following parameters are introduced: CO conversion (Eq. 2.35), H_2 conversion (Eq. 2.36), DME yield (Eq. 2.37), and DME selectivity (Eq. 2.38).

$$X_{CO} = \frac{\dot{F}_{in,CO} - \dot{F}_{out,CO}}{\dot{F}_{in,CO}} \tag{2.35}$$

$$X_{H_2} = \frac{\dot{F}_{in,H_2} - \dot{F}_{out,H_2}}{\dot{F}_{in,H_2}} \tag{2.36}$$

$$Y_{DME} = \frac{2\,\dot{F}_{out,DME}}{\dot{F}_{in,CO} + \dot{F}_{out,CO_2}} \tag{2.37}$$

$$S_{DME} = \frac{2\,\dot{F}_{out,DME}}{2\,\dot{F}_{out,DME} + \dot{F}_{out,MeOH}} \tag{2.38}$$

where $\dot{F}_i$ is the mole flow of component i in kmol/s.

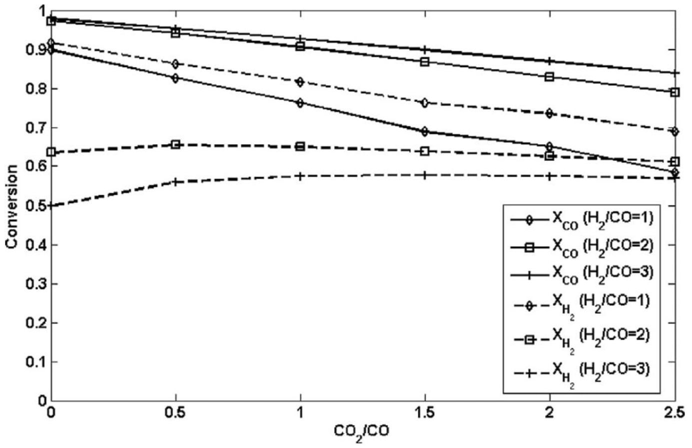

Figure 2.6: CO and H_2 conversion vs CO_2/CO varying H_2/CO (temperature = 250°C, pressure = 50 bar). [64].

Figure 2.6, shows the equilibrium CO and H_2 conversions with different feedstock compositions. In the first place, it is observable that the highest CO conversions and H_2 conversion could ideally be obtained with a CO_2 free synthesis gas, with an H_2:CO=1 (stoichiometric) composition. Increasing the CO_2 concentration has always a negative effect on CO conversion and decreases the H_2 conversion when H_2:CO=1. However, it has a positive effect on the H_2 conversion when the synthesis gas is abundant in hydrogen.

Figure 2.7 shows how DME yield and DME selectivity are influenced by the syngas composition. It is again clear that a CO_2 free feed gas is preferable. The DME selectivity is slightly influenced by the CO_2 content and much more negatively influenced by an increase in H_2 concentration. The DME yield is positively affected by an increase in H_2:CO, while the CO_2 concentration has a significant negative impact.

The negative effect of CO_2, is mainly due to the (reverse) water-gas shift reaction (Eq. 1.1). When CO_2 concentration increases, the formation of water is favoured. Water is the product of both the methanol synthesis and methanol dehydration reactions, therefore when its concentration in the mixture increases, the formation of DME is unfavoured. In addition to this, water can adsorb on the catalyst surface, inhibiting the reactions. Water also deactivates the catalysts by sintering the active sites of the hydrogenation catalysts and deteriorates the MeOH dehydration catalysts [65].

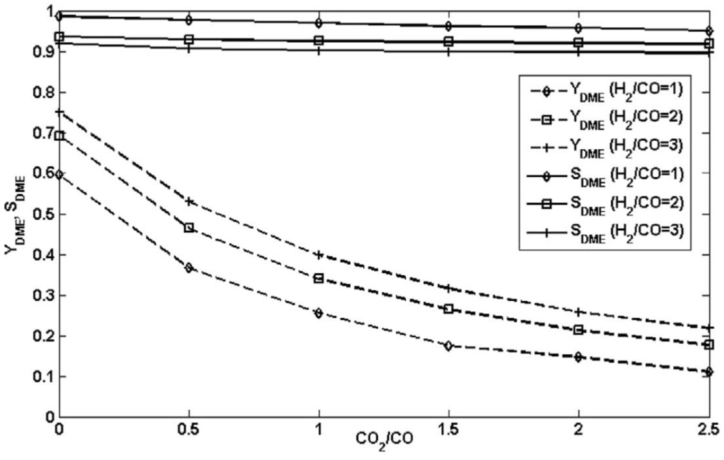

Figure 2.7: DME yield and selectivity as a function of CO_2:CO ratio at different H2:CO ratios (temperature 250°C, pressure = 50 bar) [64].

We can conclude that if DME is produced starting from a synthesis gas with a high concentration of CO_2, the values of selectivity and yield are low. Therefore the possible solutions are CO_2 sequestration upstream of the reactor (which is normally done in state-of-the-art plants as it is shown in section 2.5), or a more innovative in-situ water removal concept integrated into the reactor design.

Reactors

The most common reactors for direct DME synthesis are fixed bed reactors and slurry phase reactors [36]. Fixed bed reactors have been used in the work of Stiefel et al. [39], Wang et al. [40], and in the 10 t/day demonstration plant built by Korea Gas Corp [66]. However, fixed-bed reactors are not optimal for large-scale production. One-step slurry phase DME synthesis has been known as a potential process for large-scale DME production [36], due to their better heat transfer and lower investment. Slurry phase reactors have been used in the 10 t/day demonstration plant developed by Air Products & Chemicals, Inc [67] and in a 100 t/day plant demonstrated from 2002 to 2006 in Japan by JFE Holdings, Inc [66].

Kinetics

The majority of the available studies base the kinetic modelling of the one-step process on combining the available separate models of methanol synthesis and dehydration. However, a few studies developed models for the direct synthesis of DME. FThe kinetic model employed in this project has been developed by Lu et al. [68].

$$r_1 = \bar{K}_1 \frac{P_{CO_2} P_{H_2} \left(1 - P_{MeOH} P_{H_2O} / K_{eq1} P_{CO_2} P_{H_2}^3\right)}{\left(1 + K_{CO_2} P_{CO_2} + K_{CO} P_{CO} + \sqrt{(K_{H_2} P_{H_2})}\right)^3} \tag{2.39}$$

$$r_2 = \bar{K}_2 \frac{P_{H_2O}. - \left(P_{CO2} P_{H_2} / K_{eq2} P_{CO}\right)}{\left(1 + K_{CO_2} P_{CO_2} + K_{CO} P_{CO} + \sqrt{(K_{H_2} P_{H_2})}\right)} \tag{2.40}$$

$$r_3 = \bar{K}_3 \left(\frac{P_{MeOH}^2}{P_{H_2O}} - \frac{P_{DME}}{K_{eq3}} \right) \tag{2.41}$$

Where P_j is the partial pressure of the component j, $\bar{K}_1$, $\bar{K}_2$ and $\bar{K}_3$ are the kinetic constants in [kmol/(kg s bar^2)], K_j are the Langmuir adsorption kinetic constants of the respective compound on the catalyst in [bar^{-1}] [69], [70], and K_{eq1}, K_{eq2}, and K_{eq3} are the equilibrium constants. The kinetic and adsorption constants have been calculated according to Arrhenius'law:

$$K_j = A\, e^{\left(-\frac{B}{RT}\right)} \tag{2.42}$$

with the following constants:

Table 2.2: Coefficients for the calculation of the kinetic and adsorption constants with Eq. 2.42

Constant	A	B
$\bar{K}_1$	35.45	1.7069 $\cdot 10^4$
$\bar{K}_2$	7.3976	2.0463 $\cdot 10^4$
$\bar{K}_3$	8.2894 $\cdot 10^4$	5.2940 $\cdot 10^4$
K_{H_2}	0.2490	-3.4394 $\cdot 10^4$
K_{CO_2}	1.02$\cdot 10^{-7}$	-6.74 $\cdot 10^4$
K_{CO}	7.99$\cdot 10^{-7}$	5.81 $\cdot 10^4$

The equilibrium constants have been calculated using the temperature-dependent expressions provided by Aguayo et al. [71]:

$$K_{eq,i} = e^{\left(a + \frac{b}{T} + c\, logT + dT + eT^2 + \frac{f}{T^2}\right)} \tag{2.43}$$

with the coefficients reported in Table 2.3. Note that the coefficients in the second row of the table allow the calculation of the equilibrium for the Reverse Water Gas Shift reaction. Thus, to calculate K_{eq2} one should use the inverse of the value obtained.

Table 2.3: Coefficients for the calculation of the equilibrium constant using the model of Aguayo et al. [71]

	Reaction	**a**	**b** ·10^{-3}	c	d ·10^{4}	e ·10^{8}	f ·10^{-3}
0	Eq. 2.32	21.84	9.04	-7.66	54.07	-57.50	-6.75
2	Eq. 1.1	18.01	-5.87	-1.86	2.70	0	58.2
3	Eq. 2.34	-9,76	3.20	1.07	-6.57	4.90	6.05

Note that the coefficients for the equilibrium constant of the formation of methanol from CO_2 (Equation: 2.33) are not present, because the reaction equation is a linear combination of Equation 2.32 and Equation 1.1. Thus, the equilibrium constant can be calculated as the ratio of the equilibrium constants of the corresponding equations:

$$K_{eq1} = K_{eq0}/K_{eq2} \tag{2.44}$$

2.4.3. Process enhancement by in-situ water removal

When water is formed at the product side, in-situ water removal can significantly enhance the reaction, shifting the equilibrium towards the product side according to Le Chatelier's principle. In addition to this, in DME synthesis from CO or CO_2, water inhibits the reaction by adsorbing on the catalyst surface. For this reason, the application of in-situ water removal in the DME synthesis reactor could improve the process from different points of view. Different technologies have been suggested to remove water from reaction mediums: the most popular technologies involve sorption-enhancement and membrane reactors.

Sorption enhanced reaction process

Sorption-enhanced reactions involve the addition of a sorbent to the reaction mixture for the selective removal of one of the reaction products, thereby shifting the equilibrium. Subsequently, the product stream has to be separated from the sorbent (i.e. by filtration or distillation) and the sorbent has to be regenerated in a separate unit, typically by pressure and/or temperature swing [72], before being recirculated to the main reactor. In the context of sorption-enhanced DME synthesis (SEDMES), the solid adsorbent is generally a zeolite, capable of withstanding the operating conditions of the process.

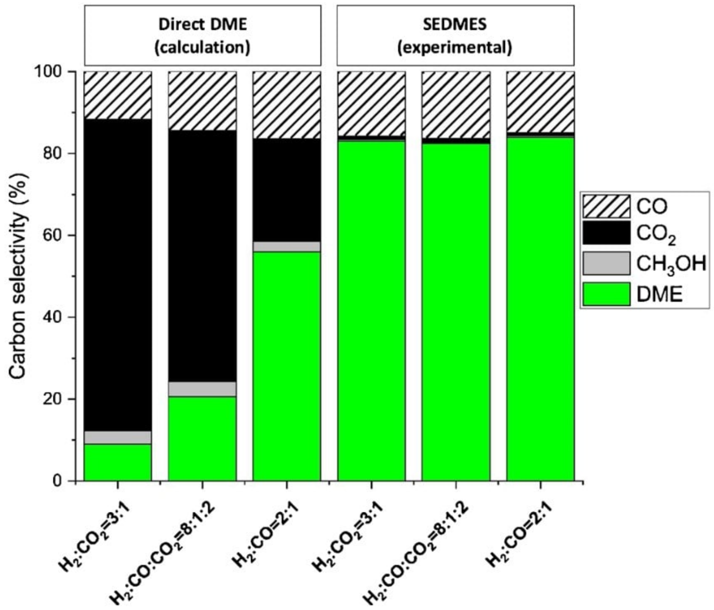

Figure 2.8: Product distribution in a thermodynamic study of direct DME synthesis (left) versus experimentally obtained results for sorption-enhanced DME synthesis (right). Temperature = 275°C, pressure = 40 bar [73].

The first researchers to study sorption-enhanced DME synthesis were Kim, Jung, and Lee [74], who studied the effect of water on the performance of direct DME synthesis over a CuO-ZnO-Al_2O_3/γ-Al_2O_3 catalyst. By doing

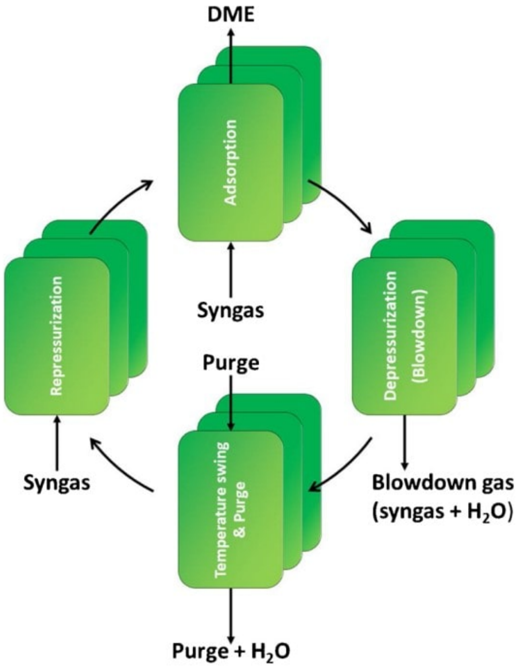

Figure 2.9: Schematic overview of the sorption-enhanced DME synthesis [73].

the experiments with and without a water adsorption pre-treatment of the catalysts, they found out that H_2O negatively affects the activity of both catalysts.
After that, sorption-enhanced direct DME synthesis has been evaluated numerically [75] and experimentally [72], [76], proving increased DME yield and selectivity. This superiority is shown in Figure 2.8, where we can also observe how the CO_2 concentration in the products is significantly lower in the SEDMES. This can be explained by the fact that the CO_2 is consumed by the WGS reaction, which is favoured due to the removal of H_2O.

As explained above, the adsorbent must be regenerated constantly. The regeneration procedure typically consists of multiple steps and, in general, requires more time than reactive adsorption. A combination of temperature and pressure swing regeneration results in the best system performance regarding the DME yield and CO2 conversion. However, it has been indicated that both temperature swing adsorption and pressure swing adsorption alone could be an option [73]. A simplified schematic of the process with both pressure and temperature swing is shown in Figure 2.9. Syngas is fed to a reactor where DME is formed during reactive adsorption. The second and third steps consist of depressurization and temperature swing, to separate syngas and water from the sorbent. Eventually, the sorbent is repressurized before re-entering the reactor.
As stated, one of the two regeneration techniques can be sufficient. To validate this, Van Kampen et al. developed and tested a pressure swing regeneration cycle for SEDMES, achieving DME selectivities up to 80% [76].

Hydrophilic membranes and membrane reactors

A membrane reactor with a hydrophilic membrane for in-situ water removal works by placing the membrane in contact with the reaction mixture, allowing water to selectively pass through the membrane while the other components of the mixture remain in the reactor. The permeate that passes through the membrane is removed from the system, thereby reducing the concentration of water in the reactor and driving the reaction forward.

The hydrophilic membrane to be integrated must be stable at the temperatures and pressures obtained in the reactor, highly selective to water steam, and with a high water steam permeability. High-temperature hydrophilic membranes that can be used at temperatures higher than 200°C are microporous zeolite ones [77].

Table 2.4: Membrane reactor vs conventional reactor in DME direct synthesis [77]

Parameter	Membrane reactor	Conventional reactor	Enhancement
Y_{DME}	0.75	0.57	+ 31.5 %
S_{DME}	0.99	0.88	+ 12.5 %
X_{CO_x}	0.75	0.65	+ 15.4 %
X_{CO_2}	0.69	0.53	+ 30.2 %

More recently, Rodriguez-Vega et al. have performed experiments in a laboratory-scale packed bed reactor, provided with a zeolite membrane [78] and compared the results with those obtained in a conventional reactor, proving the superiority of the former.
Furthermore, Li et al. [65] incorporated a Na^+-gated water conducting membrane into a DME synthesis reactor to generate a dry reaction environment. According to the authors, the activities of the hydrogenation catalyst ($Cu/ZnO/Al_2O_3$) and of the methanol dehydration catalyst (HZSM-5) are boosted 4- and 10-fold, respectively. The CO_2 conversion reached up to 73.4% and reduced catalyst deactivation was proven.

Membrane reactors vs. sorption-enhancement

As shown above, both technologies significantly enhance the performance of DME direct synthesis. It is also worth mentioning that they are still in the research phase and have not been employed on an industrial scale yet. Membrane reactors enable the selective separation of water from the reaction mixture during the synthesis process. This technology offers the advantage of continuous water removal without the need of building around the reactor a complex separation and regeneration system. However, the main drawback of membrane reactors is the need for high-performance, durable, and selective membranes that can withstand harsh reaction conditions, including high temperatures and pressures, and resist potential fouling. In addition to this, the membrane reactor brings additional costs and complexity to the reactor design, whose volume has to increase to account for the sweep gas volume flow rate.

On the other hand, sorption-enhanced reactions offer the advantage of simplicity in the design and operation of the reactor, since the solid sorbent is typically mixed with the catalyst and the reactor does not have to be significantly modified. Moreover, sorbents can be engineered to have high selectivity and capacity for water adsorption, ensuring efficient in-situ water removal. However, sorption-enhanced reactions have some disadvantages, such as the additional complexity, capital costs, and operational challenges introduced by a continuous system for sorbent regeneration. Such a system is necessary to avoid process interruptions for sorbent regeneration.

2.4.4. DME to hydrocarbon conversion

The second step of the syngas to gasoline conversion is the conversion of DME to hydrocarbons. This process is basically the same as the conversion of the MtG but without the first step, in which methanol is dehydrated to DME [79].

Reactions

The overall reaction path for the conversion of DME to hydrocarbons consists of the olefin formation reaction, in which a molecule of water is removed from a molecule of DME to form olefins. Olefins react further to produce higher hydrocarbons. The process is shown in Figure 2.10.

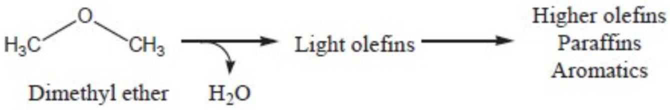

Figure 2.10: Reactions involved in the DtG process [33].

The overall reaction is exothermic, with a reaction enthalpy estimated to be between 45 kJ $\cdot$ mol^{-1} and 54 kJ $\cdot$ mol^{-1}, depending on the degree of conversion and selectivity.

As reported by Pérez-Uriarte et al. [80], the formation of hydrocarbons from oxygenates (DME and MeOH), proceeds in the hydrocarbon pool, via the dual cycle mechanism, which occurs by two routes, the aromatic cycle, and the olefin cycle. The former consists of the methylation-dealkylation of intermediate aromatics (i.e. addition of methyl groups (CH_3) and removal of the alkyl groups (C_nH_{2n+1}) attached from the aromatic compounds), while the latter consists of the methylation-cracking of olefins (addition of methyl groups to the olefins and breaking into smaller molecules). Moreover, secondary reactions of isomerization (where the position of the methyl group on the aromatic ring is changed), cyclization (where the aromatic ring is closed to form a cyclic compound), and hydrogen transfer (where hydrogen atoms are transferred between different molecules), yielding light paraffins, BTX aromatics, and C_5^+ aliphatics.

Catalysts

The catalysts used for the MtG and the DME to Gasoline (DtG) processes are zeolites. Specifically, since the development of the MtG process by Mobil in the 1970s ZSM-5 zeolite is the most common catalyst [40]. The conventional catalyst has been modified in many ways in order to increase activity and stability. Ni et al. report that a low amount of acid and the nano-sized structure of the ZSM-5 zeolite are beneficial to C_{5-11} selectivity and stability. Specifically, the low amount of acid, given by a low Si/Al ratio in the catalyst, inhibits the formation of light hydrocarbons, while the nano-sized N-ZSM-5 has better stability than the micro-sized M-ZSM-5.

Operating conditions

The temperature at which the DtG takes place is usually around 400°C, as indicated by Lee et al. [37], and Chakraborty et al. [33]. Temperature plays an important role since the activity of the catalyst increases with temperature. In their experiments, Wang et al. operated the conversion at temperatures between 380°C and 450°C [40], while Ni et al. used a lower temperature of 320°C [32].

Pressure significantly influences the process and an increase in pressure results in an increase of the C_{5-11} selectivity, as verified experimentally by Ni et al. [32]. However, higher pressure favors coke formation on the catalyst surface [33]. Thus, a trade-off must be found. Typical operating pressures range from atmospheric to 3 MPa.

Reactors

Literature review showed that up to this day, no DtG commercial plants have been built, except for the ones built in MtG plants. The conventional choice for DME to hydrocarbon reactors is the utilization of a fixed bed reactor [81], [33].

However, ExxonMobil also developed a different concept involving a fluidized bed reactor and built a large demonstration unit in Germany in the 80s which was declared technically ready. Unfortunately, this plant was never started up and has been demolished. More recently, ExxonMobil restarted testing fluidized bed reactors in China and is working on the construction of a full-scale plant in South America [82].

Furthermore, Primus Green Energy developed a gas-to-liquid process to convert natural gas into gasoline, the so-called STG+ where DME is produced from methanol and then converted to gasoline. A plant of 100000 gal/yr has been demonstrated in Hillsborough, NJ and the step of DME conversion to gasoline was been performed in a fixed-bed reactor [83].

Kinetics

Several kinetic models were developed for the MtG process, since the 80s, even before the understanding of the dual cycle mechanism. However, according to Ortega et al., they have limited applicability when DME is used directly as a feedstock [84]. Therefore, Ortega, Hessel, and Kolb developed a new kinetic model for the conversion of DME to hydrocarbons over a ZSM-5 catalyst. The model considers the main steps of the dual cycle mechanism, including (1) formation of aromatic intermediates (polymethylbenzenes); (2) dealkylation of the intermediates to produce ethylene and propylene; (3) methylation of small olefins to increase the chain size of the hydrocarbons; (4) hydrogenation of ethylene, propylene, and butenes to produce the corresponding saturated compounds; and (5) dimerization reactions between propylene and butenes to produce higher hydrocarbons. The kinetic scheme considers seven kinetic species (or lumps): oxygenates (A), polymethylbenzenes (I), ethylene (B), propylene (C), butenes (D), saturated C_2-C_4 (E), and C_5^+ hydrocarbons (G). The considered steps are:

Step 1: $A \xrightarrow{k_1} I$
Step 2: $I \xrightarrow{k_2} B$
Step 3: $I \xrightarrow{k_3} C$

Step 4: $A + C \xrightarrow{k_4} D$
Step 5: $A + D \xrightarrow{k_6} G$
Step 6: $C \xrightarrow{k_5} E$
Step 7: $D \xrightarrow{k_5} E$
Step 8: $C + C \xrightarrow{k_6} G$
Step 9: $C + D \xrightarrow{k_6} G$
Step 10: $D + D \xrightarrow{k_6} G$

The kinetic parameters and the activation energies have been estimated by Ortega et al. and are reported in Table 2.5

Table 2.5: Kinetic parameters and activation energies in the model of Ortega et al. [84]

Parameters	**Value**		**Activation energy**	**Value**
$k_{0,1}$ $[h^{-1}]$	19.25		$E_{a,1}$ $[kJ\, mol^{-1}]$	173.1
$k_{0,2}$ $[h^{-1}]$	0.69		$E_{a,2}$ $[kJ\, mol^{-1}]$	43.1
$k_{0,3}$ $[h^{-1}]$	1.85		$E_{a,3}$ $[kJ\, mol^{-1}]$	73.1
$k_{0,4}$ $[kg_{totorg} kg_{lump}^{-1} h^{-1}]$	139.83		$E_{a,4}$ $[kJ\, mol^{-1}]$	126.6
$k_{0,5}$ $[h^{-1}]$	27.70		$E_{a,5}$ $[kJ\, mol^{-1}]$	109.4
$k_{0,6}$ $[kg_{totorg} kg_{lump}^{-1} h^{-1}]$	141.99		$E_{a,6}$ $[kJ\, mol^{-1}]$	97.2

2.5. Gas Cleaning and Water Purification

2.5.1. Introduction

As introduced in Section 2.4.1, gas cleaning is necessary after bio-oil gasification before further gas processing. The synthesis gas resulting from the gasification process must be purified in order to avoid catalyst poisoning and problems such as fouling and blockages in the process equipment.
The most relevant classes of impurity species that can be found in syngas are particulate matter, tars, sulfur species (mostly H_2S and COS), chlorine species (usually HCl), alkalis, and nitrogen compounds (NH3, HCN) [42].

With respect to the gasification of solid biomass, bio-oil gasification has the advantage of a cleaner synthesis gas. This is because most of the inorganic elements present in the raw biomass are retained in the solid phase during pyrolysis and do not end up in the bio-oil, as mentioned in Section 2.1. It is also important to note that entrained flow gasifiers operate at high temperatures, ranging from 1100-1500°C. Thanks to these very high temperatures, the tar concentration in the gas is reduced. For this reason, tar cleaning can be neglected in this analysis. Nonetheless, implementing other gas cleanup technologies is still necessary.

There are different ways to classify gas cleanup technologies. They can be divided between cleaning processes that take place inside the reactor, called primary or in-situ, and measures that remove impurities from the product gas downstream of the reactor. Further classifications are based on the nature of the cleanup technology, dividing them into physical and chemical separations, and depending on the temperature range of the process into hot, warm, and cold gas cleanup. While cold gas cleanup technologies are generally more advanced in terms of development and employment, the need to cool the synthesis gas at very low temperatures is a major disadvantage in terms of overall process efficiency. A very extensive review of the different gas cleaning processes is given by Woolcock et al. [85].

2.5.2. Removal of particulate matter

For catalytic DME synthesis and further conversion to gasoline, a very effective raw syngas cleaning and conditioning system is needed.
The first step in gas cleaning should be the removal of particulate matter, constituted by the inorganic compounds and residual solid carbon from the gasification of bio-oil. This can be achieved at high or low temperatures. Many

gas particulate cleanup technologies are available and they can be classified, depending on the physical principle they use, in inertial separation, barrier filtration, and electrostatic interaction.

Cyclone separators

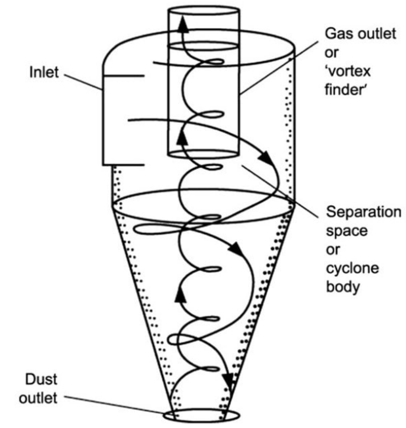

Figure 2.11: Schematic of a cyclone separator [85].

The oldest and most commonly employed devices for solids separation are cyclones [85]. Cyclones work by exploiting inertial separation based on centrifugal forces. In a typical reverse-flow cyclone (Figure 2.11), which is the most common type used, the dirty gas enters the cyclone tangentially at the top, describes a descending outer vortex, inverts the direction of motion, and ascends by an inner vortex exiting at the cyclone top through the vortex finder [86].

Particulate removal efficiency in industrial-scale cyclones can be $>99\%$ [85], [86]. Specifically, they are generally used as a first cleanup device, to remove particulate matter larger than 5 μm. Thanks to the absence of moving parts, cyclones can operate at high temperatures, being only limited by the mechanical strength of the construction materials. Finally, it is worth mentioning that cyclones have generally low investment and operating costs.

Barrier filtration

Filters are one of the most employed particulate matter removal devices. Their functioning is straightforward: a gas stream flows through fibres, granules, or porous media, and its particulate matter is trapped in the filter. Depending on their materials, filters can work at low and high temperatures. For instance, fabric filters can operate up to 250°C, while ceramic filters can operate at temperatures exceeding 400°C. The latter category has advanced in recent years to the extent that they can remove 99.99% of particulate matter smaller than μm [87].

2.5.3. Removal of sulfur compounds

In the syngas cleaning before DME synthesis and DME to hydrocarbon conversion, special attention should be given to sulfur compound removal, since the copper-Zinc-based catalysts used in direct DME synthesis suffer from sulfur poisoning, which causes its deactivation. The main sulfur compounds that must be removed from the syngas are H_2S and COS, where the former has the main focus.

The H_2S concentration in the synthesis gas can be predicted from the experimental data obtained by Leijenhorst et al., who performed bio-oil gasification experiments [47]. In the syngas produced with pine wood-derived bio-oil gasification, the H_2S concentration was 22 ppm. As reported by Abdoulmoumine, the sulfur concentration in the feed must be reduced to at least 1 ppm [88].

It is crucial to state that in the case of this process, H_2S removal must be selective, meaning that hydrogen sulfide should be extracted without removing CO_2 from the syngas stream, which would cause a carbon conversion efficiency decrease of the process.

In the extensive review by Pudi et al. [89], different hydrogen sulfide capture removal technologies are discussed.

High-temperature sulfur removal

H_2S can be removed at high temperatures by physical or chemical adsorption, using solid materials (generally metal oxides, among which ZnO is the most favourable [42]. A sulfur adsorption process usually follows three stages: reduction (where the solid sorbent is prepared for chemical adsorption), sulfidation (where a metal oxide is combined with sulfur), and regeneration (yielding the original oxide sorbent and an enriched sulfur dioxide gas) [85]. In the case of zinc-oxide sorbents, the raw synthesis gas enters the packed-bed column containing zinc-oxide and H_2S reacts with it according to the following reaction:

$$\mathrm{ZnO} + \mathrm{H_2S} = \mathrm{ZnS} + \mathrm{H_2O} \tag{2.45}$$

In addition to metal oxides, H_2S adsorbents are zeolites, carbon-based sorbents, metal–organic frameworks (MOFs), and composite materials [89].

Low-temperature sulfur removal

At low temperatures, there are many options for sulfur removal. Acid gas removal by absorption into a liquid solvent has been the dominant technique for purifying gases since the 20th century [89]. Depending on the nature of the interactions between the solvent and H_2S, the absorption mechanism can be classified as chemical, physical, or mixed chemical/physical.

Physical solvents for acid gas removal are typically polar molecules that weakly interact with the polar H_2S and CO_2 molecules. Rectisol and Selexol are the most common physical solvent processes, thanks to their ability to provide deep removal (0.1 ppm with Rectisol, and 1 ppm with Selexol). Their main disadvantage is their shallow operating temperature range (Rectisol operates down to -60°C), leading to a high refrigeration duty. Furthermore, they show low H_2S selectivity over CO_2.

In chemical H_2S absorption processes, liquid solvents react with hydrogen sulfide to form a stable product that can be separated from the gas stream. Chemical solvents are typically based on alkanolamines such as monoethanolamine (MEA), diethanolamine (DEA), and methyldiethanolamine (MDEA). Over the past twenty years, MDEA has become increasingly popular in the market due to its advantageous properties compared to MEA and DEA. These include a strong ability to remove H_2S selectively while leaving CO_2 [90], a high capacity for loading, low vapor pressure, low corrosiveness, high resistance to degradation, and effective energy usage [89]. With respect to physical solvents, they have a higher operating temperature range, which is beneficial as less refrigeration duty is necessary.
Amine units are suitable for handling large amounts of sulfur that need to be removed, while sorption-based removal is more appropriate for smaller sulfur masses. However, a middle ground is found in Liquid Redox processes, such as the Stretford process, SulFerox, or the LO-CAT process [91]. These processes are commonly referred to as ”liquid redox” in the industry due to the oxidation/reduction reactions that take place in the liquid phase. In general, these plants consist of an absorber, where H_2S comes into contact with the liquid redox solution (an iron-based aqueous solution), resulting in the conversion of H2S into elemental sulfur and water. The solution is then directed to an oxidizer, where the catalyst is regenerated, and the slurry containing elemental sulfur is separated. While the redox solution can also absorb CO_2, it has a minimal impact on the absorber’s performance, as stated by Reid [91].

2.5.4. Examples from physical plants

In their experiments, Wang et al. set requirements on tar, H_2S, and dust concentrations, which had to be lower than 10 mg/m^3, in order to prevent poisoning of the Cu-Zn-Al/γ-Al_2O_3 hybrid catalyst [40]. To achieve this a multi-stage gas cleanup system was implemented. First, particulate matter is removed with a cyclone and a baghouse filter. Secondly, a spraying water scrubber is used to remove tars. Wet scrubbing is indeed one of the most widely deployed gas cleanup technologies in the industry, because of its simplicity and effectiveness. Not only it removes tars but it is typically used to remove also particulate matter, chlorine compounds, and alkalis [85]. The last gas cleaning step implemented by Wang et al. consisted of CO_2 removal by water scrubbing.

In the pilot plant of the bioliq® process at KIT, a gas cleaning system is being developed with the final goal of operating it at temperatures close to 500°C [92]. The advantage of higher temperatures with respect to wet scrubbing is in terms of overall process efficiency. Generally speaking, cold gas cleanup induces thermal penalties on the overall plant efficiencies, however, these technologies are reliable, widely deployed, and efficient [85].

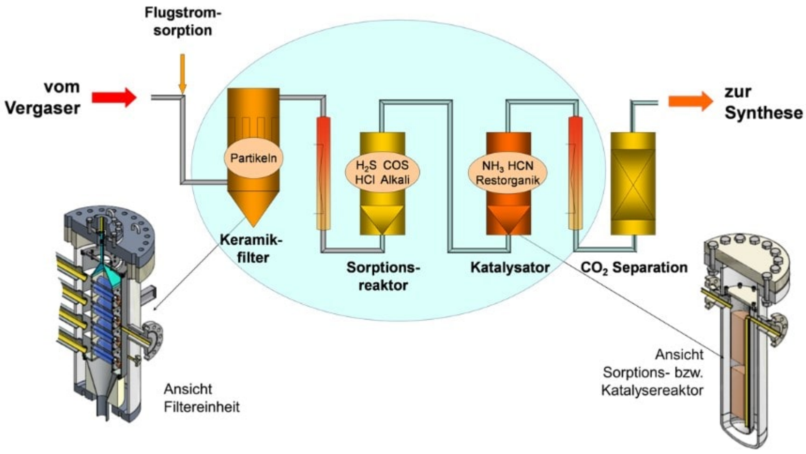

Figure 2.12: Gas cleaning system in the bioliq® process at KIT [92].

The system shown in Figure 2.12, consists of a ceramic filter that removes particulate matter, a fixed bed sorption reactor for H_2S and COS with ZnO, for HCl with Na_2CO_3, and for Alkali with an unspecified sorbent, and subsequently, a catalytic reactor for the decomposition of NH_3, HCN, and organic compounds. Finally, CO_2 absorption is carried out by the Selexol method using a conventional detergent (PEG-DME). [93].

2.5.5. Water purification: activated carbon filters

Water and hydrocarbons must be separated downstream of the DtG reactor. To be recycled and reused as an input for the electrolyser, water has to be “as pure as possible” [57]. Therefore, removing traces of hydrocarbons that might be present in water is necessary before inputting H_2O in the electrolyser stack.

This can be achieved cost-effectively with adsorption onto activated carbons, a technically viable method for liquid purification [94]. Activated carbon is a form of carbon that is processed (activated) with small, low-volume pores that increase the surface area available for adsorption, which can reach 2000 m^2 per gram of activated carbon. Activated carbon adsorption proceeds through three basic steps: (1) substances adsorb to the exterior of the carbon granules; (2) substances move into the carbon pores; (3) substances absorb to the interior walls of the carbon [95].
Activated carbon filters are widely deployed and used in water treatment to remove several types of impurities, such as organic matter, chlorine, phenols, and hydrocarbons [96]. They can remove the total suspended solids with an efficiency of over 99% [95]
Depending on the activated carbon solid form a distinction can be made between Granular Activated Carbon (GAC) and Powdered Activated Carbon (PAC) with the former category dominating the water purification sector. GAC can be made from organic materials (such as coconut shells, wood, and coal). Eventually, (with the lifetime depending on the concentration of contaminants and the average water use) the adsorption capacity of the GAC-based filters to adsorb and remove chemicals is exhausted, and the GAC needs to be changed. The spent activated carbon can be landfilled, incinerated, or regenerated and reactivated for reuse. Regeneration and reactivation have become widely adopted as they represent the most cost-effective and environmentally sound option [97]. In this case, the activated carbon is directed to the regeneration process that can be on-site or optionally at a specialized off-site facility [94].

2.6. Plant Integration

As explained in Section 1.3, Power and Biomass to Liquid fuels have received attention in the past years. Literature research showed that several processes with different final products have been studied in order to assess them from a technical and economic point of view. Researchers have studied the effect of different electrolysis technologies integrated into various plants, such as biomass to methanol, biomass to DME, and biomass to gasoline via FT or MtG. An overview of the available literature is reported in Table 2.6.

First, this overview shows that very high carbon conversion efficiencies are obtained with the integration of electrolysis, as already anticipated in Section 1.3. All the processes analyzed in the papers listed in Table 2.6 show CC values higher than 85%, with only three exceptions: [35], [34], and [18].
The low carbon efficiency in the analysis of Hennig et Haase is due to two reasons. The most significant carbon loss is caused by the decentralized pyrolysis step since the pyrolysis gas is used for heating the individual pyrolysis units but does not serve as feedstock for gasification. In addition to this, the produced hydrocarbons outside the gasoline range and the fuel gas produced and used in a gas turbine account for more carbon losses.
The lower carbon efficiency in the work of Hannula and in the one of Poluzzi can be explained by the fact that part of the carbon is lost due to the extraction of part of the gas, which is burnt in an internal combustion engine to produce electricity.

Another important observation is the absence of pyrolysis units in most processes, as already anticipated in Section 2.1. These two studies have selected an entrained flow gasifier, confirming that it is the most logical choice for bio-oil gasification.

Three different electrolysis technologies were utilized in the analyzed studies: AEL, SOEL, and PEMEL. However, only two studies opted to use AEL. The reason for its selection varied; Hannula chose it due to its widespread availability and commercial viability [104], while Henning et Haase selected it because of its compatibility with renewable energy sources [35].
PEMEL has been chosen in three different analyses. Albrecht et al. [29] and De Fournas et Wei [99] state that, because of the superior dynamic operation behavior compared to the other technologies, PEMEL has the potential to be connected to fluctuating power sources.
Dossow compared PEMEL and SOEL in the same plant. Due to its higher efficiency and the possibility of an efficient heat integration offered by the high-temperature electrolysis, SOEL integration resulted in higher plant efficiencies thanks to a $\sim$ 20% decrease in electricity demand [21]. This is also the reason behind the choice of Ostadi et al. [27] and Hillestad et al. [26].

For the studies that focused on bio-gasoline and bio-diesel production, the economic performance can be analyzed and possibly used as a reference. It is not straightforward to make comparisons between the economic performances of the plants because different authors made different economic assumptions. The price of electricity has been reported to be one of the main factors contributing to the cost of fuel, therefore the electricity cost assumed by the authors is reported in Table 2.7.

Table 2.7: Economic performance of the PbTL plants

Ref	Authors	Year	Process	Electricity price assumed	Cost of fuel	Actualized cost of fuel
[21]	Dossow et al.	2021	FT	-	-	-
[28]	Pandey et al.	2022	FT	0.066 €/kWh	1.70 €/l	1.87 €/l
[27]	Ostadi et al.	2019	FT	-	-	-
[29]	Albrecht et al.	2017[1]	FT	0.1 €/kWh	2.2 €/l	2.64 €/l
[26]	Hillestad et al.	2018	FT	0.04 €/kWh	1.18 €/l	1.36 €/l
[35]	Hennig and Haase	2021	MtG	0.044 €/kWh	2.43 €/l	2.67 €/l
[34]	Hannula	2016	MtG	0.05 €/kWh	1.78 €/l	2.13 €/l

1: Market values taken from 2014

It is important to note that the costs in dollars have been converted into euros, according to the annual average exchange rate. Furthermore, the costs have been actualized, using an online inflation calculator.
In general, these papers will serve as a reference during the basis of design and will help to validate the obtained results from the model developed in the project.

2.7. Summary and Key Findings

A comprehensive literature survey has been conducted, aiming to explore diverse technologies for the production of sustainable gasoline from bio-oil and examining the potential underlying technologies that may serve as sub-

Table 2.6: Literature Overview on PbTL

Paper			Process					
Ref	**Authors**	**Year**	**Pyrolysis Units**	**Gasifier**	**Biofuel produced**	**Electrolysis**	**Carbon Efficiency**	**Efficiency**[1]
[21]	Dossow et al.	2021	No	Entrained flow	FT fuels	SOEL	97%	50%
						PEMEL	97%	46%
[28]	Pandey et al.	2022	No	Entrained flow	FT fuels	SOEL	96%	63% [2]
[27]	Ostadi et al.	2019	No	Entrained flow	FT fuels	SOEL	91%	64% [2]
[29]	Albrecht et al.	2017	Yes	Entrained flow	FT fuels	PEMEL	98%	51%
[26]	Hillestad et al.	2018	No	Entrained flow	FT fuels	SOEL	91%	-
[98]	Mignard et al.	2008	No	Stratified downdraft	Methanol	-	87%	52%
[99]	De Fournas et al.	2022	No	Entrained flow	Methanol	PEMEL	92%	62%
[18]	Poluzzi et al.	2022	No	Dual-fluidized bed	Methanol	-	64%	61%
[100]	Ostadi et al.	2023	No	Entrained flow	Methanol	SOEL	94%	51%
[101]	Pozzo et al.	2015	No	Two-stage pyro-gasifier	DME	SOEL	91%	69%
[35]	Hennig and Haase	2021	Yes	Entrained flow	Gasoline	Alkaline	70 %	48%
[34]	Hannula	2016	No	Fluidized bed	Gasoline	Alkaline	79%	50%
					Methane		98%	58%
[102]	Zhang et al	2020	No	Entrained flow	SNG	SOEL	85%	68%
					DME		86%	63%
					Methanol		86%	64%
[103]	Giglio et al.	2015	No	Fluidized bed	SNG	SOEL	-	72%

1: The efficiency is calculated as: $\frac{\dot{m}_{output} * LHV_{output}}{\dot{m}_{input} * LHV_{input} + P_{el}}$

2: Calculated using available data

processes within the overall process.

The review began with an assessment of the pyrolysis process, underscoring the advantages of decentralized pyrolysis units in the PbTL plant. Following this, the gasification process was examined, focusing on the reactions, crucial process parameters, and operating conditions. Entrained flow gasifiers emerged as the most suitable reactors for bio-oil gasification. The study also covered the theoretical aspects of water electrolysis, and compared four different electrolysis technologies, namely AEL, PEMEL, AEMEL, and SOEL. SOEL was identified as the most efficient technology, particularly apt for integration in a plant where heat recovery is achievable from other units, such as gasification.

The review introduced various processes for upgrading syngas to gasoline, elucidating the reasons behind the selection of the process involving direct syngas conversion to DME and DME upgrading to gasoline. These two chemical conversion processes were investigated, identifying catalysts, operating conditions, prevalent reactors, and kinetic models. Furthermore, the advantages of employing in-situ water removal technologies in DME synthesis, specifically membrane reactors and sorption enhancement, were presented.
Synthesis gas purification (emphasizing particulate matter and hydrogen sulfide removal as the most critical impurity species to eliminate) and water purification using activated carbon were also analyzed.

Finally, the literature review concludes with a collection of reference papers that analyze other Power and Biomass to Liquid plants, providing additional insights and references.

3

Basis of Design

In the formulation of this process plant design, the Douglas approach has been utilized, a methodical framework outlined by James Douglas [105], which provides a hierarchical decision procedure for process synthesis. This process synthesis procedure decomposes the design problem into different levels or hierarchies of decisions. First, the decision of structuring the process as batch or continuous is made. Then, the process concepts are selected and the input-output structure of the flowsheet is formulated. Subsequently, the recycle structure of the flowsheet is determined and finally, the heat exchanger network is developed.

This chapter presents a preliminary description of the design, starting with an overview of the process, elucidating the process concepts and explaining the choices of specific units. Furthermore, information on the thermodynamic and kinetic models is given. To conclude the basic assumptions related to the location and battery limits of the plant are provided.

3.1. Description of the design

The process plant analyzed in this thesis is shown in Figure 3.1. Note that this is a preliminary schematic, which neglects some crucial components of the plant, such as heat exchangers, heaters, pumps, and compressors.

As elucidated in Chapter 1, the objective of the plant is to generate sustainable gasoline by utilizing a pyrolysis bio-oil feedstock, water, and renewable energy. The process incorporates gasification, water electrolysis, direct synthesis of dimethyl ether from syngas, and conversion of DME to gasoline. The reasons for selecting direct DME conversion and its subsequent conversion to gasoline are elaborated in Section 1.4.2.

While pyrolysis is a component of the sustainable gasoline production chain, it is not examined in this study because the plant does not include a centralized pyrolysis unit.

In Figure 3.1, the inputs of the process are at the top. Pyrolysis oil and water enter the plant and proceed downward in a parallel path. While pyrolysis oil is gasified and the resulting syngas is cleaned, water is split into its constituents, oxygen and hydrogen, in the electrolysis unit. Oxygen is partly stored and partly used as the oxidizing agent in the aforementioned gasification unit. Hydrogen and synthesis gas are mixed and enter the synthesis gas upgrading unit, where DME is formed and then converted to hydrocarbons. Finally, the products are separated and treated to obtain gasoline.

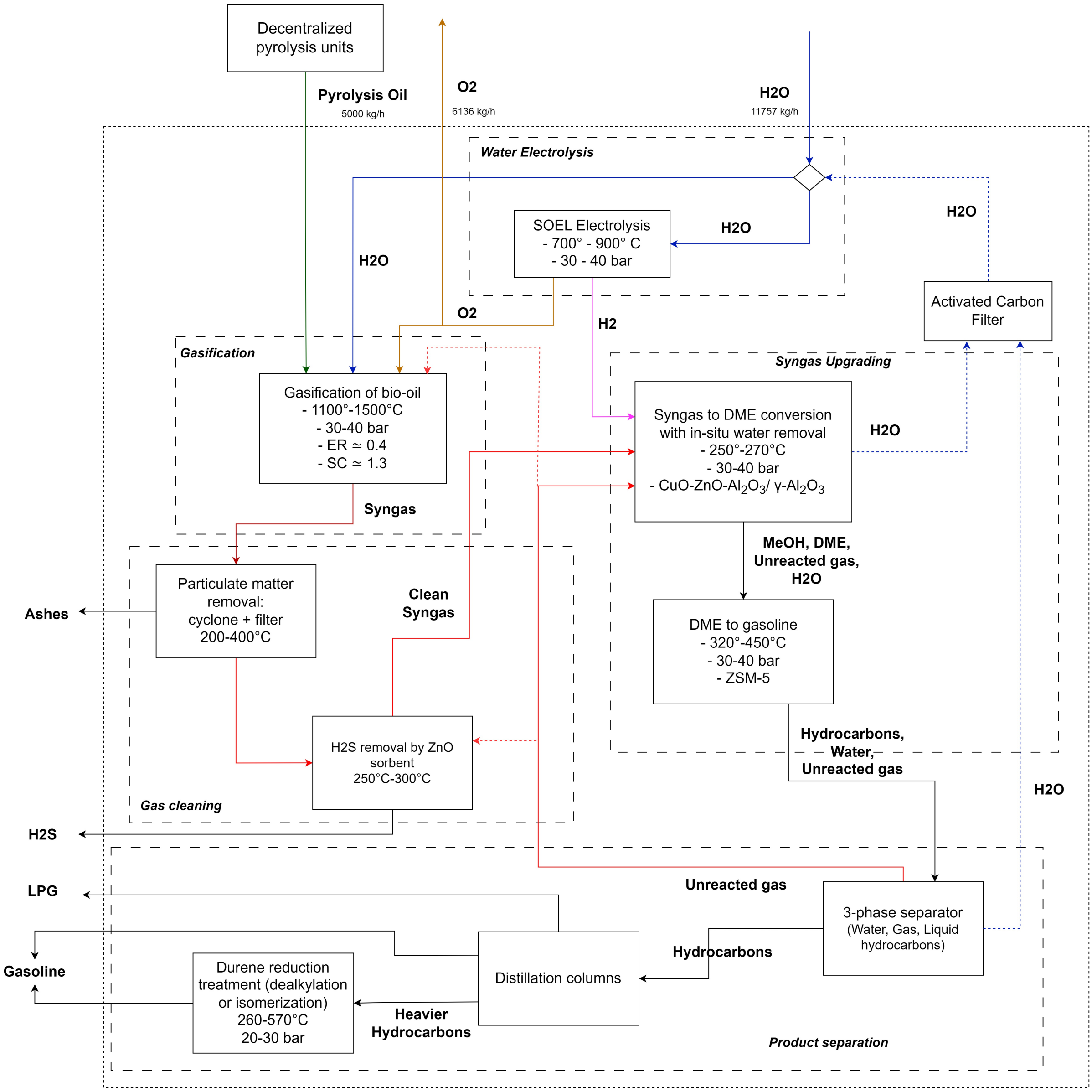

Figure 3.1: Block Scheme of the process

3.2. Process definition

The process can be divided into sub-units or sub-processes, as can be observed from the block scheme in Figure 3.1. Specifically, the sub-processes are gasification of bio-oil, water electrolysis, gas cleaning, syngas upgrading, and product separation. The decentralized pyrolysis units are not included in the battery limit of this plant and can be located strategically, close to biomass sources, as explained in Section 2.1. Bio-oil can be transported from these locations to the plant.

Batch vs Continuous

Given the scale of production (5000 kg/h of bio-oil must be processed), and considering that there is no need for product identification or batch identification, the process will be a continuous process. Continuous processes are usually more efficient and cost-effective for large-scale production.

3.2.1. Process concepts

Gasification of bio-oil

The initial sub-process in the process plant involves the gasification of bio-oil feedstock. Prior to gasification, the pyrolysis oil undergoes pre-heating and compression in a pump to reduce viscosity, increase pressure, and achieve suitable conditions for atomization. Based on the literature review, an entrained flow gasifier has been selected for this process, given its widespread adoption and superior performance. Entrained flow gasification gives the possibility of high-pressure operation, minimizing the need for further downstream compression. The oxidizing agent employed is oxygen, obtained from the water electrolyzer. The entrained flow gasifier operates at the highest temperature within the plant, ranging from 1100°C to 1500°C. As mentioned above, to minimize the need for significant compression of synthesis gas, bio-oil gasification is performed at high pressure, approximately 45 bar. As per the literature review, the optimal oxygen equivalence ratio should lie between 0.3 and 0.4, while the steam-to-carbon ratio can be adjusted to fine-tune the synthesis gas composition and enhance hydrogen content. The gasification process results in the production of syngas, a mixture of hydrogen, carbon monoxide, and carbon dioxide. Impurities might be present as explained in Sections 2.2, and 2.5.

SOEL electrolysis

The water mass flow entering the system encounters an electrolysis unit, after being evaporated. Water is split into hydrogen and oxygen and the two streams are used in the system. Part of the oxygen produced is fed to the gasifier, and hydrogen is used to adjust the H_2:CO_x ratio at the DME synthesis reactor. The remaining oxygen is compressed, cooled and stored in tanks that can be sold.
As explained at the end of Chapter 2, SOEL was found to be the most efficient and is particularly suitable for integration in a plant where heat recovery is possible from other units, such as gasification. Thanks to the high operating temperature range, it is thermodynamically superior to other electrolysis technology investigated in the literature study. Therefore, having a higher efficiency, requires a lower electrical energy input, contributing to increasing the overall plant efficiency. In order to avoid the integration of an oxygen compressor before the gasifier, the electrolyzer should be operated at a pressure higher than the one chosen for the gasifier. With the current SoA, operating a SOEL stack at 45 bar is not possible. However, as indicated by various sources [21], [26], [57], it is expected to have SOEL stack with those operating pressure in the next decades. Thus, the same assumption is made for this plant.

The main disadvantage of solid oxide electrolysis cells, with respect to PEMEL, AEMEL, and AEL, is the worse dynamic behaviour. As elucidated in Section 2.3.3, because of the high-temperature range (700°-900°C), the time necessary for a start-up sequence of a SOEL stack is significantly higher than the time necessary to turn on an AEL stack, a PEMEL stack, or an AEMEL stack. Thus, operating the electrolyzer completely off-grid, by only coupling it to a solar park or a wind park (or a combination of both), whose power outputs are fluctuating by nature, is not an option. The electrolyzer can be directly coupled with a renewable energy park but should also be connected to the grid, such that can operate continuously. The streams produced by the electrolyser are indeed crucial for the operation of the plant.

Gas cleaning

The raw synthesis gas proceeds to the gas cleaning unit within the process plant. As previously mentioned, the gas contains various impurities, including particulate matter, tars, sulfur compounds, and others. As discussed in Section 2.2, the tar concentration in the effluent gas from entrained flow gasification of bio-oil is minimal. This low concentration is attributed to the separation of most inorganics during the fast pyrolysis process, the high temperatures achieved in an entrained flow gasifier, and the selected equivalence ratio. Consequently, tar removal is not considered in this analysis. The presence of chlorine in the synthesis gas is also neglected since its content is expected to be low in the syngas obtained from pine-wood derived pyrolysis oil.

Following the gasification process, the syngas is cooled, and particulate matter is separated from the gas using a combination of a cyclone (to remove larger particles) and filters (to remove smaller particles).

The syngas necessitates further purification to decrease the hydrogen sulfide concentration to less than 1 ppm, ensuring protection for downstream catalysts. The selection of sulfur removal technology is guided by the following considerations:

- The unit must be capable of operating at pressures up to 45 bar, in order to avoid subsequent compression of syngas prior to its upgrading.

- Selective removal of sulfur compounds is required, allowing CO_2 to remain in the gas stream to prevent carbon losses and a consequent decrease in the overall carbon conversion efficiency (Eq. 2.5).
- Experimental findings by Leijenhorst et al. [47] indicate a sulfur concentration of 22 ppm in the synthesis gas derived from pine-wood bio-oil pyrolysis, which must be reduced to at least 1 ppm.
- The operational temperature should closely match 250°C, the temperature of the DME reactor, to avoid the need for gas reheating.
- The sulfur removal unit's performance should not be impacted by a high CO_2/H_2S ratio.
- The choice of the technology should consider both the mass flow of the synthesis gas and the mass flow of sulfur to be eliminated.

Considering the aforementioned factors, the chosen method for sulfur removal is the utilization of a zinc oxide sorbent bed. While the LO-CAT liquid redox process also offers selective removal capabilities, the sulfur content in the synthesis gas and the total mass flow rate indicate that solid scavengers would be more suitable, aligning with the recommendations provided in Reid's report [91]. Among the options considered, zinc oxide, iron sponges, and activated carbon were evaluated as potential sorbents. Of these choices, zinc oxide is the most commonly employed and best aligns with the specified requirements.
ZnO sorbents exhibit excellent performance under high pressures and temperatures (enhanced reaction rates are observed above 120°C due to increased diffusion rates). They are not adversely affected by elevated CO_2 concentrations in the synthesis gas and selectively remove H_2S to concentrations lower than 1 ppm [106].

H_2S removal utilizing ZnO takes place in packed bed columns, the design of which will be addressed in Chapter 4. The exact configuration of these columns falls beyond the scope of this project. However, it is crucial to note that since ZnO is continuously consumed in the reaction described by Eq. 2.45, the packed bed must undergo regeneration once the breakthrough time is reached. Consequently, the use of multiple vessels is necessary, enabling the regeneration of one vessel without shutting down the entire plant. The discussion of various strategies and potential configurations for the packed-bed columns, such as parallel configuration, series configuration, lead-lag, etc., will not be included.
Once the spent sorbent material is extracted from the vessel, it must be transported to a specialized plant located outside the battery limits for regeneration.

Syngas upgrading

The purified synthesis gas is mixed with a hydrogen stream produced via water electrolysis. It is directed to the syngas upgrading unit, which comprises two main stages: direct synthesis of DME from syngas and conversion of DME to gasoline. The optimal feed gas composition has to be evaluated by performing simulations and economic analysis. However, the model of De Falco et al. shows that, in terms of DME yield, increasing the H_2/CO_x ratio from 1 to 3 is always beneficial.

Direct DME synthesis employs a hybrid catalyst, $CuO\text{-}ZnO\text{-}Al_2O_3/\gamma\text{-}Al_2O_3$, facilitating both methanol synthesis and dehydration. The operating temperature range lies between 250°C and 270°C, while the pressure is maintained within 30-50 bar. Higher pressures offer thermodynamic advantages but introduce technical challenges, increased costs, and necessitate adjustments to the pressures of downstream operational units. As discussed in Section 2.4.3, in-situ water removal within the StD reactor creates a dry reaction environment, significantly enhancing DME yield, selectivity, CO_x conversion, and enabling a higher CO_2 concentration in the synthesis gas.

Given that both in-situ water removal technologies are currently in the research phase, and each has its own set of advantages and disadvantages, the optimal choice is not immediately apparent. In this project, a tubular membrane reactor has been chosen, as sorption enhancement may introduce additional complexity, capital, and operational costs and challenges. However, if sorption-enhanced DME synthesis is later determined to be more cost-effective and efficient than membrane reactors, this decision should be revisited. The effects of both technologies on DME synthesis are relatively similar, as they utilize the same working principle.

The second stage of syngas upgrading to gasoline involves converting DME to gasoline in a subsequent reactor. In this step, DME and a small fraction of unconverted methanol are transformed into hydrocarbons, as detailed in Section 2.4.4. Operating temperatures range from 320°C to 450°C, while the pressure remains similar to the previous reactor. The conversion process is catalyzed by a zeolite catalyst ZSM-5.

Product separation and purification

The final sub-process in the proposed design involves product separation and purification. The approach adopted for this stage is similar to the methodology employed in the bioliq® process but with some modifications, following the plant design of the Mobil MTG plant in New Zealand.

At the exit of the DME to hydrocarbons reactor, the effluent stream comprises water, unreacted synthesis gas (CO, H_2, and CO_2), and a mixture of liquid hydrocarbons. To process this effluent stream, it undergoes a cooling and depressurization step. Subsequently, following the process described in the US4788369A patent [107], a three-phase separator is employed. This separator serves to separate the stream into three components: a recycled water stream, a liquid hydrocarbon stream, and a gas stream. The gas stream contains CO, H_2, CO_2, and the majority of the C_2 hydrocarbons, which are then recycled back to the inlet of the DME membrane reactor.

A decision was made to separate the unreacted synthesis gas after the second reactor rather than between the two reactors, simplifying the separation process. This is because direct DME synthesis yields a mix of DME, water, methanol, and unreacted synthesis gas, while the DME to gasoline conversion mainly produces hydrocarbons and water, mixed with the unreacted synthesis gas. The distinct physical and chemical properties of these products allow for a more straightforward separation of unreacted synthesis gas and light hydrocarbons from the liquid products, achieved through condensation.

The water stream contains a small amount of dissolved hydrocarbons. Consequently, if the decision is made to recirculate this water stream for use in the solid oxide electrolyzer, it becomes necessary to pass it through activated carbon filters for filtration purposes. However, if the water is intended to be recirculated to the gasifier, there is no need to remove the hydrocarbons. In fact, the presence of hydrocarbons in the water may potentially have a positive effect on the gasification process. Therefore, the hydrocarbons need not be removed in this specific scenario.

The hydrocarbon mixture in discussion presents multiple paths for further processing. One plausible option involves transporting it to an established petroleum refinery through a pipeline. When reaching the refinery, it could be integrated into conventional gasoline products. Subsequently, the blended product can be transported, either via pipelines or trucks, to final blending facilities. Here, additives and oxygenates such as ethanol are introduced before the product is dispatched to filling stations.

Another alternative entails directly sending the hydrocarbon mixture to distributors, where it could be amalgamated with conventional gasoline to satisfy the required specifications prior to being distributed to filling stations. However, considering the evolving landscape of fuel production, with an increasing emphasis on reducing the reliance on fossil-derived gasoline, the decision has been taken to treat the gasoline and produce the final product within the battery limits.

As the liquid hydrocarbon stream progresses, it enters a debutanizer, a distillation column which facilitates the separation of butane from gasoline. Within this column, the C3-C4 hydrocarbons, collectively referred to as LPG, are effectively segregated from the mixture. This stream is presented with multiple paths: it can be sold as a product, utilized as fuel within the plant, or circulated back to the reactor for further processing.

Proceeding further, the composition at this juncture primarily consists of C5+ hydrocarbons. However, a crucial aspect that requires attention pertains to the concentration of 1,2,4,5-tetramethyl-benzene, commonly known as durene, within this mixture. It is noteworthy that durene possesses a relatively high freezing point (79°C) and is prone to crystallization in fuel systems if its concentration surpasses approximately 5 vol% [81]. ExxonMobil has imposed a more stringent limit of 2% on the mass fraction of durene in the produced gasoline [108]. Consequently, it is necessary to subject the C5+ hydrocarbon mixture to a treatment process to ensure compliance with this specification, as the durene content in the produced gasoline typically exceeds the permissible limit.

Therefore the hydrocarbon mixture enters a gasoline splitter, to separate the light and heavy gasoline. The heavy gasoline stream contains all the durene and must be further treated. Two options can be considered: catalytic isomerization and catalytic dealkylation of durene, processes developed and patented by Mobil (patents US4347397A [109] and US4387261A [110] respectively).

While dealkylation is superior in terms of durene conversion, isomerization does not require a hydrogen stream to be fed to the reactor, and depending on the durene wt% in the original gasoline mixture could be sufficient to obtain a $< 2\%$ durene content in the final blended gasoline.

For this process, the dealkylation treatment has been chosen. The dealkylation reactor treats a durene-containing fraction, consisting primarily of C9+ aromatics. To achieve the desired outcome of dealkylating the durene and obtaining a product with a lower melting or boiling point, the process requires specific conditions. These conditions include operating temperatures within the range of 426.67°C (800°F) to 565.56°C (1050°F) and pressures ranging from 17.24 bar (250 psig) to 68.94 bar (1000 psig). Additionally, a hydrogen-to-hydrocarbon ratio greater than 1, preferably ranging from 1 to 5, is necessary.

After, the durene reduction treatment, heavy gasoline is blended with light gasoline and the final product is stored.

3.2.2. Thermodynamics and Kinetics

Thermodynamics

In order to develop an accurate model of the system, it is essential to select the appropriate thermodynamic models and equations of state (EoS).
The chosen property method is the Peng-Robinson EoS with Boston-Mathias modifications (PR-BM). This choice is supported by the Aspen Plus® method selection assistant, which recommends this EoS for applications in hydrocarbon processing, such as gas processing, refinery, and petrochemical processes, making it suitable for the gasifier unit, DME synthesis, and hydrocarbon synthesis and gasoline purification. The Boston-Mathias modification accounts for the high-temperature conditions (reduced temperatures greater than 5) that may be encountered during these processes.
Since SOEL is performed at high temperatures, PR-BM can also be employed for the electrolysis unit.

Kinetics

The kinetic models that will be used in the syngas upgrading modelling have been discussed in detail within the literature study, in Section 2.4. For DME direct synthesis, the kinetic model developed by Lu et al. [68] is selected, while for DME to gasoline, several kinetic models have been investigated but it was not possible to find an appropriate model for the project's purpose. This issue will be addressed in Section 4.5.

3.3. Basic Assumptions

3.3.1. Location

This thesis is part of a national project, funded by the Dutch Government, as explained in Chapter 1. Therefore, the country chosen for the plant is the Netherlands. It is important to consider that the plant does not have to be built in the proximity of a biomass source, since the pyrolysis units are decentralized and bio-oil can be transported to the plant location. It is worth mentioning that The Netherlands has a leading role worldwide in the production of pyrolysis oil [23].

3.3.2. Battery limits

The demarcation between the inner and outer battery limits is indicated in the block diagram, with distinct identification of inlet and outlet streams.

Concerning the input streams, the availability of pyrolysis oil and water is presumed to be constant. A fixed mass flow of 5000 kg/h is designated for pyrolysis oil entering the battery limits, while the mass flow of water is determined by the summation of mass flows entering the electrolyzer and gasifier. For preliminary sizing, the electrolyzer is dimensioned based on the hydrogen requirement for achieving an H_2:CO_x ratio of 3, as justified previously. The water demand for the gasifier is computed, assuming the steam-to-carbon ratio referenced in Eq. (2.9). The steam-to-carbon ratio is assumed to be consistent with the value reported by Hanafi [25].
It is imperative to note that the values presented in the block diagram do not account for water recirculation, which will substantially reduce the input required from outside the battery limits.

The outlet streams consist of gasoline, LPG, surplus oxygen generated by electrolysis, hydrogen sulfide extracted from the synthesis gas, and ashes. Due to the process's complexity and the yet-to-be-defined material recycling strategy, quantifying the gasoline output necessitates the development of a more comprehensive model.
Excess oxygen is derived from the difference between the mass flow of oxygen demanded by the gasifier and the total mass flow of oxygen generated by the solid oxide electrolyzer.

4

Model Setup and Validation

In this chapter, the formulation and development of the submodels using Aspen Plus and Matlab are presented, with emphasis not only on their setup but also on their validation. The validation process was applied to certain subunits within the overall system. Three specific units have been validated: the gasification model, the SOEL electrolysis model, and the DME reactor model. As will be elaborated further, the DME to hydrocarbon reactor was built upon experimental data, making a formal validation inapplicable. The gas cleaning unit and the product purification unit were designed specifically to suit this particular process. Hence, the validation of these units becomes unfeasible due to the lack of accessible experimental data for these particular systems.

It is worth mentioning that while the process design started from the DME reactor, as suggested by the Douglas method introduced in Chapter 3, the models are presented following the flow of input streams to output streams.

4.1. Gasification model

4.1.1. Model setup

The first model presented is the gasification unit model, which has been developed on Aspen Plus V12. In the following paragraphs, the properties implementation and the flowsheet structure are described.

Components and properties

The starting point of the model setup is the definition of all the components present in the model. In the gasification unit, the following conventional components have been specified: CO, CO_2, H_2, H_2O, O_2, H_2S, S, N_2, and CH_4. In addition to these, the solid component C, and the non-conventional (NC) components Bio-oil and Ash have been added to the component list. To fully specify the non-conventional components, the property models for their enthalpy and density have been chosen to be HCOALGEN and DCOALIGT as it is done in other Aspen Plus biomass gasification models [25], [111]. These models require the specification of the ultimate, proximate and sulfur analysis of the pyrolysis oil and ash when defining their streams in the flowsheet. The properties and the composition of the bio-oil have been modelled to resemble the experimental data presented by Leijenhorst [41]. The values shown in Table 2.1, have been slightly adjusted, to include 0.09% ashes within the ultimate analysis (ULTANAL) of the NC component bio-oil. Since the ashes are prevalently made of carbon, the corresponding amount has been deducted from the carbon weight per cent. In addition to this, another small difference is the content of nitrogen which was indicated by the experimental data as < 0.1 and has been set to 0.05 in Aspen. The proximate analysis (PROXANAL) of the NC component bio-oil follows the data of Table 2.1, and for the sulfur analysis (SULFANAL) the total amount of sulfur has been specified as pyritic sulfur.

As explained in Section 3.2.2, the property method chosen for this unit is PR-BM, which is the Peng-Robinson model with Boston-Mathias modifications.

Flowsheet

In the global settings, steady-state has been selected as input mode, and MIXCINC has been chosen as stream class, in order to model conventional components, solids, and non-conventional components. The schematic representation of the gasification system is depicted in Figure 4.1. The feedstock, pyrolysis-derived bio-oil, is introduced into the process at ambient temperature (20°C) and a pressure equivalent to the gasifier pressure. The bio-oil pump has not been included in the model since Aspen Plus, recognizing bio-oil as a non-conventional component, does not perceive bio-oil as a liquid component and thus does not admit the use of the pump block. However, it is considered as part of the plant in the energy performance and economic analysis. To align with the required conditions of the downstream process, the bio-oil undergoes a thermal conditioning step, elevating the temperature to 500°C. Subsequently, the heated feedstock enters an R-Yield reactor block. Though this step lacks direct physical relevance, it is crucial for accurate model representation. The function of the R-Yield reactor is to deconstruct the non-conventional bio-oil into a spectrum of conventional components, which Aspen Plus can handle. Within this reactor, it is essential to define the yield of each component. This is accomplished by utilizing the results from the ultimate analysis, performed on a dry basis, and adjusting these yield percentages to account for the moisture content.

$$\text{Yield}_j = (1 - \text{Moisture frac.}) \cdot \text{wt\%}_j \tag{4.1}$$

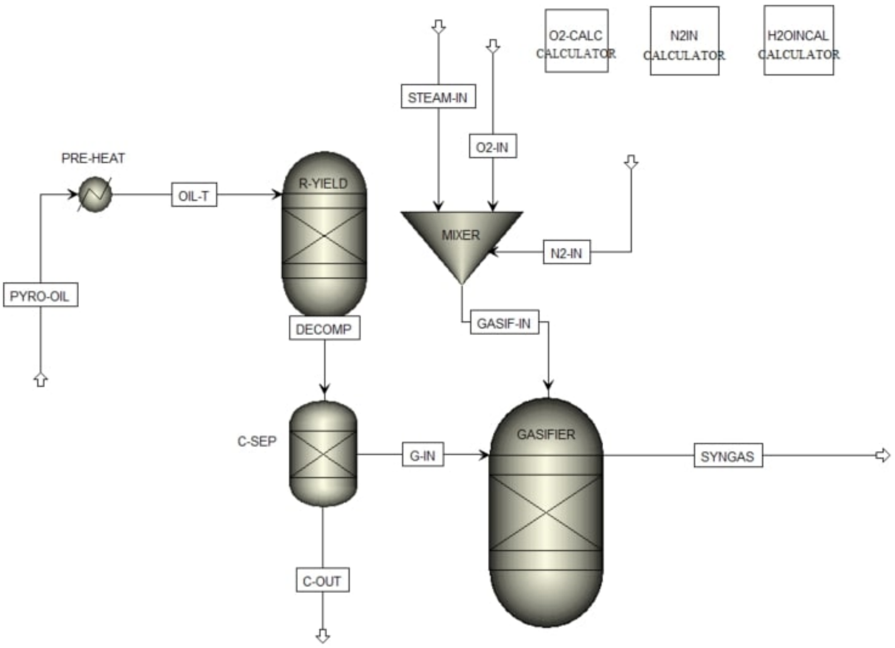

Figure 4.1: The main flowsheet of the gasification unit model on Aspen Plus.

Following, the R-yield a separator block is introduced to remove 4% of the carbon content. This is done to simulate the 96% CC efficiency (Eq. 2.5), indicated by Leijenhorst [47], and not possible to specify in the R-Gibbs block, used to simulate the gasifier. In addition to the carbon-rich stream, oxygen, steam, and nitrogen can be supplied to the gasifier. Their mass flows are calculated by Fortran calculator blocks, where the oxygen equivalence ratio, the steam-to-carbon ratio, and the nitrogen volume flow can be specified. The ER and the SC ratio have been implemented as explained in Section 2.2.1, while the nitrogen volume flow rate can be expressed as a percentage of the volume flow rate inputted in the gasifier.

4.1.2. Model validation

The model has been validated by utilizing empirical data derived from Leijenhorst's study [41]. To recreate the conditions documented in the experiments, the following input parameters were integrated into the simulation:

Table 4.1: Input conditions for the validation of the gasification unit model.

Operating conditions		
	Reference	**Model**
Gasification temperature	1250 °C	1250 °C
Gasification pressure*	5 bar	5 bar
Oxygen Equivalence Ratio	0.40-0.45	0.45
Steam-to-carbon ratio	0	0
Nitrogen volume flow	15%	15%

To assess the model's reliability the composition of the synthesis gas (determined on a dry basis and N_2 free) has been compared to the experimentally obtained values reported in the referenced publication. Prior to presenting the results, it is important to note that in the experimental investigations conducted by Leijenhorst et al., the concentrations exhibited fluctuations within a range of approximately ±2% during the 50-hour duration of the test runs, as depicted in Figure 4.2, despite maintaining consistent input conditions To facilitate a coherent comparison with the model, data from the 35th to the 40th hour of operation has been selected for consideration.

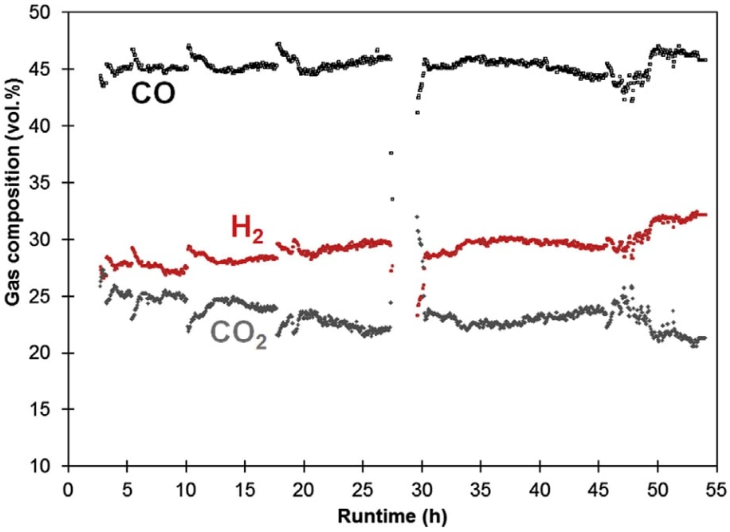

Figure 4.2: Major gas components from wood-derived pyrolysis oil gasification during the 50 h run of Leijenhorst et al. [47]

Results are presented in Table 4.2

Table 4.2: Results of the validation of the gasification unit model

Synthesis gas mole fractions			
	Reference (mol %)	**Model (mol %)**	**Relative error**
CO	45.6	46.7	2.4 %
H_2	30.1	31.9	6 %
CO_2	22.5	21.3	5.3 %
CH_4	2	< 1 ppm	(see explanation below)
H_2S	22 ppm	21 ppm	4.5 %
H_2/CO	0.66	0.68	3 %

While the model is able to reproduce the concentration of the main components (CO, H_2, and CO_2), the concentration of methane found in the experiments is significantly higher than the one predicted by the model. However, the trend of excess methane with respect to thermodynamics is well known and has been reported by different sources [41], [111]. The steam methane reforming reaction ($CH_4 + H_2O \leftrightarrow CO + 3H_2$) is limited by the reaction time and cannot reach an equilibrium state as it does in the simulation. Consequently, the hydrogen concentration predicted by the model is higher than its corresponding experimental mole fraction. This deviation can potentially

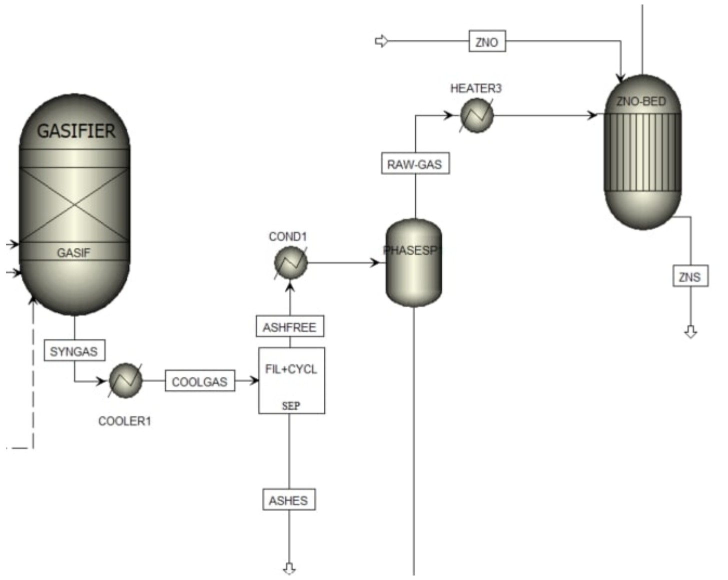

Figure 4.3: The main flowsheet of the gas cleaning unit model on Aspen Plus.

be fixed by the implementation of a constrained equilibrium modelling approach or by the development of a more complicated kinetic model of the entrained flow gasifier, which is out of the scope of this thesis.

4.2. Gas cleaning model

4.2.1. Model setup

Components and properties

In addition to the components already specified for the gasification unit, ZnO and ZnS have been added to the component list in the Properties section. The same thermodynamic model used in the gasification model (PR-BM), has been selected for treating the gas phase in this unit.

4.2.2. Flowsheet

The flowsheet of the gas cleaning unit is shown in Figure 4.3. Synthesis gas, leaving the gasifier, is cooled to 300°C prior to the gas cleaning and conditioning unit, in order to avoid the use of expensive high-temperature resistant materials in the gas cleaning unit. At this stage, the synthesis gas initially encounters a cyclone and filter - represented by a separator block in the model. Then, water is removed in a condenser, modelled by a cooler and a Flash2 block, where a temperature of 130°C and a pressure of 45 bar are specified. While a lower temperature would guarantee a higher degree of separation of water, it would also increase the heat duty necessary to bring the synthesis gas to appropriate temperatures for the following units. Thus, 130°C has been selected as a trade-off temperature.

Subsequently, the synthesis gas flow is introduced to the ZnO packed bed. The ZnO-packed bed is represented in Aspen Plus with an equilibrium reactor (REquil). Consequently, a steady artificial stream of Zinc Oxide must be supplied to the block, due to the inability to specify a fixed amount of ZnO inside the equilibrium reactor. The mole flow of zinc oxide is set equal to the mole flow of H_2S via a calculator block, thereby ensuring stoichiometric conditions. The reaction (Eq. 2.45) and the solid components present (ZnO and ZnS) are specified in the REquil. Two material streams are exiting the block: one includes the solid ZnS and the small percentage of unconverted ZnO, and the other carries the purified synthesis gas. The former stream does not have a physical meaning but it is necessary for the mass balance of the reactor, to compensate for the artificial stream of ZnO entering it.
The basic dimensioning of the packed bed columns has been carried out separately from Aspen Plus to estimate the required quantity of zinc oxide and the column's dimensions. First, the column's void fraction was derived

from an empirical correlation presented by Benyahia and O'Neill [112]:

$$\epsilon_b = \frac{1.703}{(0.611 + \frac{d_r}{d_p})^2} + 0.373 \tag{4.2}$$

Where d_r is the reactor diameter and d_p is the diameter of the ZnO cylindrical pellets. The reactor diameter has been obtained from an iterative process, as it is explained in the flowsheet section. The sorbent characteristics have been taken from a technical datasheet of commercial ZnO and are listed in Table 4.3.

Table 4.3: Characteristics of the ZnO pellets

Variable	Value	Unit
Diameter	4	mm
Height	10	mm
Pellet density	0.9-1.1	kg/m^3
Sulfur capacity at 220°C	15	wt%
Sulfur capacity at 350°C	38	wt%

Given the concentration of H_2S in the raw synthesis gas $x_{H_2S,in}$, the concentration of H_2S in the clean gas $x_{H_2S,out}$(<1 ppm), its molecular mass M_{H_2S}, and the synthesis gas molar flow rate F_{tot}, we can determine the total amount of H_2S removed per unit time. Then, multiplying by the time chosen between every sorbent replacement t^*, the total mass of H_2S to be removed in the specified time interval is obtained.

$$m_{H_2S} = \big((x_{H_2S,in} - x_{H_2S,out}) \cdot F_{tot}\big) \cdot M_{H_2S} \cdot t^* \tag{4.3}$$

Then, using the sulfur capacity on a weight basis at the operating temperature Scp(T), the corresponding mass of ZnO required to eliminate the calculated H_2S mass is determined:

$$m_{ZnO} = m_{H_2S} \,/\, Scp(T) \tag{4.4}$$

With the pellet density, the bed's void fraction, and the calculated zinc oxide mass, the columns' volume is calculated.

$$V_{bed} = \frac{m_{ZnO}}{\rho_{ZnO}\,(1-\epsilon)} \tag{4.5}$$

The calculated volume does not reflect a realistic scenario yet because it fails to account for the distinction between breakthrough time and complete sorbent utilization time. The maximum allowed time between sorbent replacements should be the breakthrough time, corresponding to the time at which the concentration of H_2 in the clean gas exceeds the specified limit, whereas we have considered t* to be equal to the time it takes to consume the entire mass of ZnO. The breakthrough time for a specific column can only be measured through experimental means, or with very detailed modelling. Nevertheless, according to a mathematical model of a ZnO packed bed column sourced from literature [113], it is predicted that 90% of the bed is utilized by the time of breakthrough. Therefore, to adjust for this discrepancy, the mass, and consequently, the volume of the reactor, is corrected by a factor of 1/0.9.

Regarding the column geometry, starting from a length/diameter ratio of 1.9, used by Kim et al. [114], the dimensions have been adjusted to obtain a reasonable pressure drop, calculated via the Ergun equation for packed bed (Eq. 4.6) [115], and in order to maintain the flow speed under the minimum fluidization velocity (Eq. 4.7. The calculated diameter has been used in Eq. 4.2 in the iterative process.

$$\frac{dP}{dz} = \frac{150\,\mu_{mix}\,v_s(1-\epsilon)^2}{(\Phi\,d_p)^2\,\epsilon^3} + \frac{1.75\rho_{mix}\,v_s^2(1-\epsilon)}{(\Phi\,d_p)\,\epsilon^3} \tag{4.6}$$

$$v_{min} = \frac{(\rho_{ZnO} - \rho_{mix})\,g}{150\mu_{mix}}\,\frac{\epsilon^3}{(1-\epsilon)}\,(\Phi\,d_p)^2 \tag{4.7}$$

Where v_s is the superficial velocity of the gas mixture in [m/s], d_p is the catalyst particle diameters in [m], ρ_{mix} is the density of the mixture in [kg/m^3], and μ_{mix} is the dynamic viscosity of the mixture in [Pa s].

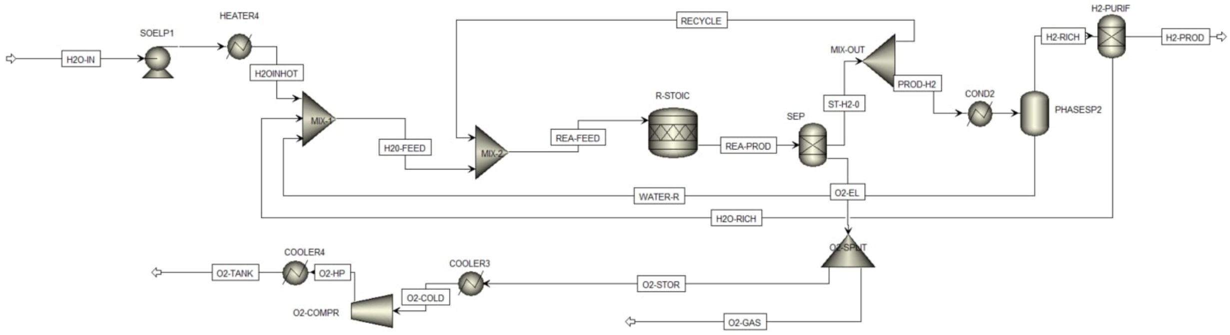

Figure 4.4: The main flowsheet of the solid oxide electrolyser unit on Aspen Plus.

4.3. Electrolyser: the SOEL model

The model of the solid oxide electrolyser was developed in collaboration with a fellow TU Delft student T. Batacchi [116]. The Aspen Plus model is complemented by a Matlab script which calculates the fundamental electrochemical parameters of the SOEL.

4.3.1. Model Setup

Properties and components

Given that the gasification model already accounted for H_2O, H_2, and O_2, there was no need to incorporate additional constituents for the SOEL. The thermodynamic model chosen is the Peng-Robinson equation of state with Boston-Mathias modifications, in line with the rest of the model, as explained in the BoD (3.2.2).

Flowsheet

Prior to the description of the structure of the main flowsheet, the underlying assumptions are explicitly stated as follows:

- The operation of the stack is conducted under thermo-neutral conditions, following similar models [25], [103], [101].
- The stack is assumed to have perfect thermal insulation, neglecting any heat dissipation to the surroundings.
- Due to a steam conversion below 100%, a mixture of steam and hydrogen is always present at the cathode outlet.
- A recirculation system is employed to maintain a constant hydrogen mole fraction of 10% in the cathode stream, thereby preventing nickel re-oxidation within the electrode [117] [118].

The flowsheet depicting the solid oxide electrolysis model is presented in Figure 4.4.
The stack is modelled as an R-Stoic, where the operating temperature (800°C), pressure (45 bar), and fractional conversion (F_{con}) of the reaction Eq. 2.10 (0.75 as indicated by [103]) are specified. The products are separated by a separator block (SEP), to obtain two different outlet streams, one for the cathode and one for the anode. The former is a pure oxygen stream, while the latter (named ST-H2-0) has a molar composition of ($1-F_{con}$)% of H_2O and F_{con}% H_2, as a result of the imposed fractional conversion.

The outgoing oxygen stream enters a splitter block, dividing it into two paths. One stream serves as the oxidizing agent for the gasifier, while the other is compressed to 100 bar, cooled and subsequently stored.
The production of pure hydrogen is accomplished by condensing the steam and separating it from water through a flash unit (FLASH) operating at a temperature that results in a hydrogen mole fraction of 95%. Subsequently, the separator block is employed to achieve a final product stream consisting of 100% hydrogen. The condensed water is reused in the process.

The recycling strategy has the purpose of keeping the aforementioned 10% hydrogen content in the stack inlet stream while recovering the separated water. Therefore, the split fraction of the MIX-OUT splitter block, is calculated from the mass balances of H_2 and H_2O as a function of the fractional conversion F_{con} and the mole fraction of hydrogen in the stack inlet feed $x_{H_2,RF}$:

$$X = \frac{x_{H2,RF}}{F_{con}} \tag{4.8}$$

In addition to this, the other unknown to be determined is the mass flow of H_2O entering the SOEL unit $\dot{m}_{H_2O,in}$. This can be expressed in terms of the mass flow of the stack feed (REA-FEED), the mole fraction of H_2O in the same flow $x_{H_2O,RF}$, X, and F_{con}.

$$\dot{m}_{H_2O,in} = (x_{H_2O,RF} - X \cdot F_{con}) \cdot \dot{m}_{H_2O,RF} \tag{4.9}$$

Matlab script: electrochemical parameters

A simple Matlab script has been coded to determine fundamental electrochemical parameters associated with the stack. Initially, the key variables are defined, including stack temperature, pressure, the standard Gibbs free energy of water, and the electrolyzer efficiency defined as the ratio between the electrical energy per kg of hydrogen produced. Additionally, partial pressures of water and oxygen at the stack outlet are extracted from the Aspen Plus model. The thermodynamic reversible cell potential (U_{rev}) is then calculated using these values following the Nernst equation (Eq. 2.21).

The script also calculates the area-specific resistance (ASR), defined by:

$$\text{ASR} = \frac{U_{op} - U_{rev}}{j} \tag{4.10}$$

where U_{op} is the operational voltage, U_{rev} is the reversible cell voltage, and j is the current density. The ASR is estimated using a correlation proposed by Giglio et al. which takes into account both temperature and pressure [117]:

$$ASR = D \cdot \exp(-B \cdot T) \cdot \exp(-C \cdot p) \tag{4.11}$$

As suggested by the authors who developed the correlation, when applied at high pressure Equation 4.11 might lead to overly optimistic results. Consequently, in this study, we acknowledge this uncertainty by incorporating an average value between the ASR estimate described earlier (lower value) and an alternative estimation (higher value) that disregards the contribution of pressure. The following coefficients have been used in Eq. 4.11: B = 0.0057 1/K; C = 0.021 1/bar; D = 71.42 Ω/cm^2, following indications of Giglio et al.

As explained above, the stack is assumed to operate at the thermoneutral potential. The corresponding value at the operating temperature is taken from Figure 2.4. Then, inverting Equation 4.10, the current density is obtained.

Model Validation

The Aspen Plus model has been compared with the model developed in the study of Zaccara et al.[119], and comparing the electrochemical parameters to the ones of other references [117], [57]. Table 4.4 lists the operating parameters used for the validation:

Table 4.4: Parameters used for the validations of the SOEL model

Parameter	Value	Unit
Temperature	877	°C
Pressure	30	bar
Fractional Conversion	0.75	-
Thermoneutral voltage	1.3	V

The Aspen Plus simulation is run and convergence of the mass balance of all blocks is reached with a tolerance of $1 \cdot 10^{-4}$ while respecting the imposed inlet conditions.

The split fraction, calculated using Equation 4.8 is 0.13. The ratio of the mass flow of water entering the electrolyzer unit and the mass flow of hydrogen leaving the unit is 8.9 kg_{H_2}/kg_{H_2O}, which matches the ratio indicated in the reference model.

The Matlab script calculates a reversible cell voltage of 0.914 V at 800°C, which together with the assumed thermoneutral potential of 1.3 V, results in a current density of 2.05 A/cm^2. This falls within the current density range indicated by IRENA's report [57], for SOEL cells by 2050 (> 2 A/cm^2).

The script calculates the number of stacks and cells per stack needed for a designated power output. First, the power generated by a single cell is computed using:

$$P_{cell} = j\ U_{op}\ A_{cell} \tag{4.12}$$

Where A_{cell} is the electrode area, assumed as A = 500 cm^2, based on IRENA's suggestion [57]. Then, the necessary number of cells per stack is estimated by dividing each stack's expected power capacity (200 kW) by the cell's power and rounding up. The power per stack is then adjusted accordingly.
Lastly, the required number of stacks is found by dividing the total power by the single stack's power and rounding up to the next integer number.

4.4. DME direct synthesis: the membrane reactor model

As explained in Chapter 3, the DME direct synthesis is performed in a membrane reactor, which allows for in-situ water removal. Since Aspen Plus does not have a specific block for this reactor type, this plant section has been modelled on Matlab. Subsequently, the Matlab model has been integrated into the Aspen Plus flowsheet. The code can be found in Appendix A.2.

4.4.1. Model Setup

The membrane reactor has been modelled as a steady-state, isothermal, 1-D plug-flow reactor, meaning that it has been assumed that the composition does not vary with the radius and there is no axial mixing of the species in the reactor [42]. The plug flow reactor assumption is justified if a high Peclet number is computed:

$$Pe = \frac{\text{advective transport rate}}{\text{diffusive transport rate}} = \frac{l\ v_s}{D_0} = Re\ Sc\ >> 1 \tag{4.13}$$

where l is the characteristic length (in our case the external diameter D_e), v_s is the flow velocity and D_0 is the diffusion coefficient of the gas mixture.

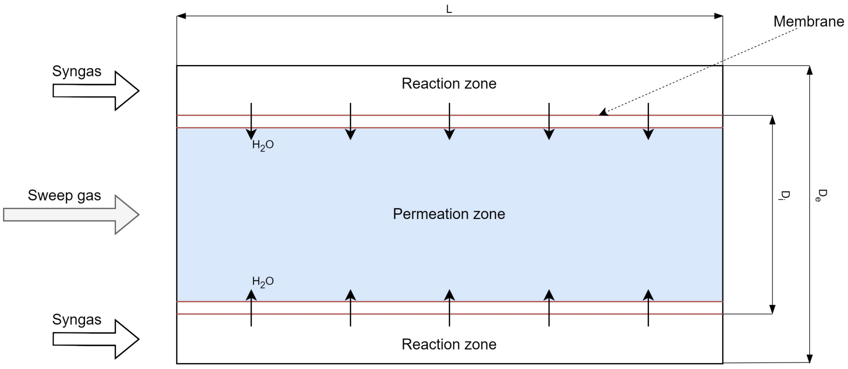

Figure 4.5: Membrane reactor geometry

The reactor geometry is shown in Figure 4.5. Two main zones can be identified in the membrane reactor: the reaction zone where the Cu-ZnO-Al_2O_3/HZSM-5 catalyst particles are packed, and the permeation zone. These two zones are separated by a selectively permeable microporous zeolite membrane, which allows only H_2O (wanted) and H_2 (unwanted) trans-membrane molar fluxes. An assumption of 0 permeation of the other components has been made, following the work of Iliuta et al. [120], and De Falco et al. [77]. The synthesis gas containing CO, CO_2, and H_2 enters the reaction zone, while a sweep gas flows through the permeation zone.
The reactor has been discretized with a 1-D grid, along the longitudinal direction.
The catalyst deactivation and water inhibition phenomena have been neglected. This is justified by the fact that the deactivation is normally caused by H_2O, and this is constantly removed from the reaction zone.

The thermodynamic model is based on a set of three linearly independent reactions, namely the methanol synthesis from CO_2 reaction (Eq. 2.33), the water-gas shift reaction (Eq. 1.1), and the methanol dehydration reaction (Eq. 2.34)). The methanol synthesis from CO (Eq. 2.32), and the overall DME synthesis reaction (Eq. 2.4.2) can be obtained as a linear combination of the first three equations and thus do not need to be implemented. For the sake of simplicity and clarity, from now on we will refer to the methanol synthesis from CO_2 as Reaction 1, to the WGS as Reaction 2, and to the methanol dehydration reaction as Reaction 3.

The mass balances in the reaction zone have been expressed as follows:

$$\frac{dF_{H_2O}}{dz} = \rho_c \left(1-\epsilon\right) \pi \left(R_e^2 - R_i^2\right) \left(r_1 - r_2 + r_3\right) - J_{H_2O} \cdot 2\pi R_i \tag{4.14}$$

$$\frac{dF_{H_2}}{dz} = -\rho_c \left(1-\epsilon\right) \pi \left(R_e^2 - R_i^2\right) \left(3r_1 - r_2\right) - J_{H_2} \cdot 2\pi R_i \tag{4.15}$$

$$\frac{dF_{CO}}{dz} = -\rho_c \left(1-\epsilon\right) \pi \left(R_e^2 - R_i^2\right) \left(r_2\right) \tag{4.16}$$

$$\frac{dF_{CO_2}}{dz} = -\rho_c \left(1-\epsilon\right) \pi \left(R_e^2 - R_i^2\right) \left(r_1 - r_2\right) \tag{4.17}$$

$$\frac{dF_{MeOH}}{dz} = \rho_c \left(1-\epsilon\right) \pi \left(R_e^2 - R_i^2\right) \left(r_1 - 2r_3\right) \tag{4.18}$$

$$\frac{dF_{DME}}{dz} = \rho_c \left(1-\epsilon\right) \pi \left(R_e^2 - R_i^2\right) \left(r_3\right) \tag{4.19}$$

Where F_j is the molar flow of the component j in [kmol/s], ρ_c is the catalyst density in [kg/m^3], r_1, r_2, r_3 are the reaction rates of the reactions 1, 2, and 3 in [kmol/(kg s)], R_e and R_i are the external and internal radii of the reactor in [m], ϵ is the void fraction of the catalyst bed, and J_j is the trans-membrane molar flux of the component j in kmol/(m^{2}s)]
The reaction rates are computed from Equation 2.39- 2.41. Similarly, in the permeation zone, the mass balance for H_2O and H_2, have been formulated, while the spatial derivatives for the other components are equal to 0.

$$\frac{dF_{H_2O}}{dz} = J_{H_2O}\, 2\pi R_i \tag{4.20}$$

$$\frac{dF_{H_2}}{dz} = J_{H_2}\, 2\pi R_i \tag{4.21}$$

The driving force of the trans-membrane fluxes is the partial pressure difference of the respective component in the reaction and permeation zone:

$$J_{H_2O} = PermH_2O \left(P_{H_2O} - \bar{P}_{H_2O}\right) \tag{4.22}$$

$$J_{H_2} = PermH_2 \left(P_{H_2} - \bar{P}_{H_2}\right) \tag{4.23}$$

Where Perm$_{H_2O}$, and Perm$_{H_2}$ are the temperature-dependent permeabilities of steam and hydrogen in [kmol/(m^2 s bar)]. DEpending on the temperature, the values are looked up from a matrix containing the data shown in Figure 4.6.
The reactions rate have been expressed following the model of Lu et al. [68] as explained in Section 2.4.2.
While the pressure in the permeation zone is generally low (< 5 bar), the pressure in the reaction zone can be significantly higher (up to 70 bar). As a consequence, the partial pressures of the components can also be relevant. This means that caution should be used if applying Dalton's law, as steam can be far from an ideal gas behaviour. Thus, the partial pressures have been computed using an approximate equation developed by Hayez [122], which takes into consideration the second virial coefficients B_{ii} of the pure components of the mixture as well as the mixed coefficients of interaction B_{ij}:

$$P_i = x_i P \left(\frac{RT + B_{imix}P}{RT + B_{mix}P} \right) \tag{4.24}$$

Where the B_{mix} is the second virial coefficient of the mixture, and B_{imix} is the second virial coefficient of component i in a mixture of n components, computed from the expressions:

$$B_{mix} = \sum_{i=1}^{n} \sum_{j=1}^{n} x_i x_j B_{ij} \tag{4.25}$$

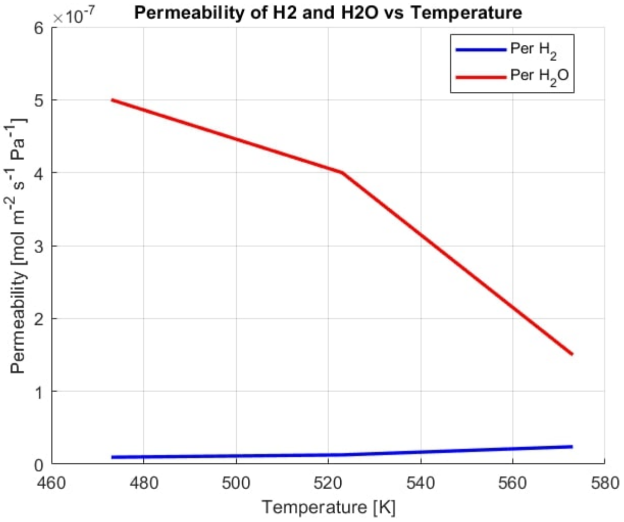

Figure 4.6: Steam and hydrogen permeabilities of the selectively permeable membrane vs temperature [121].

$$B_{mix} = \sum_{j=1}^{n} x_j B_{ij} \tag{4.26}$$

Where n is the number of components in the mixture, and B_{ij} are the binary interaction coefficients or second virial cross-coefficients. The binary interaction coefficients have been computed from an empirical correlation valid for both non-polar and polar components developed by Tsonopoulos [123].

The conservation equations are complemented by the momentum balance, which considers the characteristics of the mixture, the design of the reactor, and the specifics of the catalytic bed. This allows us to assess the pressure drop from the Ergun equation for packed beds (assuming spherical particles) (Eq. 4.6) [115]. The models and the equations used for the calculation of the density of the mixture and the single components are reported in Appendix A.1.

The pressure in the permeation zone P_{per} is assumed to be constant and it is defined as a fraction of the reactor pressure (Eq. 4.27), while the sweep gas molar flow is defined as a multiple of the inlet syngas molar flow:

$$\eta = \frac{\bar{P}}{P_{per}} \tag{4.27}$$

$$SW = \frac{F_{sweep}}{F} \tag{4.28}$$

Another crucial parameter is the reactants mixture space velocity, named Gas Hourly Space velocity (GHSV) in [h^{-1}] and defined in the reference paper used for validation [77] as the ratio between the volume flow rate of the inlet syngas and the reactor zone volume, corrected for pressure and temperature:

$$GHSV_1 = 3600 \frac{\dot{V}}{L\,A_r} \frac{273}{T} P = 3600 \frac{v_s}{L} \frac{273}{T} P \tag{4.29}$$

Where v_s is the syngas inlet flow velocity in m/s, L is the reactor length in meters, P is the inlet pressure in bar and T is the inlet temperature in K.

However, since this definition does not take into account the void fraction and thus the actual volume available for the syngas, a more rigorous definition has been introduced:

$$GHSV_2 = 3600 \frac{v_s}{L\,(1-\epsilon)} \frac{273}{T} P \tag{4.30}$$

The boundary conditions have been imposed at the first grid point, and the governing equations have been solved with the Matlab function ode15s, a variable-step, variable-order multistep solver used for solving stiff ordinary differential equations.

4.4.2. Model validation

The model has been validated with the work of De Falco et al. [77], who have developed a similar model for DME synthesis in a membrane reactor.
The model under discussion diverges from the reference primarily in three significant aspects. Firstly, De Falco and colleagues have constructed a non-isothermal model, thereby formulating the heat balance within the reactor and computing the temperature at each grid point within the reactor. Secondly, the model in the reference employs Dalton's law, which serves as a simplification relative to the model developed in this thesis. Lastly, the equilibrium constants have been expressed differently in the two studies.

In light of these considerations, the model has been validated through the introduction of two modifications to the Matlab code. First, the calculation of partial pressures has been adapted to conform to Dalton's law. Second, the temperature profile found by De Falco et al. has been digitized and imposed on each grid point, thereby creating a non-isothermal model. This implies that in contrast to the isothermal model, the equilibrium constants, the kinetic and adsorption constants, the permeabilities, the viscosities, and the densities are updated at each grid point.

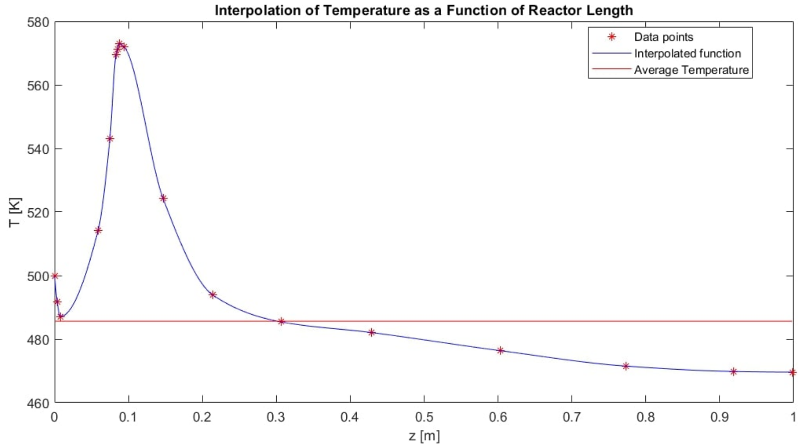

Figure 4.7: Temperature profile imposed in the reactor

The membrane reactor geometry, the catalyst properties, and the operating conditions indicated in the reference paper have been matched in order to perform the validation.

Table 4.5: Reactor geometry, catalyst properties, and operating conditions for the model validation

Reactor Geometry			**Operating conditions**		
External diameter	D_e	0.048 m	Inlet temperature	T	500 K
Internal diameter	D_i	0.038 m	Inlet pressure	P	70 bar
Bed length	L	1 m	P ratio	η	0.05
Catalyst Properties			Flow ratio	SW	3
Particle diameter	d_p	0.0002 m	Space velocity	GHSV1	7000 h^{-1}
Catalyst density	ρ_c	1900 kg/m^3	Feed composition 1	H_2/CO_x	3
Void fraction of the bed	ϵ	0.33	Feed composition 2	CO_2/CO	3

As can be observed from Figure 4.8, the model follows the reference data very well, both qualitatively and quantitatively. On the left side the spatial evolution of the mole fractions of the reactants in the reaction zone are plotted, while on the right side, the same thing can be observed for the products. The small deviations can be explained by the difference in the equilibrium constants and the error that can be generated when digitalizing the temperature profile and interpolating the data points extracted with a polynomial function.

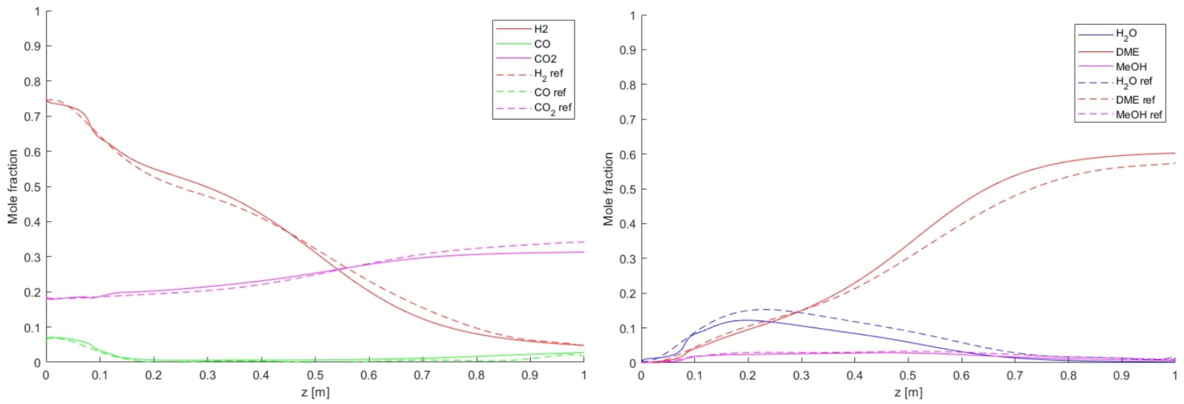

Figure 4.8: Non-isothermal model vs. reference data: mole fractions of the reactants (left) and the products (right) along the reaction zone.

Discrepancies emerge in the permeation zone, where the concentrations of hydrogen and water appear to be inverted. This raises the suspicion that the authors of the reference paper may have erroneously represented the legend of their plot. As illustrated in Fig. 4.9, both H_2O and H_2 approach similar concentrations at the outlet of the permeation zone, but a divergence in the trend is observable in the initial segment of the reactor. Specifically, in this initial segment, the spatial derivative of the H_2 concentration exceeds that of H_2O.

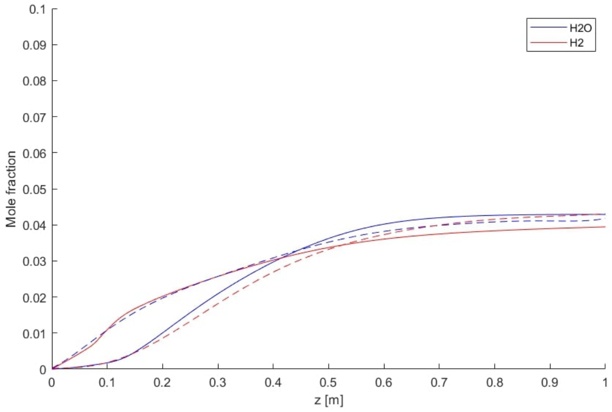

Figure 4.9: Non-isothermal model vs. reference data: mole fractions of H_2 and H_2O along the permeation zone

Although the steam permeability is always greater than the one of hydrogen, the driving force for trans-molar flows is dictated by the difference in partial pressures, as indicated in Eq. 4.22 and Eq. 4.23. In the initial part of the reactor, the concentration of hydrogen in the reaction zone significantly exceeds the concentration of water. Consequently, it is logical that more hydrogen than water permeates through the membrane in the beginning.

The isothermal model is subsequently compared with the reference data. The selected temperature corresponds to the average value derived from the temperature profile utilized for the precedent validation, while the remaining operating conditions have been maintained constant.

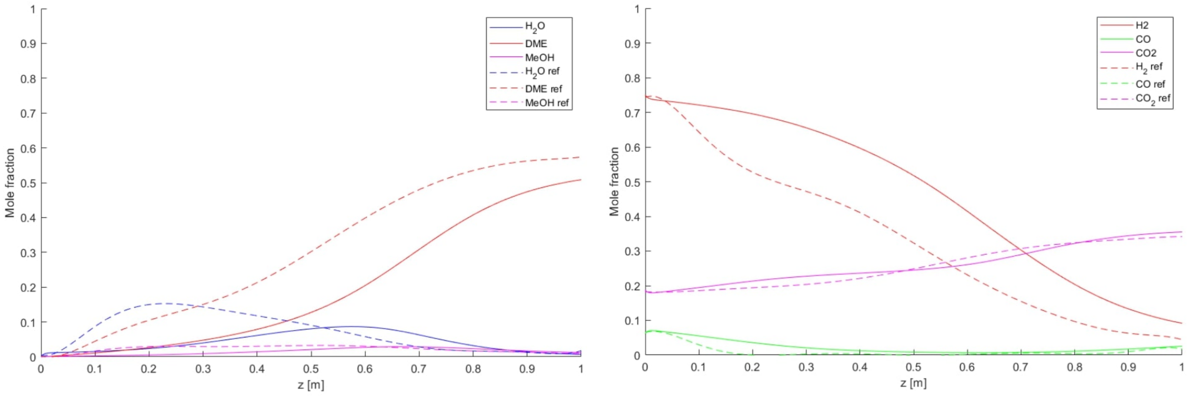

Figure 4.10: Isothermal model vs. reference data: mole fractions of the reactants (left) and the products (right) along the reaction zone.

Figure 4.10 presents the outcomes of this comparative analysis. As expected, qualitative differences emerge in the concentration profiles of both reactants and products, given that in the isothermal model, the equilibrium constants, kinetic and adsorption constants, permeabilities, viscosities, and densities are held constant throughout the entire simulation. Discrepancies are more significant in the first half of the reactor, where the difference between the average temperature and the reactor temperature of the reference model is larger, due to the hot spot in the reaction zone, as can be observed in Figure 4.7. However, in the second half of the reactor, the average temperature is higher than the reference reactor temperature, partly balancing the effect of the hot spot. As a result, towards the end of the reactor, the predicted mole fractions are closer to the reference model.
The quantitative discrepancy is not substantial and has been deemed acceptable within the context of integrating this model into a more comprehensive Aspen Plus model, wherein all other units are isothermal.

To summarize the validation of the two models, the values of DME yield (Eq. 2.37), DME selectivity (Eq. 2.38), and CO_x conversion 2.35, have been reported in Table 4.6 and compared to the reference values.

Table 4.6: Quantitative performance comparison between the reference, the non-isothermal, and the isothermal model.

	Reference	Non-isothermal model	Error (rel)	Isothermal model	Error (rel)
Y_{DME}	0.75	0.78	4%	0.72	4%
S_{DME}	0.99	0.99	0%	0.99	0%
X_{CO_x}	0.75	0.78	4%	0.73	2.7%

4.4.3. Implementation in the Aspen Plus Flowsheet

To integrate the Matlab membrane reactor model into the Aspen Plus main flowsheet, an intermediate step using Excel has been employed. Firstly, Aspen Plus communicates data to an Excel sheet named ”AspenInput” through the utilization of a ”User2” block. This block serves as a conduit, transferring relevant data from Aspen Plus to the designated Excel sheet.
Next, utilizing Visual Basic code in the Excel Developer tab (see Appendix A.4), the Excel sheet automatically sends a matrix comprising the feed specifications to Matlab. This matrix serves as input for the membrane reactor code, which has been implemented as a Matlab function. The membrane reactor function processes the provided matrix and generates an array containing temperatures, pressures, molar flows, and composition of the streams exiting both the reaction zone and the permeation zone. Subsequently, the obtained values are automatically printed into an Excel sheet named ”AspenOutput” and transmitted back to the User2 model within Aspen Plus. This process allows for automatic data exchange and integration between Aspen Plus, Excel, and Matlab, facilitating the utilization of the membrane reactor model within the Aspen Plus simulation environment.

The flowsheet of the DME reactor unit is shown in Figure 4.11.

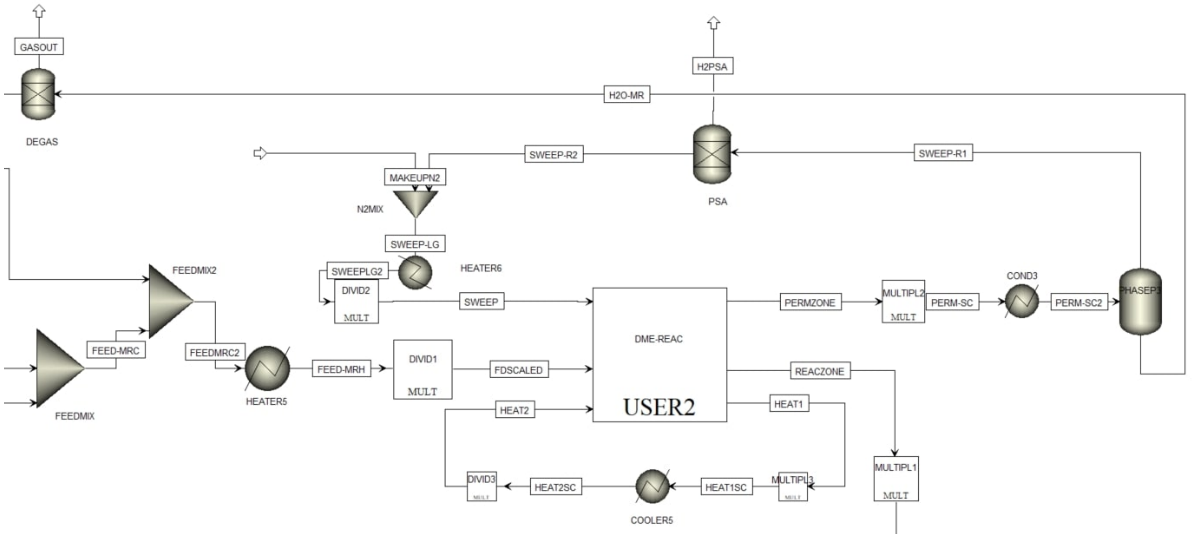

Figure 4.11: DME reactor unit flowsheet

Upstream of the reactor, the feedstock is heated to 250°C using a heater block. While in the reference paper used for validation, a lower temperature was deemed beneficial for both thermodynamic equilibrium and membrane performance [77], a temperature of 250°C is necessary for Cu-based catalysts, as explained in Chapter 2 2.4.4. To simulate the operation of multiple reactors running in parallel, multiplier blocks are introduced before the User2 block. These downscale the flow streams by a factor reciprocal to the number of reactors. After the reactor block, other multiplier blocks are employed to upscale the flows, effectively compensating for the prior reduction.

After exiting the permeation zone, the sweep flow undergoes a recirculation loop. Firstly, it passes through a condenser to cool down and remove permeated water. The water can be collected and potentially recirculated. Next, a degasser (modelled as a separator block) removes the very small amount of dissolved CO_2 and CO from the liquid water. To avoid H_2 accumulation, the stream enters a hydrogen separation unit (here a pressure swing adsorption (PSA) as indicated by De Falco et al. [77] and Haro et al. [124]), where 99% of the H_2 is removed. The PSA unit has been modeled in a simplistic way. According to Linde [125], the separation of the sweep gas (CO_2 or N_2) and hydrogen can be achieved using this technology. To err on the side of caution, the highest adsorption pressure in the range indicated by Linde (10-40 bar) has been chosen. In AspenPlus, the material stream undergoes the following steps: an isoentropic compressor block, a cooler to reduce the temperature to 55°C (minimum temperature ensuring a stream liquid fraction of 0), a sep block, and a valve to simulate depressurization (needed for the adsorber regeneration in the PSA cycle). Subsequently, nitrogen is introduced into the system to compensate for any potential losses in the recirculated nitrogen within the mentioned unit.
Compared to the validation case, the sweep gas has been replaced from CO_2 to N_2. Since the molar ratio between the sweep gas and the syngas is kept constant, there is no effect on the performance of the reactor when replacing CO_2 with N_2. The driving force for the permeation of water is indeed given by the partial pressure, which depends on the mole fraction. At the same time, for the same molar flow, the mass flow of N_2 is approximately 1.6 times lower than the mass flow of CO_2. This, combined with the lower price of nitrogen with respect to CO2, results in a cheaper investment. Finally, nitrogen can be purged in the atmosphere since it is not a greenhouse gas like CO_2.
As depicted in figure 4.11, an auxiliary loop has been incorporated into the flowsheet. Given that the reactor is modelled as an isothermal system, it is assumed that the heat from the reaction is absorbed by a steam stream in a drum around the reactor. However, the User2 model does not allow the utilization of heat streams, necessitating the use of an alternative method. The heat generated within the reactor is computed based on the reaction's heat at 250°C and the number of DME moles produced. An artificial stream named "HEAT1" is introduced, with a specific heat capacity equal to the average specific heat capacity of the gas flowing through the reaction zone, and an identical mass flow (see Appendix A.1 for the equations used). The consequential temperature increase, $Delta$T, from the exothermic reactions is then calculated and incorporated into the temperature of HEAT1. The HEAT1 stream is subsequently cooled down back to 250°C by the cooler block prior to its re-entry into the reactor. This mechanism allows for the transfer of the heat generated within the reactor to the cooler block.

Reactor Scaling

As stated by Chompupun et al. [126], scaling up a membrane reactor is not straightforward. In order to guarantee the same performance, the residence time (and thus the GHSV) has to be kept the same. In addition to this, a crucial parameter in the design of a membrane reactor is the ratio between the membrane area and the reaction volume, which has to be maximized to exploit the membrane. Furthermore, the flow velocity has to be limited, to prevent an excessive pressure drop.

Starting from the known GHSV and the volume flow rate of the inlet syngas, the new reaction zone volume is calculated from Eq.4.30.

The flow velocity has been imposed to be 10 times larger with respect to the validation case where it was approximately 0.05 m/s. Thus, the cross-sectional area of the new reactor A_{new} can be computed:

$$A_{new} = \frac{1}{10} \, A_{valid} \, \frac{\dot{V}_{new}}{\dot{V}_{valid}} \tag{4.31}$$

The length of the reactor L_{new} is calculated by dividing the new reactor volume by the cross-sectional area.
The internal radius is calculated by imposing the same reactor volume to membrane area ratio:

$$R_i = \frac{V_{new}}{V_{old}} A_{m,old} / (2\, \pi \, L_{new}) \tag{4.32}$$

Finally, the external radius is calculated from the cross-sectional area A_{new} and the internal radius R_i.

It is important to note that adhering to these reactor scaling conditions may not always be feasible. Under circumstances where the gas flow rate is significantly high, the calculations may yield an internal radius that surpasses the external radius, indicating an impossible reactor design. Rather than settling for a reduced membrane area-to-volume ratio, a proposed solution entails the use of additional reactors operating in parallel to reduce the flow through each individual reactor.

4.5. DME to hydrocarbons reactor

Positioned downstream of the DME membrane reactor, the DME to hydrocarbon reactor receives the effluent stream from the reaction zone of the aforementioned DME reactor. Therefore, unreacted synthesis gas act as inerts while oxygenates (DME and MeOH) react over a ZSM-5 catalyst to form a hydrocarbon mixture.

4.5.1. Model Setup

Properties and components

Gasoline is a mixture where more than 150 hydrocarbons can be identified. For simplicity, and to be able to follow the experimental results presented in the report of the US Department of Energy [127], some isomers have been lumped together because they will all be included in the final product and will stay together through the fractionation steps. However, several components add to be added to the component list in Aspen Plus: Ethane, Ethylene, Propane, Propene, n-Butane, i-Butane, Butene, Pentane, Pentene, Hexane, Hexene, Heptane, Heptene, Octane, Iso-octane, Octene, Nonane, Benzene, Toluene, Ethylbenzene, Xylene, 1,2,4-trimethylbenzene, 1,2,4,5-tetramethylbenzene, 1,2,3,5-tetramethylbenzene, and 1,2,3,4-tetramethylbenzene.
The property method used is PR-BM, as explained in the BoD (3.2.2).

Flowsheet

The main flowsheet of the DME to hydrocarbons reactor and the product separation and purification unit is shown in Figure 4.12.

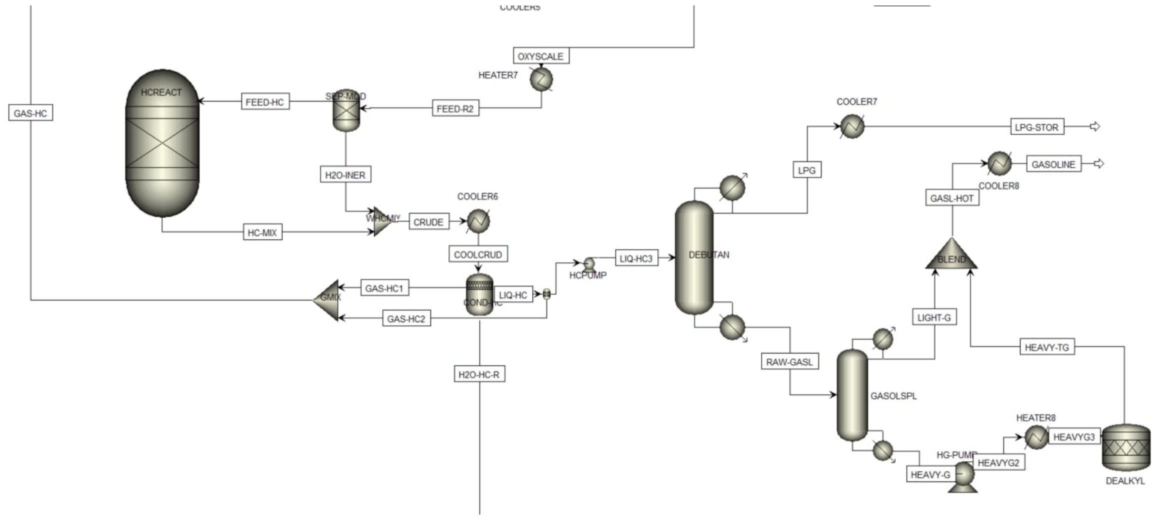

Figure 4.12: DME to Hydrocarbons reactor unit and product purification unit flowsheet

As it is observable from Figure 4.12, the effluent stream from the DME reactor is heated up in a heater block, where it reaches the inlet temperature of 329.44°C before entering the DME to hydrocarbon reactors. The reactor has been simulated using an RYield model, which enforces a specific distribution of products in the hydrocarbon mixture. This approach, observed in the relevant literature focusing on techno-economic analyses of MtG conversion [35], [34], [124], [81], eliminates the need for detailed information about stoichiometry or kinetics.
Several attempts were made to identify a kinetic model to implement on Aspen Plus, but they were unsuccessful. The complexity arises from the simultaneous occurrence of multiple reactions and the presence of numerous components in the reaction environment. Consequently, all identified kinetic models are based on lumps, which are conglomerates of various components like oxygenates, light olefins, and aromatics [84], [79], [128], [129]. However, Aspen Plus expects the specification of individual components instead of lumps and necessitates rigorous stoichiometric descriptions for reactions, rather than the lump conversion steps described in the kinetic models (i.e. Step 1 in Ortega et al. [84]: Oxygenates $\xrightarrow{k1}$ Polymethylbenzenes). Moreover, the existing models do not account for the formation of water, which is significant as experimental data reveals that it constitutes approximately 50% of the product weight in a MtG process. In addition to these models, an elaborate model based on 53 reactions developed by Mihail et al. [130] has been implemented into Aspen Plus. However, due to the difficulty in defining intermediate species such as carbene and carbenium ions within the software, the resulting product distribution did not adequately represent experimental results.

In the specifications of the RYield reactor, the flash type is based on the temperature change and the reactor pressure. Yield specifications are based on the work of Schreiner where the experimental results of the conceptual MtG plant built by Mobil in Wyoming are reported [127]. To accommodate the conversion of DME to hydrocarbons, the product distribution has been adjusted accordingly, as the modelling focuses on DME to hydrocarbon conversion rather than methanol to gasoline. Literature reports indicate that the product distribution of the hydrocarbon mixture remains the same for both MtG and DtG processes, as DtG is a subset of the MtG process [37]. The primary difference lies in the water content, as H_2O is generated during DME synthesis. Consequently, the product distribution in an MtG process exhibits a higher fraction of water compared to what is expected in a DtG process. Therefore, the water content has been determined in a spreadsheet by balancing the oxygen atoms between the reactants and products. Oxygen is present only in DME, methanol, and water, as no oxygenates remain at the reactor outlet. The product distribution on a mass basis is reported in Table 4.7.

Table 4.7: DME to Hydrocarbon product distribution. Adapted from [127]

Product Distribution					
Component	**Chemical Formula**	**Yield (wt%)**	**Component**	**Chemical Formula**	**Yield (wt%)**
Water	H_2O	39.105	Heptene	C_7H_{14}	1.240
Methane	CH_4	0.372	Octane	C_8H_{18}	0.992
Ethane	C_2H_6	0.248	I-Octane	C_8H_{18}	1.178
Ethylene	C_2H_4	0.000	Octene	C_8H_{16}	2.977
Propane	C_3H_8	2.853	Nonane	C_9H_{20}	0.558
Propene	C_3H_6	0.124	Nonene	C_9H_{18}	1.364
N-Butane	C_4H_{10}	1.674	Benzene	C_6H_6	0.124
I-Butane	C_4H_{10}	5.333	Toluene	C_7H_8	1.116
Butene	C_4H_8	0.682	Ethylbenzene	C_8H_{10}	0.310
Pentane	C_5H_{12}	8.310	Xylene	C_8H_{10}	5.209
Pentene	C_5H_{10}	2.294	124TriMB	C_9H_{12}	6.139
Hexane	C_6H_{14}	8.000	1245TetraMB	$C_{10}H_{14}$	2.604
Hexene	C_6H_{12}	1.364	1235TetraMB	$C_{10}H_{14}$	0.372
Heptane	C_7H_{16}	3.597	1234TetraMB	$C_{10}H_{14}$	1.860

It is important to note that the adjustment of water content depends on the composition of the oxygenate stream entering the reactor. While DME constitutes the major fraction, there might be some residual methanol present in the feed. This is dehydrated to DME within the reactor since the catalyst present (ZSM-5) is also a methanol dehydration catalyst. Additionally, CO, CO_2, and H_2 are designated as inert components. A small amount of residual water could also be present in the feed. However, due to the impossibility of specifying a component as both an inert and a product, water is artificially separated using a separator block and subsequently added to the product stream after the RYield reactor. Thanks to the implementation of a DME membrane reactor, the quantity of water in the feed is minimal, allowing the influence on the product distribution to be disregarded.

The main limitation of this methodology is its inability to scrutinize the impacts of temperature, pressure, and space velocity on the plant's comprehensive performance. Nonetheless, the operating conditions selected are the same employed in Schreiner's pilot plant [127], ensuring elevated gasoline selectivity without excessive coke production.

4.6. Product separation and purification

4.6.1. Flowsheet

The stream exiting the reactor enters a cooler, where its temperature is lowered to 40°C, as indicated in the US4788369 patent [107]. The three-phase separator is modelled by a Flash3 block, a three-outlet flash which models vapour-liquid-liquid equilibrium. Three different streams are separated: water is collected and possibly recirculated, unreacted synthesis gas and light gases (C_1-C_2) are separated and possibly recirculated to the inlet of the DME reactor, while the remaining fraction of liquefied hydrocarbons is sent to the fractionation unit. The pressure of the 3-phase separator has been chosen in order to minimize the concentration of light gases (CO, CO_2, H_2) hydrocarbons in the liquid hydrocarbon stream. As a result, the separator operates at 7 bar, which corresponds to the value indicated in the patent US4788369A [107].

The debutanizer and the gasoline splitter distillation columns have been modelled rigorously with RadFrac blocks. However, in order to identify the optimal reflux ratio and the feed stage, simulations were carried out with the simpler DSTWU models, which were later substituted with the RadFrac blocks.

In the debutanizer modelling employing the DSTWU approach, the light key and heavy key components are designated as isobutane and pentene respectively. Butane, typically accounting for approximately 2-3% volume in gasoline [131], plays a critical role due to its volatility, facilitating the vaporization of gasoline, a fundamental prerequisite for the smooth operation of internal combustion engines, particularly during cold weather. However, excessive butane content may induce complications such as vapour lock in the engine. Thus, the recovery of the light key component - quantified as the ratio of the moles of the light key in the distillate to the moles in the feed - has been manipulated to achieve a butane mole fraction of 0.02 in the column's bottom stream, while the heavy

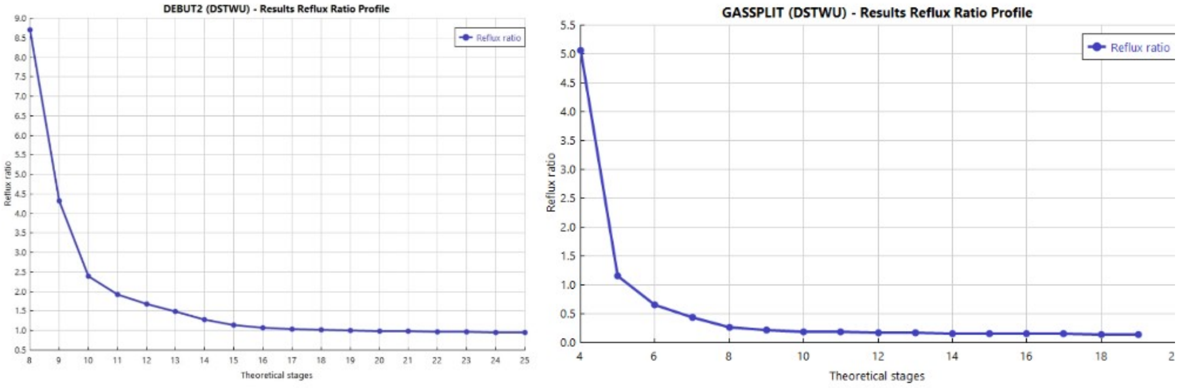

Figure 4.13: Reflux ratio vs number of theoretical stages for the debutanizer column (left). Reflux ratio vs number of theoretical stages for the gasoline splitter (right).

key recovery has been set to 0.01, to avoid the loss of C_5+ hydrocarbons in the distillate stream.
The condenser used in this model is a total condenser with LPG as distillate. In order to facilitate the condenser's cooling duty during heat integration, the distillate temperature has been maintained above 50°C. Furthermore, to determine the optimal number of stages required, a sensitivity analysis was conducted. Figure 4.13 illustrates that increasing the number of stages beyond 16 does not further decrease the reflux ratio. Thus, this value was adopted for this column. Finally, the column was set to operate at 11 bar, and the pressure drop within the column was neglected at this stage. The DSTWU model predicts the optimal feed stage to be the 14th, with a minimum reflux ratio of 0.875, and an actual reflux ratio of 1.079. These values were used as the initial parameters for the RadFrac block implementation.

An analogous procedure was applied to the design of the gasoline splitter. The primary aim of this column is to separate the C_9+ hydrocarbons from the rest of the blend, facilitating their treatment to reduce the durene concentration, as elaborated in Section 3.2. Consequently, xylene is identified as the light key component with a recovery rate of 0.9, while durene is classified as the heavy key. The recovery of durene was modulated to ensure the mass fraction of durene in the light gasoline stream remains below 2%. To avert the potential risk of solidification, the temperature of the bottom effluent is maintained well above 80°C. The total condenser pressure is held at 2 bar, while the pressure drop in the column is disregarded. As illustrated in Figure 4.13, an increase in the number of stages beyond 8 marginally influences the reflux ratio. As such, this value was employed in the RadFrac block. The DSTWU model provides an optimum feed stage prediction of 6.16 (above stage 6), a minimum reflux ratio of 0.1148, and an actual reflux ratio of 0.1952, which were subsequently implemented in the RadFrac model.

The heavy gasoline fraction, containing high concentrations of durene, is subjected to further processing to reduce its durene content. In this step, the heavy gasoline fraction is pressurized to 28.59 bar and heated to a temperature of 482.22°C before being directed to the dealkylation reactor. Within the reactor, the heavy gasoline fraction undergoes a reaction in the presence of a hydrogen-rich environment, with a mole ratio of 2.5. The reactor is modelled with an RStoic block, in order to reproduce the experimental results presented in the US4387261A patent [110]. The specified fractional conversion of durene is 83%.

Light and heavy gasoline are reblended and cooled down to ambient temperature before being stored.

4.7. Process design overview

The aforementioned models have been integrated together to form the overall flowsheet, representing the plant as a whole. The main flowsheet of the process is shown in Figure 4.14. Furthermore, a larger visualisation of the flowsheet is present in Appendix B. Additionally, the operating conditions and the most important parameters characterizing the various sub-units are reported in Table 4.8.

Table 4.8: Process design overview: operating conditions of the sub-units.

Process Design: operating conditions					
Gasification			**DME to hydrocarbons reactor**		
Temperature	1170.86	°C	Reactor inlet T	329.44	°C
Pressure	45	bar	Reactor outlet T	400	°C
ER	0.3		Reactor pressure	21	bar
S-C	1.2		**3 Phase separator**		
Oxygen inlet T	600	°C	Separator T	40	°C
Steam inlet T	600	°C	Separator pressure	7	bar
Solid oxide electrolyser			**Debutanizer**		
Temperature	800	°C	Min reflux ratio	0.875	mole basis
Pressure	45	bar	Actual reflux ratio	1.08	mole basis
Thermoneutral Voltage	1.3	V	Distillate to feed ratio	0.00968	mass basis
Reversible Voltage	0.886	V	Condenser type	Total	
Current density	3.8	A/cm^2	Min number of stages	7	
Single stack Power	200	kW	Number of stages	16	
Number of stacks	155		Feed stage	14	
Gas cleaning			Condenser pressure	10	bar
Syngas cooler T	300	°C	**Gasoline splitter**		
Condenser T	130	°C	Min reflux ratio	0.1148	mole basis
Condenser pressure	45	bar	Actual reflux ratio	0.1952	mole basis
ZnO column T	250	°C	Distillate to feed ratio	0.419	mass basis
ZnO column pressure	45	bar	Condenser type	Total	
ZnO mass	2716.8	kg	Min number of stages	3	
ZnO void fraction	0.37		Number of stages	8	
ZnO Column volume	5.63	m^3	Feed stage	Above 6	
ZnO Column diameter	1.81	m	Condenser pressure	2	bar
Zno Column height	2.44	m	**Dealkylation reactor**		
Pressure drop	4.5	bar	Reactor temperature	454	°C
Breaktrhough time	120	days	Reactor pressure	27.579	bar
DME membrane reactor			**Storage conditions**		
Number of reactors	10		Oxygen tank T	25	°C
Internal Radius	1.611	m	Oxygen tank pressure	150	bar
External Radius	1.605	m	LPG tank T	25	°C
Length	8.703	m	LPG tank pressure	10	bar
Inlet flow velocity	0.494	m/s	Gasoline tank T	25	°C
Reactor temperature	250	°C	Gasoline tank pressure	1	atm
Reactor pressure	40	bar			
GHSV	6900	1/h			
SW	3				
η	11.42				
H2:CO$_x$	3				

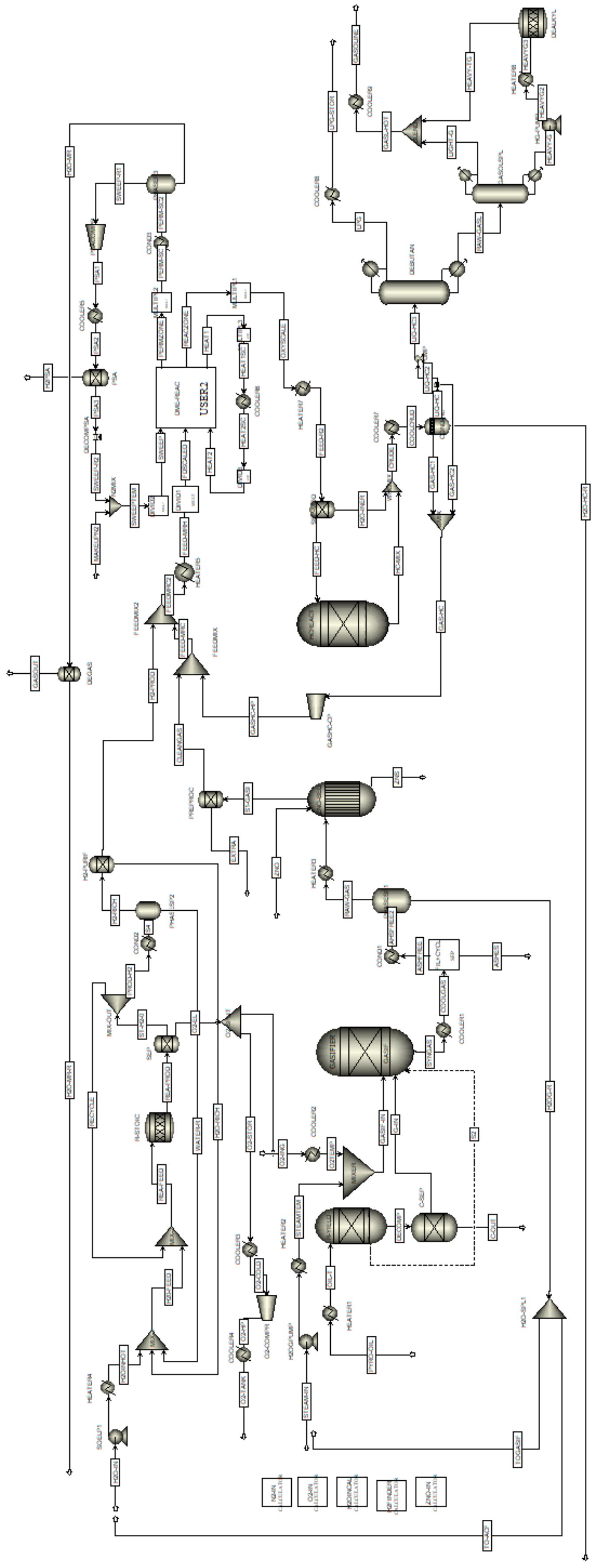

Figure 4.14: Main flowsheet of the whole process. Exported from Aspen Plus

5

Model Results

This chapter presents and elaborates on the results obtained from the simulations conducted. The description begins by discussing the sensitivity analyses performed to select the operating conditions of the process. Following this, detailed explanations are provided regarding the strategies employed for material recycling and heat integration. Subsequently, an analysis of the plant performance is presented, discussing the energy efficiency and carbon efficiency of the process and the improvement deriving from heat integration and material recycling. Finally, the main results of the sub-units of the plant are presented.

5.1. Sensitivity Analyses

5.1.1. Gasifier

The computational study on the gasifier sub-unit focused on identifying the operating conditions for the entrained flow gasifier. The objective was to maximize the H_2:CO_x ratio while maintaining a relatively high CO/CO_2 ratio, which guarantees a higher DME yield and CO_x conversion in the DME membrane reactor.

As addressed in Section 2.2.1, the oxygen equivalence ratio significantly influences the composition of the synthesis gas. Since the typical oxygen ER for entrained flow gasifier ranges from 0.3-0.4, simulations have been performed in this range to select the value yielding the highest H_2:CO_x ratio. As Figure 2.3 The H_2:CO_x is maximized at 0.3, leading to the setting of the oxygen equivalence ER at this value, corresponding to an oxygen mass flow of around 2014 kg/hr.

The effect of the SC ratio on synthesis gas composition is more complex, as discussed in Section 2.2.1. Therefore, a sensitivity analysis was conducted, varying the SC ratio to assess its impact on plant performance. It should be noted that this analysis does not take into account heat integration or material recycling.
To evaluate performance, a new metric, ”DME production specific consumption”, was introduced. It represents the energy required for DME production, as calculated by dividing the total energy input needed for the gasifier, SOEL, and DME units by the mass flow of the produced DME and expressed in kWh/kg.

An increase in the SC ratio raises the hydrogen content in the synthesis gas, implying less electrolysis-produced hydrogen is needed to maintain the same H_2:CO_x ratio. This leads to a reduction in the heat required to preheat water for the SOEL unit but necessitates more heat to bring the steam to the necessary temperature for the gasifier.
For higher SC ratios, the feed, oxygen, and steam preheating temperatures were adjusted to ensure a gasifier temperature above 1150°C. Lower gasification temperatures could potentially increase the CO_2/CO ratio and decrease the carbon conversion efficiency in the gasifier. Starting from 500°C, preheating temperatures were adjusted to 600°, 620°C, 675°C, and 720° for SC ratios of 1.2, 1.4, 1.6, and 1.8, respectively.

The analysis revealed that a high SC value is advantageous for minimizing specific consumption. As it is observable from Figure B.3 in the Appendix B, a rapid decrease in specific consumption is observed when the SC increases from 0.46 (corresponding to zero added steam mass flow) to 1. Beyond this point, the influence of the

SC on specific consumption diminishes. As a result, an SC value of 1.2 (corresponding to an H_2O mass flow of around 1671 kg/hr) was deemed optimal. This selection reflects the need to balance the SC increase with the requisite preheating of steam and oxygen to extremely high temperatures, to ensure that the gasification temperature remains sufficiently high.
The decrease in DME production specific consumption for high SC ratios can be explained by an increase in the H_2:CO_x ratio which varies from 0.68 at SC = 0.463 (corresponding to no steam fed to the gasifier) to 0.8 at SC = 1.2 as Figure B.4 in the appendix shows.

5.1.2. DME membrane reactor

Simulations were performed to assess the optimal operating conditions of the DME membrane reactor, in order to achieve the highest DME yield.

Sensitivity analyses

The GHSV is a crucial parameter that exerts a significant influence on reactor performance. An optimization process was conducted in Matlab to determine the GHSV value that yields the highest DME yield (Eq. 2.37). The GHSV was varied within a range of 2000 1/h to 10000 1/h, with increments of 100 1/h (see Appendix A.3 for the optimization code). Through this analysis, the optimum GHSV value of 6900 1/h was identified, resulting in an associated DME yield of approximately 0.73. Figure 5.1 presents the outcomes of the sensitivity analysis.

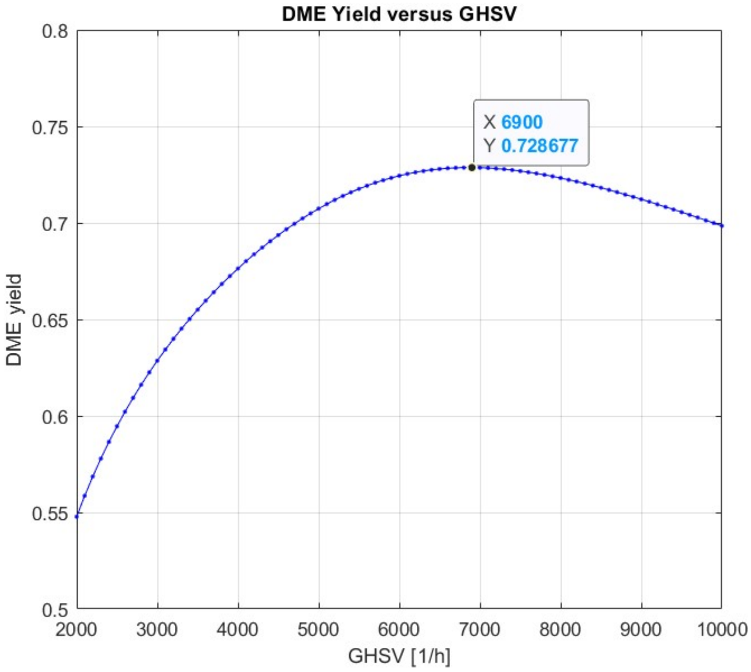

Figure 5.1: Optimization of the Gas Hourly Space Velocity for the DME membrane reactor: GHSV vs DME yield

The ratio SW, representing the molar flow rate of the sweep gas divided by the molar flow rate of the feed, is another important parameter that can be varied. Increasing SW positively affects the DME reactor performance, as it reduces the partial pressure of H_2O in the permeation zone, thereby increasing the driving force for the transmembrane flux of water (J_{H_2O}). However, this adjustment entails consequences in terms of equipment dimensions and associated costs. Thus, a trade-off must be considered.
As observed in Figure 5.2, the DME yield exhibits an increasing trend with a decreasing derivative as SW increases from 0.5 to 10. However, beyond SW = 3, the impact on DME yield becomes negligible. Therefore, an SW value of 3 has been selected for the plant, striking a balance between DME yield and cost considerations.

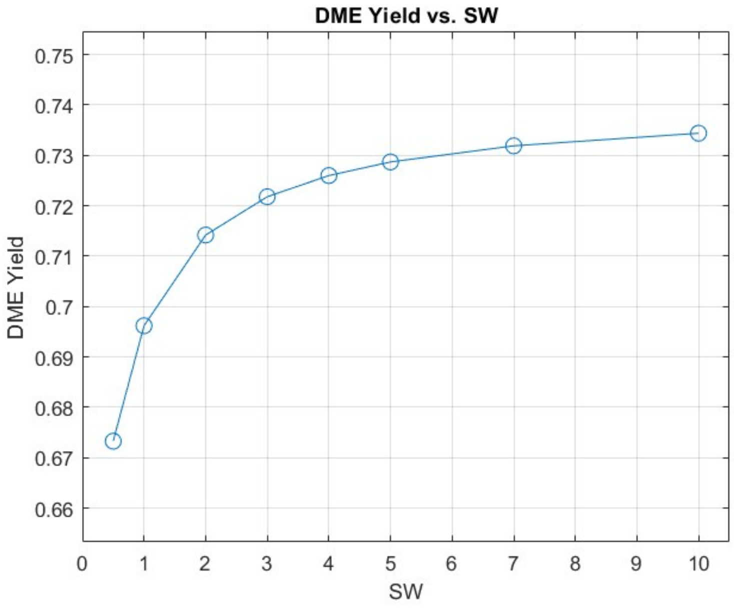

Figure 5.2: Optimization of the sweep to syngas molar flow ratio: SW vs DME Yield

5.2. Material Recycling

Material recycling can be used to recover effluent streams that do not represent the final product of the plant. In this section, the material recycling strategy employed in this process is explained.

5.2.1. Unreacted syngas and light hydrocarbons recycling

The gas stream at the outlet of the 3-phase separator, situated downstream of the DME to hydrocarbon reactor, comprises unreacted synthesis gas (CO, CO_2, H_2), light hydrocarbons (C_1-C_4), and traces of heavier hydrocarbons. This stream can be compressed and rerouted to the DME membrane reactor's inlet for exploiting the unreacted synthesis gas.

One potential drawback of this approach lies in the fact that hydrocarbons, acting as inert substances within the DME reactor, reduce the partial pressures of the reactants, which could potentially impart negative effects on the reaction kinetics. Consequently, purging part of the gas was considered. A sensitivity analysis was conducted to assess how the mass flow of gasoline produced by the plant fluctuates in relation to the recycle rate (RR), defined as:

$$RR = \frac{\dot{m}_{gas,recycled}}{\dot{m}_{gas,tot}} \tag{5.1}$$

The results of the sensitivity analyses (see Figure B.5 in Appendix B), showed that the plant produces the highest mass flow of gasoline when the entirety of the gas stream is recycled. This can be explained by the low mole fraction of hydrocarbons in the gas stream being recycled, which all together account for only 0.11. When merged with the feed, their mole fraction further diminishes to less than 0.02, rendering their impact on DME reaction kinetics insignificant.

For this reason, it has been decided to recycle the entirety of the gas stream extracted from the 3-phase separator downstream of the DME to hydrocarbon reactor.

Furthermore, the hydrogen separated from the membrane reactor's sweep gas by the PSA unit can be partially recycled and partially utilized for the dealkylation reaction. The high concentration of H_2 in the syngas and the significant pressure difference across the membrane, result in substantial hydrogen permeation. Around 38% of the H_2 flows through the membrane. Partial recirculation of the recovered gas to the DME reactor inlet reduces the amount of hydrogen required from the solid oxide electrolyzer, therefore decreasing the electrical energy demand. In addition to this, separating hydrogen from nitrogen and recirculating the latter to the permeation zone inlet, allows for lower requirements of nitrogen to be supplied from outside of the plant.

Due to these considerations, it has been decided to include the separation unit downstream of the permeation zone and recycle the recovered H_2.

5.2.2. Water Recycling

Together with pyrolysis oil, water is one of the main streams entering the battery limits of the plant. Substantial quantities of H_2O are necessary at the solid oxide electrolyzer and the entrained flow gasifier inlets. At the same time, water is separated from the gas stream in three distinct units throughout the plant. In the gas cleaning unit, a condenser placed downstream of the cyclone and filters facilitates the recovery of water by separating it from the synthesis gas. In the membrane reactor, water accumulates in the permeation zone and is subsequently separated from hydrogen and nitrogen through condensation. Furthermore, water is also retrieved from the DME-to-hydrocarbon reactor effluent stream via a 3-phase water separator.
Therefore, these recovered water streams offer an opportunity for treatment and recirculation within the system. This mitigates the dependence on external water sources beyond the plant's battery limits and allows for thermal saving.

Recycling water does not directly impact the operational performance of the single sub-units. The only alterations occur in the duty of the heaters which pre-heat the steam entering the SOEL and the gasifier, and the required mass flow from outside of the battery limits. Given these considerations, it was not required to reconnect the recovered H_2O material streams in Aspen Plus to the SOEL and the gasifier thus generating loops which would increase the computational cost. A distinct flowsheet for analyzing water recycling was developed separately and it is shown in Figure 5.3.

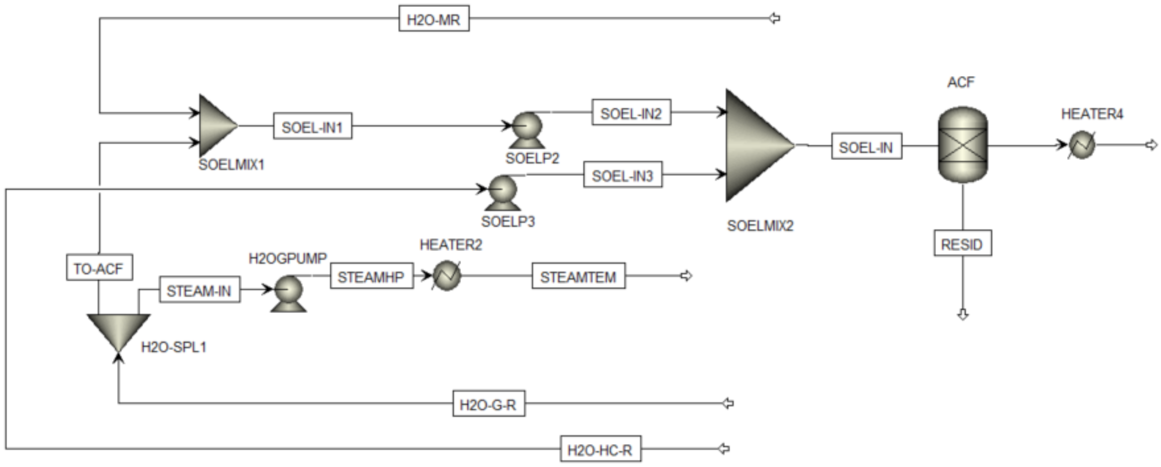

Figure 5.3: Flowsheet of the adopted water recycling strategy

An overview of the water streams in the plant is given in Table 5.1.

It is noticeable that the total amount recovered slightly surpasses the amount required as input for the process. This means that thanks to the implementation of material recycling, the water requirement of the plant can be reduced by 100%, making the plant auto-sufficient.

As per the data in Table 5.1, each of the three separate water streams provides a quantity sufficient to fulfil the gasifier's requirements. This indicates that each stream, independently, might be recycled and used for the gasifier's operation.
The chosen stream for this purpose is the one exiting the first condenser in the gas cleaning unit, primarily due to its proximal location to the gasifier. The condenser operates at 45 bar, ensuring that the separated water is readily available at the required pressure level, neglecting the pressure drop. In addition to this, recycling this water stream reduces the heat duty of the steam preheater (Heater2 in Figure 4.1) since the separated water enters the heater at 130°C.

Table 5.1: Overview of the water streams in the process.

Recycling - Water			
	Input streams	**Mass flow (kg/s)**	
1	Electrolyser	1.3598	kg/s
2	Gasifier	0.4641	kg/s
	Total	1.824	kg/s
	Output streams		
1	Membrane reactor	0.80661	kg/s
2	3-phase separator	0.47298	kg/s
3	Gasifier condenser	0.5603	kg/s
	Total	1.8399	kg/s
	Difference	-0.0159	kg/s
	Water saved	1.824	kg/s

The remaining water recovered from the process is rerouted to the SOEL. Due to high purity requirements at the electrolyser inlet, a water treatment procedure employing activated carbon filters is required, as explained in Chapter 3. This is especially crucial for water from the 3-phase separator, which needs rigorous cleaning to remove hydrocarbon traces. Also, differing pressure levels exist at the outlets: 3.5 bar at the membrane reactor and 7 bar post the DME to hydrocarbon reaction. Consequently, to meet the SOEL's operational pressure of 45 bar, these streams necessitate pressurization through two separate pumps before being merged.

5.3. Heat Integration

Heat integration is a process optimization technique aimed at minimizing the energy consumption of a plant by harnessing the potential of waste heat. It facilitates the redistribution of thermal energy from streams requiring cooling to those necessitating heating, thus reducing the overall demand for external utilities. Implementing heat integration can markedly enhance the overall energy efficiency of the plant, thereby improving operational performance, and fostering sustainable and economically viable operations. In this section, the heat integration strategy and its effect on the performance of the plant is presented.

Heat integration of the process under investigation has been carried out by performing a pinch analysis, following the method by Seider et al. [132].
The first step in this procedure is the selection of a minimum temperature difference between hot and cold streams in the heat exchangers, named minimum approach temperature. This has been selected to be 10°C, a typical value used in industry.
This procedure can be divided into two main phases. The first one is the ”Temperature Interval Method”, in order to determine the minimum hot and cold utilities needed and the location of the pinch point (if present). Following this step, the heat exchanger network is developed.

Since many multiple sub-units constitute the plant, a choice has been made to subdivide it into two main sections and perform heat integration on those two sections separately. This was primarily motivated by the quest for simplicity and practicality. Splitting the plant simplifies this task. Moreover, it pragmatically addresses the physical reality of the plant. As streams in a large plant can be physically distant, creating extensive heat transfer connections can be challenging and cost-prohibitive. Dividing the plant allows for localized heat recovery, minimizing the need for long-distance piping.
In addition to this, the gasifier and SOEL units are complementary in terms of heat integration: a lot of heat can be extracted from the hot synthesis gas and can be used to pre-heat the electrolyser unit.
Following these considerations, the plant has been divided in:

- Part 1: Gasifier, gas cleaning, and SOEL.
- Part 2: Reactors and hydrocarbon treatment.

5.3.1. Temperature interval method

The temperature interval method involved the following steps:

1. The streams destined for heaters (cold streams) and coolers (hot streams) were identified from the Aspen Plus model with their respective mass flow rates (in kg/s), specific heat capacities (in kJ/kg K), heat capacities ($C = \dot{m}\,cp$) (in kW/kg), and inlet and outlet temperatures (in °C).
2. The approach temperature was deducted from the temperatures of the hot streams, while the temperatures of the cold streams were left unaltered.
3. Temperatures were sorted in decreasing order, and the temperature difference between each interval was calculated.
4. Streams present in each interval were identified and the heat duty (in kW) in every interval was computed.
5. Starting from the highest temperature, the residual heat in every interval was calculated.
6. The most negative residual heat duty, representing the hot utility of the process, was placed at the top and for each interval, the heat duty was subtracted from it in a cascade diagram. The resulting heat duty represents the cold utility of the process. If no negative values are present, the process does not need a hot utility. Thus, 0 is placed at the top of the cascade.
7. The temperature at which the heat duty approaches 0 in the cascade diagram represents the pinch point.

The analysis allowed the determination of the minimum hot and cold utilities needed for the two sections of the plant. Results are documented in Table 5.2. For more details on the temperature interval method, please refer to the tables in Appendix C, where every performed step is shown.

Table 5.2: Heat integration summary: minimum hot and cold utilities needed for the process

Heat Integration - Utilities	
Type	**Heat Duty**
Part 1: Hot	142.12 kW
Part 1: Cold	5.3 kW
Part 2: Hot	70.92 kW
Part 2: Cold	1465.75 kW

5.3.2. Heat exchanger network

In this part of the heat integration procedure, the heat exchanger network has been determined, matching hot and cold streams above and below the pinch point, without violating the minimum temperature approach specified. To do so, some guidelines have to be followed. For blocks above the pinch points:

- The network design starts from the pinch point and proceeds toward higher temperatures.
- For streams that touch the pinch point, it must hold that $\mathrm{C}_{hot} \leq \mathrm{C}_{cold}$. If this does not hold, split the hot streams.

For blocks below the pinch points:

- The network design starts from the pinch point and proceeds toward lower temperatures.
- For streams that touch the pinch point, it must hold that $\mathrm{C}_{hot} \geq \mathrm{C}_{cold}$. If this does not hold split the cold streams.

For detailed information about the heat exchanging network, the different heat exchangers, and the composite curves, refer to Appendix C.

Following the development of the network, every heat exchanger has been sized, following the Log Mean Temperature Difference (LMTD) method. This method allows for the calculation of the heat transfer area, starting from the duty Q, the overall heat transfer coefficient U, and the temperature differences at the two sides of the heat exchanger: ΔT_1 and outlet temperature difference ΔT_2. Counterflow shell and tube heat exchangers have been considered as heat exchanger types. The log mean temperature difference is a logarithmic average of the temperature difference between the hot and cold streams, calculated as:

$$\mathrm{LMTD} = \frac{\Delta T_1 - \Delta T_2}{\ln\left(\frac{\Delta T_1}{\Delta T_2}\right)} \tag{5.2}$$

The heat exchanging area is computed from Eq. 5.3:

$$A = \frac{Q}{\text{LMTD} \cdot \text{U} \cdot F_c} \tag{5.3}$$

Where F_t is a correction factor, which accounts for the deviation from a perfect counterflow arrangement (see Appendix C). U has been assumed based on the type of flow inside the heat exchanger.
For heat exchangers in which one fluid undergoes a phase change at a constant temperature, the LMTD has been replaced by an average temperature, calculated as $(T_{hot} + T_{cold})/2 - T_{pc}$, where T_{pc} is the phase change temperature.

5.4. Plant energy performance

In this section, an analysis of the plant's energy performance is presented. The impact of the aforementioned material recycling strategy and heat integration is also discussed.

5.4.1. Energy efficiency

The energy efficiency of the plant (on an LHV basis) was calculated by dividing the energy output, represented by the energy content of the gasoline and of the LPG produced, by the total energy input of the plant. The energy input takes into account the pyrolysis oil energy content, the total heat duty required, the electric energy required by the SOEL unit, and the total power of the compressors.

$$\eta = \frac{\dot{m}_{\text{gasoline}} \cdot LHV_{\text{gasoline}} + \dot{m}_{\text{LPG}} \cdot LHV_{\text{LPG}}}{\dot{m}_{\text{biooil}} \cdot LHV_{\text{biooil}} + P_{\text{el}} + P_{\text{comp}}} \tag{5.4}$$

The calculated energy efficiency is 51.8 %.

The adopted integration strategies significantly increase the efficiency of the plant, as expected. With heat integration and material recycling, the energy efficiency is more than doubled, especially thanks to heat integration, which reduces the total heat duty from 13262 kW to 213 kW.

In comparison to similar processes for producing bio-derived gasoline, (documented in Table 2.6 of Chapter 2), the energy efficiency of this plant is superior. The highest reported energy efficiency in these processes is 50%. Furthermore, it is crucial to note that in the investigated process, a significant portion of the energy input is attributed to the compression required for the Pressure Swing Adsorption (PSA) unit. As discussed in Section 4.4, the modelling of hydrogen separation from the sweep gas was not detailed in this project. Therefore, a simplified model incorporating several assumptions was developed, and the energy consumption of the PSA unit may not reflect reality, necessitating further analysis.
The calculated energy efficiency is notably influenced by the power consumed by the PSA unit. By reducing the PSA adsorption pressure to 20 bar, the plant's efficiency increases to 61.8%. Consequently, it can be concluded that the implementation of a hydrogen-nitrogen separation unit with lower energy intensity would enhance the process efficiency, surpassing the efficiency of the best PBtL process reported in the literature by almost 12%.
It should also be considered that while oxygen represents a valuable product of the process, it is not included in the energy outputs of the plant.
An overview of the energy inputs and outputs of the plant is given in Table 5.3.

Table 5.3: Energy inputs and energy outputs of the process.

Energy Efficiency					
Input	**Value**	Unit	**Output**	**Value**	**Unit**
$\dot{m}$ pyrolysis oil	1.389	kg/s	$\dot{m}$ gasoline	0.6885	kg/s
LHV pyrolysis oil	17.2	MJ/kg	LHV gasoline	43.4	MJ/kg
Heat Duty	213.05	kW	$\dot{m}$ LPG	0.00546	kg/s
Compressor PSA	11681	kW	LHV LPG	45.5	MJ/kg
Compressor O_2	59.16	kW			
Compressor hc recycling	359.8797	kW			
SOEL power	21471.2	kW			

5.4.2. Carbon Efficiency

Another significant key performance indicator is Carbon Efficiency, which gives an indication of how much carbon is retained in the final product. For this process it has been calculated as follows:

$$\eta_C = \frac{\dot{m}_{\text{C,gasoline}} + \dot{m}_{\text{C,LPG}}}{\dot{m}_{\text{C,biooil}}} \tag{5.5}$$

The calculated carbon efficiency is 95.7%, which is significantly superior to 79%, the highest value found in literature for an MTG process (see. Tab 2.6). The main difference between this process and the others in literature is that, in order to keep the carbon efficiency of the process as high as possible, efforts have been made to avoid CO_2 sequestration. Specifically, as explained in Section 2.4.3, the implementation of in-situ water removal for DME synthesis, allows to have a higher CO_2:CO ratio in the feed of the synthesis gas and thus excludes the need to remove carbon dioxide before the reactor inlet. Furthermore, high carbon efficiency is achieved thanks to the material recycling strategy.

Very high carbon efficiencies, even slightly superior to the one found for this process were found in Fischer-Tropsch-based PBtL processes, as shown in 2.4.3. The loss of carbon in this process is mainly due to the carbon loss in the gasifier, where 4% of the carbon is lost. The remaining carbon lost is trapped in the activated carbon filter which removes the hydrocarbons dissolved in the water being recirculated to the SOEL inlet.

5.4.3. Gasoline discussion

The characteristics of the produced gasoline have been compared with the mandatory environmental directives issued by the European Union and contained in the Euro 5, Directive 2009/30/EC [133]:

Table 5.4: Gasoline characteristics: comparison of model results and Euro 5 standards

Gasoline Characteristics			
Parameter	**Model Results**	**Standard (limits)**	**Source**
Aromatics	14 vol%	35 vol%	Directive 2009/30/EC [133]
Olefins	16 vol%	18 vol%	Directive 2009/30/EC [133]
Benzene	0.2 vol%	1 vol%	Directive 2009/30/EC [133]
RON	90-100 [127]	95 (min)	Directive 2009/30/EC [133]
Durene wt%	1.1 wt%	2 wt%	ExxonMobil [108]

Table 5.4 illustrates that gasoline complies with the standard limits for the most significant parameters. However, due to the lumping of certain hydrocarbons together in the development of the RYield, as explained in Section 4.5, it is not possible to calculate the Research Octane Number (RON) based on the compositions using models like the one proposed by Albahri et al. [134]. Nevertheless, it has been reported by Schreiner [127] that the RON for this process falls within the range of 90 to 100. Additionally, the gasoline produced through the conversion of DME to gasoline does not contain oxygenates, as also noted by Schreiner [127]. Therefore, if the RON falls below the required standards, methanol or ethanol can be blended (within the limits set by the Euro 5 standard) to enhance the RON and combustion characteristics of the mixture. Both methanol and ethanol can be obtained from bio sources, which means that blending them would maintain a low environmental impact of the fuel.

5.5. Results of the plant sub-units

5.5.1. Gasifier

The entrained flow gasifier operates at 45 bar and 1170.86 °C. As stated above, an oxygen equivalence ratio of 0.3 and a steam-to-carbon ratio of 1.2 are used, which correspond to 2014 kg/hr of oxygen and 1671 kg/hr of steam introduced in the unit. The streams are preheated to 600°C before being mixed and fed to the gasifier.

As a result of this operating condition, the synthesis gas has the composition shown by Table 5.5.

Table 5.5: Synthesis gas composition

Syngas composition	
Component	**Mole fraction**
H_2	0.313
CO	0.284
CO_2	0.108
H_2O	0.295

5.5.2. Gas Cleaning

The combination of cyclone and filters remove 3.55 kg/hr of ashes, cleaning the synthesis gas from the particulate matter.

In the subsequent condenser, 2017.25 kg/hr of liquid H_2O are separated from the syngas, thus reducing its mole fraction in the syngas from 0.295 to 0.068.

The last unit of the gas cleaning section is the ZnO packed bed. Its characteristics are presented in Table 4.8. An inlet stream of 6574 kg/hr enters the column, with a concentration of H_2S equal to 30 ppm. The outlet concentration of H_2S is 1 ppm, which corresponds to a removal of 4.6 kg of H_2S per day. Given the geometrical characteristic of the column, the inlet flow velocity of the gas is 2.23 m/s, which is below the minimum fluidization velocity of 5.52 m/s, calculated according to Equation 4.7. The resulting pressure drop, calculated with Eq. 4.6 is 4.94 bar. Thus, the clean gas reaches the DME reactor with a pressure of approximately 40 bar.

5.5.3. SOEL

The solid oxide electrolysis cell produces the required amount of hydrogen to set the H_2:CO_x ratio to 3. The mass flow of H_2 produced changes depending on the material recycling strategy chosen. When unreacted synthesis gas and the H_2 recovered from the permeation zone of the reactor are recirculated to the reactor inlet, the amount of hydrogen that the SOEL unit produces is 547.79 kg/hr.

This corresponds to 4347.64 kg/hr of O_2, which is more than two times the amount necessary for the entrained flow gasifier. This confirms that the choice of sizing the electrolyser based on the hydrogen required, rather than the oxygen required is correct. The excess oxygen is compressed to 100 bar, cooled and stored.

The required electrical power is 21.91 MW. As was already indicated in Table 4.8, this means that 80 stacks with a power of 200 kW each, should be included in the plant.

It is noteworthy that heat integration allows saving a significant amount of energy since the energy needed to preheat the H_2O (6.03 MW) is obtained from the syngas exiting the gasifier, one of the oxygen coolers at the outlet of the SOEL, and the condenser in the SOEL unit.

5.5.4. DME membrane reactor

In section 4.4.1, it was stated that depending on the Peclet number (Eq. 4.13), the assumption of plug flow reactor might or might not be valid. Given the operating conditions of the DME reactor shown in Table 4.8, the Peclet number is calculated with the external diameter of the reactor, the inlet flow velocity, and the average diffusivity of the mixture (obtained from Aspen Plus). The calculated Peclet number is $\sim= 10^5$, which justifies the assumption of a plug flow reactor.

As explained in Chapter 2, the performance of the reactor can be quantified with CO_x conversion (Eq. 2.35), DME Yield (Eq. 2.37), and DME selectivity (Eq. 2.38). For the reactor integrated in the plant under investigation Y_{DME} = 0.68, X_{CO_x} = 0.69 and S_{DME} = 0.98. These values are slightly lower with respect to the case without recirculation, where Y_{DME} = 0.70, X_{CO_x} = 0.72, and S_{DME} = 0.98. This can be explained by the presence of light hydrocarbons, which act as inerts, thus decreasing the performance. However, as it has been already stated, recirculating the unreacted synthesis gas is beneficial for the plant's overall performance.

5.5.5. DME to Hydrocarbon reactor

The distribution of the products of the second reactor has been discussed in Chapter 4 and can be found in Table 4.7. The reactor produces 8905.69 kg/hr of hydrocarbons which enter the product separation and purification section.

5.5.6. Product separation and purification

The 3-phase separator yields three separate streams. In the case without material recycling, these correspond to 4645.08 kg/hr of gas, 1702.74 kg/hr of liquid water, and 2557.98 kg/hr of liquid hydrocarbons. The liquid hydrocarbon stream is fed to the debutanizer.

The reboiler at the bottom of the debutanizer operates at 180.3° C, with a bottoms rate of 25.06 kmol/hr, a boilup rate of 21.84 kmol/hr and a boilup ratio of 0.91. The total condenser operates at 41.07 °C, with a distillate rate of 0.37 kmol/hr, a reflux rate of 0.407 and a reflux ratio of 1.1.

The gasoline splitter receives the bottom stream of the debutanizer and separates the light and heavy hydrocarbons. The reboiler works at a temperature of 142.3° C, with a bottoms rate of 4.407 kmol/hr, a boilup rate of 14.46 kmol/hr and a boilup ratio of 3.28. The total condenser operates at 66.3° C, with a distillate rate of 20.65 kmol/hr, and a reflux rate of 4.03 kmol/hr, thus a reflux ratio of 0.195.

Durene accounts for 11 wt% of the heavy gasoline stream. Its content is reduced to 1.5 wt% by dealkylation in the last reactor of the plant.

6

Economic Analysis

6.1. Methodology

The economic analysis methodology for the plant, developed by the National Energy Technology Laboratory (NETL) [135], seeks to determine the conditions under which the plant achieves profitability. This feasibility is determined through a discounted cash flow analysis, centered around the net present value (NPV) given by:

$$\mathrm{NPV} = \sum_{k=0}^{N} \frac{CF_k}{(1+i)^k} \tag{6.1}$$

In this equation, CF_k symbolizes the net cash flow during the k-th year, i signifies the discount rate or the opportunity cost of capital, and N is the project's total duration in years.
This analysis differentiates between two distinct phases: the construction phase, during which the plant is constructed, and the subsequent operational phase.

6.1.1. Cash flow in the construction phase

Throughout the construction phase, the cash flow for any year k is quantified by the equity portion of the total as-spent capital (TASC). To comprehend its derivation, one must examine its components.

Capital cost levels

The determination of the TASC begins with an understanding of capital costs. NETL has outlined multiple levels of capital costs. Starting with the Bare Erected Cost (BEC), comprises refers to the direct expenses associated with constructing a facility. The engineering, procurement and construction cost (EPCC) includes the cost of services provided by contractors and is calculated as 15% of the BEC [135]. When BEC, EPCC, and a contingency margin (30% of BEC) are combined, the Total Plant Cost (TPC) is obtained.
Moreover, several supplementary costs should be considered. These include pre-production expenses (2% of TPC), an inventory capital for spares (0.5% of TPC), a financing charge (2.7% of TPC) to cover the cost of securing funds, and other owner-associated costs (15% of TPC). When these expenses are summed with TPC, the result is the Total Overnight Cost (TOC). The TOC represents what the project would cost if it were completed ”overnight” with no interest charges during its construction.
However, as capital expenditure occurs over the construction's entirety and not immediately, the TOC must be escalated:

$$\mathrm{ETOC} = \sum_{i=1}^{Y} \mathrm{TOC}_i \times (1 + r_{cap})^{i-1} \tag{6.2}$$

Here, TOC_i is the yearly portion of the TOC, with the construction period Y, assumed to span 2 years. The plant's finance structure comprises both debt and equity, represented by ξ_D and ξ_E, respectively.
Debt repayment commences with the onset of plant operations. Meanwhile, the loan, distributed across the entire expenditure duration, incurs additional interest. The interest during construction (IDC) is evaluated using the

total debt disbursement (TDD) as:

$$\text{IDC} = \sum_{i=1}^{Y} \text{TDD}_i \times r_d = \sum_{i=1}^{Y} \text{ETOC}_i \times \xi_D \times r_d \tag{6.3}$$

In this context, r_D represents the interest rate on debt.
With these calculations in place, TASC is then derived from the escalated total overnight cost combined with the construction interest:

$$\text{TASC} = \text{ETOC} + \text{IDC} \tag{6.4}$$

For a specific year k within the capital expenditure phase, the cash flow $CF_{k,cp}$ is defined by the TASC of that year:

$$CF_{k,cp} = -(\text{ETOC} + \text{IDC}) \times \xi_E \tag{6.5}$$

Only the equity portion of the total as-spent cost is represented in the cash flow, not accounting for the debt-financed portion. This is because the debt portion is considered a financial obligation to be repaid during the operational period, and is not treated as an immediate outflow during construction.

BEC estimation

The bare erected cost is calculated on the basis of costs estimations available in other studies, as suggested by Haro et al. [124]:

$$BEC_{new} = BEC_{ref} \left(\frac{\text{Design Scale}}{\text{Base Scale}} \right)^{\gamma} \tag{6.6}$$

where γ is the scaling factor, specific for each component.
For the equipment where reference data were not available, correlations have been used to estimate the costs. Specifically, correlations from the book Analysis, Synthesis and Design of Chemical Processes by Turton et al. have been used for pumps, compressors, and vessels, while the correlation proposed by Fiaschi et al. [136] has been used to estimate the cost of the heat exchanging network.
The correlations can be consulted in Appendix D.

6.1.2. Cash flow in the operating phase

The operational period corresponds to the lifetime of the plant, from the first plant start-up to its definitive shut-down. The cashflow $CF_{k,op}$

$$CF_{k,op} = Rev_k - Exp_k - Tx_k - An_k \tag{6.7}$$

where Rev_k and Exp_k are operating revenues and expenses respectively, Tx_k represents taxes and An_k is the annuity for debt repayment.

Operating expenses

The operating expenses are the outcomes required to ensure the activity of the plant. In this analysis the following expenses have been taken into consideration:

- Consumable costs, associated with the inlet streams, electricity, and catalyst costs;
- Average maintenance costs, calculated per year as 2% of the total plant cost;
- Personnel costs
- Insurance costs, calculated per year as 1% of the total plant cost;
- Transport costs, related to the expenses to bring the consumables to the plant site.

The calculations for the consumable costs, the labour costs, and the transport costs are shown in Appendix D.

Revenues

Revenues represent the earnings obtained by selling the products of the plant. In this case, the main product is gasoline, and the other products are LPG and excess oxygen. An assumption is made that the whole amount of products produced is sold on the market.

Annuity

Annuity refers to a series of equal payments made at regular intervals over a certain period. When calculating the annuity for a loan, various factors are considered, including the principal loan amount, the interest rate, and the duration of the loan. The goal is to determine a constant payment amount that ensures the loan will be entirely paid off (including interest) by the end of the loan term.

$$An = \frac{r_d\,(1+r_d)^n}{(1+r_d)^n - 1}\,TASC\,\xi_D \tag{6.8}$$

where r_d is the debt interest rate, n is the number of years for full repayment and TASC ξ_D is the total amount owed. As the loan is paid out, the interest portion declines, whereas the principal portion increases. The interest expense IE$_k$ for a generic year is:

$$IE_k = r_d\,RD_{k-1} \tag{6.9}$$

RDk_1 is the residual debt at the previous period. Residual debt before repayment starts coincides with the entire loan (TASC ξ_D). The calculation of principal repayment, as the difference between annuity (constant) and interest portion (variable), is then possible:

$$PR_k = An - IE_k \tag{6.10}$$

Taxes

Taxes are a complicated matter, and may significantly vary depending on many aspects, starting from the type of products. For instance for Gasoline and LPG, taxation can be broken down into excise duty, whose amount varies over time based on government policy decisions, inflation adjustments, and other factors, and BTW (VAT), calculated not just on the basic price of the gasoline but also on the excise duty. In order to simplify the analysis taxes are calculated as follows:

$$Tx_k = r_t\,(Rev_k - Exp_k - IE_k - Dep_k) \tag{6.11}$$

Where Dep$_k$ is the depreciation, which is the reduction in the value of an asset over time and is calculated with the straight-line method assuming a final value of 10% of the original one. Taxes are only applied in case of a positive cash flow. The assumption of r_t = 60% is based on a report by Shell on fuel price [137], where the taxation is broken down per type of fuel.

Key Economic Performance Indicators

The economic performance of the plant is first of all quantified by the NPV, obtained from Eq. 6.1.
Furthermore, another important indicator is the levelized cost of fuel, which quantifies the cost of a unit of fuel produced. This is obtained by dividing the summation of TASC and the total operating expenses over the operating lifetime by the total volume of fuel in liters produced over the same period of time.

$$\text{LCOF} = \frac{\text{TASC} + \sum_{k=0}^{Y} Exp_k}{V_{fuel}} \tag{6.12}$$

6.1.3. Economic assumptions

The main economic assumptions are reported in Table 6.1

Table 6.1: Main economic assumptions of the analysis

Economic Assumptions	
Debth share ξ_D	40%
Equity share ξ_E	60%
Debth interest rate r_D	4.5%
Rate for capital cost escalation r_{cap}	3%
Time for construction	2 years
Repayment period	8 years
Operating days	334 (8000 h)
Plant lifetime	20 years
Taxation	25.8%

6.2. Results

The main parameters quantifying the costs are reported in Table 6.2

Table 6.2: Costs of the plant: BEC, TPC, TOC, TASC

Costs		
BEC	53.263	M€
TPC	77.232	M€
TOC	96.694	M€
TASC	99.911	M€

The LCOF has been determined to be 1.96 €/l, falling within the comparable range for other PBtL plants documented in literature, and illustrated in Table 2.7, which lists values from a minimum of 1.36 €/l to a maximum of 2.67 €/l.

An oxygen selling price of 50 €/ton has been assumed. This is consistent with suggestions from Poluzzi, who proposed 54 €/ton [18], and other sources like [138] that selected 50 €/ton. Taking into account the current price of electricity in the Netherlands as of July 2023, 92.04 €/MWh, the selling price of gasoline which would make the plant break even at the end of the operating period can be computed. This is calculated to be 2.33 €/L. The price of LPG has been taken to be 0.728 €/L, which is the current price of the fuel in the Netherlands. The detailed cash flow examination can be found in Appendix D.

Considering that the average price of gasoline at refuelling stations in the Netherlands is 2.077 €/L, it can be inferred that under the current conditions, the plant does not promise profitability. Even if we exclude the excises on the price of gasoline, and suppose to sell bio-gasoline at a price of 2.077 €/L, the plant has a NPV of - 25.815 M€. This aligns with the insights from studies on enhanced MTG plants explored in the literature [34], [35], which also stated that their processes were unprofitable with the current economic conditions.

Subsequently, a sensitivity analysis concerning the Net Present Value was executed. This was done by varying the gasoline prices and the electricity costs, as they play pivotal roles in contributing to revenues and expenses (making up 97.6% and 61% respectively). The outcomes of this analysis are visually represented in a 3D plot, depicted in Figure 6.1.
With the current gasoline price standing at 2.077 €/l, the plant could reach a break-even point if the electricity price was lowered to 63.88 €/MWh. However, this does not take into account excises, and assumes that the selling price of gasoline coincides with the consumer cost.
One pathway to make the plant economically viable would be through the reduction of the taxation rate. This could potentially act as a stimulus from governing bodies to facilitate the shift from fossil fuels to bio-derived alternatives. By hypothetically slashing the anticipated taxation rate by 50% (from 0.258 to 0.129), an electricity price of 70.65 €/MWh would guarantee to reach the break-even point. This observation underscores the fact that while the plant might not be financially tenable at present, a combination of decreasing electricity prices, coupled with policy-driven incentives, could make it economically appealing in the forthcoming years.

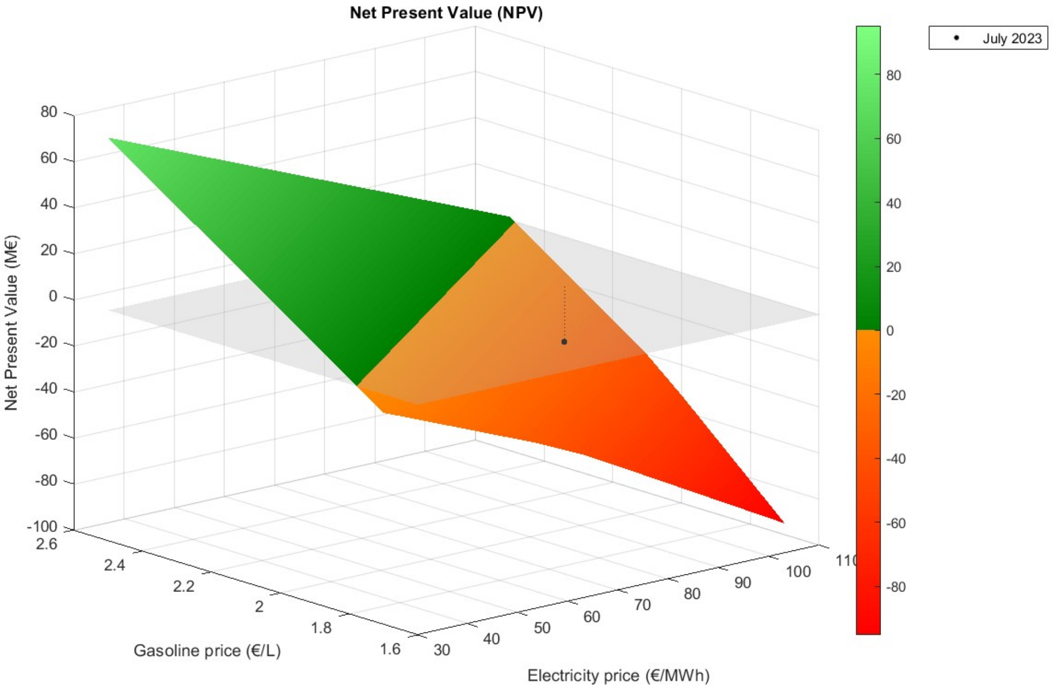

Figure 6.1: Sensitivity analysis on the net present value: NPV vs electricity price in €/MWh and vs gasoline selling price in €/l

7

Conclusion and Recommendations

7.1. Conclusion

In this project, a novel Power and Biomass to Liquid plant to convert pyrolysis bio-oil into gasoline for transport purposes has been analysed from both a technical and economical point of view. After discussing the motivation behind the project, the study started with a literature review, with the goal of forming the Basis of Design of the process, selecting suitable process sub-units and determining their operating conditions to achieve a technically viable design. Through the literature review, the theoretical background and the state of the art of the technologies involved in the process were explored. After laying down the process concepts the project proceeded with the development of a model of the plant, using Aspen Plus, Matlab and Excel. Then, material recycling and heat integration were employed to enhance the plant's energy efficiency. Finally, an economic analysis was conducted to evaluate the project's economic viability.

At the beginning of the project, the main research question was stated and three sub-research questions were formulated to address different aspects of the research. Thanks to the analysis conducted, these questions can now be answered.

1. *Which process sub-units, along with their corresponding characteristics and operating conditions, must be chosen to attain a feasible integrated plant?* This question was addressed through the literature study and the development of a process model integrating Aspen Plus, Matlab, and Excel. Entrained flow gasification was identified as the most suitable method for pyrolysis oil gasification, offering the possibility of high-pressure gasification, which minimizes the need for compression, thus saving energy. Moreover, it provides high-quality syngas with low tar content, simplifying gas cleaning. The synthesis gas cleaning process focuses on removing particulate matter through a combination of filters and cyclones, along with H_2S, which could poison the methanol synthesis catalyst. The selected H_2S removal technology was ZnO packed bed due to its high selectivity towards H_2S (avoiding carbon losses by not removing CO_22), and its ability to work at high pressure and with high CO_2/H_2S concentrations. For electrolysis, solid oxide electrolysis was chosen for its high efficiency and the possibility of recovering heat from synthesis gas cooling and other hot streams within the process. Synthesis gas upgrading involved direct DME synthesis from syngas in a membrane reactor, facilitating in-situ water removal and subsequent DME to hydrocarbon conversion, which was thermodynamically advantageous compared to the conventional methanol-to-gasoline process. Lastly, hydrocarbon separation and purification employed 3-phase separation, followed by two distillation columns and a dealkylation reactor to reduce durene content in the products.

2. *How can heat integration and material recycling strategies enhance the overall performance of the integrated plant?* Material recycling is used primarily to recover the water separated along the process and make the plant auto-sufficient in terms of water demand. Furthermore, at the outlet of the DME to hydrocarbon reactor, unreacted synthesis gas and light hydrocarbon gases are recirculated to the inlet of the DME synthesis reactor, recovering kg/hr of unreacted synthesis gas, which represents 35.7% of the DME membrane reactor inlet feed. The hydrogen which permeates through the membrane in the DME synthesis reactor is separated through PSA and recirculated at the inlet of the DME reactor.

Heat integration has been performed on two separate parts of the plant: gasification, gas cleaning and electrolysis, and reactors and product separation and purification. The heat integration strategy adopted allows for saving 13048 kW thus, increasing the overall energy efficiency of the plant by 9,5% and yielding an overall energy efficiency which ranges between 51.8% and 61.8%, depending on the power requirements of the PSA unit, which requires further modelling.
In addition to this, the plant's calculated carbon efficiency (Eq. 5.5 of 95.7% is superior to similar PBtL processes based on the MtG process. This is primarily due to the integration of the DME membrane reactor, which allows for a higher CO_2 concentration in the syngas, and thus, excludes the need for carbon dioxide sequestration.

3. *What are the essential conditions for ensuring the economic viability of the proposed integrated plant?* The economic analysis has shown that the plant is not profitable under the current economic conditions. The factors mainly influencing the profitability of the plant are the price of electricity and the selling price of gasoline. With the current gasoline price standing at 2.077 €/l, the plant could reach a break-even point if the electricity price was lowered to 63.88 €/MWh. Conversely, with the current electricity charge of 92.04 €/MWh, an NPV = 0 could be attained with a gasoline selling rate of 2.33 €/L.
This suggests that incentives from political institutions for instance by reducing taxes on bio-gasoline or increasing the ones on fossil-derived gasoline would help the transition from fossil fuel to biomass-derived fuels.

7.2. Recommendations

This study is a preliminary techno-economic assessment. Therefore, numerous areas for potential further research can be suggested.
From the technical point of view, the research should be expanded in the following areas:

- Sub-unit selection: The choice of the membrane reactor should be carefully evaluated, as it has shown promise in enhancing DME yield and eliminating the need for CO_2 sequestration before DME synthesis. However, the implications of its implementation on the overall process need to be thoroughly assessed. The issue of unwanted hydrogen permeation through the membrane requires the incorporation of a separation system downstream of the reactor permeation zone. Although pressure swing adsorption has been utilized, it is essential to explore other possible solutions and model them in greater detail. Additionally, since membrane reactor technology for DME synthesis is still in the research phase, continuous monitoring of its developments and scale-up progress is necessary. Furthermore, the potential of sorption-enhanced DME synthesis, which has demonstrated comparable performance to membrane reactors, should also be closely monitored.

- Improvement of the DME membrane reactor model: Moving beyond the current isothermal plug-flow reactor implementation, the integration of the energy balance into the governing equations is the next crucial step. This integration will enable a deeper understanding of temperature variations within the reactor, considering their influence on the thermodynamics of the reaction and membrane performance.

- Development of a kinetic model for DME to hydrocarbon conversion: Despite conducting thorough research, a suitable kinetic model for the DME to hydrocarbon reactor could not be identified for implementation in Aspen Plus. As a result, the approach adopted was based on experimental findings, which may limit the ability to finely adjust the reactor's operating conditions. In order to address this limitation and enhance the accuracy of hydrocarbon yield predictions, the next step in the research would involve the development of a kinetic model.
The development of this kinetic model will require a combination of both modelling and experimental work. The goal will be to create a more realistic representation of the reaction kinetics within the DME to hydrocarbon reactor. By incorporating the kinetics of the reactions involved, it will become possible to better understand the behaviour of the process and optimize the reactor's operating conditions.

- SOEL electricity source modelling: In the project, it has been decided to connect the electrolyser directly to the electrical grid. However, it is important to consider the potential of coupling it directly with renewable electricity sources, such as solar panels and wind turbines.

By integrating the SOEL system with renewable energy sources, a more sustainable and cleaner energy approach can be achieved. To ensure efficient integration, advanced modelling and control algorithms should be utilized, optimizing power exchange and enabling continuous hydrogen production.
Incorporating energy storage solutions will also play a key role in managing the intermittent nature of renewable energy sources. Storing excess energy during peak times allows for later hydrogen production during periods of low-energy generation.

- Development of a strategy for the operation of the ZnO packed beds and their configurations: In order to optimize the operation of the ZnO packed beds and their configurations, it is crucial to consider the requirements for safety measures and efficient sorbent regeneration. The current model includes a single column, but a practical plant should have at least two columns arranged in a parallel configuration.
  Furthermore, it should be investigated how to operate the different columns present in the plant. The simplest way is an on/off operational framework for the two columns, meaning that only one column operates at any given time to handle the entire gas stream. When sorbent replacement is needed, the gas stream is diverted to the other column. Each column is designed to eliminate H_2S over a specified time duration, known as the breakthrough time. This strategy is obviously not the most efficient since different regeneration strategies could lead to smaller vessels. For instance, two smaller columns could operate concurrently in a parallel configuration. When one column is disconnected for sorbent replacement, the other column's sorbent might be consumed more rapidly than under nominal conditions. However, if the sorbent replacement duration is short and the columns are appropriately designed, a single packed bed could be sufficient to eliminate the required amount of H_2S while the other remains non-operational. Evaluating different regeneration strategies will help identify the most efficient approach for the ZnO packed bed operation, leading to enhanced system safety and cost-effectiveness.

Further research should also be conducted from an economic and environmental point of view.

- Verification of equipment cost: Models were used to estimate the prices of the process equipment. In a later stage, real quotations should be obtained from suppliers to verify the assumptions and calculated bare erected cost of the plant.

- Finally, it is also recommended to perform a Life Cycle Assessment (LCA) for a holistic understanding of the environmental footprint of the entire process. The LCA identifies potential environmental hotspots and quantifies greenhouse gas emissions, energy consumption, and other environmental burdens. This helps in identifying areas where improvements can be made to minimize negative impacts on the environment.

References

[1] Charles D Keeling. *Climate change and carbon dioxide: An introduction*. 1997, pp. 8273–8274.

[2] *Carbon dioxide concentration*. Aug. 2022. URL: `https://climate.nasa.gov/vital-signs/carbon-dioxide/`.

[3] Susan Solomon et al. “Irreversible climate change due to carbon dioxide emissions”. In: *Proceedings of the National Academy of Sciences of the United States of America* 106 (6 Feb. 2009), pp. 1704–1709. ISSN: 00278424. DOI: `10.1073/pnas.0812721106`.

[4] Dennis L Hartmann et al. “Observations: atmosphere and surface”. In: *Climate change 2013 the physical science basis: Working group I contribution to the fifth assessment report of the intergovernmental panel on climate change*. Cambridge University Press, 2013, pp. 159–254.

[5] Susan Solomon et al. “Persistence of climate changes due to a range of greenhouse gases”. In: *Proceedings of the National Academy of Sciences of the United States of America* 107 (43 Oct. 2010), pp. 18354–18359. ISSN: 00278424. DOI: `10.1073/pnas.1006282107`.

[6] *Carbon dioxide concentration*. Aug. 2022. URL: `https://www.nasa.gov/press-release/nasa-says-2022-fifth-warmest-year-on-record-warming-trend-continues`.

[7] *Consequences of climate change*. URL: `https://climate.ec.europa.eu/climate-change/consequences-climate-change_en`.

[8] United Nations. *Paris Agreement*. 2015.

[9] COP26. *Glasgow Pact*. 2021. URL: `https://www.ipcc.ch/report/ar6/wg1/..`

[10] COP26. *COP26 Presidency Outcomes: The Glasgow Climate Pact*. 2021.

[11] McKinsey & Company. *Global Energy Perspective 2022 Executive Summary*. 2022.

[12] Iea. *Transport – analysis*. URL: `https://www.iea.org/reports/transport`.

[13] International Energy Agency. *Global Energy Review: CO2 Emissions in 2021 Global emissions rebound sharply to highest ever level*. 2021. URL: `www.iea.org/t&c/`.

[14] Jody Emlyn Muelaner. *Unsettled Technology Domains for Pathways to Automotive Decarbonization*. Tech. rep. SAE Technical Paper, 2020.

[15] S.C. Bhatia. “26 - Issues relating to biofuels”. In: *Advanced Renewable Energy Systems*. Ed. by S.C. Bhatia. Woodhead Publishing India, 2014, pp. 688–718. ISBN: 978-1-78242-269-3. DOI: `https://doi.org/10.1016/B978-1-78242-269-3.50026-7`. URL: `https://www.sciencedirect.com/science/article/pii/B9781782422693500267`.

[16] I. B. Ocko and S. P. Hamburg. “Climate consequences of hydrogen emissions”. In: *Atmospheric Chemistry and Physics* 22.14 (2022), pp. 9349–9368. DOI: `10.5194/acp-22-9349-2022`. URL: `https://acp.copernicus.org/articles/22/9349/2022/`.

[17] *Second-generation biofuels (2023) Wikipedia*. URL: `https://en.wikipedia.org/wiki/Second-generation_biofuels`.

[18] Alessandro Poluzzi et al. “Flexible Power & Biomass-to-Methanol plants: Design optimization and economic viability of the electrolysis integration”. In: *Fuel* 310 (Feb. 2022). ISSN: 00162361. DOI: `10.1016/j.fuel.2021.122113`.

[19] Carlo N Hamelinck and André PC Faaij. “Outlook for advanced biofuels”. In: *Energy policy* 34.17 (2006), pp. 3268–3283.

[20] Renato Cruz Neves et al. “A vision on biomass-to-liquids (BTL) thermochemical routes in integrated sugarcane biorefineries for biojet fuel production”. In: *Renewable and Sustainable Energy Reviews* 119 (2020), p. 109607. ISSN: 1364-0321. DOI: `https://doi.org/10.1016/j.rser.2019.109607`. URL: `https://www.sciencedirect.com/science/article/pii/S1364032119308159`.

[21] Marcel Dossow et al. "Improving carbon efficiency for an advanced Biomass-to-Liquid process using hydrogen and oxygen from electrolysis". In: *Renewable and Sustainable Energy Reviews* 152 (Dec. 2021). ISSN: 18790690. DOI: `10.1016/j.rser.2021.111670`.

[22] Government of the Nethelands. *Climate Agreement*. 2019.

[23] *Biomass4Transport*. URL: `https://projecten.topsectorenergie.nl/projecten/duurzame-transportbrandstof-via-vergassing-van-pyrolyse-olie-33499`.

[24] *Biomass Technology Group: Your partner in the Bioeconomy*. URL: `https://www.btgworld.com/`.

[25] Onsi Hanafi. *Process Integration of Gasification and Electrolysis for Biofuel Production A techno-economic assessment*. 2021. URL: `http://repository.tudelft.nl/.`.

[26] M. Hillestad et al. "Improving carbon efficiency and profitability of the biomass to liquid process with hydrogen from renewable power". In: *Fuel* 234 (Dec. 2018), pp. 1431–1451. ISSN: 00162361. DOI: `10.1016/j.fuel.2018.08.004`.

[27] Mohammad Ostadi, Erling Rytter, and Magne Hillestad. "Boosting carbon efficiency of the biomass to liquid process with hydrogen from power: The effect of H2/CO ratio to the Fischer-Tropsch reactors on the production and power consumption". In: *Biomass and Bioenergy* 127 (Aug. 2019). ISSN: 18732909. DOI: `10.1016/j.biombioe.2019.105282`.

[28] Umesh Pandey et al. "Conceptual design and techno-economic analysis of biomass to liquid processes". In: *Frontiers in Energy Research* 10 (Sept. 2022). ISSN: 2296598X. DOI: `10.3389/fenrg.2022.993376`.

[29] Friedemann G. Albrecht et al. "A standardized methodology for the techno-economic evaluation of alternative fuels – A case study". In: *Fuel* 194 (2017), pp. 511–526. ISSN: 00162361. DOI: `10.1016/j.fuel.2016.12.003`.

[30] Peng Gao et al. "Direct conversion of CO2 into liquid fuels with high selectivity over a bifunctional catalyst". In: *Nature chemistry* 9.10 (2017), pp. 1019–1024.

[31] Wei Zhou et al. "New horizon in C1 chemistry: breaking the selectivity limitation in transformation of syngas and hydrogenation of CO 2 into hydrocarbon chemicals and fuels". In: *Chemical Society Reviews* 48.12 (2019), pp. 3193–3228.

[32] Youming Ni et al. "Realizing high conversion of syngas to gasoline-range liquid hydrocarbons on a dual-bed-mode catalyst". In: *Chem Catalysis* 1 (2 July 2021), pp. 383–392. ISSN: 26671093. DOI: `10.1016/j.checat.2021.02.003`.

[33] Jyoti Prasad Chakraborty, Satyansh Singh, and Sunil K. Maity. *Advances in the conversion of methanol to gasoline*. Elsevier, Jan. 2021, pp. 177–200. ISBN: 9780128233061. DOI: `10.1016/B978-0-12-823306-1.00008-X`.

[34] Ilkka Hannula. "Hydrogen enhancement potential of synthetic biofuels manufacture in the European context: A techno-economic assessment". In: *Energy* 104 (June 2016), pp. 199–212. ISSN: 03605442. DOI: `10.1016/j.energy.2016.03.119`.

[35] "Techno-economic analysis of hydrogen enhanced methanol to gasoline process from biomass-derived synthesis gas". In: *Fuel Processing Technology* 216 (June 2021). ISSN: 03783820. DOI: `10.1016/j.fuproc.2021.106776`.

[36] Zoha Azizi et al. *Dimethyl ether: A review of technologies and production challenges*. 2014. DOI: `10.1016/j.cep.2014.06.007`.

[37] Sunggyu Lee, Makarand Gogate, and Conrad J Kulik. "Methanol-to-gasoline vs. dme-to-gasolne II. process comparison and analysis". In: *Fuel science & technology international* 13.8 (1995), pp. 1039–1057.

[38] J. Topp-Jørgensen. "TOPS0E integrated gasoline synthesis- The tigas process". In: vol. 36. Elsevier Inc., 1988, pp. 293–305. DOI: `10.1016/S0167-2991(09)60523-1`.

[39] Miriam Stiefel et al. "Direct synthesis of dimethyl ether from carbon-monoxide-rich synthesis gas: Influence of dehydration catalysts and operating conditions". In: *Fuel Processing Technology* 92 (8 Aug. 2011), pp. 1466–1474. ISSN: 03783820. DOI: `10.1016/j.fuproc.2011.03.007`.

[40] Zhiqi Wang et al. "Design and operation of a pilot plant for biomass to liquid fuels by integrating gasification, DME synthesis and DME to gasoline". In: *Fuel* 186 (Dec. 2016), pp. 587–596. ISSN: 00162361. DOI: `10.1016/j.fuel.2016.08.108`.

[41] Leijenhorst, Evert Johannes. “Biomass gasification via fast pyrolysis”. eng. PhD thesis. Ghent University, 2016, XVI, 278. ISBN: 9789059898943.

[42] J Ruud Van Ommen and Wiebren de Jong. *Biomass as a sustainable energy source for the future: fundamentals of conversion processes*. John Wiley & Sons, 2014.

[43] Matthew S. Mettler, Dionisios G. Vlachos, and Paul J. Dauenhauer. *Top ten fundamental challenges of biomass pyrolysis for biofuels*. 2012. DOI: `10.1039/c2ee21679e`.

[44] Linghong Zhang, Chunbao (Charles) Xu, and Pascale Champagne. “Overview of recent advances in thermo-chemical conversion of biomass”. In: *Energy Conversion and Management* 51 (5 May 2010), pp. 969–982. ISSN: 01968904. DOI: `10.1016/j.enconman.2009.11.038`.

[45] Mark Eberhard et al. *The bioliq® Entrained-Flow Gasifier – A Model for the German Energiewende*. Aug. 2020. DOI: `10.1002/cben.202000006`.

[46] “A review of gasification of bio-oil for gas production”. In: *Sustainable Energy and Fuels* 3 (7 2019), pp. 1600–1622. ISSN: 23984902. DOI: `10.1039/c8se00553b`.

[47] E. J. Leijenhorst et al. “Entrained flow gasification of straw- and wood derived pyrolysis oil in a pressurized oxygen blown gasifier”. In: *Biomass and Bioenergy* 79 (2015), pp. 166–176. ISSN: 18732909. DOI: `10.1016/j.biombioe.2014.11.020`.

[48] Lopamudra Devi, Krzysztof J Ptasinski, and Frans J J G Janssen. *A review of the primary measures for tar elimination in biomass gasiÿcation processes*. 2003, pp. 125–140.

[49] Chunshan Li and Kenzi Suzuki. *Tar property, analysis, reforming mechanism and model for biomass gasification-An overview*. Apr. 2009. DOI: `10.1016/j.rser.2008.01.009`.

[50] Fredrik Weiland et al. “Pressurized oxygen blown entrained-flow gasification of wood powder”. In: *Energy and Fuels* 27 (2 Feb. 2013), pp. 932–941. ISSN: 15205029. DOI: `10.1021/ef301803s`.

[51] Ji Lu Zheng et al. “Gasification of bio-oil: Effects of equivalence ratio and gasifying agents on product distribution and gasification efficiency”. In: *Bioresource Technology* 211 (July 2016), pp. 164–172. ISSN: 18732976. DOI: `10.1016/j.biortech.2016.03.088`.

[52] Xifeng Zhu and Robbie Venderbosch. “A correlation between stoichiometrical ratio of fuel and its higher heating value”. In: *Fuel* 84 (7-8 May 2005), pp. 1007–1010. ISSN: 00162361. DOI: `10.1016/j.fuel.2004.12.002`.

[53] Haijun Guo et al. “Production of hydrogen rich bio-oil derived syngas from co-gasification of bio-oil and waste engine oil as feedstock for lower alcohols synthesis in two-stage bed reactor”. In: *International Journal of Hydrogen Energy* 39 (17 June 2014), pp. 9200–9211. ISSN: 03603199. DOI: `10.1016/j.ijhydene.2014.04.008`.

[54] Alexander Buttler and Hartmut Spliethoff. *Current status of water electrolysis for energy storage, grid balancing and sector coupling via power-to-gas and power-to-liquids: A review*. Feb. 2018. DOI: `10.1016/j.rser.2017.09.003`.

[55] S. Shiva Kumar and Hankwon Lim. *An overview of water electrolysis technologies for green hydrogen production*. Nov. 2022. DOI: `10.1016/j.egyr.2022.10.127`.

[56] Ragnhild Hancke, Thomas Holm, and Øystein Ulleberg. “The case for high-pressure PEM water electrolysis”. In: *Energy Conversion and Management* 261 (2022), p. 115642. ISSN: 0196-8904. DOI: `https://doi.org/10.1016/j.enconman.2022.115642`. URL: `https://www.sciencedirect.com/science/article/pii/S0196890422004381`.

[57] International Renewable Energy Agency. *Green hydrogen cost reduction scaling up electrolysers to meet the 1.5°C climate goal*. 2020. ISBN: 9789292602956. URL: `www.irena.org/publications`.

[58] P. Trinke et al. “Hydrogen Crossover in PEM and Alkaline Water Electrolysis: Mechanisms, Direct Comparison and Mitigation Strategies”. In: *Journal of The Electrochemical Society* 165 (7 2018), F502–F513. ISSN: 0013-4651. DOI: `10.1149/2.0541807jes`.

[59] Saarinen V et al. *Experimental campaign results at system level*. URL: `https://ec.europa.eu/research/participants/documents/downloadPublic?documentIds=080166e5cba3f8f3&appId=PPGMS`.

[60] Gyubin Min, Saeyoung Choi, and Jongsup Hong. *A review of solid oxide steam-electrolysis cell systems: Thermodynamics and thermal integration*. Dec. 2022. DOI: `10.1016/j.apenergy.2022.120145`.

[61] Javier Sanz-Bermejo et al. “Part load operation of a solid oxide electrolysis system for integration with renewable energy sources”. In: *International Journal of Hydrogen Energy* 40 (26 July 2015), pp. 8291–8303. ISSN: 03603199. DOI: `10.1016/j.ijhydene.2015.04.059`.

[62] Floriane Petipas, Annabelle Brisse, and Chakib Bouallou. “Modelled behaviour of a high temperature electrolyser system coupled with a solar farm”. In: *Chemical Engineering Transactions* 45 (Oct. 2015), pp. 1015–1020. ISSN: 22839216. DOI: `10.3303/CET1545170`.

[63] Sadegh Papari et al. “DME direct synthesis from syngas in a large-scale three-phase slurry bubble column reactor: transient modeling”. In: *Chemical Engineering Communications* 201.5 (2014), pp. 612–634.

[64] Marcello De Falco, Mauro Capocelli, and Gabriele Centi. “Dimethyl ether production from CO2 rich feedstocks in a one-step process: Thermodynamic evaluation and reactor simulation”. In: *Chemical Engineering Journal* 294 (June 2016), pp. 400–409. ISSN: 13858947. DOI: `10.1016/j.cej.2016.03.009`.

[65] Huazheng Li et al. “The high-yield direct synthesis of dimethyl ether from CO 2 and H 2 in a dry reaction environment”. In: *Journal of Materials Chemistry A* 9.5 (2021), pp. 2678–2682.

[66] Kaoru Takeishi. “Dimethyl ether and catalyst development for production from syngas”. In: *Biofuels* 1 (1 Jan. 2010), pp. 217–226. ISSN: 17597269. DOI: `10.4155/bfs.09.16`.

[67] Air Products and Chemicals Inc. *Liquid Phase Dimethyl Ether Demonstration In The Laporte Alternative Fuels Development Unit*. Jan. 2001.

[68] Wen Zhi Lu, Li Hua Teng, and Wen De Xiao. “Simulation and experiment study of dimethyl ether synthesis from syngas in a fluidized-bed reactor”. In: vol. 59. Nov. 2004, pp. 5455–5464. DOI: `10.1016/j.ces.2004.07.031`.

[69] K.M.Vanden Bussche and G.F. Froment. “A Steady-State Kinetic Model for Methanol Synthesis and the Water Gas Shift Reaction on a Commercial Cu/ZnO/Al2O3Catalyst”. In: *Journal of Catalysis* 161.1 (1996), pp. 1–10. ISSN: 0021-9517. DOI: `https://doi.org/10.1006/jcat.1996.0156`. URL: `https://www.sciencedirect.com/science/article/pii/S0021951796901566`.

[70] “Catalytic synthesis of methanol from COH2: I. Phase composition, electronic properties, and activities of the Cu/ZnO/M2O3 catalysts”. In: *Journal of Catalysis* 56.3 (1979), pp. 407–429. ISSN: 0021-9517. DOI: `https://doi.org/10.1016/0021-9517(79)90132-5`. URL: `https://www.sciencedirect.com/science/article/pii/0021951779901325`.

[71] Andrés T. Aguayo et al. “Kinetic modeling of dimethyl ether synthesis in a single step on a CuO-ZnO-Al2O3/γ-Al2O3 catalyst”. In: *Industrial and Engineering Chemistry Research* 46 (17 Aug. 2007), pp. 5522–5530. ISSN: 08885885. DOI: `10.1021/ie070269s`.

[72] Jasper Van Kampen et al. *Regeneration Conditions as the Key to Sorption Enhanced Dimethyl Ether Synthesis Highlights □ SEDMES: direct synthesis of DME from syngas by in situ H 2 O adsorption □ Steam adsorbent easily regenerated by pressure swing, without temperature swing □ Catalytic conversion and activity improve by temperature swing regeneration*.

[73] Jasper Van Kampen et al. “Sorption enhanced dimethyl ether synthesis for high efficiency carbon conversion: Modelling and cycle design”. In: *Journal of CO2 Utilization* 37 (Apr. 2020), pp. 295–308. ISSN: 22129820. DOI: `10.1016/j.jcou.2019.12.021`.

[74] Hak-Ju Kim, Heon Jung, and Kwan-Young Leet. “Effect of Water on Liquid Phase DME Synthesis from Syngas over Hybrid Catalysts Composed of Cu!ZnO/ Al 2 0 3 and y-AI 2 0 3”. In: *KoreanJ. Chern. Eng* 18 (6 2001), pp. 838–841.

[75] Ion Iliuta, Maria C. Iliuta, and Faical Larachi. “Sorption-enhanced dimethyl ether synthesis-Multiscale reactor modeling”. In: *Chemical Engineering Science* 66 (10 May 2011), pp. 2241–2251. ISSN: 00092509. DOI: `10.1016/j.ces.2011.02.047`.

[76] Jasper Van Kampen et al. “Sorption enhanced dimethyl ether synthesis under industrially relevant conditions: Experimental validation of pressure swing regeneration”. In: *Reaction Chemistry and Engineering* 6 (2 Feb. 2021), pp. 244–257. ISSN: 20589883. DOI: `10.1039/d0re00431f`.

[77] Marcello De Falco, Mauro Capocelli, and Angelo Basile. “Selective membrane application for the industrial one-step DME production process fed by CO2 rich streams: Modeling and simulation”. In: *International Journal of Hydrogen Energy* 42 (10 Mar. 2017), pp. 6771–6786. ISSN: 03603199. DOI: `10.1016/j.ijhydene.2017.02.047`.

[78] Pablo Rodriguez-Vega et al. “Experimental implementation of a catalytic membrane reactor for the direct synthesis of DME from H2+CO/CO2”. In: *Chemical Engineering Science* 234 (Apr. 2021). ISSN: 00092509. DOI: `10.1016/j.ces.2020.116396`.

[79] Clarence D Chang and Anthony J Silvestri. *The Conversion of Methanol and Other O-Compounds to Hydrocarbons over Zeolite Catalysts*. 1977, pp. 249–259.

[80] Paula Pérez-Uriarte et al. “Kinetic model for the reaction of DME to olefins over a HZSM-5 zeolite catalyst”. In: *Chemical Engineering Journal* 302 (Oct. 2016), pp. 801–810. ISSN: 13858947. DOI: `10.1016/j.cej.2016.05.096`.

[81] Steven D Phillips et al. *Gasoline from wood via integrated gasification, synthesis, and methanol-to-gasoline technologies*. Tech. rep. National Renewable Energy Lab.(NREL), Golden, CO (United States), 2011.

[82] Fengrong Chen and Victoria Satizabal. *Presentation: Fluidized bed Methanol to Gasoline (MTG): A reliable and cost-effective solution for production of renewable gasoline*. URL: `https://www.exxonmobilchemical.com/en/resources/library/library-detail/87913/mtg_afpm_fengrong_and_victoria_recorded_oct_2021`.

[83] Daniel David Tocco, Joseph Tyler Giesecke, and Sam Vincent Miraglia. *Primus Green Energy*. 2013. URL: `https://digitalcommons.wpi.edu/iqp-all`.

[84] Carlos Ortega, Volker Hessel, and Gunther Kolb. “Dimethyl ether to hydrocarbons over ZSM-5: Kinetic study in an external recycle reactor”. In: *Chemical Engineering Journal* 354 (Dec. 2018), pp. 21–34. ISSN: 13858947. DOI: `10.1016/j.cej.2018.07.178`.

[85] Patrick J Woolcock and Robert C Brown. “A review of cleaning technologies for biomass-derived syngas”. In: *Biomass and bioenergy* 52 (2013), pp. 54–84.

[86] Romualdo L. Salcedo and Mário J. Pinho. “Pilot- and industrial-scale experimental investigation of numerically optimized cyclones”. In: *Industrial and Engineering Chemistry Research* 42 (1 Jan. 2003), pp. 145–154. ISSN: 08885885. DOI: `10.1021/ie020195e`.

[87] S. D. Sharma et al. “A critical review of syngas cleaning technologies - fundamental limitations and practical problems”. In: *Powder Technology* 180 (1-2 Jan. 2008), pp. 115–121. ISSN: 00325910. DOI: `10.1016/j.powtec.2007.03.023`.

[88] Nourredine Abdoulmoumine et al. “A review on biomass gasification syngas cleanup”. In: *Applied Energy* 155 (Oct. 2015), pp. 294–307. ISSN: 03062619. DOI: `10.1016/j.apenergy.2015.05.095`.

[89] Abhimanyu Pudi et al. “Hydrogen sulfide capture and removal technologies: A comprehensive review of recent developments and emerging trends”. In: *Separation and Purification Technology* (2022), p. 121448.

[90] Bishnu P Mandal, AK Biswas, and SS Bandyopadhyay. “Selective absorption of H2S from gas streams containing H2S and CO2 into aqueous solutions of N-methyldiethanolamine and 2-amino-2-methyl-1-propanol”. In: *Separation and Purification Technology* 35.3 (2004), pp. 191–202.

[91] Laurance Reid. *Fundamentals of Low-Tonnage Sulfur Removal and Recovery*. Gas Conditioning Conference, 2017. URL: `www.merichem.com`.

[92] *Gas Cleaning and Conditioning - bioliq®*. URL: `https://www.bioliq.de/english/69.php`.

[93] N Dahmen et al. *Bioliq® Pilot Plant for the Preparation of Synthetic Fuels - Operating Experience*.

[94] J Przepiòrski. “Activated Carbon Surfaces in Environmental Remediation Activated carbon filters and their industrial applications”. In: (2006).

[95] YK Siong, J Idris, and M Atabaki. “Performance of activated carbon in water filters”. In: *Water Resources* (2013), pp. 1–19.

[96] *Activated carbon filter*. URL: `https://www.eurowater.com/en/water-treatment-plants/filtration/activated-carbon-filter`.

[97] Michele Clements and J Haarhoff. *Granular Activated Carbon Management at a Water Treatment Plant*. 2002.

[98] Dimitri Mignard and Colin Pritchard. "On the use of electrolytic hydrogen from variable renewable energies for the enhanced conversion of biomass to fuels". In: *Chemical Engineering Research and Design* 86 (5 May 2008), pp. 473–487. ISSN: 02638762. DOI: `10.1016/j.cherd.2007.12.008`.

[99] Nicolas de Fournas and Max Wei. "Techno-economic assessment of renewable methanol from biomass gasification and PEM electrolysis for decarbonization of the maritime sector in California". In: *Energy Conversion and Management* 257 (Apr. 2022). ISSN: 01968904. DOI: `10.1016/J.ENCONMAN.2022.115440`.

[100] Mohammad Ostadi et al. "Flexible methanol production process using biomass/municipal solid waste and hydrogen produced by electrolysis and natural gas pyrolysis". In: *Fuel* 334 (Feb. 2023), p. 126697. ISSN: 0016-2361. DOI: `10.1016/J.FUEL.2022.126697`.

[101] Matteo Pozzo, Andrea Lanzini, and Massimo Santarelli. "Enhanced biomass-to-liquid (BTL) conversion process through high temperature co-electrolysis in a solid oxide electrolysis cell (SOEC)". In: *Fuel* 145 (Apr. 2015), pp. 39–49. ISSN: 00162361. DOI: `10.1016/j.fuel.2014.12.066`.

[102] Hanfei Zhang et al. "Techno-economic evaluation of biomass-to-fuels with solid-oxide electrolyzer". In: *Applied Energy* 270 (July 2020). ISSN: 03062619. DOI: `10.1016/j.apenergy.2020.115113`.

[103] Emanuele Giglio et al. "Integration between biomass gasification and high-temperature electrolysis for synthetic methane production". In: *Biomass and Bioenergy* 148 (May 2021). ISSN: 18732909. DOI: `10.1016/j.biombioe.2021.106017`.

[104] Ilkka Hannula. "Co-production of synthetic fuels and district heat from biomass residues, carbon dioxide and electricity: Performance and cost analysis". In: *Biomass and Bioenergy* 74 (Mar. 2015), pp. 26–46. ISSN: 18732909. DOI: `10.1016/j.biombioe.2015.01.006`.

[105] James M Douglas. "A hierarchical decision procedure for process synthesis". In: *AIChE journal* 31.3 (1985), pp. 353–362.

[106] Maurice Stewart and Ken Arnold. *Gas Sweetening and Processing Field Manual*. Elsevier, 2011, pp. 1–140. DOI: `10.1016/b978-1-85617-982-9.00002-8`.

[107] Susan K. Marsh, Hartley Owen, and Bernard S. Wright. "Conversion of Methanol to Gasoline". US4788369A. Nov. 1987. URL: `https://patents.google.com/patent/US4788369A/en`.

[108] F Fitch and W Lee. "Methanol-to-gasoline, an alternative route to high quality gasoline". In: *SAE Transactions* (1981), pp. 4193–4207.

[109] Francis G. Dwyer and Jr. Albin Huss. "Treatment of effluent resulting from conversion of methanol to gasoline in order to decrease durene and produce distillate". US4347397A. Aug. 1982. URL: `https://patents.google.com/patent/US4347397`.

[110] Arthur W. Chester and Yung F. Chu. "Treatment of effluent resulting from conversion of methanol to gasoline in order to decrease durene and produce distillate". US4387261A. June 1983. URL: `https://patents.google.com/patent/US4387261`.

[111] Zhihai Zhang et al. *Syngas via pyrolysis-oil gasif.* 2020, pp. 729–745.

[112] F Benyahia and KE O'Neill. "Enhanced voidage correlations for packed beds of various particle shapes and sizes". In: *Particulate science and technology* 23.2 (2005), pp. 169–177.

[113] Mohammad Sadegh Parandin and Hamed Rashidi. "Deep desulfurization of natural gas by a commercial ZnO adsorbent: A mathematical study for fixed-bed reactors". In: *Journal of Natural Gas Science and Engineering* 59 (2018), pp. 116–123.

[114] Kiseok Kim and Nokuk Park. "Effect of non-steam component of steam-hydrogasifier product gas upon sulfidation of zinc oxide sorbent". In: *Korean Journal of Chemical Engineering* 27 (2010), pp. 1715–1717.

[115] Sabri Ergun. "Fluid flow through packed columns". In: *Chem. Eng. Prog.* 48.2 (1952), pp. 89–94.

[116] T Batacchi. *Mars in-situ propellant fuel production*. 2023.

[117] Emanuele Giglio et al. "Synthetic natural gas via integrated high-temperature electrolysis and methanation: Part I—Energy performance". In: *Journal of Energy Storage* 1 (2015), pp. 22–37.

[118] Sune Dalgaard Ebbesen et al. "Durable SOC stacks for production of hydrogen and synthesis gas by high temperature electrolysis". In: *International Journal of Hydrogen Energy* 36.13 (2011). Hysydays, pp. 7363–7373. ISSN: 0360-3199. DOI: `https://doi.org/10.1016/j.ijhydene.2011.03.130`. URL: `https://www.sciencedirect.com/science/article/pii/S0360319911007208`.

[119] Antonella Zaccara et al. "Renewable hydrogen production processes for the off-gas valorization in integrated steelworks through hydrogen intensified methane and methanol syntheses". In: *Metals* 10.11 (2020), p. 1535.

[120] I. Iliuta, F. Larachi, and P. Fongarland. "Dimethyl ether synthesis with in situ H2O removal in fixed-bed membrane reactor: Model and simulations". In: *Industrial and Engineering Chemistry Research* 49 (15 Aug. 2010), pp. 6870–6877. ISSN: 08885885. DOI: `10.1021/ie901726u`.

[121] MP Bernal et al. "Mordenite and ZSM-5 hydrophilic tubular membranes for the separation of gas phase mixtures". In: *Catalysis today* 56.1-3 (2000), pp. 221–227.

[122] Bernard Hayez. "Approximate Equation To Calculate Partial Pressures in a Mixture of Real Gases". In: *Journal of chemical education* 95.11 (2018), pp. 1982–1988.

[123] Constantine Tsonopoulos. "An empirical correlation of second virial coefficients". In: *AIChE Journal* 20.2 (1974), pp. 263–272.

[124] Pedro Haro et al. "Bio-syngas to gasoline and olefins via DME - A comprehensive techno-economic assessment". In: *Applied Energy* 108 (2013), pp. 54–65. ISSN: 03062619. DOI: `10.1016/j.apenergy.2013.03.015`.

[125] Linde AG. *Hydrogen Recovery by Pressure Swing Adsorption*. Tech. rep. Linde AG. URL: `https://www.linde-engineering.com/en/images/HA_H_1_1_e_09_150dpi_NB_tcm19-6130.pdf`.

[126] Thitima Chompupun et al. "Experiments, modeling and scaling-up of membrane reactors for hydrogen production via steam methane reforming". In: *Chemical Engineering and Processing-Process Intensification* 134 (2018), pp. 124–140.

[127] M Schreiner. *Research guidance studies to assess gasoline from coal by methanol-to-gasoline and sasol-type Fischer–Tropsch technologies. Final report*. Tech. rep. Mobil Research and Development Corp., Princeton, NJ (USA), 1978.

[128] Clarence D. Chang. "A kinetic model for methanol conversion to hydrocarbons". In: *Chemical Engineering Science* 35.3 (1980), pp. 619–622. ISSN: 0009-2509. DOI: `https://doi.org/10.1016/0009-2509(80)80011-X`. URL: `https://www.sciencedirect.com/science/article/pii/000925098080011X`.

[129] "Novel kinetic modelling of methanol-to-gasoline (MTG) reaction on HZSM-5 catalyst: Product distribution". In: *Journal of the Indian Chemical Society* 98.2 (2021), p. 100003. ISSN: 0019-4522. DOI: `https://doi.org/10.1016/j.jics.2021.100003`. URL: `https://www.sciencedirect.com/science/article/pii/S0019452221000030`.

[130] R Mihail et al. "A kinetic model for methanol conversion to hydrocarbons". In: *Chemical engineering science* 38.9 (1983), pp. 1581–1591.

[131] Hannes Pichler. *Optimising profits by blending butane (TIA)*. June 2015. URL: `https://www.digitalrefining.com/article/1001142/optimising-profits-by-blending-butane-ti`.

[132] Warren D Seider et al. *Product and process design principles: synthesis, analysis, and evaluation*. John Wiley & Sons, 2017.

[133] European Parliament, Council of the European Union. *Directive 2009/30/EC*. Apr. 2009. URL: `https://eur-lex.europa.eu/legal-content/EN/ALL/?uri=CELEX:32009L0030`.

[134] TA Albahri, MR Riazi, and AA Alqattan. "Octane number and aniline point of petroleum fuels". In: *Fuel Chemistry Division Preprints* 47.2 (2002), pp. 710–711.

[135] Joel Theis. *Quality Guidelines for Energy Systems Studies: Cost Estimation Methodology for NETL Assessments of Power Plant Performance-Feb 2021*. Tech. rep. National Energy Technology Laboratory (NETL), Pittsburgh, PA, Morgantown, WV …, 2021.

[136] Moein Shamoushaki et al. "Development of cost correlations for the economic assessment of power plant equipment". In: *Energies* 14.9 (2021), p. 2665.

[137] *Opbouw Brandstofprijs*. URL: `https://www.shell.nl/consumenten/shell-fuels/opbouw-brandstofprijs.html`.

[138] Qingxi Fu et al. "Syngas production via high-temperature steam/CO 2 co-electrolysis: an economic assessment". In: *Energy & Environmental Science* 3.10 (2010), pp. 1382–1397.

[139] CR Wilke. "A viscosity equation for gas mixtures". In: *The journal of chemical physics* 18.4 (1950), pp. 517–519.

[140] John H Perry. *Chemical engineers' handbook*. 1950.

[141] Emanuele Giglio et al. "Synthetic natural gas via integrated high-temperature electrolysis and methanation: Part II—Economic analysis". In: *Journal of Energy Storage* 2 (2015), pp. 64–79.

A

Appendix

A.1. DME membrane reactor model - additional equations

Density of the mixture The density of the mixture has been calculated as the weighted average of the single component densities, while the viscosity of the mixture has been computed with Wilke's method [139]:

$$\mu_{mix} = \sum_{i=1}^{n} \frac{\mu_i}{\sum_{j=1}^{n} \phi_{ij} \frac{x_j}{x_i}} \tag{A.1}$$

$$\phi_{ij} = \frac{\left(1 + \sqrt{\frac{\mu_i}{\mu_j}} \left(\frac{M_j}{M_i}\right)^{\frac{1}{4}}\right)^2}{8\left(1 + \frac{M_i}{M_j}\right)^{\frac{1}{2}}} \tag{A.2}$$

where M_i is the molecular mass of component i in [kg/kmol].
Expressions for the dynamic viscosities of the components [140]:

$$\mu_{H_2O} = 10^{-3}\left(0.008115 + 3.9343 \times 10^{-5}(T^*) - 7.1973 \times 10^{-9}(T^*)^2 + 7.2056 \times 10^{-12}(T^*)^3\right) \tag{A.3}$$

$$\mu_{CO} = 10^{-3}\left(0.016456 + 5.0435 \times 10^{-5}(T^*) - 3.4705 \times 10^{-8}(T^*)^2 + 1.7166 \times 10^{-11}(T^*)^3\right) \tag{A.4}$$

$$\mu_{CO_2} = 10^{-3}\left(0.0013799 + 4.8847 \times 10^{-5}(T^*) - 1.7863 \times 10^{-8}(T^*)^2 + 3.4755 \times 10^{-12}(T^*)^3\right) \tag{A.5}$$

$$\mu_{H_2} = 10^{-3}\left(0.0083337 + 2.2 : 2 \times 10^{-5}(T^*) - 1.1216 \times 10^{-8}(T^*)^2 + 5.1704 \times 10^{-12}(T^*)^3\right) \tag{A.6}$$

$$\mu_{DME} = 2.68 \times 10^{-7} T[^\circ K]^{0.3975} \left(1 + \frac{534}{T}\right) \tag{A.7}$$

$$\mu_{MeOH} = 3.0663 \times 10^{-7} T[^\circ K]^{0.69655} \left(1 + \frac{205}{T}\right) \tag{A.8}$$

Note that T* is the temperature in °C.

Expressions for the specific heats of the components [140]:

$$cp_{CO2} = 4.18 \cdot (10.34 + 0.00274 \cdot T + \frac{195500}{T^2}), \tag{A.9}$$

$$cp_{CO} = 4.18 \cdot (6.6 + 0.00012 \cdot T), \tag{A.10}$$

$$cp_{H2} = 4.18 \cdot (6.62 + 0.00081 \cdot T), \tag{A.11}$$

$$cp_{H2O} = 4.18 \cdot (8.22 + 0.00015 \cdot T + 1.34 \cdot 10^{-6} \cdot T^2), \tag{A.12}$$

$$cp_{MeOH} = 10^{-3} \cdot (39252 + 87900 \cdot \left(\frac{1916.5/T}{\sinh(1916.5/T)}\right)^2 + 53650 \cdot \left(\frac{896.7/T}{\cosh(896.7/T)}\right)^2), \tag{A.13}$$

$$cp_{DME} = 10^{-3} \cdot (51480 + 144200 \cdot \left(\frac{1603.4/T}{\sinh(1603.4/T)}\right)^2 + 77470 \cdot \left(\frac{725.4/T}{\cosh(725.4/T)}\right)^2), \tag{A.14}$$

Expression for the specific heat of the mixture:

$$cp_{\text{mixture}} = \sum_{i=1}^{n} x_i \cdot cp_i, \tag{A.15}$$

A.2. DME reactor Matlab code

```
function toExcel = IsoMembraneReactor(Aspen_Input)
close all

%---------Translate variables from Aspen------
N_H2_0 =  Aspen_Input(3,1); %Molar Flows in kmol/s
N_CO_0 =  Aspen_Input(1,1);
N_CO2_0 = Aspen_Input(2,1);
N_H2O_0 = Aspen_Input(4,1);
N_DME_0 = Aspen_Input(13,1);
N_MeOH_0 = Aspen_Input(14,1);
Np_sweep_0 = Aspen_Input(9,2); %Change here if you change the sweep gas!
Np_H2_0 = Aspen_Input(3,2);
Np_H2O_0 = Aspen_Input(4,2);
N_hc_0 = Aspen_Input(10,1);%initialize the inert stream and add the first HC (methane).
for hc = 15 :  40
    N_hc_0 = N_hc_0 + Aspen_Input(hc,1); %Hydrocarbon tot molar flow in kmol/s
end

T = Aspen_Input(42,1); %in K Note: from here when adding N other compounds on Aspen, add +N to the index
P_r_0 = Aspen_Input(43,1)/100000; %Arrives in Pa, translated in bar
P_p = Aspen_Input(43,2)/100000; %Arrives in Pa, translated in bar
N_syngas = Aspen_Input(41,1); %in kmol/s
N_perm =  Aspen_Input(41,2); %in kmol/s  Change here if you want to change the sweep gas
M_avg = Aspen_Input(49,1); %in kmol/kg
rho_gas = Aspen_Input(48,1); %in kg/m^3
rho_sweep = Aspen_Input(48,2); %in kg/m^3

%Mole fractions in reaction zone
x_H2_0 = N_H2_0 / N_syngas;
x_CO_0 = N_CO_0 / N_syngas;
x_CO2_0 = N_CO2_0 / N_syngas;
x_H2O_0 = N_H2O_0 / N_syngas;
x_DME_0 = N_DME_0 / N_syngas;
x_MeOH_0 = N_MeOH_0 / N_syngas;
x_hc_0 = N_hc_0/ N_syngas;

%Checks to aovid dividing by zero: replace 0 with small number
if x_H2_0 == 0
    x_H2_0 = 1e-12;
end
if x_CO_0 == 0
    x_CO_0 = 1e-12;
end
if x_CO2_0 == 0
    x_CO2_0 = 1e-12;
end
if x_H2O_0 == 0
    x_H2O_0 = 1e-12;
end
if x_DME_0 == 0
    x_DME_0 = 1e-12;
end
if x_MeOH_0 == 0
```

```
    x_MeOH_0 = 1e-12;
end

%Mole fractions in permeation zone
xp_H2O = Np_H2O_0 / N_perm;
xp_H2 = Np_H2_0 / N_perm;
xp_sweep = Np_sweep_0 / N_perm;

if xp_H2O == 0
    xp_H2O = 1e-12;
end
if xp_H2 == 0
    xp_H2 = 1e-12;
end
if xp_sweep == 0
    xp_sweep = 1e-12;
end

%Perform checks on the total mole fraction
x_sum = x_H2_0+ x_CO_0+ x_H2O_0+ x_DME_0+ x_MeOH_0+ x_CO2_0+ x_hc_0;
if x_sum ~= 1 && x_sum > 1+6*1e-12
    disp('Watch out! The sum of the molar fractions at the inlet of the reaction zone is
        different from 1.')
end

xp_sum = xp_H2O + xp_H2 + xp_sweep;
if xp_sum ~= 1 && x_sum > 1+3*1e-12
    disp('Watch out! The sum of the molar fractions at the inlet of the reaction zone is
        different from 1.')
end

%-----CONSTANTS------------%

R = 8.314;%universal gas constant in J/mol K

%Constants for the calculation of the equilibrium constants
%Reactions: CO hydrogenation = 2; CO2 hydrogenation = 1; WGS = 3; Methanol dehydration = 4
coef_keq = zeros (3,6);
coef_keq(1,1)= 21.84; %a
coef_keq(1,2)= 9.04*10^(3); %b
coef_keq(1,3)= -7.66; %c
coef_keq(1,4)= 54.07*10^(-4); %d
coef_keq(1,5)= -57.50*10^(-8); %e
coef_keq(1,6)= -6.75*10^(3);%f
coef_keq(2,1)= 18.01; %a
coef_keq(2,2)= -5.87*10^(3); %b
coef_keq(2,3)= -1.86; %c
coef_keq(2,4)= 2.70*10^(-4); %d
coef_keq(2,5)= 0; %e
coef_keq(2,6) = 58.2 * 10^(3); %f
coef_keq(3,1)= -9.76; %a
coef_keq(3,2)= 3.20*10^(3); %b
coef_keq(3,3)= 1.07; %c
coef_keq(3,4)= -6.57*10^(-4); %d
coef_keq(3,5)=4.9 *10^(-8); %e
coef_keq(3,6)=6.05*10^(3); %f

%Constants for the calculations of kinetic and adsorption constants
A_K1_bar = 35.450;
A_K2_bar = 7.3976;
A_K3_bar = 8.2894*10^4;
A_K_H2 = 0.2490;
A_K_CO2 = 1.02*10^(-7);
A_K_CO = 7.99 * 10^(-7);
B_K1_bar = 1.7069 * 10^4;
B_K2_bar = 2.0463 * 10^4;
B_K3_bar = 5.2940 * 10^4;
B_K_H2 = -3.4394 * 10^4;
B_K_CO2 = -6.74 * 10^4;
B_K_CO = -5.81 * 10^4;

```

```
% ---------Molecular masses in g/mol or kg/kmol
M_H2 = 2.016;
M_CO = 28.01;
M_N2 = 28.0134;
M_CO2 = 44.01;
M_DME = 46.07;
M_MeOH = 32.04;
M_H2O = 18.015;

M = [M_H2, M_CO, M_N2, M_CO2, M_DME, M_MeOH, M_H2O];


%---------EEND OF COEFF DEFINITION----------%

%------------- INPUT VARIABLES--------------%

GHSV = 4800; % in 1/h

%-----------Flow rates of the syngas-------------%

m_syngas = N_syngas * M_avg; %in kg/s
V_syngas = m_syngas / rho_gas; %Volume flow in m^3/s

%-----------Reactor geometry -------------------%

R_vol = V_syngas*3600 *273 * P_r_0/ (GHSV*T); %in m^3
ReaGeom = MRscaling(1, 0.024, 0.019, 0.000033376944600, V_syngas, R_vol); %Function to calculate the reactor geometry
Re = ReaGeom(1);
Ri = ReaGeom(2);
L = ReaGeom(3);
A_r = (Re^2-Ri^2)*pi;
A_sweep = pi*Ri^2; %Internal area
v_s = V_syngas / A_r;
GHSV_backcalc = 3600 * P_r_0 * 273 * v_s / (L * T);
prop = L/(Re+Ri);

% --------------Catalyst properties--------------%

void = 0.33; % Packed bed void fraction
rho_c = 1900; % Catalyst bed density in kg/m^3
dp = 0.002; % Particle diameter in meters
cat = [rho_c, void, dp];

%-------------Viscosity of the gas mixture-----------%

% Calculate viscosities in Pa.s
Mu_H2O = 10^-3 * (0.008115 + 3.9343e-5*(T - 273) - 7.1973e-9*(T - 273)^2 + 7.2056e-12*(T - 273)^3);
Mu_CO = 10^-3 * (0.016456 + 5.0435e-5*(T - 273) - 3.4705e-8*(T - 273)^2 + 1.7166e-11*(T - 273)^3);
Mu_CO2 = 10^-3 * (0.0013799 + 4.8847e-5*(T - 273) - 1.7863e-8*(T - 273)^2 + 3.4755e-12*(T - 273)^3);
Mu_H2 = 10^-3 * (0.0083337 + 2.2e-5*(T - 273) - 1.1216e-8*(T - 273)^2 + 5.1704e-12*(T - 273)^3);
Mu_DME = 2.68*10^-7 * T^0.3975 / (1 + 534/T);
Mu_MeOH = 3.0663*10^-7 * T^0.69655 / (1 + 205/T);

Mu = [Mu_H2, Mu_CO, Mu_CO2, Mu_H2O, Mu_DME, Mu_MeOH];
Mu_mix = 0;
x = [x_H2_0, x_CO_0, x_CO2_0, x_H2O_0, x_DME_0, x_MeOH_0];
for m = 1:6
    % Calculate the denominator of the Wilke method for the ith component
    denominator = 0;
    for k = 1:6
        if k ~= m
            phi_yk = ((1 + (Mu(m) / Mu(k))^(0.5) * (M(k) / M(m))^(0.25))^2) / (8 * (1 + M(m) / M(k))^(0.5));
            denominator = denominator + x(k) / phi_yk;
        end
    end
```

```
    % Add the contribution of the ith component to the average viscosity
    Mu_mix = Mu_mix + x(m) * Mu(m) / denominator;
end
%-----------Calculate minimum fluidization velocity and check-----%

v_min = ((rho_c -rho_gas)*9.81 /(150*Mu_mix) )*(void^3/(1-void))*dp^2;

if v_s > v_min
    disp('Watch out! The syngas velocity is higher than the minimum fluidization velocity.')
end

%Membrane parameters
Per_H2O = fun_perm_H2O(T)*10^2;  %Water Permeance in kmol/(s m^2 Bar)
Per_H2  = fun_perm_H2(T)*10^2;  %Hydrogen Permeance in kmol/(s m^2 Bar)
memb = [Per_H2O, Per_H2];

%Sweep gas flow: note to change the gas from N2 to CO2 or vicecersa, change
%the molecular mass

m_sweep = N_perm * M_N2; %Assume that the sweep gas is N2 and calculate its mass flow in kg/s
v_sw = m_sweep / (rho_sweep * A_sweep); %velocity of the sweep gas in m/s

%-------------Equilibrium Constants-------------%

ln_K_eq_2 = coef_keq(1,1)+ coef_keq(1,2)/T+ coef_keq(1,3)*log(T) + coef_keq(1,4)*T + coef_keq(1,5)*T^2 + coef_keq(1,6)/T^2;
K_eq_2 = exp (ln_K_eq_2); %equilibrium constant for reaction 2, methanol synthesis from CO

ln_K_eq_3 = coef_keq(2,1)+ coef_keq(2,2)/T+ coef_keq(2,3)*log(T) + coef_keq(2,4)*T + coef_keq(2,5)*T^2 + coef_keq(2,6)/T^2;
K_eq_3 = 1/exp (ln_K_eq_3); %equilibrium constant for reaction 3, water gas shift

ln_K_eq_4 = coef_keq(3,1)+ coef_keq(3,2)/T+ coef_keq(3,3)*log(T) + coef_keq(3,4)*T + coef_keq(3,5)*T^2+coef_keq(3,6)/T^2;
K_eq_4 = exp (ln_K_eq_4); %equilibrium constant for reaction 4, methanol dehydration

K_eq_1 = K_eq_2/K_eq_3; %equilibrium constant for reaction 1, methanol synthesis from CO2

%Calculate the constants at the inlet of the reactor
K1_bar = A_K1_bar * exp(-B_K1_bar/(R*T));
K2_bar = A_K2_bar * exp(-B_K2_bar/(R*T));
K3_bar= A_K3_bar * exp(-B_K3_bar/(R*T));
K_H2 = A_K_H2 * exp(-B_K_H2/(R*T));
K_CO2 = A_K_CO2 * exp(-B_K_CO2/(R*T));
K_CO = A_K_CO * exp(-B_K_CO/(R*T));

% Packing the constants into a vector
Arr_const = [K1_bar, K2_bar, K3_bar, K_H2, K_CO2, K_CO, K_eq_1, K_eq_3, K_eq_4];

% Define the specific heat functions in J/mol K
cpCO2 = 4.18 .* (10.34 + 0.00274 * T + 195500 / T^2);
cpCO = 4.18 .* (6.6 + 0.00012 * T);
cpH2 = 4.18 .* (6.62 + 0.00081 * T);
cpH2O = 4.18 .* (8.22 + 0.00015 * T + 1.34 * 10^-6 * T^2);
cpMeOH = 10^-3 .* (39252 + 87900 * ((1916.5/T) / sinh(1916.5/T))^2 + 53650 * ((896.7 /T)/cosh(896.7/T))^2);
cpDME = 10^-3 .* (51480 + 144200 * ((1603.4/T) / sinh(1603.4/T))^2 + 77470 * ((725.4 /T)/cosh(725.4/T))^2);


% Define the range of z over which to solve ODEs
zspan = [0 L];

% Define initial conditions:
y0 = [N_H2O_0, N_H2_0, N_CO_0, N_CO2_0, N_MeOH_0, N_DME_0, N_hc_0, Np_H2O_0, Np_H2_0, Np_sweep_0, P_r_0];

%---------------------SOLVE ODEs------------------------%

% Solve the ODEs
options = odeset('RelTol',1e-10,'AbsTol',1e-12);
```

```
[z, N] = ode15s(@(z, y) mrODEs(z, y, Re, Ri, T, v_s, P_p, cat, memb, Arr_const, M, Mu), zspan
    , y0, options);

% Calculate the mole fractions
% Unpack molar flow rates from the solution
N_H2O = N(:,1);
N_H2 = N(:,2);
N_CO = N(:,3);
N_CO2 = N(:,4);
N_MeOH = N(:,5);
N_DME = N(:,6);
N_hc = N(:,7);
Np_H2O = N(:,8);
Np_H2 = N(:, 9);
Np_sweep = N(:,10);
P_r = N(:,11);

% Calculate total molar flow rate
N_total = N_H2O + N_H2 + N_CO + N_CO2 + N_MeOH + N_DME + N_hc;
Np_total = Np_H2O + Np_H2 + Np_sweep;

% Calculate mole fractions
x_H2O = N_H2O ./ N_total;
x_H2 = N_H2 ./ N_total;
x_CO = N_CO ./ N_total;
x_CO2 = N_CO2 ./ N_total;
x_MeOH = N_MeOH ./ N_total;
x_DME = N_DME ./ N_total;
x_hc = N_hc ./ N_total;
xp_H2O = Np_H2O./Np_total;
xp_H2 = Np_H2./Np_total;
xp_sweep = Np_sweep./Np_total;

% Plot the concentration profiles of the products along the reactor length
figure;
hold on
plot(z, x_H2O, 'b-', z, x_DME, 'r-', z, x_MeOH, 'm-');
xlim([0 L]);
ylim([0 1]);
xlabel('z [m]');
ylabel('Mole fraction');
legend('H_2O', 'DME', 'MeOH');

% Plot the concentration profiles of the reactants along the reactor length
figure;
hold on
plot(z, x_H2, 'r-', z, x_CO, 'g-', z, x_CO2, 'b-', z, x_hc);
xlim([0 L]);
ylim([0 1]);
xlabel('z [m]');
ylabel('Mole fraction');
legend('H2', 'CO', 'CO2');

% Plot the concentration profiles along the reactor length in the permeation zone
figure;
hold on
plot(z, xp_H2O, 'b-',z, xp_H2, 'r-');
xlim([0 L]);
ylim([0 1]);
xlabel('z [m]');
ylabel('Mole fraction');
legend('H2O','H2');

%------------------Heat of reaction-------------%
%First, integrate the cps over dT to obtain the heat of raction at the reaction temperature
%Define the functions for the specific heats in J/mol K

fun_cpCO2 = @(T) 4.18 .* (10.34 + 0.00274 .* T + 195500 ./ T.^2);
fun_cpCO = @(T) 4.18 .* (6.6 + 0.00012 .* T);
fun_cpH2 = @(T) 4.18 .* (6.62 + 0.00081 .* T);
fun_cpDME = @(T) 10^-3 .* (51480 + 144200 .* ((1603.4./T) ./ sinh(1603.4./T)).^2 + 77470 .*
```

```
    ((725.4 ./T)./cosh(725.4./T)).^2);

% Define the function to integrate
f = @(T) fun_cpDME(T) + fun_cpCO2(T) - 3 .* fun_cpCO(T) - 3 .* fun_cpH2(T);

% Perform the integration from 298 to T
Integr = integral(f, 298, T); % in J/mol

%Calculate the reaction heat
DeltaH0DME = -258.3*10^3; %in J/mol
DeltaH = DeltaH0DME + Integr; %in J/mol
Q_reac =  N(6) *1000 * DeltaH; %in J/s
% Calculate the average cp of the mixture at each grid point
cp_mixture = x_CO2 .* cpCO2 + x_CO .* cpCO + x_H2 .* cpH2 + x_H2O .* cpH2O + x_MeOH .* cpMeOH + x_DME .* cpDME;
cp_avg = mean(cp_mixture);
DeltaT = -Q_reac/(cp_avg * N_syngas(end)*1000);

%Prepare the vector to be passed to Excel
Temp = T;
T_hot = T + DeltaT;
Pres_r = P_r(end);
Pres_p = P_p;
totmolflow_r = N_total(end);
totmolflow_p = Np_total(end);
mfr_H2 = x_H2(end);
mfr_CO = x_CO(end);
mfr_CO2 = x_CO2(end);
mfr_DME = x_DME(end);
mfr_MeOH = x_MeOH(end);
mfr_H2O = x_H2O(end);
mfp_N2 = xp_sweep(end);
mfp_H2 = xp_H2(end);
mfp_H2O = xp_H2O(end);
vap_frac = 1;
Y_DME = 2* N_DME(end) / (N_CO_0 + N_CO2_0);
S_DME = 2* N_DME(end) / (2*N_DME(end)+ N_MeOH(end));
X_CO_x = (N_CO2_0+N_CO_0-N_CO2(end)-N_CO(end))/(N_CO_0+N_CO2_0);

toExcel = [Temp; Pres_r; Pres_p; totmolflow_r; totmolflow_p; mfr_H2; mfr_CO; mfr_CO2; mfr_DME; mfr_MeOH; mfr_H2O; mfp_N2; mfp_H2; mfp_H2O; vap_frac; Y_DME; S_DME; X_CO_x; T_hot; L; Re; Ri; prop; v_s;];

end

function ReaGeom = MRscaling(L1, Re1, Ri1, Vfl1, Vfl2, V2)
%Function to calculate the reactor geometry. It takes as inputs the
%length, external and internal radii from the base case, volume flow rate
%of the base case and volume flow rate of the new case and the new reactor
%volume

    % Calculate k1 k2 and k3
    V1 = L1 * pi * (Re1^2 - Ri1^2); %Reaction zone volume of the base case
    A_r1 = pi*(Re1^2-Ri1^2); %Cross sectional area of the base case
    A_m1 = 2 * pi * Ri1 * L1; %Membrane area of the base case
    ratio = V1/A_m1;
    A_r2 = A_r1 * (Vfl2/Vfl1)/10; %the velocity is ten times the base case velocity
    L2 = V2/A_r2;
    A_m2 = V2/ratio;
    Ri2 = A_m2/(2*pi*L2);
    Re2 = sqrt(A_r2/pi + Ri2^2);

    % Solve the system
    ReaGeom = [Re2,Ri2,L2];

end

function dydz = mrODEs(z, y, Re, Ri, T, v_s, P_p, cat, memb, Arr_const, M, Mu)
    % Here you define your ODEs

    %Unpack coefficients;
```

```
    M_H2 = M(1);
    M_CO = M(2);
    M_N2 = M(3);
    M_CO2 = M(4);
    M_MeOH = M(5);
    M_DME = M(6);
    M_H2O = M(7);

    % Unpacking the constants
    K1_bar = Arr_const(1);
    K2_bar = Arr_const(2);
    K3_bar = Arr_const(3);
    K_H2 = Arr_const(4);
    K_CO2 = Arr_const(5);
    K_CO = Arr_const(6);
    K_eq_1 = Arr_const(7);
    K_eq_3 = Arr_const(8);
    K_eq_4 = Arr_const(9);

    R = 8.314; %universal gas constant in J/mol K

    % Unpack catalyst properties:
    rho_c = cat(1);
    void = cat(2);
    dp = cat(3);

    % Unpack membrane properties
    Per_H2O = memb(1);
    Per_H2 = memb(2);

    % unpack y
    % Reaction zone
    N_H2O = y(1);
    N_H2 = y(2);
    N_CO = y(3) ;
    N_CO2 = y(4);
    N_MeOH = y(5);
    N_DME = y(6);
    N_hc = y(7);
    N_total = N_H2O + N_H2 + N_CO + N_CO2 + N_MeOH+ N_DME + N_hc;

    %Permeation zone
    Np_H2O  = y(8);
    Np_H2 = y(9);
    Np_sweep = y(10);
    Np_total = Np_H2O + Np_H2 + Np_sweep;

    %Pressure
    P_r = y(11);

    %Update mole fractions
    x_H2O = N_H2O/N_total;
    x_H2 = N_H2/N_total;
    x_CO = N_CO/N_total;
    x_CO2 = N_CO2/N_total;
    x_MeOH = N_MeOH/N_total;
    x_DME = N_DME/N_total;
    x_hc = N_hc/N_total;

    xp_H2O = Np_H2O/Np_total;
    xp_H2 = Np_H2/Np_total;
    xp_sweep = Np_sweep/Np_total;

    %Checks to aovid dividing by zero: replace 0 with small number
    if x_H2 == 0
        x_H2 = 1e-12;
    end
    if x_CO == 0
        x_CO = 1e-12;
    end
    if x_CO2 == 0
```

```
        x_CO2 = 1e-12;
    end
    if x_H2O == 0
        x_H2O = 1e-12;
    end
    if x_DME == 0
        x_DME = 1e-12;
    end
    if x_MeOH == 0
        x_MeOH = 1e-12;
    end
    if xp_H2O == 0
        xp_H2O = 1e-12;
    end
    if xp_H2 == 0
        xp_H2 = 1e-12;
    end
    if xp_sweep == 0
        xp_sweep = 1e-12;
    end

        x_sum = x_H2+ x_CO+ x_H2O+ x_DME+ x_MeOH + x_CO2+ x_hc;
    if x_sum ~= 1 && x_sum > 1+6*1e-10
        disp('Watch out! The sum of the molar fractions at the inlet of the reaction zone is different from 1.')
    end


    %Update dynamic viscosity, based on the new composition
    Mu_mix = 0;
    x = [x_H2, x_CO, x_CO2, x_H2O, x_DME, x_MeOH];
    for m = 1:6
        % Calculate the denominator of the Wilke method for the ith component
        denominator = 0;
        for k = 1:6
            if k ~= m
                phi_yk = ((1 + (Mu(m) / Mu(k))^(0.5) * (M(k) / M(m))^(0.25))^2) / (8 * (1 + M(m) / M(k))^(0.5));
                denominator = denominator + x(k) / phi_yk;
            end
        end
        % Add the contribution of the ith component to the average viscosity
        Mu_mix = Mu_mix + x(m) * Mu(m) / denominator;
    end

    %Calculate the second virial coefficients at z=0- calculations based on Tsonopoulos;

    molefractions_r = [x_CO, x_CO2, x_H2, x_H2O, x_DME, x_MeOH]; % Mole fractions of CO, CO2, H2, H2O, DME, and MeOH
    Bmix_r = calculate_Bmix(T, molefractions_r); %Calculates the 2nd virial coefficient for the mixture in the reaction, gives back a number
    Bimix_r = calculate_Bimix(T, molefractions_r); %Calculates the 2nd virial coefficient for each component in the reaction zone, gives back an array: Bimix(1) is for CO, Bimix(6) is for MeOH

    %note: if the sweep changes from CO2 to N2 you have to change the parameters in the Tsonopoulos_Bij_p function!

    molefractions_p = [xp_H2O, xp_H2, xp_sweep]; % Mole fractions of H2O, H2, sweep gas CO2, in permeation zone.
    Bmix_p = calculate_Bmix(T, molefractions_p); %Calculates the 2nd virial coefficient for the mixture in the permeation zone, gives back a number
    Bimix_p = calculate_Bimix(T, molefractions_p); %Calculates the 2nd virial coefficient for each component in the permeation zone, gives back an array: Bimix(1) is for H2O, Bimix(3) is for CO2 (sweep=).

    %Update gas density
    M_avg =x_H2 * M_H2 + x_CO * M_CO + x_CO2 * M_CO2 + x_H2O * M_H2O + x_DME * M_DME + x_MeOH * M_MeOH;
    rho_gas = (P_r * 1e5)*M_avg/(1000*T*R);

```

```
    %Partial pressures
    P_CO = P_r * x_CO*((R*T + Bimix_r(1)*P_r*10^5)/(R*T + Bmix_r*P_r*10^5)) ;
    P_CO2 = P_r * x_CO2*((R*T + Bimix_r(2)*P_r*10^5)/(R*T + Bmix_r*P_r*10^5));
    P_H2 = P_r * x_H2*((R*T + Bimix_r(3)*P_r*10^5)/(R*T + Bmix_r*P_r*10^5));
    P_H2O = P_r * x_H2O*((R*T + Bimix_r(4)*P_r*10^5)/(R*T + Bmix_r*P_r*10^5));
    P_DME = P_r * x_DME*((R*T + Bimix_r(5)*P_r*10^5)/(R*T + Bmix_r*P_r*10^5));
    P_MeOH = P_r * x_MeOH*((R*T + Bimix_r(6)*P_r*10^5)/(R*T + Bmix_r*P_r*10^5));

    Pp_H2O = P_p * xp_H2O*((R*T + Bimix_p(1)*P_p*10^5)/(R*T + Bmix_p*P_p*10^5));
    Pp_H2 = P_p * xp_H2 *((R*T + Bimix_p(2)*P_p*10^5)/(R*T + Bmix_p*P_p*10^5));

    %Update molar flow through membrane
    J_H2O = Per_H2O * (P_H2O-Pp_H2O); %in kmol/(s * m^2)
    J_H2 = Per_H2 * (P_H2-Pp_H2); %in kmol/(s * m^2)

    %Update reaction rates in kmol / (kg_cat s)
    r_1 = K1_bar * (P_CO2 * P_H2 * (1-P_MeOH * P_H2O/(K_eq_1 * P_CO2 * P_H2^3))) / (1+K_CO2 * P_CO2+K_CO * P_CO + sqrt(K_H2*P_H2))^3;
    r_2 = K2_bar * (P_H2O-(P_CO2*P_H2/(K_eq_3*P_CO)))/(1+K_CO2*P_CO2+K_CO*P_CO+sqrt(K_H2*P_H2));
    r_3 = K3_bar * (P_MeOH^2/P_H2O - P_DME/K_eq_4);

    % ------------Derivatives----------------------%
    %reaction zone
    dN_H2Odz = rho_c*(1-void)*pi* (Re^2-Ri^2)*(r_1 - r_2+ r_3)- J_H2O*2*pi*Ri;
    dN_H2dz = -rho_c*(1-void)*pi*(Re^2-Ri^2)*(3*r_1-r_2)-J_H2*2*pi*Ri;
    dN_COdz = -rho_c*(1-void)*pi*(Re^2-Ri^2)*r_2;
    dN_CO2dz = -rho_c*(1-void)*pi*(Re^2-Ri^2)*(r_1-r_2);
    dN_MeOHdz = rho_c*(1-void)*pi*(Re^2-Ri^2)*(r_1-2*r_3);
    dN_DMEdz = rho_c* (1-void)* pi* (Re^2-Ri^2)*r_3;
    dN_hcdz = 0;

    %permeation zone
    dNp_H2Odz = J_H2O*2*pi*Ri;
    dNp_H2dz = J_H2*2*pi*Ri;
    dNp_sweepdz = 0;

    %Pressure
    dP_rdz = -10^(-5)*((150*Mu_mix*(1-void)^2 * v_s)/(void^3*dp^2) + (1.75*(1-void)*rho_gas* v_s^2)/(void^3*dp));

    % Pack the derivatives into a column vector
    dydz = [dN_H2Odz; dN_H2dz; dN_COdz; dN_CO2dz; dN_MeOHdz; dN_DMEdz; dN_hcdz; dNp_H2Odz; dNp_H2dz; dNp_sweepdz; dP_rdz];
end

function Per_H2 = fun_perm_H2(T)
    % Input: T - temperature in K
    % Output: Per_H2 - value of Per_H2 for given temperature

      % Given data points
    T_data = [473, 523, 573];
    Per_H2_data = [0.096e-7, 0.128e-7, 0.24e-7];

    % Calculate the coefficients for the two lines
    m1 = (Per_H2_data(2) - Per_H2_data(1)) / (T_data(2) - T_data(1));
    b1 = Per_H2_data(1) - m1 * T_data(1);

    m2 = (Per_H2_data(3) - Per_H2_data(2)) / (T_data(3) - T_data(2));
    b2 = Per_H2_data(2) - m2 * T_data(2);

    % Calculate the value of Per_H2O for the given temperature
    if T >= T_data(1) && T <= T_data(2)
        Per_H2 = m1 * T + b1;
    elseif T > T_data(2) && T <= T_data(3)
        Per_H2 = m2 * T + b2;
    else
        error('Temperature must be within the range of given T_data points.')
    end
end

```

```
function Per_H2O = fun_perm_H2O(T)
    % Input: T - temperature in K
    % Output: Per_H2O - value of Per_H2O for given temperature

      % Given data points
    T_data = [473, 523, 573];
    Per_H2O_data = [5e-7, 4e-7, 1.5e-7];

    % Calculate the coefficients for the two lines
    m1 = (Per_H2O_data(2) - Per_H2O_data(1)) / (T_data(2) - T_data(1));
    b1 = Per_H2O_data(1) - m1 * T_data(1);

    m2 = (Per_H2O_data(3) - Per_H2O_data(2)) / (T_data(3) - T_data(2));
    b2 = Per_H2O_data(2) - m2 * T_data(2);

    % Calculate the value of Per_H2O for the given temperature
    if T >= T_data(1) && T <= T_data(2)
        Per_H2O = m1 * T + b1;
    elseif T > T_data(2) && T <= T_data(3)
        Per_H2O = m2 * T + b2;
    else
        error('T= %i\n;  Temperature must be within the range of given T_data points.')
    end
end

function Bimix = calculate_Bimix(T, composition)
    % Calculate the second virial coefficients matrix (Bij)
    if length(composition) == 6
        Bij_matrix = Tsonopoulos_r(T);
    elseif length(composition) == 3
        Bij_matrix = Tsonopoulos_p(T);
    else
        fprintf('There is something wrong')
    end

    % Calculate Bimix for each component
    Bimix = zeros(1, length(composition));
    for i = 1:length(composition)
        for j = 1:length(composition)
            Bimix(i) = Bimix(i) + composition(j) * Bij_matrix(i, j);
        end
    end
end

function Bmix = calculate_Bmix(T, composition)
    % Calculate the second virial coefficients matrix (Bij)
    if length(composition) == 6
         Bij_matrix = Tsonopoulos_r(T);
    elseif length(composition) == 3
         Bij_matrix = Tsonopoulos_p(T);
    else
        fprintf('There is something wrong')
    end

    % Calculate Bmix
    Bmix = 0;
    for i = 1:length(composition)
        for j = 1:length(composition)
            Bmix = Bmix + composition(i) * composition(j) * Bij_matrix(i, j);
        end
    end
end

function Bij = Tsonopoulos_p(T)
    % Define the components' critical properties and acentric factors
    % [Tc (K), Pc (Pa), acentric factor, vc(cm^3/mol), a, b]

    H2O  = [647.10, 2.21e7, 0.344, 56, 0.0279, 0.0229];
    H2   = [33.19, 1.30e6, -0.219, 65, 0, 0];
    CO2  = [304.13, 7.39e6, 0.228, 94, 0, 0];

```

```
    components = [H2O; H2; CO2];
    R = 8.314; % Gas constant (J/(mol*K))

    n_components = size(components, 1);
    Bij = zeros(n_components);

    for i = 1:n_components
        for j = 1:n_components
            if i~=j %non-diagonal components
            %calculate critical temperature, pressure, and accentric factor
            Tcij = sqrt(components(i, 1) * components(j, 1)); %Uses simple mixing rules neglect kij for now
            Pcij = 4*Tcij*(components(i, 2)*components(i, 4)/components(i, 1)+components(j, 2)*components(j, 4)/components(j, 1))/((components(i, 4)^(1/3))+components(j, 4)^(1/3))^3;
            Omij = (components(i, 3) + components(j, 3)) / 2;

            % Calculate a and b parameters. Note: for polar/non polar Bij
            % is assumed to have no polar term. Thus aij and bij = 0
            aij=0;
            if components(i, 5) ~= 0 && components(j,5) ~= 0
                aij = 0.5 * (components(i, 5) + components(j,5));
            end
            bij=0;
            if components(i, 6) ~= 0 && components(j,6) ~= 0
                bij = 0.5 * (components(i, 6) + components(j,6));
            end

            else
                Tcij = components(i, 1);
                Pcij = components(i, 2);
                Omij = components(i, 3);
                aij = components(i, 5);
                bij = components(i, 6);
            end

            Tr = T/Tcij;
            f2 = aij/Tr^6 - bij/Tr^8;
            f1 = 0.0637 + 0.331/Tr^2 - 0.423/Tr^3 - 0.008/Tr^8;
            f0 = 0.1445 - 0.330/Tr - 0.1385/Tr^2 - 0.0121/Tr^3 - 0.000607/Tr^8;

            % Calculate the second virial coefficient (Bij), units:
            % m^3/mol
            Bij(i, j) = (R*Tcij/Pcij) * (f0 + f1*Omij + f2);


        end
    end
end


function Bij = Tsonopoulos_r(T)
    % Define the components' critical properties and acentric factors
    % [Tc (K), Pc (Pa), acentric factor, vc(cm^3/mol), a, b]

    CO   = [134.45, 3.77e6, 0.049, 93, 0, 0];
    CO2  = [304.13, 7.39e6, 0.228, 94, 0, 0];
    H2   = [33.19, 1.30e6, -0.219, 65, 0, 0];
    H2O  = [647.10, 2.21e7, 0.344, 56, 0.0279, 0.0229];
    DME  = [400.00, 5.34e6, 0.200, 167, -0.01513, 0];
    MeOH = [513.00, 8.10e6, 0.564, 114, 0.0878, 0.0560];

    components = [CO; CO2; H2; H2O; DME; MeOH];
    R = 8.314; % Gas constant (J/(mol*K))

    n_components = size(components, 1);
    Bij = zeros(n_components);

    for i = 1:n_components
        for j = 1:n_components
            if i~=j %non-diagonal components
```

```
            %calculate critical temperature, pressure, and accentric factor
            Tcij = sqrt(components(i, 1) * components(j, 1)); %Uses simple mixing rules neglect kij for now
            Pcij = 4*Tcij*(components(i, 2)*components(i, 4)/components(i, 1)+components(j, 2)*components(j, 4)/components(j, 1))/((components(i, 4)^(1/3))+components(j, 4)^(1/3))^3;
            Omij = (components(i, 3) + components(j, 3)) / 2;

            % Calculate a and b parameters. Note: for polar/non polar Bij
            % is assumed to have no polar term. Thus aij and bij = 0
            aij=0;
            if components(i, 5) ~= 0 && components(j,5) ~= 0
                aij = 0.5 * (components(i, 5) + components(j,5));
            end
            bij=0;
            if components(i, 6) ~= 0 && components(j,6) ~= 0
                bij = 0.5 * (components(i, 6) + components(j,6));
            end

            else
                Tcij = components(i, 1);
                Pcij = components(i, 2);
                Omij = components(i, 3);
                aij = components(i, 5);
                bij = components(i, 6);
            end

            Tr = T/Tcij;
            f2 = aij/Tr^6 - bij/Tr^8;
            f1 = 0.0637 + 0.331/Tr^2 - 0.423/Tr^3 - 0.008/Tr^8;
            f0 = 0.1445 - 0.330/Tr - 0.1385/Tr^2 - 0.0121/Tr^3 - 0.000607/Tr^8;

            % Calculate the second virial coefficient (Bij), units:
            % m^3/mol
            Bij(i, j) = (R*Tcij/Pcij) * (f0 + f1*Omij + f2);


        end
    end
end
```

A.3. Matlab GHSV optimization code

```
% Define the function
functionValue = @(Aspen_Input, GHSV) IsoMembraneReactor(Aspen_Input, GHSV);

% Initialize variables
maxValue = -Inf;
maxGHSV = -1;
optimizedValues = [];

% Loop over GHSV values
for GHSV = 2000:100:10000
    % Compute the function value
    currentFunctionValue = functionValue(Aspen_Input, GHSV);

    % Check if the current value is greater than the maximum value
    if currentFunctionValue > maxValue
        maxValue = currentFunctionValue;
        maxGHSV = GHSV;
    end

    % Store the optimized values for plotting
    optimizedValues = [optimizedValues, currentFunctionValue];
end

% Display the maximum value and corresponding GHSV
disp("Maximum value: " + maxValue);
disp("Corresponding GHSV: " + maxGHSV);
```

```

% Plot the optimized values versus GHSV
GHSVValues = 2000:100:10000;
plot(GHSVValues, optimizedValues, 'b.-');
xlabel('GHSV [1/h]');
ylabel('DME yield');
ylim([0.5 0.8]);
title('DME Yield versus GHSV');
grid on;
```

A.4. Visual Basic code for software communication

Note: This code was primarily sourced from the "usertemplate" Excel file provided by Aspen Plus, and it is accessible via the Developer tab in Excel. However, it has been tailored to function optimally with our specific files and needs.

```

"""
'Global to hold the current block id.  Set in AspenStartIteration, and
'cleared in AspenEndIteration.
Dim g_blockId As String

Public Function AspenCalculate() As String
'Called to solve the model for the given inputs.  Called after writing out all of the input data.
'By default we just call Calculate.  If you are writing VBA code to solve your model call it from here.

MLPutRanges
MLEvalString "toExcel = IdealNonIsoMembraneReactor(Aspen_Input);"
MLGetMatrix "toExcel", "Aspen_Output!G2"
MatlabRequest

Calculate
AspenCalculate = ""

'Range("aspen_output").Value = 20.5
'AspenCalculate = "This is an error in calc"
End Function

Public Function AspenStartIteration(blockId As String) As String
'Called at the start of each iteration of the model, before the model
'gets calculated.
g_blockId = blockId
AspenStartIteration = ""
End Function

Public Function AspenEndIteration() As String
'Called at the end of each iteration of the model, after the model has been calculated.

'If you want to save the last table of data to a uniquely named sheet, this would be the place to do it.
'The following line will create a sheet called Aspen_Output_B2, if the block id is B2, and copy all of
'the data currently held in the Aspen_Output sheet.
CopySheetForBlock "Output", g_blockId
AspenEndIteration = ""
End Function

Public Function AspenEndRun(runid As String)
'Called when the Aspen Plus engine is quitting, after all blocks have been processed.  The runid is
'passed from the engine.  You may want to use the runid as part of the filename if saving the sheet at the
'end of a run.

'To save at the end of a run comment out the following
ThisWorkbook.Save
AspenEndRun = ""
End Function
```

```

Private Function GetSheet(sheetName As String) As Worksheet
'Create the sheet if it is not already there.
On Error Resume Next
Set GetSheet = Nothing
Set GetSheet = Worksheets(sheetName)
If Err = 9 Then 'subscript out of range
    Err.Clear
    On Error GoTo 0
    Set GetSheet = Worksheets.Add
    GetSheet.Name = sheetName
End If
End Function

Private Sub CopySheetForBlock(sheetNameToCopy As String, blockName As String)
Dim sheetNameForBlock As String
Dim sheetToCopy As Worksheet
Dim sheetForBlock As Worksheet

Set sheetToCopy = Worksheets("Aspen_" & sheetNameToCopy)
sheetNameForBlock = "Aspen_" & sheetNameToCopy & "_" & blockName
Set sheetForBlock = GetSheet(sheetNameForBlock)
sheetToCopy.UsedRange.Copy
sheetForBlock.Range("A1").PasteSpecial Paste:=xlPasteValues
End Sub

Public Function ahtest() As Integer
Dim testSheet As Worksheet

Set testSheet = GetSheet("Aspen_TestMacros")
testSheet.Cells.Clear

' Write out all the counts
testSheet.Cells(1, 1).Value = "Number of Input Streams:"
testSheet.Cells(1, 2).Value = ahNumStreams([aspen_input])

testSheet.Cells(2, 1).Value = "Number of Ouput Streams:"
testSheet.Cells(2, 2).Value = ahNumStreams([Aspen_Output])

testSheet.Cells(3, 1).Value = "Number of Components:"
testSheet.Cells(3, 2).Value = ahNumComps([aspen_input])

testSheet.Cells(4, 1).Value = "Number of Integer Parameters:"
testSheet.Cells(4, 2).Value = ahNumParams([Aspen_IntParams])

testSheet.Cells(5, 1).Value = "Number of Real Parameters:"
testSheet.Cells(5, 2).Value = ahNumParams([Aspen_RealParams])

' Write out all the input stream data
Dim rowNum As Integer
rowNum = 7
Dim n As Integer
For n = 1 To ahNumStreams([aspen_input])
    testSheet.Cells(rowNum, n + 1).Value = ahStreamName([aspen_input], n)
Next n

For n = 1 To ahNumComps([aspen_input])
    testSheet.Cells(rowNum + n, 1).Value = ahCompName([aspen_input], n)
Next n

n = 8 + ahNumComps([aspen_input])
testSheet.Cells(n, 1).Value = "FLOW"
testSheet.Cells(n + 1, 1).Value = "TEMP"
testSheet.Cells(n + 2, 1).Value = "PRES"

Dim i As Integer
Dim j As Integer

For i = 1 To ahNumStreams([aspen_input])
    For j = 1 To ahNumComps([aspen_input])
        testSheet.Cells(rowNum + j, i + 1).Value = ahGetValue([aspen_input], j, i)
```

```
    Next j
Next i

n = 8 + ahNumComps([aspen_input])

For i = 1 To ahNumStreams([aspen_input])
    testSheet.Cells(n, i + 1).Value = ahGetValue([aspen_input], j, i)
    testSheet.Cells(n + 1, i + 1).Value = ahGetValue([aspen_input], j + 1, i)
    testSheet.Cells(n + 2, i + 1).Value = ahGetValue([aspen_input], j + 2, i)
Next i

test = 1
End Function
Public Function ahGetValue(r As Range, row As Variant, Optional col As Variant) As Variant
If VarType(row) = vbString Then
    row = FindRowFromHeader(r, row)
End If
If IsMissing(col) Then
    col = 1
ElseIf VarType(col) = vbString Then
    col = FindColFromHeader(r, col)
End If
ahGetValue = r.Cells(row, col)
End Function
Public Sub ahSetValue(r As Range, row As Variant, col As Variant, vNewValue As Variant)
If VarType(row) = vbString Then
    row = FindRowFromHeader(r, row)
End If
If VarType(col) = vbString Then
    col = FindColFromHeader(r, col)
End If
r.Cells(row, col) = vNewValue
End Sub
Public Function FindRowFromHeader(r As Range, row As Variant)
FindRowFromHeader = 0
With r
    Dim i As Integer
    For i = 1 To .rows.Count
        If .Cells(i, 0).Value = row Then
            FindRowFromHeader = i
            Exit For
        End If
    Next i
End With
End Function
Public Function FindColFromHeader(r As Range, col As Variant)
FindColFromHeader = 0
With r
    Dim i As Integer
    For i = 1 To .Columns.Count
        If .Cells(0, i).Value = col Then
            FindColFromHeader = i
            Exit For
        End If
    Next i
End With
End Function

Public Function ahCompName(r As Range, compNum As Integer) As String
ahCompName = r.Cells(compNum, 0)
End Function
Public Function ahStreamName(r As Range, streamNum As Integer) As String
ahStreamName = r.Cells(0, streamNum)
End Function

Public Function ahNumParams(r As Range) As Integer
ahNumParams = r.rows.Count
End Function
Public Function ahNumStreams(r As Range) As Integer
ahNumStreams = r.Columns.Count
End Function
```

```
Public Function ahNumComps(r As Range) As Integer
ahNumComps = r.rows.Count - 9
End Function
```

B

Aspen Plus Simulations

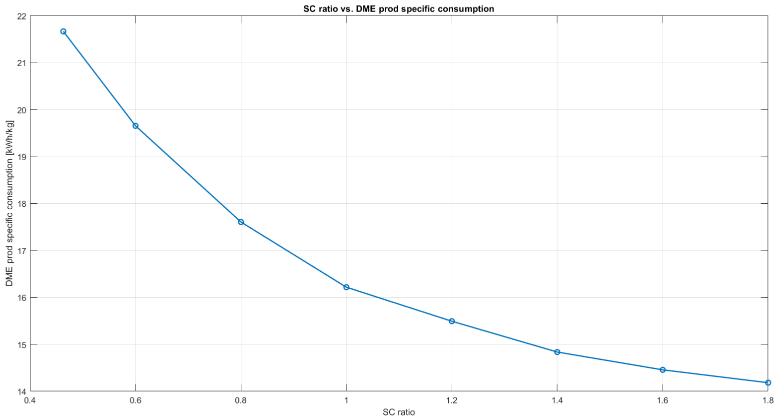

Figure B.3: Effect of the SC ratio on the DME specific consumption

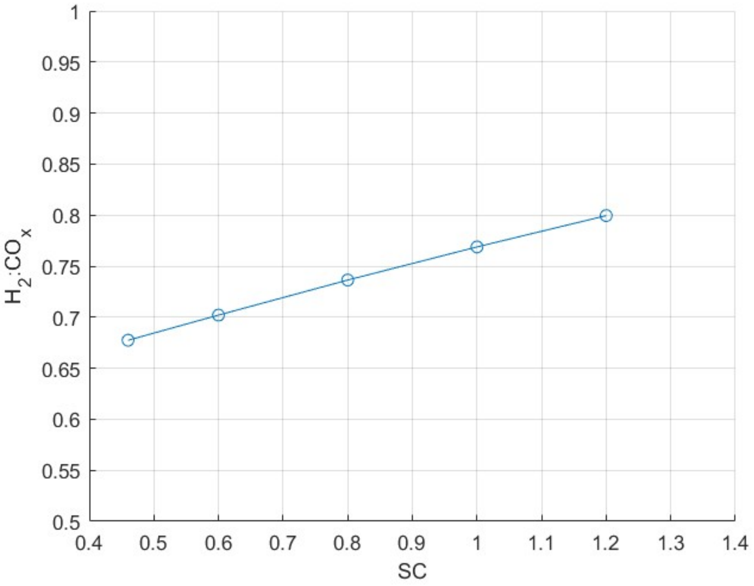

Figure B.4: Effect of the SC ratio on the H_2:CO_x ratio

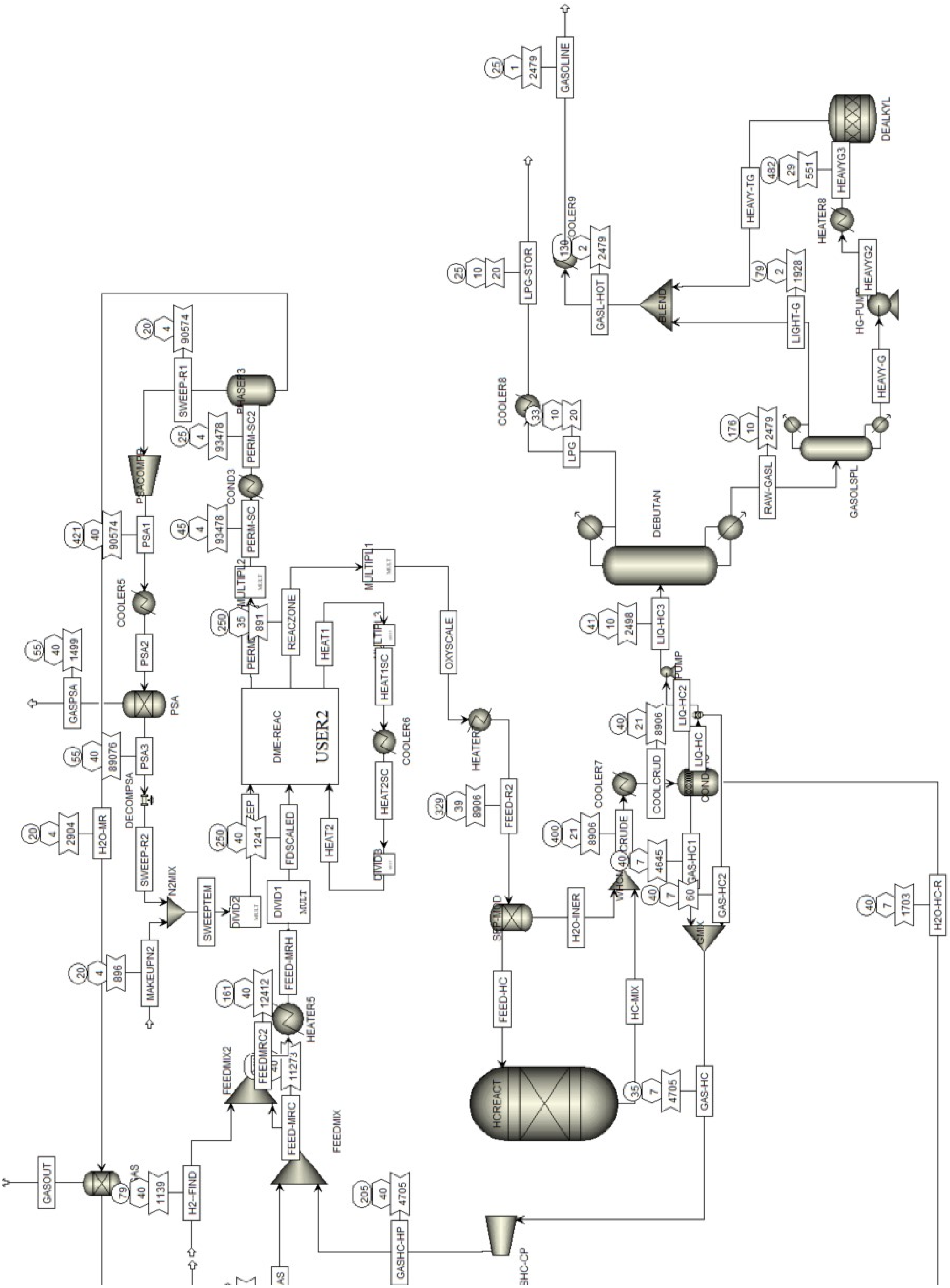

Figure B.1: Main flowsheet: part 2

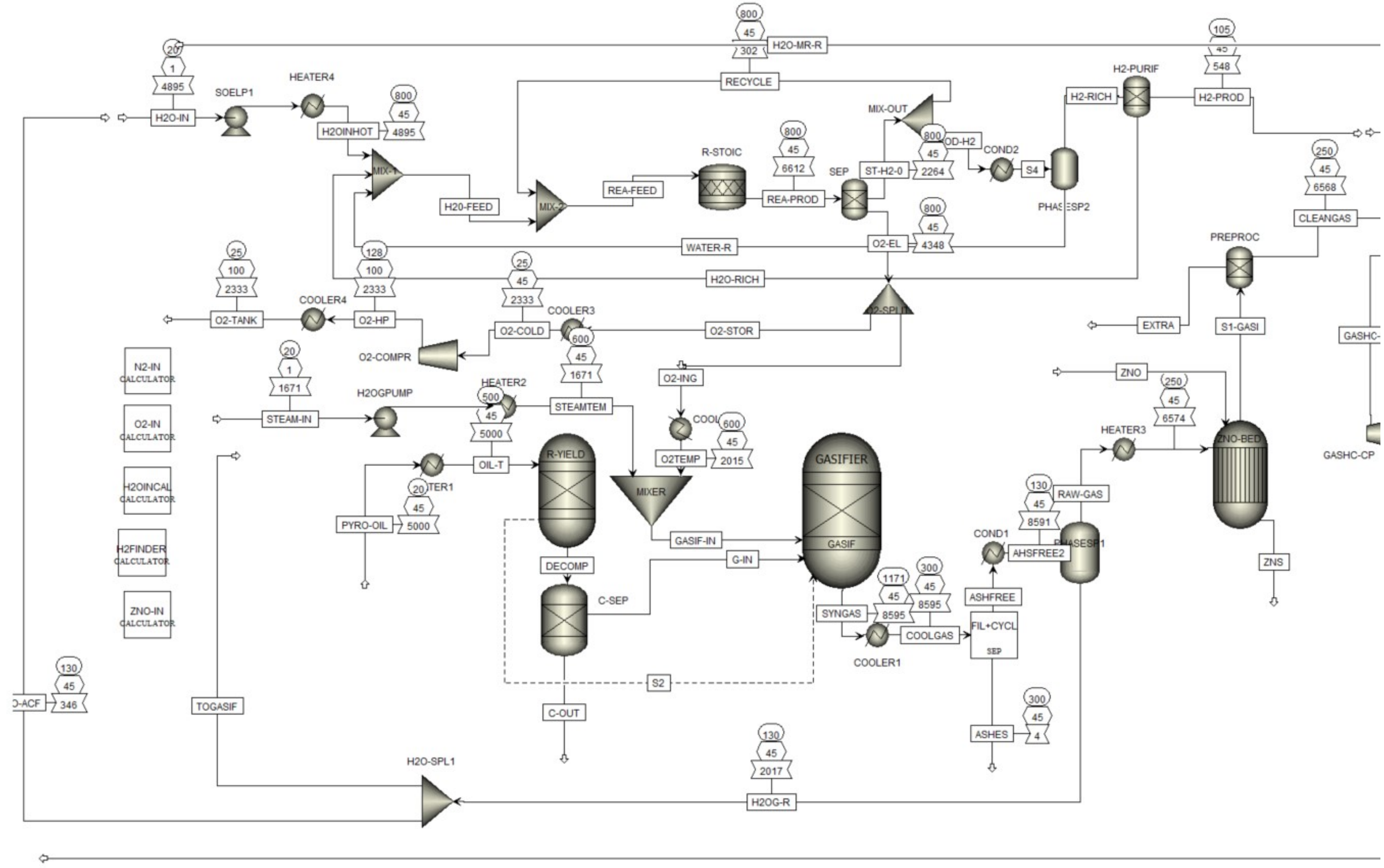

Figure B.2: Main flowsheet: part 1

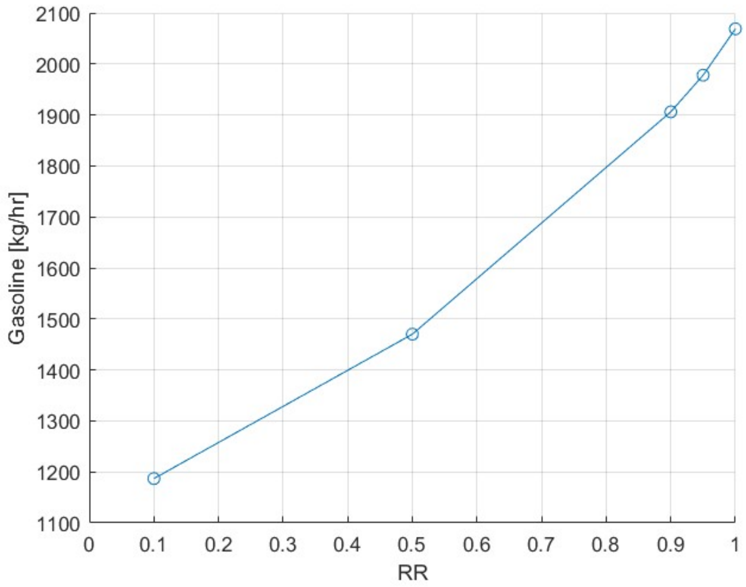

Figure B.5: Effect of the recycle rate on the gasoline yield of the plant.

B.1. Aspen Plus streams summary

In the two following tables, an overview of the most important mass flows is reported. The total mass flow is reported as well as the single component mass flows.

Table B.1: Stream overview from the Aspen Plus flowsheet. Mass flows in **kg/hr**

Location **Stream Name**	After gasifier SYNGAS	After SOEL stack REA-PROD	Before DME reactor FEED-MRH	After DME reactor OXYSCALE	After DME to HC reactor CRUDE	Before Debutanizer LIQ-HC3
Total	8594.94	0.00	12412.25	8905.81	8905.81	2498.32
CO	3670.61	0.00	4195.66	525.15	525.15	0
CO2	2180.82	0.00	4933.24	2753.95	2753.95	0
H2	291.04	632.09	1583.78	153.32	153.32	0
H2O	2442.74	1631.81	475.07	52.97	1750.56	0
O2	0	4347.65	0	0	0	0
H2S	0.19	0	0	0	0	0
C	0	0	0	0	0	0
S	0	0	0	0	0	0
BIOOIL	0	0	0	0	0	0
ASH	3.55	0	0	0	0	0
N2	1.97	0	0	0	0	0
CH4	4.02	0	22.65	22.65	22.75	0.10
ZNO	0	0	0	0	0	0
ZNS	0	0	0	0	0	0
DME	0	0	0	4064.95	0	0
MEOH	0	0	0	130.96	0	0
ETHANE	0	0	14.80	14.80	15.16	0.37
ETHYLENE	0	0	0	0	0	0
PROPANE	0	0	161.54	161.54	174.39	12.85
PROPENE	0	0	7.08	7.08	7.58	0.51
N-BUTANE	0	0	81.43	81.43	102.36	20.93
I-BUTANE	0	0	275.33	275.33	326.03	50.70
BUTENE	0	0	34.03	34.03	41.70	7.67
PENTANE	0	0	282.84	282.84	508.00	225.16
PENTENE	0	0	85.87	85.87	140.27	54.40
HEXANE	0	0	145.70	145.70	489.05	343.35
HEXENE	0	0	27.54	27.54	83.40	55.87
HEPTANE	0	0	28.15	28.15	219.88	191.73
HEPTENE	0	0	10.17	10.17	75.82	65.66
OCTANE	0	0	3.11	3.11	60.66	57.55
I-OCTANE	0	0	10.26	10.26	72.03	61.77
OCTENE	0	0	10.41	10.41	181.97	171.56
NONANE	0	0	0.65	0.65	34.12	33.47
NONENE	0	0	1.86	1.86	83.40	81.54
BENZENE	0	0	1.86	1.86	7.58	5.72
TOLUENE	0	0	6.48	6.48	68.24	61.76
ETHYLBEN	0	0	0.68	0.68	18.96	18.27
XYLENE	0	0	8.32	8.32	318.45	310.13
124TMB	0	0	3.06	3.06	375.31	372.26
1245TETR	0	0	0.43	0.43	159.22	158.79
1235TETR	0	0	0.06	0.06	22.75	22.69
1234TETR	0	0	0.22	0.22	113.73	113.51

Table B.2: Stream overview from the Aspen Plus flowsheet. Mass flows in **kg/hr**

Location	Debutanizer bottoms	Debutanizer distillate	Gasolsplit bottoms	Gasolsplit distillate	After Dealkylation reactor	Gasoline
Stream Name	RAW-GASL	LPG	HEAVY-G	LIGHT-G	HEAVY-TG	GASOLINE
Total	0	8594.94	12412.25	8905.81	8905.81	2498.32
CO	0	3670.61	4195.66	525.15	525.15	0
CO2	0	2180.82	4933.24	2753.95	2753.95	0
H2	632.09	291.04	1583.78	153.32	153.32	0
H2O	1631.81	2442.74	475.07	52.97	1750.56	0
O2	4347.65	0	0	0	0	0
H2S	0	0.19	0	0	0	0
C	0	0	0	0	0	0
S	0	0	0	0	0	0
BIOOIL	0	0	0	0	0	0
ASH	0	3.55	0	0	0	0
N2	0	1.97	0	0	0	0
CH4	0	4.02	22.65	22.65	22.75	0.10
ZNO	0	0	0	0	0	0
ZNS	0	0	0	0	0	0
DME	0	0	0	4064.95	0	0
MEOH	0	0	0	130.96	0	0
ETHANE	0	0	14.80	14.80	15.16	0.37
ETHYLENE	0	0	0	0	0	0
PROPANE	0	0	161.54	161.54	174.39	12.85
PROPENE	0	0	7.08	7.08	7.58	0.51
N-BUTANE	0	0	81.43	81.43	102.36	20.93
I-BUTANE	0	0	275.33	275.33	326.03	50.70
BUTENE	0	0	34.03	34.03	41.70	7.67
PENTANE	0	0	282.84	282.84	508.00	225.16
PENTENE	0	0	85.87	85.87	140.27	54.40
HEXANE	0	0	145.70	145.70	489.05	343.35
HEXENE	0	0	27.54	27.54	83.40	55.87
HEPTANE	0	0	28.15	28.15	219.88	191.73
HEPTENE	0	0	10.17	10.17	75.82	65.66
OCTANE	0	0	3.11	3.11	60.66	57.55
I-OCTANE	0	0	10.26	10.26	72.03	61.77
OCTENE	0	0	10.41	10.41	181.97	171.56
NONANE	0	0	0.65	0.65	34.12	33.47
NONENE	0	0	1.86	1.86	83.40	81.54
BENZENE	0	0	1.86	1.86	7.58	5.72
TOLUENE	0	0	6.48	6.48	68.24	61.76
ETHYLBEN	0	0	0.68	0.68	18.96	18.27
XYLENE	0	0	8.32	8.32	318.45	310.13
124TMB	0	0	3.06	3.06	375.31	372.26
1245TETR	0	0	0.43	0.43	159.22	158.79
1235TETR	0	0	0.06	0.06	22.75	22.69
1234TETR	0	0	0.22	0.22	113.73	113.51

C

Heat Integration

C.1. Overview and Temperature Interval Method

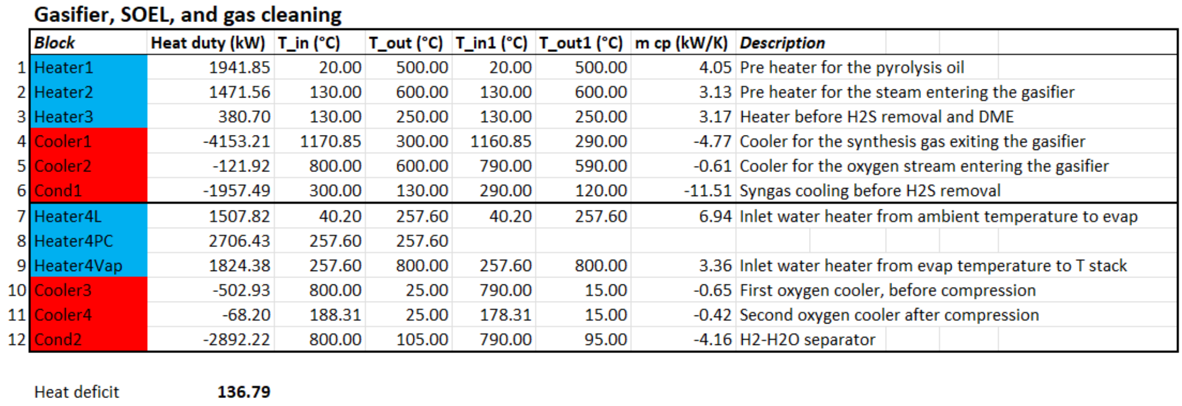

Gasifier, SOEL, and gas cleaning

	Block	Heat duty (kW)	T_in (°C)	T_out (°C)	T_in1 (°C)	T_out1 (°C)	m cp (kW/K)	*Description*
1	Heater1	1941.85	20.00	500.00	20.00	500.00	4.05	Pre heater for the pyrolysis oil
2	Heater2	1471.56	130.00	600.00	130.00	600.00	3.13	Pre heater for the steam entering the gasifier
3	Heater3	380.70	130.00	250.00	130.00	250.00	3.17	Heater before H2S removal and DME
4	Cooler1	-4153.21	1170.85	300.00	1160.85	290.00	-4.77	Cooler for the synthesis gas exiting the gasifier
5	Cooler2	-121.92	800.00	600.00	790.00	590.00	-0.61	Cooler for the oxygen stream entering the gasifier
6	Cond1	-1957.49	300.00	130.00	290.00	120.00	-11.51	Syngas cooling before H2S removal
7	Heater4L	1507.82	40.20	257.60	40.20	257.60	6.94	Inlet water heater from ambient temperature to evap
8	Heater4PC	2706.43	257.60	257.60				
9	Heater4Vap	1824.38	257.60	800.00	257.60	800.00	3.36	Inlet water heater from evap temperature to T stack
10	Cooler3	-502.93	800.00	25.00	790.00	15.00	-0.65	First oxygen cooler, before compression
11	Cooler4	-68.20	188.31	25.00	178.31	15.00	-0.42	Second oxygen cooler after compression
12	Cond2	-2892.22	800.00	105.00	790.00	95.00	-4.16	H2-H2O separator

Heat deficit **136.79**

Figure C.1: Heat integration: overview of the hot and cold streams present in the first part of the plant

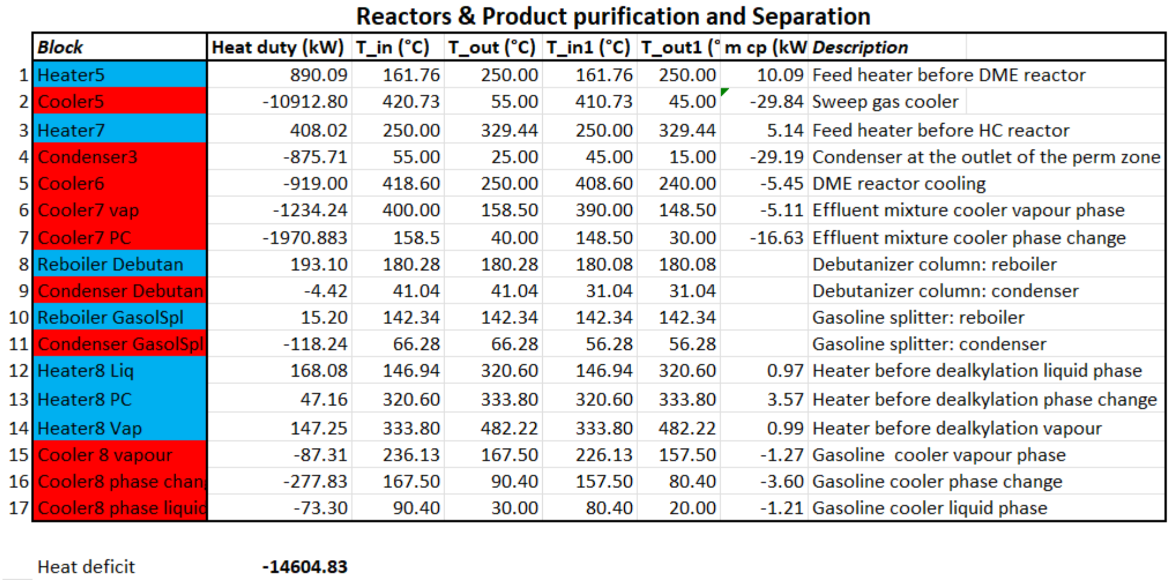

Reactors & Product purification and Separation

	Block	Heat duty (kW)	T_in (°C)	T_out (°C)	T_in1 (°C)	T_out1 (°	m cp (kW	*Description*
1	Heater5	890.09	161.76	250.00	161.76	250.00	10.09	Feed heater before DME reactor
2	Cooler5	-10912.80	420.73	55.00	410.73	45.00	-29.84	Sweep gas cooler
3	Heater7	408.02	250.00	329.44	250.00	329.44	5.14	Feed heater before HC reactor
4	Condenser3	-875.71	55.00	25.00	45.00	15.00	-29.19	Condenser at the outlet of the perm zone
5	Cooler6	-919.00	418.60	250.00	408.60	240.00	-5.45	DME reactor cooling
6	Cooler7 vap	-1234.24	400.00	158.50	390.00	148.50	-5.11	Effluent mixture cooler vapour phase
7	Cooler7 PC	-1970.883	158.5	40.00	148.50	30.00	-16.63	Effluent mixture cooler phase change
8	Reboiler Debutan	193.10	180.28	180.28	180.08	180.08		Debutanizer column: reboiler
9	Condenser Debutan	-4.42	41.04	41.04	31.04	31.04		Debutanizer column: condenser
10	Reboiler GasolSpl	15.20	142.34	142.34	142.34	142.34		Gasoline splitter: reboiler
11	Condenser GasolSpl	-118.24	66.28	66.28	56.28	56.28		Gasoline splitter: condenser
12	Heater8 Liq	168.08	146.94	320.60	146.94	320.60	0.97	Heater before dealkylation liquid phase
13	Heater8 PC	47.16	320.60	333.80	320.60	333.80	3.57	Heater before dealkylation phase change
14	Heater8 Vap	147.25	333.80	482.22	333.80	482.22	0.99	Heater before dealkylation vapour
15	Cooler 8 vapour	-87.31	236.13	167.50	226.13	157.50	-1.27	Gasoline cooler vapour phase
16	Cooler8 phase chan	-277.83	167.50	90.40	157.50	80.40	-3.60	Gasoline cooler phase change
17	Cooler8 phase liquid	-73.30	90.40	30.00	80.40	20.00	-1.21	Gasoline cooler liquid phase

Heat deficit **-14604.83**

Figure C.2: Heat integration: overview of the hot and cold streams present in the second part of the plant

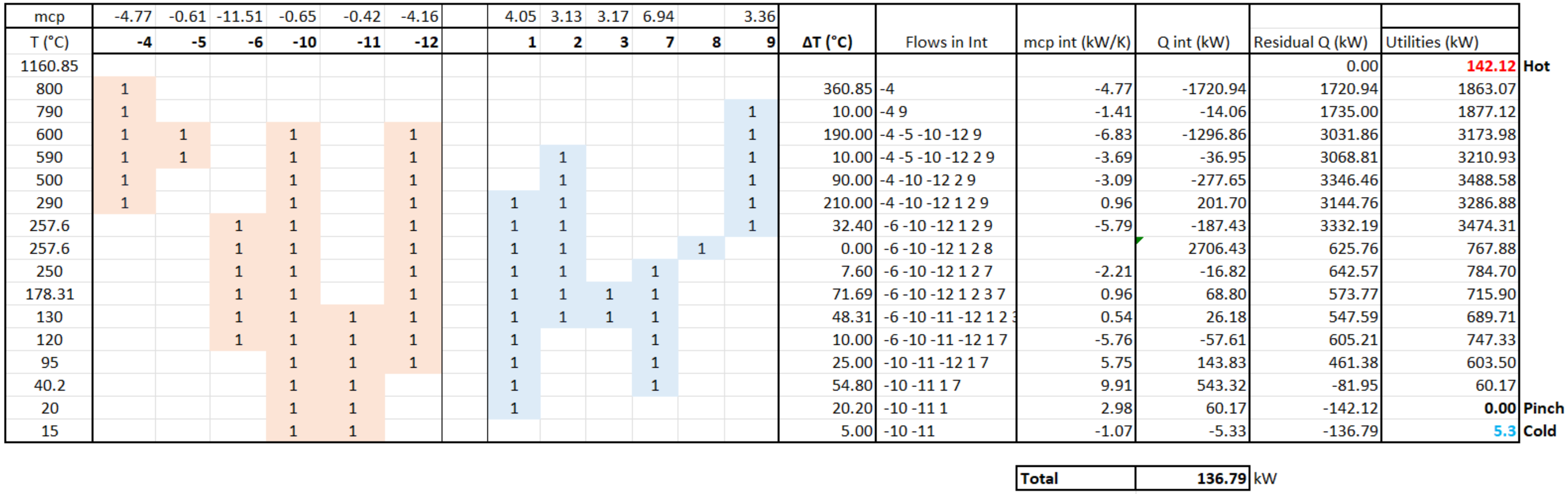

mcp	-4.77	-0.61	-11.51	-0.65	-0.42	-4.16		4.05	3.13	3.17	6.94		3.36							
T (°C)	**-4**	**-5**	**-6**	**-10**	**-11**	**-12**		**1**	**2**	**3**	**7**	**8**	**9**	**ΔT (°C)**	Flows in Int	mcp int (kW/K)	Q int (kW)	Residual Q (kW)	Utilities (kW)	
1160.85																		0.00	142.12	**Hot**
800	1													360.85	-4	-4.77	-1720.94	1720.94	1863.07	
790	1												1	10.00	-4 9	-1.41	-14.06	1735.00	1877.12	
600	1	1		1		1							1	190.00	-4 -5 -10 -12 9	-6.83	-1296.86	3031.86	3173.98	
590	1	1		1		1			1				1	10.00	-4 -5 -10 -12 2 9	-3.69	-36.95	3068.81	3210.93	
500	1			1		1			1				1	90.00	-4 -10 -12 2 9	-3.09	-277.65	3346.46	3488.58	
290	1			1		1		1	1				1	210.00	-4 -10 -12 1 2 9	0.96	201.70	3144.76	3286.88	
257.6			1	1		1		1	1				1	32.40	-6 -10 -12 1 2 9	-5.79	-187.43	3332.19	3474.31	
257.6			1	1		1		1	1			1		0.00	-6 -10 -12 1 2 8		2706.43	625.76	767.88	
250			1	1		1		1	1		1			7.60	-6 -10 -12 1 2 7	-2.21	-16.82	642.57	784.70	
178.31			1	1		1		1	1	1	1			71.69	-6 -10 -12 1 2 3 7	0.96	68.80	573.77	715.90	
130			1	1	1	1		1	1	1	1			48.31	-6 -10 -11 -12 1 2	0.54	26.18	547.59	689.71	
120			1	1	1	1		1			1			10.00	-6 -10 -11 -12 1 7	-5.76	-57.61	605.21	747.33	
95				1	1	1		1			1			25.00	-10 -11 -12 1 7	5.75	143.83	461.38	603.50	
40.2				1	1			1			1			54.80	-10 -11 1 7	9.91	543.32	-81.95	60.17	
20				1	1			1						20.20	-10 -11 1	2.98	60.17	-142.12	**0.00**	**Pinch**
15				1	1									5.00	-10 -11	-1.07	-5.33	-136.79	5.3	**Cold**

Total	**136.79**	kW

Figure C.3: Heat integration: cascade diagram of the first part of the plant

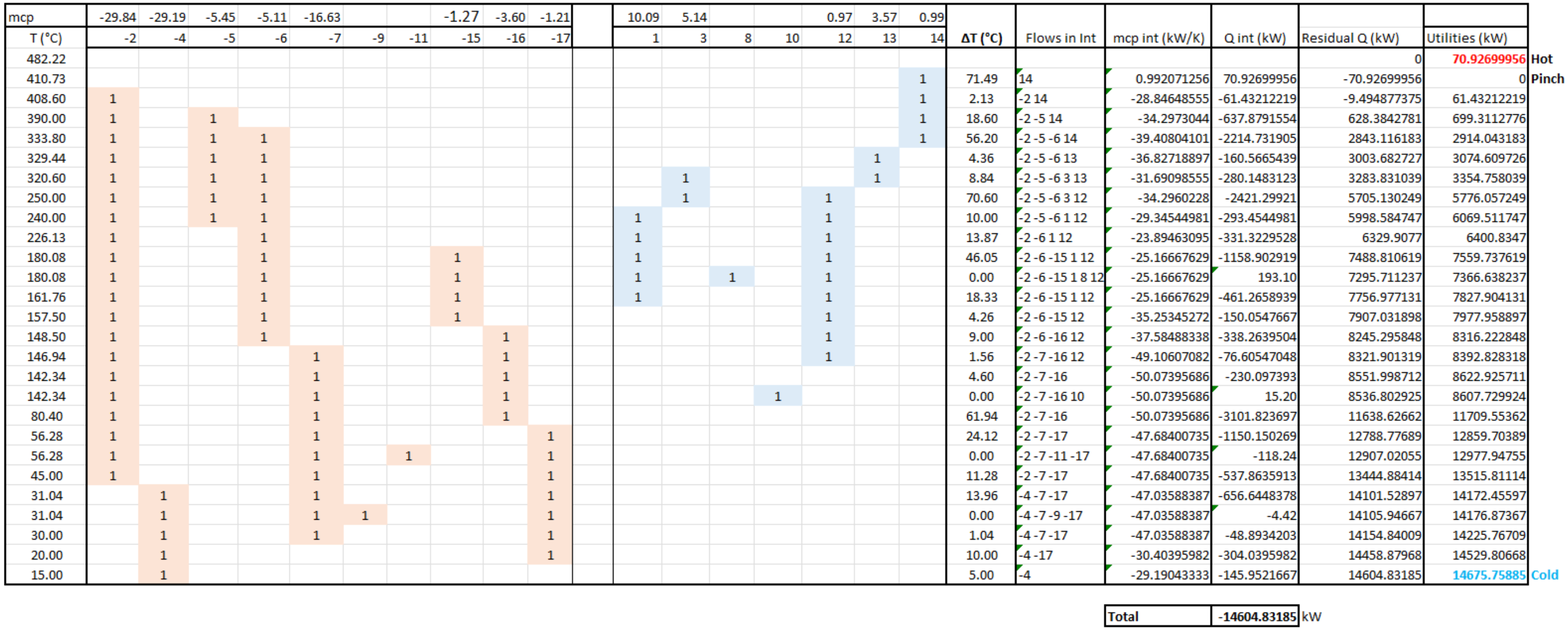

mcp	-29.84	-29.19	-5.45	-5.11	-16.63			-1.27	-3.60	-1.21		10.09	5.14			0.97	3.57	0.99							
T (°C)	-2	-4	-5	-6	-7	-9	-11	-15	-16	-17		1	3	8	10	12	13	14	ΔT (°C)	Flows in Int	mcp int (kW/K)	Q int (kW)	Residual Q (kW)	Utilities (kW)	
482.22																							0	70.92699956	Hot
410.73																		1	71.49	14	0.992071256	70.92699956	-70.92699956	0	Pinch
408.60	1																	1	2.13	-2 14	-28.84648555	-61.43212219	-9.494877375	61.43212219	
390.00	1		1															1	18.60	-2 -5 14	-34.2973044	-637.8791554	628.3842781	699.3112776	
333.80	1		1	1														1	56.20	-2 -5 -6 14	-39.40804101	-2214.731905	2843.116183	2914.043183	
329.44	1		1	1													1		4.36	-2 -5 -6 13	-36.82718897	-160.5665439	3003.682727	3074.609726	
320.60	1		1	1									1				1		8.84	-2 -5 -6 3 13	-31.69098555	-280.1483123	3283.831039	3354.758039	
250.00	1		1	1									1			1			70.60	-2 -5 -6 3 12	-34.2960228	-2421.29921	5705.130249	5776.057249	
240.00	1		1	1								1				1			10.00	-2 -5 -6 1 12	-29.34544981	-293.4544981	5998.584747	6069.511747	
226.13	1			1								1				1			13.87	-2 -6 1 12	-23.89463095	-331.3229528	6329.9077	6400.8347	
180.08	1			1				1				1				1			46.05	-2 -6 -15 1 12	-25.16667629	-1158.902919	7488.810619	7559.737619	
180.08	1			1				1				1		1		1			0.00	-2 -6 -15 1 8 12	-25.16667629	193.10	7295.711237	7366.638237	
161.76	1			1				1				1				1			18.33	-2 -6 -15 1 12	-25.16667629	-461.2658939	7756.977131	7827.904131	
157.50	1			1				1								1			4.26	-2 -6 -15 12	-35.25345272	-150.0547667	7907.031898	7977.958897	
148.50	1			1					1							1			9.00	-2 -6 -16 12	-37.58488338	-338.2639504	8245.295848	8316.222848	
146.94	1				1				1							1			1.56	-2 -7 -16 12	-49.10607082	-76.60547048	8321.901319	8392.828318	
142.34	1				1				1										4.60	-2 -7 -16	-50.07395686	-230.097393	8551.998712	8622.925711	
142.34	1				1				1						1				0.00	-2 -7 -16 10	-50.07395686	15.20	8536.802925	8607.729924	
80.40	1				1				1										61.94	-2 -7 -16	-50.07395686	-3101.823697	11638.62662	11709.55362	
56.28	1				1					1									24.12	-2 -7 -17	-47.68400735	-1150.150269	12788.77689	12859.70389	
56.28	1				1		1			1									0.00	-2 -7 -11 -17	-47.68400735	-118.24	12907.02055	12977.94755	
45.00	1				1					1									11.28	-2 -7 -17	-47.68400735	-537.8635913	13444.88414	13515.81114	
31.04		1			1					1									13.96	-4 -7 -17	-47.03588387	-656.6448378	14101.52897	14172.45597	
31.04		1			1	1				1									0.00	-4 -7 -9 -17	-47.03588387	-4.42	14105.94667	14176.87367	
30.00		1			1					1									1.04	-4 -7 -17	-47.03588387	-48.8934203	14154.84009	14225.76709	
20.00		1								1									10.00	-4 -17	-30.40395982	-304.0395982	14458.87968	14529.80668	
15.00		1																	5.00	-4	-29.19043333	-145.9521667	14604.83185	14675.75885	Cold

Total	-14604.83185	kW

Figure C.4: Heat integration: cascade diagram of the second part of the plant

C.2. Composite curves

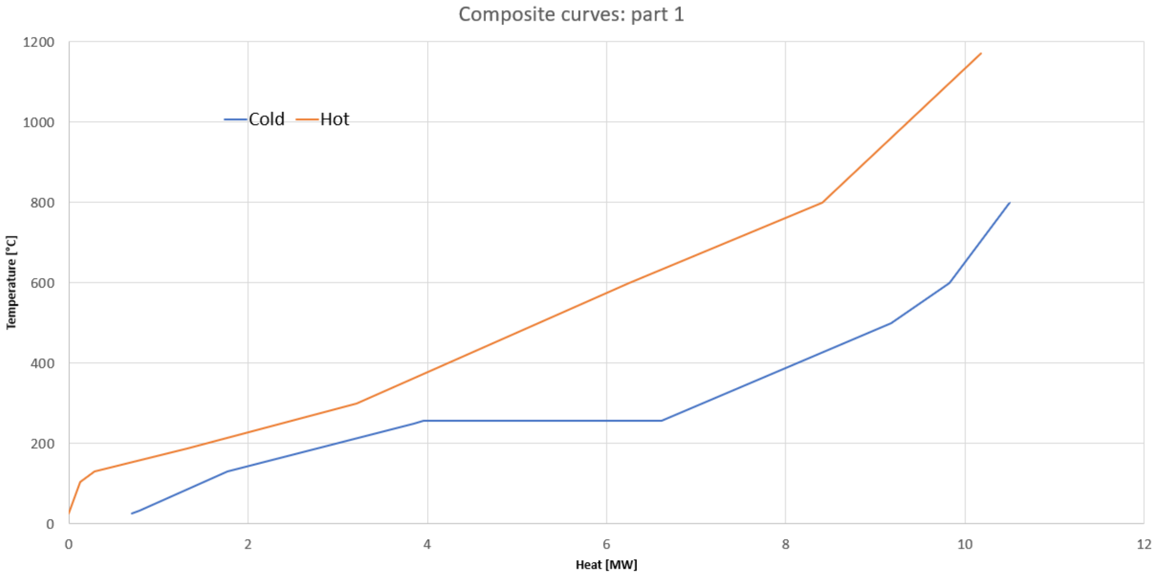

Figure C.5: Heat integration: composite curves of the first part of the plant

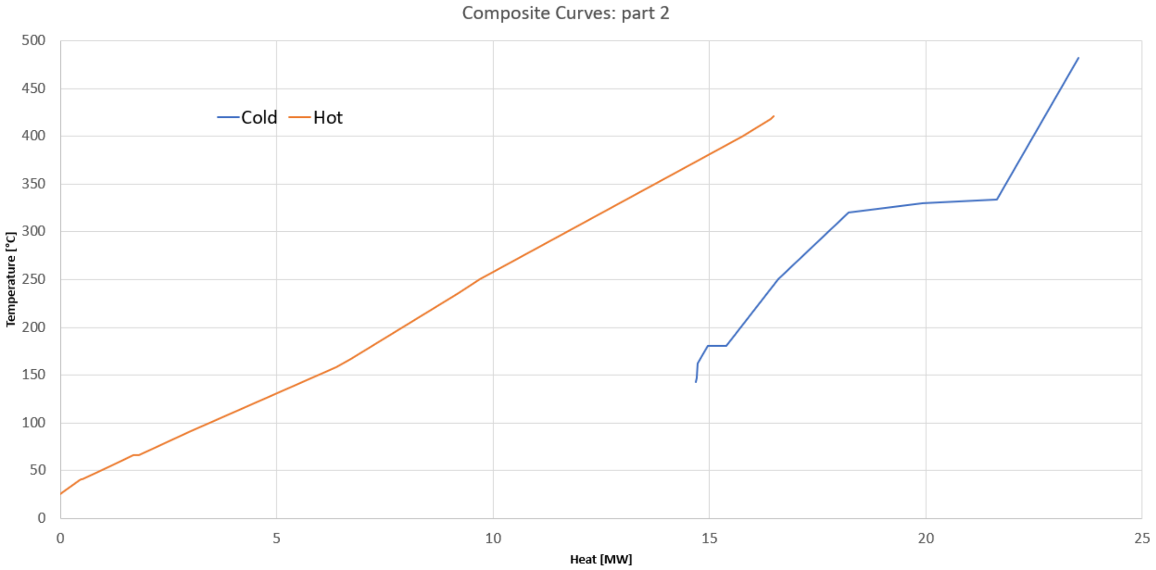

Figure C.6: Heat integration: composite curves of the second part of the plant

C.3. Heat Exchanger Network

C.4. Heat Exchangers Ovevrview

Heat exchangers have been designed with a minimum temperature approach of 10°C.
Shell and tube heat exchangers have been selected.
The temperature differences at the inlet ($\Delta 1$) and at the outlet ($\Delta 2$) are:

$$\Delta T_1 = T_{hot,in} - T_{cold,out} \tag{C.1}$$

$$\Delta T_2 = T_{hot,out} - T_{cold,in} \tag{C.2}$$

The logarithmic mean temperature difference (LMTD) is computed from the following equation:

$$LMTD = \frac{\Delta T_1 - \Delta T_2}{ln(\frac{\Delta T_1}{\Delta T_2})} \tag{C.3}$$

The correction factor F is calculated as:

$$F = \frac{\sqrt{R^2+1} \cdot \ln\left(\frac{1-S}{1-RS}\right)}{(R-1) \cdot \ln\left(\frac{2-S(R+1-\sqrt{R^2+1})}{2-S(R+1+\sqrt{R^2+1})}\right)} \tag{C.4}$$

Where R and S are expressed as:

$$R = \frac{T_{hot,in} - T_{hot,out}}{T_{cold,out} - T_{cold,in}} \tag{C.5}$$

$$S = \frac{T_{cold,out} - T_{cold,in}}{T_{hot,in} - T_{cold,out}} \tag{C.6}$$

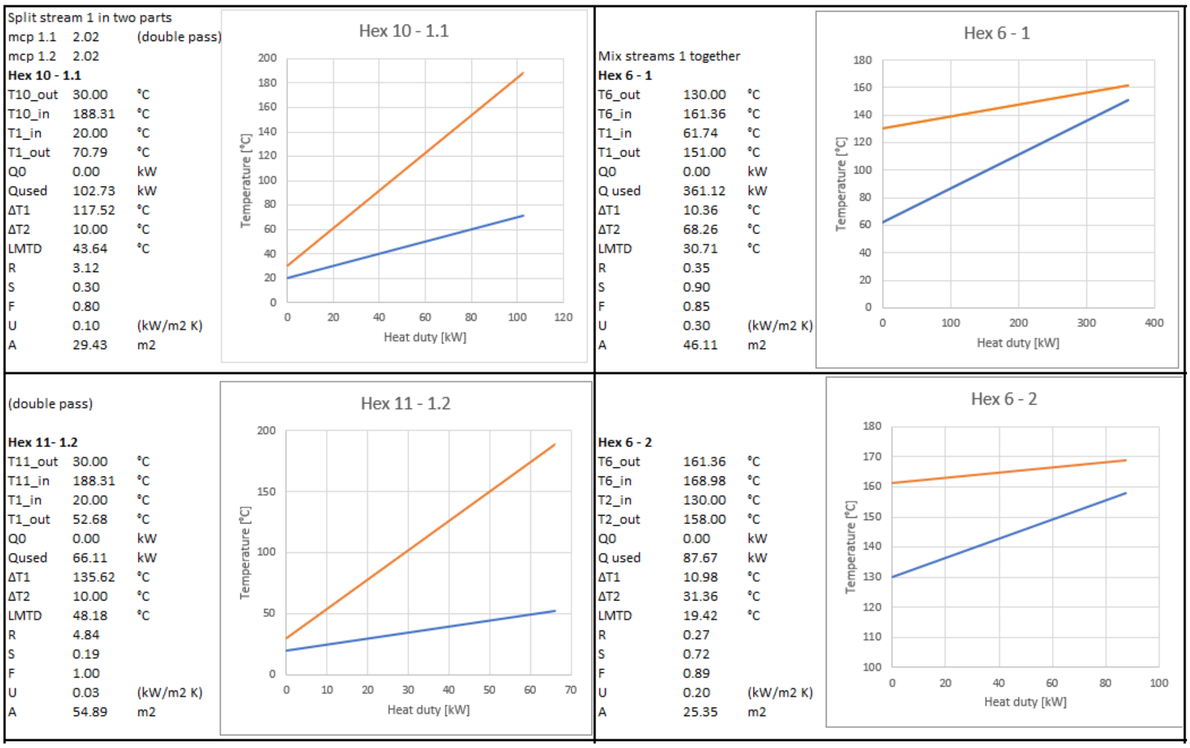

Split stream 1 in two parts		
mcp 1.1	2.02	(double pass)
mcp 1.2	2.02	
Hex 10 - 1.1		
T10_out	30.00	°C
T10_in	188.31	°C
T1_in	20.00	°C
T1_out	70.79	°C
Q0	0.00	kW
Qused	102.73	kW
ΔT1	117.52	°C
ΔT2	10.00	°C
LMTD	43.64	°C
R	3.12	
S	0.30	
F	0.80	
U	0.10	(kW/m2 K)
A	29.43	m2

Mix streams 1 together		
Hex 6 - 1		
T6_out	130.00	°C
T6_in	161.36	°C
T1_in	61.74	°C
T1_out	151.00	°C
Q0	0.00	kW
Q used	361.12	kW
ΔT1	10.36	°C
ΔT2	68.26	°C
LMTD	30.71	°C
R	0.35	
S	0.90	
F	0.85	
U	0.30	(kW/m2 K)
A	46.11	m2

(double pass)		
Hex 11- 1.2		
T11_out	30.00	°C
T11_in	188.31	°C
T1_in	20.00	°C
T1_out	52.68	°C
Q0	0.00	kW
Qused	66.11	kW
ΔT1	135.62	°C
ΔT2	10.00	°C
LMTD	48.18	°C
R	4.84	
S	0.19	
F	1.00	
U	0.03	(kW/m2 K)
A	54.89	m2

Hex 6 - 2		
T6_out	161.36	°C
T6_in	168.98	°C
T2_in	130.00	°C
T2_out	158.00	°C
Q0	0.00	kW
Q used	87.67	kW
ΔT1	10.98	°C
ΔT2	31.36	°C
LMTD	19.42	°C
R	0.27	
S	0.72	
F	0.89	
U	0.20	(kW/m2 K)
A	25.35	m2

Figure C.9: Heat Exchangers: first part of the plant

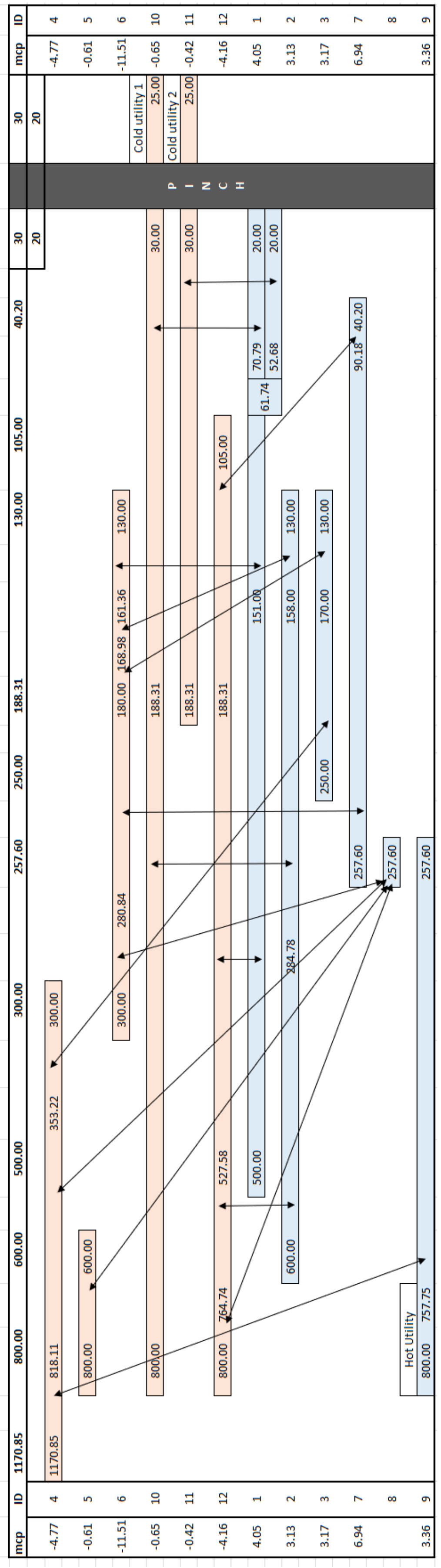

Figure C.7: Heat integration: heat exchanger network of the first part of the plant

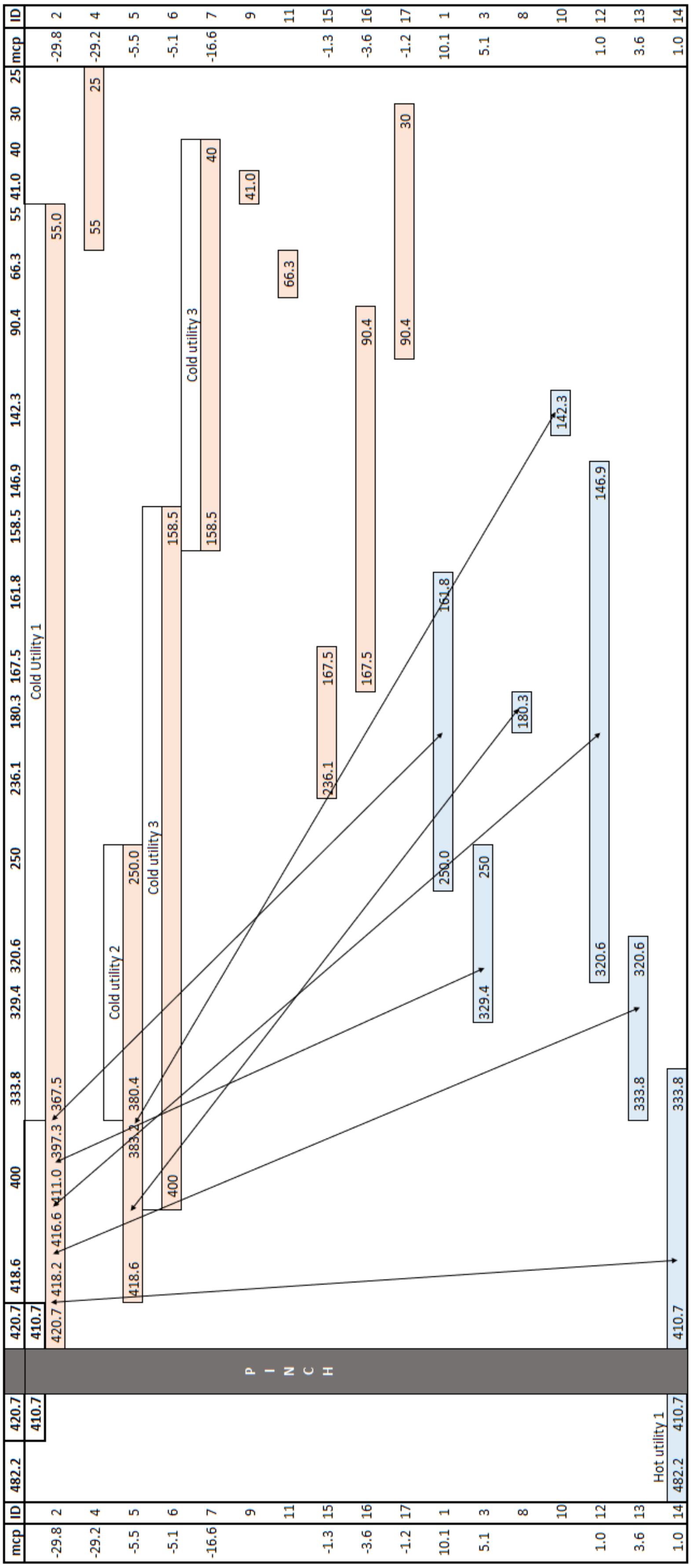

Figure C.8: Heat integration: heat exchanger network of the second part of the plant

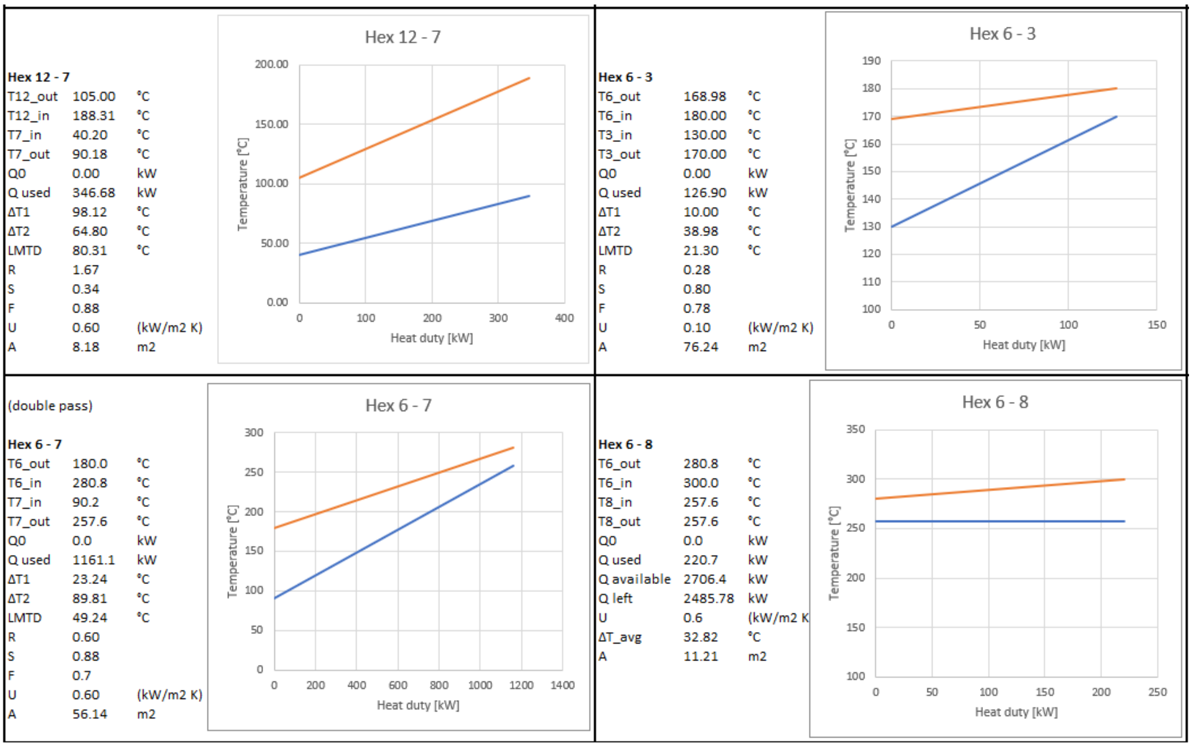

Hex 12 - 7

T12_out	105.00	°C
T12_in	188.31	°C
T7_in	40.20	°C
T7_out	90.18	°C
Q0	0.00	kW
Q used	346.68	kW
ΔT1	98.12	°C
ΔT2	64.80	°C
LMTD	80.31	°C
R	1.67	
S	0.34	
F	0.88	
U	0.60	(kW/m2 K)
A	8.18	m2

Hex 6 - 3

T6_out	168.98	°C
T6_in	180.00	°C
T3_in	130.00	°C
T3_out	170.00	°C
Q0	0.00	kW
Q used	126.90	kW
ΔT1	10.00	°C
ΔT2	38.98	°C
LMTD	21.30	°C
R	0.28	
S	0.80	
F	0.78	
U	0.10	(kW/m2 K)
A	76.24	m2

(double pass)

Hex 6 - 7

T6_out	180.0	°C
T6_in	280.8	°C
T7_in	90.2	°C
T7_out	257.6	°C
Q0	0.0	kW
Q used	1161.1	kW
ΔT1	23.24	°C
ΔT2	89.81	°C
LMTD	49.24	°C
R	0.60	
S	0.88	
F	0.7	
U	0.60	(kW/m2 K)
A	56.14	m2

Hex 6 - 8

T6_out	280.8	°C
T6_in	300.0	°C
T8_in	257.6	°C
T8_out	257.6	°C
Q0	0.0	kW
Q used	220.7	kW
Q available	2706.4	kW
Q left	2485.78	kW
U	0.6	(kW/m2 K
ΔT_avg	32.82	°C
A	11.21	m2

Figure C.10: Heat Exchangers: first part of the plant

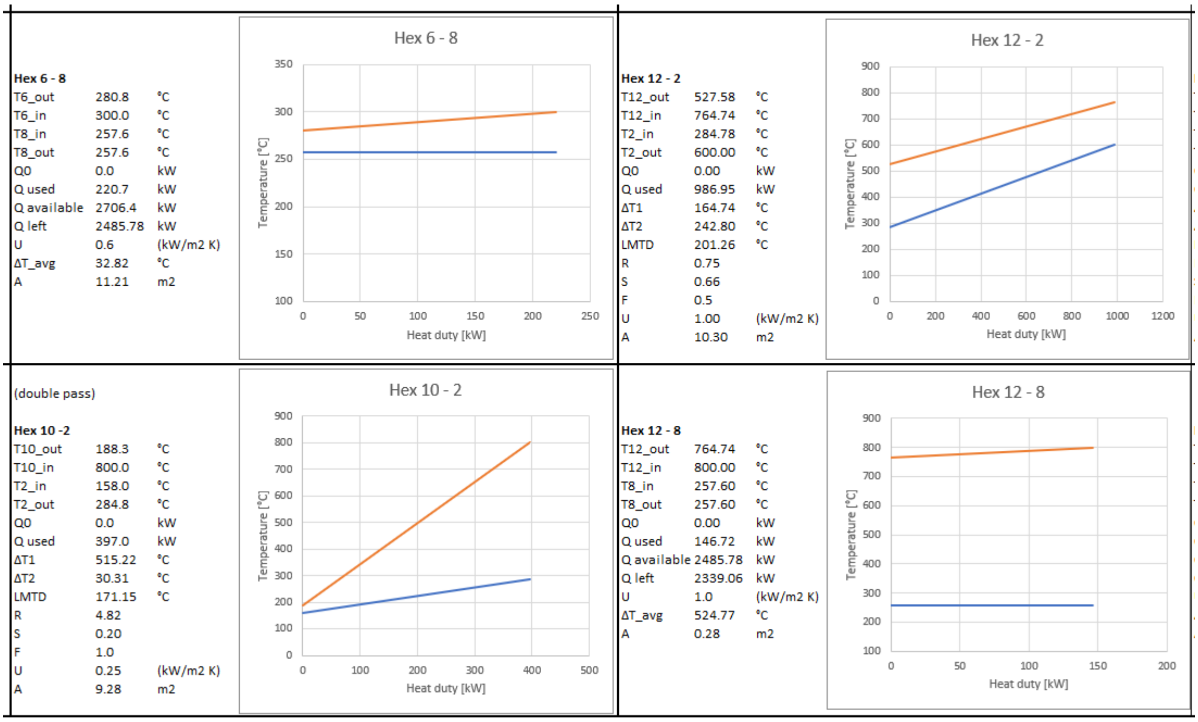

Hex 6 - 8

T6_out	280.8	°C
T6_in	300.0	°C
T8_in	257.6	°C
T8_out	257.6	°C
Q0	0.0	kW
Q used	220.7	kW
Q available	2706.4	kW
Q left	2485.78	kW
U	0.6	(kW/m2 K)
ΔT_avg	32.82	°C
A	11.21	m2

Hex 12 - 2

T12_out	527.58	°C
T12_in	764.74	°C
T2_in	284.78	°C
T2_out	600.00	°C
Q0	0.00	kW
Q used	986.95	kW
ΔT1	164.74	°C
ΔT2	242.80	°C
LMTD	201.26	°C
R	0.75	
S	0.66	
F	0.5	
U	1.00	(kW/m2 K)
A	10.30	m2

(double pass)

Hex 10 -2

T10_out	188.3	°C
T10_in	800.0	°C
T2_in	158.0	°C
T2_out	284.8	°C
Q0	0.0	kW
Q used	397.0	kW
ΔT1	515.22	°C
ΔT2	30.31	°C
LMTD	171.15	°C
R	4.82	
S	0.20	
F	1.0	
U	0.25	(kW/m2 K)
A	9.28	m2

Hex 12 - 8

T12_out	764.74	°C
T12_in	800.00	°C
T8_in	257.60	°C
T8_out	257.60	°C
Q0	0.00	kW
Q used	146.72	kW
Q available	2485.78	kW
Q left	2339.06	kW
U	1.0	(kW/m2 K)
ΔT_avg	524.77	°C
A	0.28	m2

Figure C.11: Heat Exchangers: first part of the plant

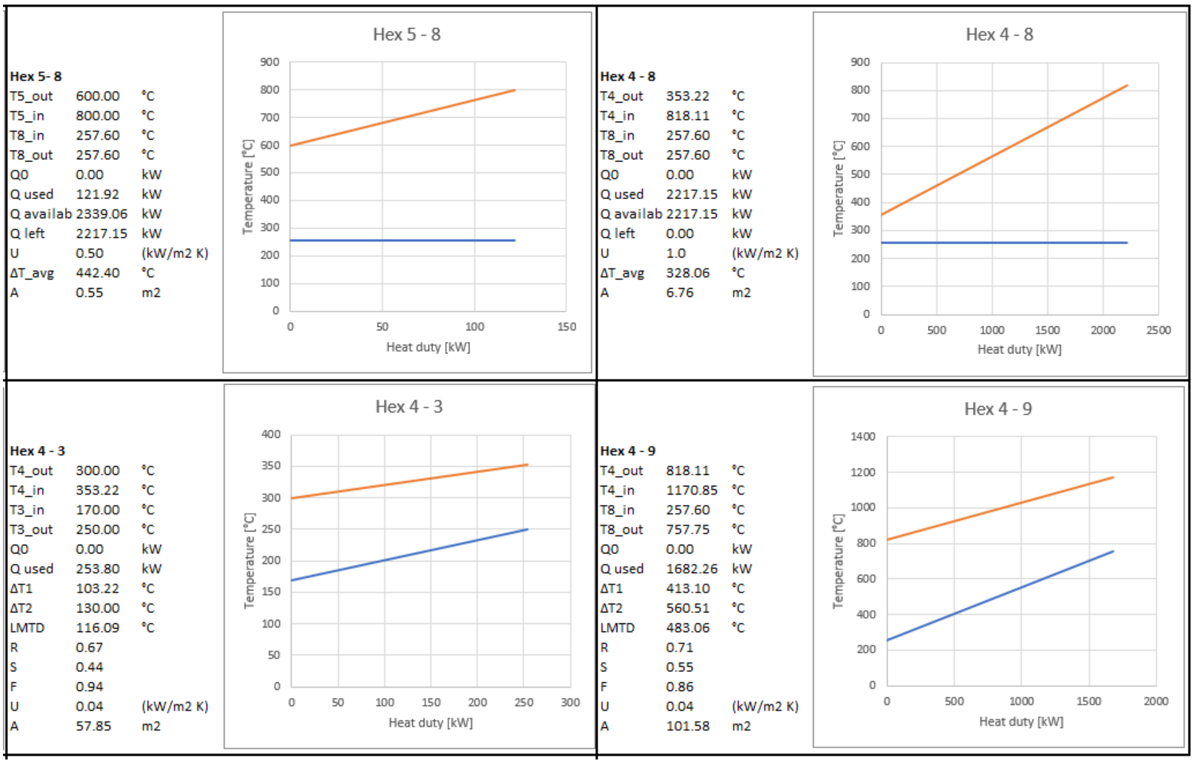

Hex 5- 8		
T5_out	600.00	°C
T5_in	800.00	°C
T8_in	257.60	°C
T8_out	257.60	°C
Q0	0.00	kW
Q used	121.92	kW
Q availab	2339.06	kW
Q left	2217.15	kW
U	0.50	(kW/m2 K)
ΔT_avg	442.40	°C
A	0.55	m2

Hex 4 - 8		
T4_out	353.22	°C
T4_in	818.11	°C
T8_in	257.60	°C
T8_out	257.60	°C
Q0	0.00	kW
Q used	2217.15	kW
Q availab	2217.15	kW
Q left	0.00	kW
U	1.0	(kW/m2 K)
ΔT_avg	328.06	°C
A	6.76	m2

Hex 4 - 3		
T4_out	300.00	°C
T4_in	353.22	°C
T3_in	170.00	°C
T3_out	250.00	°C
Q0	0.00	kW
Q used	253.80	kW
ΔT1	103.22	°C
ΔT2	130.00	°C
LMTD	116.09	°C
R	0.67	
S	0.44	
F	0.94	
U	0.04	(kW/m2 K)
A	57.85	m2

Hex 4 - 9		
T4_out	818.11	°C
T4_in	1170.85	°C
T8_in	257.60	°C
T8_out	757.75	°C
Q0	0.00	kW
Q used	1682.26	kW
ΔT1	413.10	°C
ΔT2	560.51	°C
LMTD	483.06	°C
R	0.71	
S	0.55	
F	0.86	
U	0.04	(kW/m2 K)
A	101.58	m2

Figure C.12: Heat Exchangers: first part of the plant

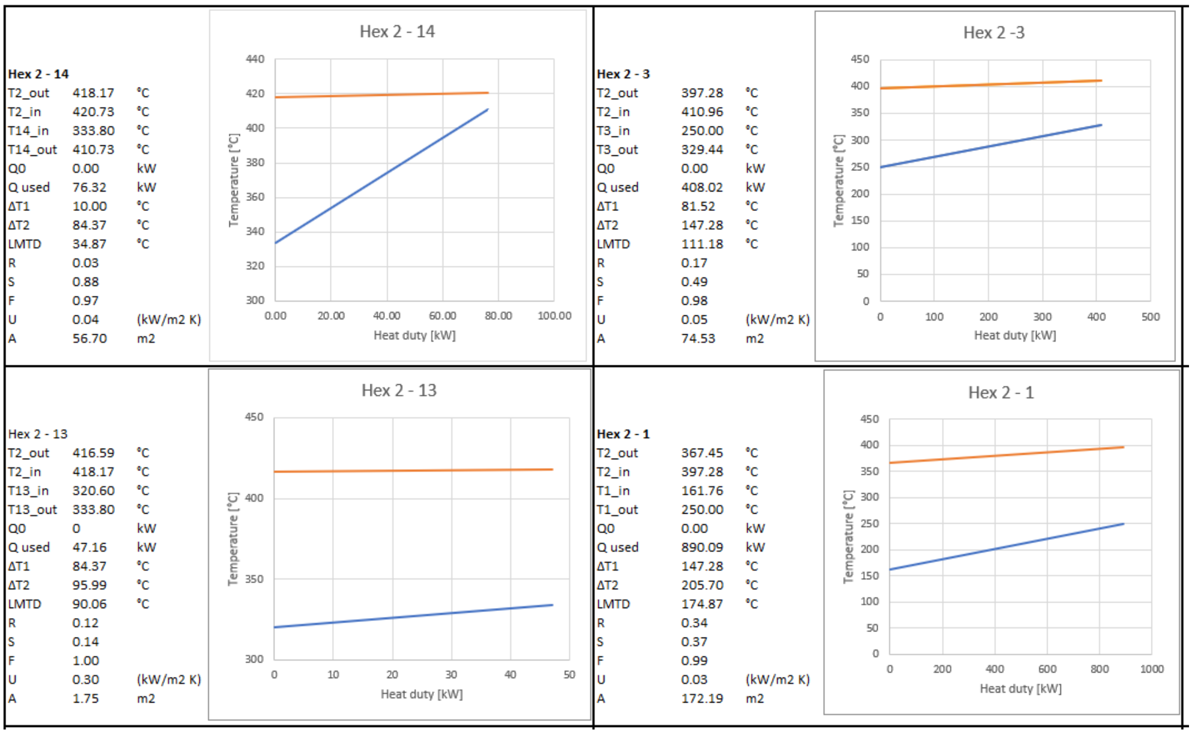

Hex 2 - 14		
T2_out	418.17	°C
T2_in	420.73	°C
T14_in	333.80	°C
T14_out	410.73	°C
Q0	0.00	kW
Q used	76.32	kW
ΔT1	10.00	°C
ΔT2	84.37	°C
LMTD	34.87	°C
R	0.03	
S	0.88	
F	0.97	
U	0.04	(kW/m2 K)
A	56.70	m2

Hex 2 - 3		
T2_out	397.28	°C
T2_in	410.96	°C
T3_in	250.00	°C
T3_out	329.44	°C
Q0	0.00	kW
Q used	408.02	kW
ΔT1	81.52	°C
ΔT2	147.28	°C
LMTD	111.18	°C
R	0.17	
S	0.49	
F	0.98	
U	0.05	(kW/m2 K)
A	74.53	m2

Hex 2 - 13		
T2_out	416.59	°C
T2_in	418.17	°C
T13_in	320.60	°C
T13_out	333.80	°C
Q0	0	kW
Q used	47.16	kW
ΔT1	84.37	°C
ΔT2	95.99	°C
LMTD	90.06	°C
R	0.12	
S	0.14	
F	1.00	
U	0.30	(kW/m2 K)
A	1.75	m2

Hex 2 - 1		
T2_out	367.45	°C
T2_in	397.28	°C
T1_in	161.76	°C
T1_out	250.00	°C
Q0	0.00	kW
Q used	890.09	kW
ΔT1	147.28	°C
ΔT2	205.70	°C
LMTD	174.87	°C
R	0.34	
S	0.37	
F	0.99	
U	0.03	(kW/m2 K)
A	172.19	m2

Figure C.13: Heat Exchangers: second part of the plant

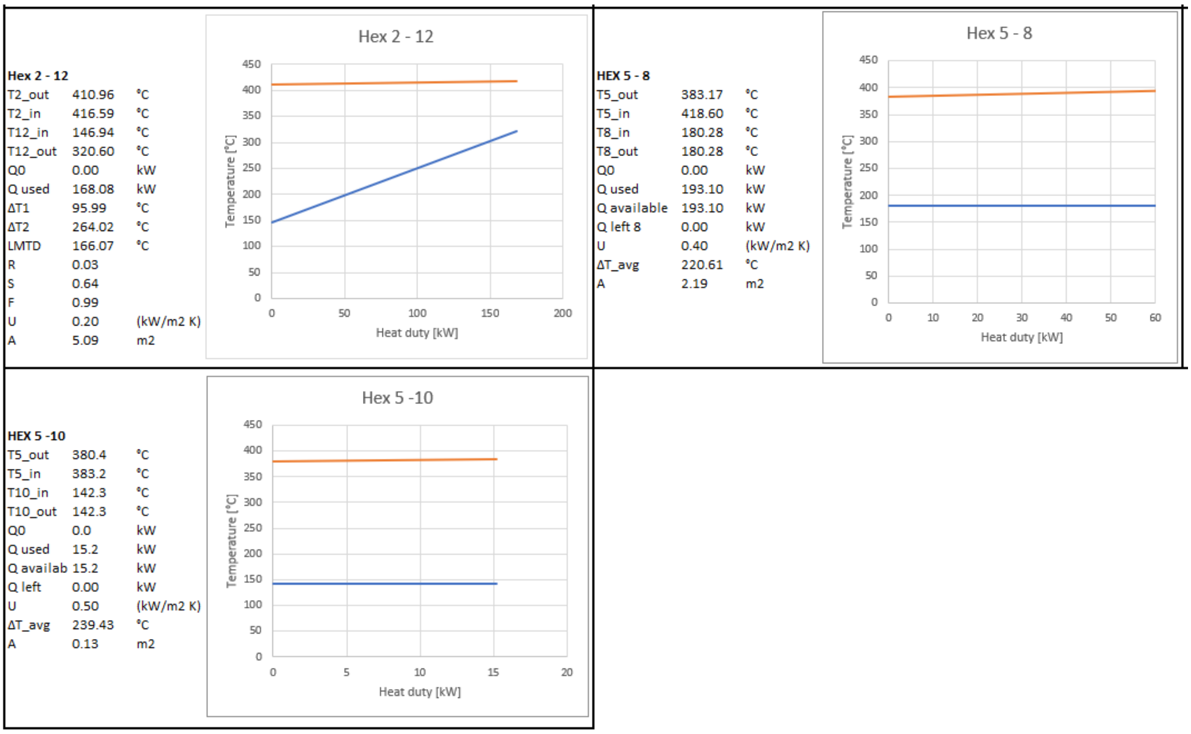

Hex 2 - 12

T2_out	410.96	°C
T2_in	416.59	°C
T12_in	146.94	°C
T12_out	320.60	°C
Q0	0.00	kW
Q used	168.08	kW
ΔT1	95.99	°C
ΔT2	264.02	°C
LMTD	166.07	°C
R	0.03	
S	0.64	
F	0.99	
U	0.20	(kW/m2 K)
A	5.09	m2

HEX 5 - 8

T5_out	383.17	°C
T5_in	418.60	°C
T8_in	180.28	°C
T8_out	180.28	°C
Q0	0.00	kW
Q used	193.10	kW
Q available	193.10	kW
Q left 8	0.00	kW
U	0.40	(kW/m2 K)
ΔT_avg	220.61	°C
A	2.19	m2

HEX 5 -10

T5_out	380.4	°C
T5_in	383.2	°C
T10_in	142.3	°C
T10_out	142.3	°C
Q0	0.0	kW
Q used	15.2	kW
Q availab	15.2	kW
Q left	0.00	kW
U	0.50	(kW/m2 K)
ΔT_avg	239.43	°C
A	0.13	m2

Figure C.14: Heat Exchangers: second part of the plant

Utilities

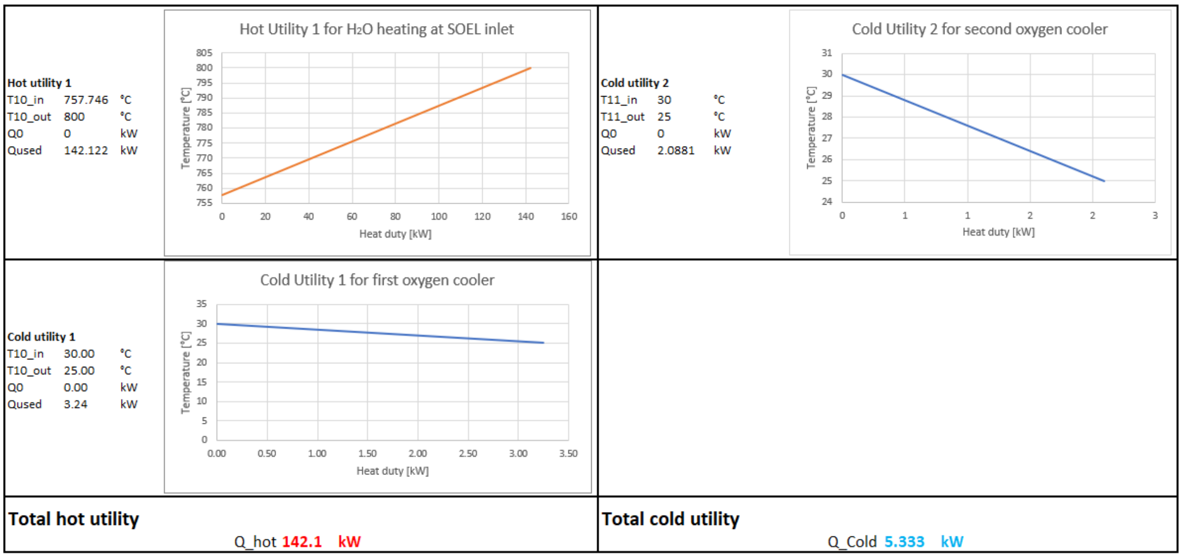

Hot utility 1

T10_in	757.746	°C
T10_out	800	°C
Q0	0	kW
Qused	142.122	kW

Cold utility 2

T11_in	30	°C
T11_out	25	°C
Q0	0	kW
Qused	2.0881	kW

Cold utility 1

T10_in	30.00	°C
T10_out	25.00	°C
Q0	0.00	kW
Qused	3.24	kW

Total hot utility Q_hot 142.1 kW

Total cold utility Q_Cold 5.333 kW

Figure C.15: Utilities: first part of the plant

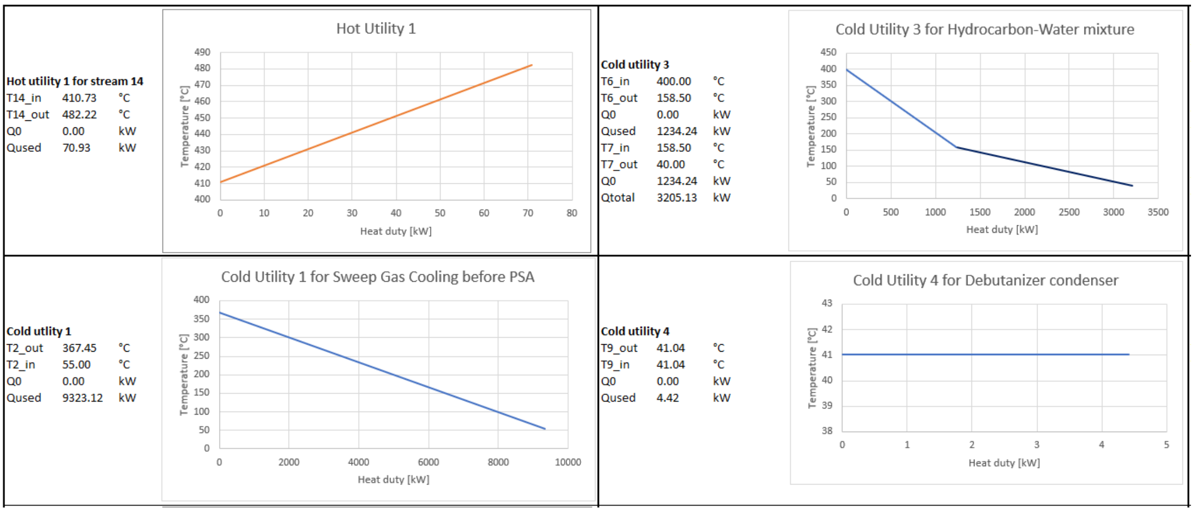

Hot utility 1 for stream 14		
T14_in	410.73	°C
T14_out	482.22	°C
Q0	0.00	kW
Qused	70.93	kW

Cold utility 3		
T6_in	400.00	°C
T6_out	158.50	°C
Q0	0.00	kW
Qused	1234.24	kW
T7_in	158.50	°C
T7_out	40.00	°C
Q0	1234.24	kW
Qtotal	3205.13	kW

Cold utlity 1		
T2_out	367.45	°C
T2_in	55.00	°C
Q0	0.00	kW
Qused	9323.12	kW

Cold utility 4		
T9_out	41.04	°C
T9_in	41.04	°C
Q0	0.00	kW
Qused	4.42	kW

Figure C.16: Utilities: second part of the plant

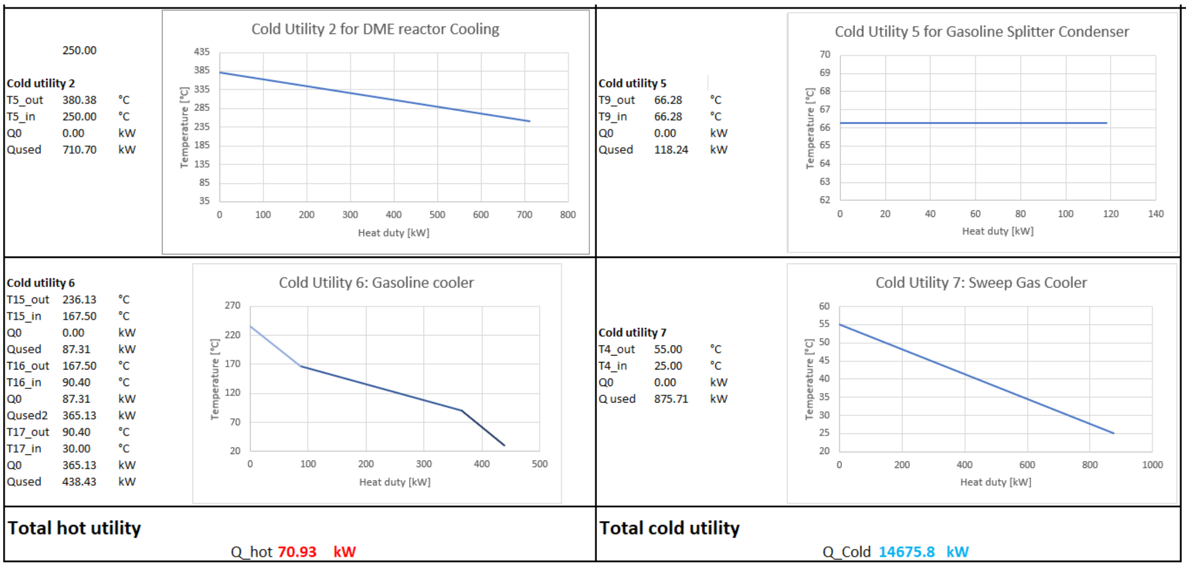

250.00

Cold utility 2		
T5_out	380.38	°C
T5_in	250.00	°C
Q0	0.00	kW
Qused	710.70	kW

Cold utility 5		
T9_out	66.28	°C
T9_in	66.28	°C
Q0	0.00	kW
Qused	118.24	kW

Cold utility 6		
T15_out	236.13	°C
T15_in	167.50	°C
Q0	0.00	kW
Qused	87.31	kW
T16_out	167.50	°C
T16_in	90.40	°C
Q0	87.31	kW
Qused2	365.13	kW
T17_out	90.40	°C
T17_in	30.00	°C
Q0	365.13	kW
Qused	438.43	kW

Cold utility 7		
T4_out	55.00	°C
T4_in	25.00	°C
Q0	0.00	kW
Q used	875.71	kW

Total hot utility

Q_hot 70.93 kW

Total cold utility

Q_Cold 14675.8 kW

Figure C.17: Utilities: second part of the plant

D

Economic Analysis

D.1. Bare Erected Cost

The calculation for the BEC starts from the calculation of the Purchased Equipment Cost:

$$log_{10}(\mathrm{PEC}_0) = k_1 + k_2\, log_{10}(C) + k_3[log_{10}(C)]^2 \tag{D.1}$$

where k_1, k_2, and k_3 are constant values depending on the equipment type and C is the capacity (a different quantity representative of the specific equipment). Pressure effects are taken into account through a pressure factor F_p. This is calculated with two different correlations. The correlation for process vessels is given by:

$$F_p = \frac{\frac{(p+1)D}{2[850-0.6(p+1)]} + 0.00315}{0.0063} \tag{D.2}$$

The correlation for pumps is defined as follows:

$$log_{10}(\mathrm{F}_p) = z_1 + z_2\, log_{10}(p) + z_3[log_{10}(p)]^2 \tag{D.3}$$

where z_1, z_2, and z_3 are equipment-specific constants and p is the pressure expressed in barg. Finally, the bare erected cost is estimated using:

$$\mathrm{BEC} = \mathrm{PEC}_0(B_1 + B_2\, F_M\, F_p) \tag{D.4}$$

The calculated BEC must then be escalated to account for inflation.

Bare Erected Cost Calculation from Correlations

Description	**Capacity**	**Unit**	**PEC$_0$ (M$)**	**p (barg)**	**Fp**	**Fm**	**Mater.**	**B$_1$**	**BEC (M€)**
Bio-oil pump (pos displ)	25.532	kW	0.20146	44	1.392	1.500	C steel	1.890	0.854
Steam Pump (centrifugal)	8.119	kW	0.04371	44	1.781	1.000	Cast Fe	1.890	0.169
HC pump (pos displ)	4.357	kW	0.020416	9	0.976	1.500	C steel	1.890	0.071
ZnO column	6.259	m^3	0.06462	44	8.3	0.700	Au ss	2.250	0.749

Bare Erected Cost Calculation from references						
Description	**Base Scale**	**Unit**	**Design Scale**	**Scaling Factor**	**Reference**	**BEC 2023 (M€)**
Debutanizer	16650.002	kg/hr (feed)	2089.095	0.680	[81]	0.306
Gasoline Splitter	14672.794	kg/hr (feed)	73060.077	0.680	[81]	3.861
Dealkylation reactor	6507.231	kg/hr (feed)	1200.643	0.650	[81]	3.327
DME membrane reactor	128464.512	kg/hr (feed)	102055.389	0.560	[81]	3.629
DME to hc reactor	38261.846	kg/hr (feed)	8722.198	0.650	[81]	2.692
SOEL system	0.001	MW	21.471	-	[57]	4.294
PSA					Assumed	2.000
Cyclone					Supplier	0.050
Filters					Supplier	0.150
Others	-	-	-	-	-	5.000

Regarding the heat exchanger network, the correlation used to estimate the cost of shell and tube heat exchangers [136] has the following form:

$$\text{BEC} = log_{10}(A) + c_1\,(A) + c_2\,(A)^2 + c_3 \tag{D.5}$$

Bare Erected Cost Calculation from references			
	Description	**Area (m^2)**	**BEC (M€)**
First part of the plant	Hex 10 - 1.1	29.429	1.322
	Hex 11 -1.2	54.890	1.566
	Hex12 - 7	8.180	0.821
	Hex 6 - 1	46.110	1.497
	Hex 6 - 2	25.350	1.264
	Hex 6 - 3	76.240	1.694
	Hex 6 - 7	56.140	1.574
	Hex 6 - 8	11.210	0.945
	Hex 10 - 2	9.280	0.871
	Hex 12 - 1	230.779	2.127
	Hex 12 - 2	10.300	0.912
	Hex 12 -8	0.280	-0.498
	Hex 5 - 8	0.550	-0.234
	Hex 4 - 3	57.850	1.586
	Hex 4 - 8	6.760	0.747
	Hex 4 - 9	101.580	1.806
Second part of the plant	Hex 2 -14	56.700	1.578
	Hex 2 - 13	1.750	0.219
	Hex 2 - 12	5.090	0.636
	Hex 2 - 3	74.530	1.685
	Hex 2 - 1	172.190	2.012
	Hex 5 - 8	2.190	0.306
	Hex 5 -10	0.130	0.080

D.2. Operating expenses

Operating expenses							
Consumable costs	**Price**		**Source**	**Amount**		**Cost**	
Pyrolysis oil	0.25	€/kg	[25]	40080000	kg/yr	10.02	M€/yr
Electricity	92.04	€/MWh	[25]	21.47	MW	15.84129	M€/yr
ZnO	4	€/kg	Supplier	12074.54	kg/yr	0.048298	M€/yr
MeOH catalyst cost	30	€/kg	Supplier	18.11503	kg/yr	0.000543	M€/yr
ZSM-5 cost	10	€/kg	Supplier	163.0352	kg/yr	0.00163	M€/yr
Nitrogen	0.0072	€/kg	[141]	7165006	kg/yr	0.051588	M€/yr
Transport costs	**Value**	**Unit**	**Source**				
Average transport distance	200	km	(Enschede - Rotterdam)				
Volume transported per day	100000	L/day	Bio-oil				
Volume carried per truck	25000	L	Standard				
Number of tracks	4						
Driver Wage (hourly)	20	€/hr	Assumption				
Truck consumption	0.3	L/km	Assumption				
Fuel needed for a round trip	90	L/truck					
Total fuel needed	360	L/day					
Total fuel cost per day	540	€/day					
Transportation cost per day	1020	€/day					
Personnel costs	**Value**		**Note**				
Shifts	3	8h duration					
Technicians/Operators	12	per shift					
Mainteinance Personnel	6						
Quaity control	4	per shift					
Administration and Support	10						
Management	4						
Technician Salary	35000	€/yr	Assumption				
Maintenance Salary	40000	€/yr	Assumption				
Quality Control Salary	40000	€/yr	Assumption				
Administration Salary	35000	€/yr	Assumption				
Management Salary	80000	€/yr	Assumption				
Others salary	40000	€/yr	Assumption				

D.3. Cash Flow and Net Present Value

Table D.1: Cash Flow and Net Present Value. Values in M€. Gasoline cost 2.326€/L, Electricity price 92.04 €/MWh

Construction Phase										
Yr	**ETOC$_i$**	**YDD**	**IDC**						**Cash Flow**	**NPV**
1	48.347	19.339	0.870						-29.530	-26.85
2	49.797	19.919	0.896						-30.416	-51.98
Operating Phase										
	An$_k$	**RD$_k$**	**IE$_k$**	**PR$_k$**	**Rev$_k$**	**Exp$_k$**	**Dep$_k$**	**Taxes**	**Cash Flow**	**NPV**
3	6.06	35.70	1.80	4.26	42.28	30.22	4.50	1.80		-47.93
4	6.06	31.25	1.61	4.45	42.28	30.22	4.50	1.85	5.35	-44.27
5	6.06	26.60	1.41	4.65	42.28	30.22	4.50	1.90	5.30	-40.98
6	6.06	21.74	1.20	4.86	42.28	30.22	4.50	1.95	5.25	-38.02
7	6.06	16.66	0.98	5.08	42.28	30.22	4.50	2.01	5.19	-35.36
8	6.06	11.35	0.75	5.31	42.28	30.22	4.50	2.07	5.13	-32.96
9	6.06	5.80	0.51	5.55	42.28	30.22	4.50	2.13	5.07	-30.81
10	6.06	0.00	0.26	5.80	42.28	30.22	4.50	2.19	5.00	-28.89
11	0.00	0.00	0.00	0.00	42.28	30.22	4.50	2.26	11.00	-25.03
12	0.00	0.00	0.00	0.00	42.28	30.22	4.50	2.26	11.00	-21.53
13	0.00	0.00	0.00	0.00	42.28	30.22	4.50	2.26	11.00	-18.34
14	0.00	0.00	0.00	0.00	42.28	30.22	4.50	2.26	11.00	-15.45
15	0.00	0.00	0.00	0.00	42.28	30.22	4.50	2.26	11.00	-12.81
16	0.00	0.00	0.00	0.00	42.28	30.22	4.50	2.26	11.00	-10.42
17	0.00	0.00	0.00	0.00	42.28	30.22	4.50	2.26	11.00	-8.25
18	0.00	0.00	0.00	0.00	42.28	30.22	4.50	2.26	11.00	-6.27
19	0.00	0.00	0.00	0.00	42.28	30.22	4.50	2.26	11.00	-4.47
20	0.00	0.00	0.00	0.00	42.28	30.22	4.50	2.26	11.00	-2.84
21	0.00	0.00	0.00	0.00	42.28	30.22	4.50	2.26	11.00	-1.35
22	0.00	0.00	0.00	0.00	42.28	30.22	4.50	2.26	11.00	0.00